UC Berkeley
UC Berkeley Electronic Theses and Dissertations

Title
The Deaths of Massive Stars: Core-Collapse Supernovae and Pre-Explosion Mass Loss

Permalink
https://escholarship.org/uc/item/172293nb

Author
Shivvers, Isaac Steven

Publication Date
2017

Peer reviewed|Thesis/dissertation

eScholarship.org Powered by the California Digital Library
University of California

The Deaths of Massive Stars: Core-Collapse Supernovae and Pre-Explosion Mass Loss

By

Isaac Steven Shivvers

A dissertation submitted in partial satisfaction of the

requirements for the degree of

Doctor of Philosophy

in

Astrophysics

in the

Graduate Division

of the

University of California, Berkeley

Committee in charge:

Professor Alexei V. Filippenko, Chair
Professor Daniel Kasen
Professor Peter E. Nugent
Professor Steven E. Boggs

Spring 2017

The Deaths of Massive Stars:
Core-Collapse Supernovae and Pre-Explosion Mass Loss

Copyright 2017
by
Isaac Steven Shivvers

Abstract

The Deaths of Massive Stars:
Core-Collapse Supernovae and Pre-Explosion Mass Loss

by

Isaac Steven Shivvers

Doctor of Philosophy in Astrophysics

University of California, Berkeley

Professor Alexei V. Filippenko, Chair

This thesis addresses some of the gaps in our current understanding of the deaths of massive stars ($M \gtrsim 10\,\mathrm{M}_\odot$) using observations of supernovae (SNe) obtained at frequencies from the radio up to the ultraviolet. I use new data collected by myself and the other researchers in the Berkeley SN research group using telescopes at the Lick and Keck Observatories; new data collected by my collaborators using many different telescopes, from the Very Large Array to the Hubble Space Telescope; and every category of relevant archived data available. Most of this work is organized by event: SNe 1998S and 2011dh provide representative case studies of their types (the interacting Type IIn SNe and the stripped-envelope Type IIb SNe, respectively), and I use SNe 2015G and 2015U to explore the properties of the rare and confounding subclass of Type Ibn SNe (which are both stripped-envelope and interacting). In addition to these focused analyses of single SNe, I use a curated sample of events to refine our measures of the relative rates of core-collapse SNe in an effort to better understand the populations of massive stars from which these events arise.

I dedicate this dissertation to dying stars, and to dead friends.

Contents

Acknowledgments v

1 Introduction 1
- 1.1 The Physics of Massive Stars . . . 2
- 1.2 The Physics of Core-Collapse Supernovae . . . 3
- 1.3 Clarifying Our Understanding of the Normal . . . 5
- 1.4 Testing Our Understanding through Examinations of the Peculiar . . . 6

2 Nebular Spectroscopy of the Nearby Type IIb Supernova 2011dh 7
- 2.1 Introduction . . . 8
- 2.2 Observations and Data Reduction . . . 9
  - 2.2.1 Spectroscopy . . . 9
  - 2.2.2 Data Reduction . . . 10
  - 2.2.3 Distance . . . 10
  - 2.2.4 Absolute Flux Calibration . . . 11
- 2.3 Analysis . . . 12
  - 2.3.1 The Spectrum of SN 2011dh at 600+ Days . . . 14
  - 2.3.2 The Oxygen Line Profile and the Ejecta Geometry . . . 19
- 2.4 Nebular Models . . . 23
- 2.5 Conclusions . . . 25

3 Early Emission from the Type IIn Supernova 1998S at High Resolution 27
- 3.1 Introduction . . . 28
- 3.2 Observations and Data Reduction . . . 29
  - 3.2.1 Young SN 1998S in High Resolution . . . 32
- 3.3 Modeling . . . 32
  - 3.3.1 CMFGEN . . . 32
  - 3.3.2 A Model of SN 1998S in High Resolution . . . 32
- 3.4 Discussion . . . 38
  - 3.4.1 A Cartoon . . . 38
  - 3.4.2 The SN Ejecta and Opaque CSM . . . 40
  - 3.4.3 The Inner CSM . . . 41

3.4.4 The Outer CSM . . . 46
3.4.5 Dust Extinction of SN 1998S . . . 47
3.4.6 Wolf-Rayet, Luminous Blue Variable, Red Supergiant? . . . 48
3.4.7 SN 2013cu . . . 50
3.5 Conclusion . . . 51

4 SN 2015U: A Rapidly Evolving and Luminous Type Ibn Supernova 52
4.1 Introduction . . . 53
4.2 Observations . . . 54
4.2.1 Photometry . . . 54
4.2.2 Spectroscopy . . . 57
4.2.3 Spectropolarimetry . . . 59
4.3 Analysis . . . 60
4.3.1 Dust Corrections . . . 60
4.3.2 Spectra . . . 63
4.3.3 Photometry . . . 71
4.3.4 Comparisons with Other Supernovae . . . 74
4.3.5 Temperature and Luminosity Evolution . . . 77
4.3.6 Nickel Content . . . 79
4.3.7 Progenitor Mass-Loss Rate . . . 80
4.3.8 Constraints on Progenitor Variability . . . 81
4.4 Conclusion . . . 83

5 The Nearby Type Ibn Supernova 2015G: Signatures of Asymmetry and Progenitor Constraints 84
5.1 Introduction . . . 85
5.2 Observations . . . 86
5.2.1 Ultraviolet through Infrared Imaging . . . 86
5.2.2 Radio . . . 89
5.2.3 Ultraviolet and Optical Spectra . . . 89
5.2.4 Line-of-Sight Extinction . . . 92
5.3 Analysis . . . 93
5.3.1 SN 2015G's Spectral Evolution . . . 93
5.3.2 Comparisons with Other SNe . . . 95
5.3.3 Spectropolarimetry . . . 99
5.3.4 The Ultraviolet Spectra . . . 100
5.3.5 The Spectral Energy Distribution . . . 101
5.3.6 Limits on Radio Luminosity . . . 102
5.3.7 Progenitor Constraints . . . 105
5.3.8 A Rough Schematic of the SN 2015G System . . . 109
5.4 Conclusion . . . 110

6 Revisiting the Lick Observatory Supernova Search Volume-Limited Sample: Updated Classifications and Revised Stripped-Envelope Supernova Fractions **112**
6.1 Introduction . . . 113
6.2 Data . . . 114
6.3 Classification Methods . . . 116
6.4 Updated Classifications . . . 120
6.4.1 Reclassified Objects . . . 123
6.4.2 Low-Certainty Classifications and Peculiar Events . . . 129
6.4.3 SNe Ia . . . 138
6.4.4 SNe Ic-BL . . . 139
6.4.5 SN 1987A-like SNe . . . 139
6.4.6 Ca-Rich Transients . . . 139
6.4.7 Type IIn SNe and SN Impostors . . . 140
6.4.8 SNe That Lack Spectra . . . 140
6.5 Updated Fraction Calculations . . . 141
6.6 Progenitor Constraints on Stripped-Envelope SNe . . . 144
6.7 Conclusion . . . 145
6.8 Journal of Data Presented Here . . . 147

Bibliography **153**

Acknowledgments

Thanks to my family, who have proven themselves boundlessly supportive of my journey into astrophysics these past few years. To my parents, Steve and Diane: thanks for the love and the education you've given me. To my older sister Elizabeth (and your growing family): thanks for leading the way.

Many thanks to my advisor Prof. Alex Filippenko for the years of support, for the opportunities you've given me, and for your work to keep Lick Observatory alive and available as a resource for me and my fellow students.

Thanks to my new friends, who have made the last six years fun (BADGrads! Wild Couch!), and thanks to my old friends, who have been there with me through so much (Domus! NHS!).

A heartfelt thanks to the many mentors who have shared with me their time and their thoughts throughout graduate school. I also owe a huge debt of gratitude to the researchers who came before me and built the strong foundation of observational supernova studies here at Berkeley, on top of which impressive edifice I am honored to add my own small contributions.

Thank you.

Chapter 1

Introduction

Stellar behemoths, stars born with masses $M \gtrsim 10\,\mathrm{M}_\odot$, end their lives in the catastrophic and luminous explosions we call supernovae (SNe). These SNe are the dominant mechanism by which our universe enriches itself — when massive stars die, they seed their environments with a variety of heavy elements fused out of the primordial mixture of simple hydrogen and helium created in the big bang. (Note that, when discussing the "life" of a star, astronomers generally mean the time span during which the star is a nuclear fusion engine in hydrostatic equilibrium with its own self-gravity — a few millions to many billions of years, depending on the mass of the star.) SN explosions from massive stars are triggered by the collapse of the stellar core, giving these events the moniker "core-collapse supernovae."

Astronomers have understood the basic physics of core-collapse SNe for a half century or more (e.g., Colgate & White 1966; Arnett 1971), but new observations continue to find extreme examples, many of which test the boundaries of our understanding. Nature continues to surprise us with its diversity and its complexity. The taxonomy of a few of these extreme events — an examination of how they relate to (and are different from) other examples within the family tree of SNe whose physics we understand — forms a substantive part of this thesis (Chapters §4 and §5). Another part works toward an ever-more-detailed understanding of the physics underlying relatively normal SNe, using two well-observed events as representative case studies (Chapters §2 and §3). The final chapter of this thesis (Chapter §6) uses observations of a curated sample of SNe to help solidify our understanding of the role of binarity within massive star populations.

In this introduction, I strive to place these works into the broader context of theoretical physics. The field is complex and rapidly changes as new methods of inquiry become technologically feasible — I apologize for the unavoidable brevity of this discussion and point the interested reader to the textbook of Arnett (1996), which (though now somewhat dated) provides an excellent overview of the field, and to the upcoming Handbook of Supernovae (Athem Alsabti 2015), which is scheduled to be finalized and published soon.

1.1 The Physics of Massive Stars

Stars spend most of their lives as more-or-less stable hydrogen fusion reactors. Nuclear fusion in their cores replenishes the energy they radiate away and maintains their hydrostatic equilibrium: internal pressure holds them up against the contractive force of their own self-gravity. For those stars that formed with $0.08 \lesssim M \lesssim 0.45\,\mathrm{M}_\odot$ (the low end of masses which provide the pressures and temperatures necessary to ignite hydrogen fusion in the core — less massive objects do not fuse and instead remain "brown dwarfs"), the story of fusion ends there. These "red dwarf" stars burn stably and slowly: they can remain alive for many billions to trillions of years (longer than the current age of the universe) and the helium created by hydrogen fusion never reaches the temperatures and densities required to fuse. These stars will someday end their lives as "white dwarfs" after their reserves of hydrogen fuel run out. However, none have yet made that transition, given their extreme lifespans and the current age of the universe (exempting some in binary systems, whose evolution has been strongly modified by interaction with their companion).

Somewhat more massive stars ($0.5 \lesssim M \lesssim 8\,\mathrm{M}_\odot$) undergo further evolution. Their helium accumulates in the core of the star, and these helium cores do eventually reach the intense conditions required to ignite the next stage: the fusion of helium into carbon and oxygen. This helium-burning phase of the star's life is much shorter than the hydrogen-burning phase. While helium fusion goes on near the center, a shell of hydrogen can remain ablaze at larger radii, raining helium ash down into the helium fusion zone, which then rains carbon and oxygen ash down onto the inner core. The transition from simple hydrogen burning in the core to this more complex internal structure of fusion produces a major change in the appearance of these stars. They expand into "red giants" and then shed their outer envelopes before ending their lives as white dwarfs — slowly cooling coals made up of helium, carbon, and oxygen. Most of the heavy elements created by these stars' fusion remain buried within these white dwarfs; they are not returned to the interstellar medium and therefore cannot be recycled into new stars.

More massive stars undergo further stages of this process before their deaths, the ashes of one process becoming the fuel for the next and each successive burning phase occurring more rapidly than the last. Each transition changes the appearance of the star and, though they can get quite complex, the evolutionary tracks of stars across a temperature-luminosity (Hertzprung-Russell) diagram are generally understood and can be modeled in detail.

Moderately massive stars ($8 \lesssim M \lesssim 10\,\mathrm{M}_\odot$) eventually begin to fuse carbon in their core, primarily producing oxygen, neon, and magnesium. This fusing core is sheathed by quiescent carbon and oxygen, all of which is surrounded by further shells of burning helium, then quiescent helium, then burning hydrogen, and finally the extended envelope of quiescent hydrogen reaching to the surface of the star. Again, a large fraction of the nucleosynthetic yield of these stars remains buried in their white dwarf remnants, after their outer envelopes are ejected.

At the cores of even more massive stars ($M \gtrsim 10\,\mathrm{M}_\odot$), neon burns to produce more oxygen and magnesium, then oxygen burns and leaves behind silicon and sulfur, and finally

silicon burns into iron and nickel, building up a complex "onion-skin" structure with the heaviest elements at the center. These last few stages of burning occur violently and rapidly: silicon burning lasts only about a day before catastrophe strikes (core collapse).

1.2 The Physics of Core-Collapse Supernovae

The dense cores of massive stars ($M \gtrsim 10\,\mathrm{M}_\odot$) exhibit truly extreme conditions at the end of the star's life. Their intense gravity overcomes the core's electron degeneracy pressure, the quantum-mechanical phenomenon that provides structural support for the cores of less massive stars. When electron degeneracy pressure fails, the innermost regions of the star rapidly collapse down until they have roughly the same density as an atomic nucleus — they are stopped from further collapse by neutron degeneracy pressure and the strong nuclear force. This forms a compact, degenerate neutron star core within the extended star, onto which the outer regions of the star then fall. When the collapse of the core is abruptly halted by nuclear forces, a shock wave is sent outward again into the rest of the infalling star (the "bounce"). A battle is thereby begun: the shock strives to move outward as the rest of the star is collapsing down upon it. The eventual emergence of this shock wave out through the stellar envelope, transforming the energy of the gravitational collapse into an explosion, is what we observe to be a core-collapse SN. However, the details of how exactly the shock overcomes the infall of material are still uncertain.

Most simulations of this process argue that the shock wave should be stalled by the material raining down upon it: that the dissociation of iron and the emission of neutrinos rob much of the energy from the shock, allowing the gravitational binding energy of the star to overwhelm it. If this happens, the outer parts of the star will not explode but instead will accrete onto the newborn neutron star at the core. The continued accretion of the star down onto the dense core can even overwhelm the structural support provided by neutron degeneracy pressure and the strong nuclear force, so that the entire star continues to collapse into a black hole. This is often called a "failed supernova." There is every reason to expect that these failed SNe sometimes occur in nature, but they are incredibly difficult to identify and observe, and no incontrovertible examples have yet been identified. Astronomers do, however, regularly find examples of luminous core-collapse SNe, showing that the shock wave is able to overcome the self-gravity of the collapsing star at least some significant fraction of the time. Exactly why computational models so often fail to explode remains an active topic of investigation by groups around the world.

Regardless, if the shock wave does overwhelm the star's gravitational pull, it then travels out through the star at great speed, heating the stellar material and accelerating it to velocities of $10{,}000\,\mathrm{km\,s^{-1}}$ or more. The shock launches the remnants of the star outward, and we call this rapidly expanding gas the "ejecta" of the SN. Depending upon the exact mass of the original star (and other parameters, to a lesser degree), the inner core remains as either a neutron star or black hole cinder, with the SN ejecta exploding out away from it.

The SN shock can be quite hot, and it therefore radiates blackbody emission, but the

heat left by the shock wave often does not last. If the SN's progenitor star had a large hydrogen envelope when it died (if it was a "red supergiant"), that envelope is ionized by the shock wave and the shock energy will be radiated away as the hydrogen recombines — this process often keeps the SN bright for about 100 days. If the progenitor was surrounded by dense circumstellar material (CSM), the shock's luminosity can be extended as the shock continues its travel out through the CSM, but this is relatively rare. If the progenitor star has neither an extended hydrogen envelope nor a dense CSM, however, the shock energy will be dissipated very quickly and last just a few days (sometimes less). Yet we find that these SNe remain luminous for much longer than that — how? The answer lies in their nucleosynthetic yield. Large quantities of radioactive nickel are created and, over the timespan of weeks to months, this nickel decays into cobalt and then again down into stable iron, emitting gamma rays and positrons which dump their energy into the ejected gas to keep it hot and luminous. This radioactivity is important for nearly all SNe, and it provides the main source of luminosity for many.

Diversity amongst core-collapse SNe illustrates the interplay between a few dominant factors — the mass, radius, and composition of the star at the moment of core collapse, the amount of radioactive nickel launched in the ejecta, the extent of the star's outer envelope, and the density, composition, and geometry of the star's surrounding CSM. Different combinations of the above parameters produce the different SNe that astronomers have designated Types II, Ib, Ic, etc. (for a review of the spectroscopic classifications of SNe, see Filippenko 1997). In contrast, the Type Ia SNe, whose utility as "standardizable candles" led to the discovery that the expansion of the universe is accelerating and thereby to our current understanding of ΛCDM cosmology, are not core-collapse SNe: they arise from an entirely different process. If the conditions are right, some carbon-oxygen white dwarfs (the remnants of stars born with low masses — $M \lesssim 8\,\mathrm{M}_\odot$), can also explode. These Type Ia SNe are not triggered by the gravitational collapse of a stellar core. Instead, the white dwarf (which is very dense) can be driven to the point at which a catastrophic "thermonuclear" detonation occurs, explosively burning the fuel of the white dwarf into heavier elements. This destroys the white dwarf entirely, scattering its material and leaving no remnant behind. Though the radioactivity of newly synthesized nickel also powers the luminosity of these SNe, many of their properties are quite different from those of the core-collapse SNe.

The above description of core-collapse SNe is, in its broad strokes, well understood. This thesis takes this scenario as its starting point and then strives to address a few of the uncertainties at the edges of our understanding. One of the biggest questions in the field today is how interaction with a binary companion may affect a massive star's evolution and explosion. Our physical understanding of these stars has been developed through analytical examinations and models of single stars, but it now seems clear that many (even most) massive stars do not live alone. Instead, they are often formed in binary pairs (sometimes even in triplets or higher multiplets) and they can undergo significant interaction with their companions before core collapse (e.g., Sana et al. 2012). This modifies the stars' behavior while alive and the observable signatures of their explosive deaths. The important work of mapping out the parameter spaces for numerical models of these interacting binary systems

is underway (e.g., Kim et al. 2015; Dessart et al. 2016), but binarity introduces substantial complexity to the physical models, making them more difficult to understand and use. Most stripped-envelope core-collapse SNe (Types IIb, Ib, and Ic) are now suspected to arise from massive stars that have lost their outer hydrogen envelopes through binary interactions, though some probably lose their envelopes through their own stellar winds (e.g., Matheson et al. 2001; Drout et al. 2011; Modjaz et al. 2014; Liu et al. 2016). Much of the below work attempts to better understand the connections between binary stellar models and the observed signatures of stripped-envelope SNe. The other fundamental topic addressed by this thesis is the surprising finding that a large subset of core-collapse SNe explode within a dense cloud of CSM lost by their progenitor star shortly before its death (Type IIn SNe; e.g., Schlegel 1990; Smith 2014). It is not clear exactly what processes drive such vigourous pre-explosion mass loss from a subset of progenitor stars (though plausible theoretical explanations have been put forth; e.g., Quataert & Shiode 2012), and observations of interacting SNe continue to map out their properties in advance of a complete physical understanding.

1.3 Clarifying Our Understanding of the Normal

The progenitors of SNe have, in several cases, been directly imaged by the Hubble Space Telescope (HST; e.g., Smartt 2009). The red supergiant progenitors of normal Type II SNe are those most commonly found, since Type II SNe are the most common type and their progenitors are luminous at the optical wavelengths where HST is most sensitive, but the nearby Type IIb SN 1993J provided astronomers with our first example of a stripped-envelope SN having direct images of its massive binary progenitor system. The progenitor of the Type IIb SN 2011dh was also detected by HST, and it also appears likely to have arisen from a binary star system (e.g., Maund et al. 2011; Van Dyk et al. 2013). In Chapter §2, I present and discuss spectroscopy of the fading SN 2011dh taken after the SN had become a transparent (but still glowing) cloud of expanding gas — the "nebular" phase. I discuss what we can learn about the geometry and power source for this SN, and I provide further information about its binary progenitor.

SN 1998S was a Type IIn SN; its expanding ejecta collided with a dense, hydrogen-rich cloud of CSM shed from its progenitor. As the first truly well-observed example of its class, it helped astronomers to identify and understand the physics governing these interacting SNe. In Chapter §3, I present a single unique and extremely high-resolution spectrum of the young SN 1998S, observed under unusual circumstances and forgotten in the archives for years. After re-examining the data in detail, I use them to provide a new window onto the intense shock interaction between the SN ejecta and the dense CSM. I present a detailed model of the spectrum, analyzing the composition and density profile of the CSM and, by extension, the history of pre-explosion mass-loss from the progenitor.

A largely self-consistent scenario of massive single-star evolution, enabled by the advent of numerical models running on modern computers, has been in place for at least 20 years

(e.g., Woosley et al. 2002). However, detailed comparisons to observations have recently shown that this scenario is incomplete at best — the relative rates of various core-collapse SN subtypes are inconsistent with its predictions, and these rates instead seem to be better understood as the results of binary interactions (e.g., Li et al. 2011b; Smith et al. 2011b). In Chapter §6, after implementing some methodological improvements to our classification techniques, I present updated measures of the relative rates of core-collapse SN types in an attempt to better constrain the effects of binarity in massive star systems.

1.4 Testing Our Understanding through Examinations of the Peculiar

At the boundary between normal stripped-envelope SNe (Types IIb, Ib, Ic) and normal interacting SNe (Type IIn) lie the markedly abnormal Type Ibn SNe (e.g., Pastorello et al. 2007; Foley et al. 2007). These extremely rare events (only ∼20 have been confirmed to date, out of the ∼10,000 SNe that have been classified) appear to be core-collapse SNe arising from hydrogen-poor stars which explode inside dense and hydrogen-poor clouds of CSM. Many uncertainties remain about the progenitors of these SNe Ibn. Two relatively nearby SNe Ibn exploded in 2015 (SNe 2015U and 2015G), and my team and I obtained large datasets on both of them. In Chapters §4 and §5 I present our observations and endeavor to understand the physical implications of those data.

Chapter 2

Nebular Spectroscopy of the Nearby Type IIb Supernova 2011dh

First published in the Monthly Notices of the Royal Astronomical Society:
Shivvers et al. (2013).
Co-Authors: Paolo Mazzali, Jeffrey M. Silverman, János Botyánszki, S. Bradley Cenko, Alexei V. Filippenko, Daniel Kasen, Schuyler D. Van Dyk, Kelsey I. Clubb

Chapter Abstract

We present nebular spectra of the nearby Type IIb supernova (SN) 2011dh taken between 201 and 678 days after core collapse. At these late times, SN 2011dh exhibits strong emission lines including a broad and persistent Hα feature. New models of the nebular spectra confirm that the progenitor of SN 2011dh was a low-mass giant ($M \approx 13$–$15\,\mathrm{M}_\odot$) that ejected $\sim 0.07\,\mathrm{M}_\odot$ of ^{56}Ni and $\sim 0.27\,\mathrm{M}_\odot$ of oxygen at the time of explosion, consistent with the recent disappearance of a candidate yellow supergiant progenitor. We show that light from the SN location is dominated by the fading SN at very late times ($\sim 2\,\mathrm{yr}$) and not, for example, by a binary companion or a background source. We present evidence for interaction between the expanding SN blastwave and a circumstellar medium at late times and show that the SN is likely powered by positron deposition $\gtrsim 1\,\mathrm{yr}$ after explosion. We also examine the geometry of the ejecta and show that the nebular line profiles of SN 2011dh indicate a roughly spherical explosion with aspherical components or clumps.

2.1 Introduction

Type IIb supernovae (SNe; Woosley et al. 1987; Filippenko 1988) are a relatively rare class of core-collapse supernova (SN), constituting only $\sim$7% of all SNe (Li et al. 2011b). Like other SNe II, they show strong hydrogen features in their early-time spectra, yet within only a few weeks after core collapse the H fades and the spectra of SNe IIb most closely resemble those of stripped-envelope SNe Ib (for a review of the spectral classification of SNe, see Filippenko 1997). SNe IIb therefore represent a transitional class of core-collapse SNe with only partially stripped envelopes. Exactly what process removes most (but not all) of their hydrogen envelope is still an open question, though interaction with a binary companion increasingly appears to be the most likely answer.

Thus far, there have been only a handful of nearby and intensely studied SNe IIb, including SN 2008ax ($\sim$9.6 Mpc; e.g., Chornock et al. 2011), SN 2001ig ($\sim$11.5 Mpc; e.g., Silverman et al. 2009), SN 2003bg ($\sim$21.7 Mpc; e.g., Hamuy et al. 2009; Mazzali et al. 2009), and SN 1993J ($\sim$3.69 Mpc; e.g., Filippenko et al. 1993; Matheson et al. 2000b). SN 2011dh in M51 ($\sim$8.05 Mpc; see §2.2.3 below) has become another nearby and very well-observed example of this unusual class of SN.

In early June 2011, SN 2011dh (also known as PTF11eon) was independently discovered within $\sim$1 day of core collapse by several amateur astronomers (Griga et al. 2011) and the Palomar Transient Factory collaboration (PTF; Rau et al. 2009; Law et al. 2009; Arcavi et al. 2011). The SN is apparent in an image taken by A. Riou of France on May 31.893 (UT dates are used throughout), while a PTF image taken May 31.275 does not detect a source down to a 3σ limiting magnitude of $m_g = 21.44$ (Arcavi et al. 2011). These observations most likely bracket the time of explosion, and for this paper we assume an explosion date of May 31.5. After discovery, a spectrum was promptly obtained by Silverman et al. (2011), and a possible progenitor star was first identified in archival *Hubble Space Telescope (HST)* images by Li & Filippenko (2011).

Maund et al. (2011) and Van Dyk et al. (2011) confirmed the identification of the likely progenitor star in *HST* images through ground-based adaptive optics imaging of the SN, measuring a spatial coincidence of the *HST* source and the SN to within 23 and 7 mas, respectively. Both reported that the source in the *HST* images has a spectral energy distribution consistent with a single star: a yellow (mid-F) supergiant with an extended envelope ($R \approx 200\,R_\odot$), a temperature of $\sim$6000 K, and a mass of 13–18 $M_\odot$. However, Van Dyk et al. (2011) expressed doubt that the yellow supergiant (YSG) is the true progenitor of SN 2011dh, instead preferring a scenario with a faint and compact progenitor as a binary companion to the YSG. This was largely motivated by the results of Arcavi et al. (2011), who favored a compact (10^{11} cm) binary companion based on the rapidity of the shock breakout and the relatively cool early photospheric temperature. Soderberg et al. (2012) supported this interpretation with radio and X-ray observations, estimating the progenitor size to be $\sim 10^{11}$ cm through modeling of the cooling envelope. In this compact-star scenario, the progenitor of SN 2011dh was theorised to be a faint Wolf-Rayet star with a zero-age main sequence mass $\gtrsim 25\,M_\odot$ and a history of mass loss through vigorous winds.

Bersten et al. (2012) disagreed; their hydrodynamical models suggested that an extended progenitor was required to produce the early-time light curve, at odds with the analytic relation used by Arcavi et al. (2011), originally from Rabinak & Waxman (2011). Bersten et al. (2012) found that a progenitor with a zero-age main sequence mass of 12–15 $M_\odot$ and a radius $\sim 200\,R_\odot$ was consistent with the early-time light curve and photospheric temperature, and showed that any model with a zero-age main sequence mass $\gtrsim 25\,M_\odot$ (i.e., a Wolf-Rayet star) was strongly disfavoured. Benvenuto et al. (2013) presented a model of a possible binary progenitor scenario with a $\sim 16\,M_\odot$ YSG primary star losing material to a much fainter $\sim 10\,M_\odot$ companion (undetectable in the pre-explosion *HST* images).

In addition, Murphy et al. (2011) argued that the mass of the SN 2011dh progenitor must be either $13^{+2}_{-1}\,M_\odot$ or $> 29\,M_\odot$, based upon an analysis of the star-formation history of the SN's environment. Star formation in the vicinity of the SN overwhelmingly occurred in two discrete bursts at < 6 and 17^{+3}_{-4} Myr; the zero-age main sequence mass of the SN is constrained by assuming the star is associated with one of those events, taking into account errors due, for example, to uncertain late-stage stellar evolution and mass loss. This result is consistent with the YSG progenitor scenario. Throughout 2012 other authors presented further panchromatic observations, some of which favoured a compact progenitor while others suggested an intermediate or extended progenitor, emphasising the need for a definitive progenitor identification (e.g., Krauss et al. 2012; Bietenholz et al. 2012; Campana & Immler 2012; Horesh et al. 2013; Sasaki & Ducci 2012).

The desired identification was provided by Van Dyk et al. (2013), who reported that the YSG progenitor candidate had disappeared from new *HST* images. Specifically, at an age of ~ 641 days SN 2011dh had faded down to 1.30 and 1.39 mag fainter than the YSG progenitor in the *HST* Wide Field Camera 3 (WFC3) $F555W$ and $F814W$ passbands, respectively. This result is corroborated by Ergon et al. (2014), who report a significant decline in the B, V, and r-band fluxes between pre-explosion imaging of the YSG progenitor and imaging of the SN at 600+ days past explosion. These results clearly point toward the extended YSG progenitor found in archival *HST* images as the progenitor star of SN 2011dh.

In this paper, we present six new spectra of SN 2011dh taken between 201 and 678 days after core collapse, in the nebular phase of its evolution. During the nebular phase, the SN ejecta are optically thin and we can directly observe the products of explosive nucleosynthesis without reprocessing through a photosphere. Our very late-time spectra show that the flux observed by Van Dyk et al. (2013) and Ergon et al. (2014) was produced primarily by the fading SN and not a stellar source. We present models of the nebular emission spectra and detailed analyses of the line profiles and the late-time flux energetics, providing constraints on the progenitor's mass and composition and the geometry of the explosion. We describe our observations and data-reduction procedure in §2.2, present our spectra and analysis in §2.3, discuss our model spectra in §2.4, and conclude in §2.5.

Table 2.1: Journal of spectroscopic observations

UT Date	Day$^{\alpha}$	Instrument	Range (Å)	Resolution$^{\beta}$ (Å)	Exposure time (s)
2011 Dec. 18	201	Kast	3480–10114	7	2400
2011 Dec. 24	207	Kast	3428–10100	6	2100
2012 Feb. 23	268	Kast	3444–10166	6	3000
2012 Apr. 29	334	LRIS	3312–7360	3	600
2013 Feb. 17	628	DEIMOS	4500–9640	3	2400
2013 Apr. 8	678	DEIMOS	4450–9603	3	3600

$^{\alpha}$Days since explosion (2011 May 31.5).
$^{\beta}$Approximate resolution (averaged over spectrum).

2.2 Observations and Data Reduction

2.2.1 Spectroscopy

Following its discovery in early June 2011, we began an extensive spectroscopic monitoring campaign of SN 2011dh. Some of our early-time spectra from the Lick and Keck Observatories (including a spectrum obtained only 2.4 days after explosion) have already been presented by Arcavi et al. (2011), and other groups have published their own spectra (Marion et al. 2014; Ergon et al. 2014; Sahu et al. 2013). This study focuses on the nebular phase of SN 2011dh.

We collected spectra using both the Lick and Keck Observatories, moving to a larger aperture as the SN faded away. We used the Kast double spectrograph on the Shane 3 m telescope at Lick Observatory (Miller & Stone 1993), the Low Resolution Imaging Spectrometer (LRIS) mounted on the 10 m Keck I telescope (Oke et al. 1995), and the DEep Imaging Multi-Object Spectrograph (DEIMOS) on the 10 m Keck II telescope (Faber et al. 2003) to collect 3, 1, and 2 nebular spectra of SN 2011dh, respectively. Table 2.1 summarises observing details for these 6 spectra.

2.2.2 Data Reduction

All observations were collected and reduced following standard techniques as described by Silverman et al. (2012). All spectra were taken with the slit oriented at the parallactic angle to minimise flux losses caused by atmospheric dispersion (Filippenko 1982). We use a low-order polynomial fit to arc-lamp observations to calibrate the wavelength scale, and we flux calibrate each spectrum with a spline fit to standard-star spectra observed the same night at a similar airmass. In addition, we have removed telluric absorption lines from all spectra. Upon publication, all raw spectra presented in this paper will be made available

in electronic format on WISeREP (the Weizmann Interactive Supernova data REPository; Yaron & Gal-Yam 2012).[1]

2.2.3 Distance

The distance to M51 has been measured through several independent methods with significant scatter among their results. We follow Marion et al. (2014) and adopt $D = 8.05 \pm 0.35$ Mpc, an average of four of these measures (Tonry et al. 2001; Tully & Fisher 1988; Vinkó et al. 2012; Feldmeier et al. 1997). All spectra have been deredshifted by M51's recession velocity, $600\,\mathrm{km\,s^{-1}}$ ($z = 0.002$, NED; Rush et al. 1996). M51 is at very low redshift and so we neglect time-dilation effects due to cosmological expansion. Both Arcavi et al. (2011) and Vinkó et al. (2012) use high-resolution spectra to measure the reddening toward M51 using Na I D absorption-line widths. Both find the host-galaxy extinction to be negligible and the Milky Way extinction to be consistent with values measured by Schlegel et al. (1998): $E(B-V) = 0.035$ mag. We deredden all spectra by this value prior to analysis, using the reddening law of Cardelli et al. (1989) and assuming $R_V = 3.1$. Note that Ergon et al. (2014) adopted a slightly higher value of $E(B-V) = 0.07^{+0.07}_{-0.04}$ mag, corresponding to a $\sim$5–10% difference in absolute flux level across the optical spectrum, not enough to significantly affect the discussion below.

2.2.4 Absolute Flux Calibration

Our observation techniques and data-reduction methods record the relative flux with high fidelity, but absolute flux calibrations are a persistent difficulty in long-slit spectroscopy. Variations in atmospheric seeing between flux-standard observations and science observations can result in varying amounts of flux falling out of the slit and spectral observations are often taken in less-than-photometric conditions with nonnegligible (and possibly varying) levels of cloud cover. Parts of our analysis (see §§2.3.1, 2.4) require an absolute flux measure, however, so we address this problem by flux calibrating our spectra to late-time photometry of SN 2011dh wherever possible.

Tsvetkov et al. (2012) present $UBVRI$ light curves of SN 2011dh extending to just over 300 days; we assume a linear decay in R-band magnitudes beyond $\sim$70 days and perform a maximum-likelihood analysis to estimate the R magnitude of SN 2011dh at the time each spectrum was taken. We chose the R band because of its relatively dense coverage and because several of the strongest nebular lines ([O I], [Ca II], Na I, Hα) fall within the passband, making it a good tracer of the SN's decline. We match synthetic photometry of our 201–334 day spectra to these values. All synthetic photometry has been calculated with `pysynphot` (Laidler et al. 2008). As shown in Figure 2.1, we find an R-band decline rate of of $0.0195 \pm 0.0006\,\mathrm{mag\,day^{-1}}$ and a V-band decline rate of $0.0207 \pm 0.0009\,\mathrm{mag\,day^{-1}}$ (reported errors are 68% confidence levels; $\sim 1\sigma$).

[1] http://wiserep.weizmann.ac.il

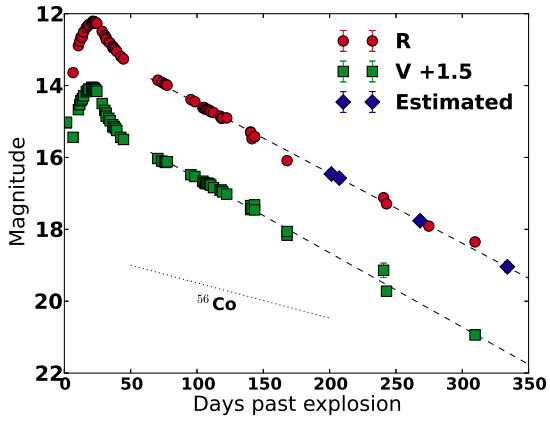

Figure 2.1: Photometric decline of SN 2011dh from Tsvetkov et al. (2012), with our best-fit decline rates and the ^{56}Co decay rate overplotted. The blue (diamond) points are the estimated values used to flux calibrate our spectra between days 201 and 334. Note that error bars for most points are smaller than the plotted symbol.

A linear decay in magnitudes is a reasonable assumption so long as emission is primarily driven by the radioactive decay of ^{56}Co (e.g., Colgate & McKee 1969; Arnett 1996). It is common for SNe Ib/IIb to display decline rates significantly faster than the $^{56}\mathrm{Co} \rightarrow {}^{56}\mathrm{Fe}$ rate ($0.0098\,\mathrm{mag\,day^{-1}}$) – a steep decline rate is reasonably interpreted as evidence for a declining γ-ray trapping fraction in the ejecta (as the ejecta expand and the density drops, more of the γ-rays produced by ^{56}Co decay escape before depositing their energy). The decline rate of SN 2011dh is slightly faster than those measured for both SN 1993J and SN 2008ax, two well-understood SNe IIb which had decline rates of 0.0157 and $0.0164\,\mathrm{mag\,day^{-1}}$, respectively (fit to days $\sim$60–300; Taubenberger et al. 2011). See §2.3.1 for a comparison between these early-time nebular decline rates and the flux observed at very late times (>600 days).

We do not assume that the same decay law holds true out to our last two spectra, at 628 and 678 days after core collapse. Instead, we repeat the analysis described above using photometry from Ergon et al. (2014), who report Nordic Optical Telescope (NOT) observations in V at 601 and 685 days.

2.3 Analysis

By 201 days past explosion SN 2011dh was well into the nebular phase, with a spectrum dominated by strong emission lines and little or no continuum. Figure 2.2 shows our complete spectral sequence of SN 2011dh in the nebular phase with spectra from 201 to 678 days after explosion and a few prominent lines identified, and compares the spectra of SN 2011dh to those of a few other prominent SNe IIb at comparable epochs.

Throughout the first year after explosion the nebular spectra of SN 2011dh are dominated by strong [O I] $\lambda\lambda$6300, 6364 and [Ca II] $\lambda\lambda$7291, 7324 emission lines, alongside a strong Mg I] λ4571 emission line and persistent Na I D and Hα lines. Table 2.2 lists relative line strengths of several prominent lines in the early nebular phase. We measured these fluxes by subtracting a local linear continuum and integrating over each line. Note that the continuum here is not from the photosphere of the SN, but rather is likely a mixture of blended lines,

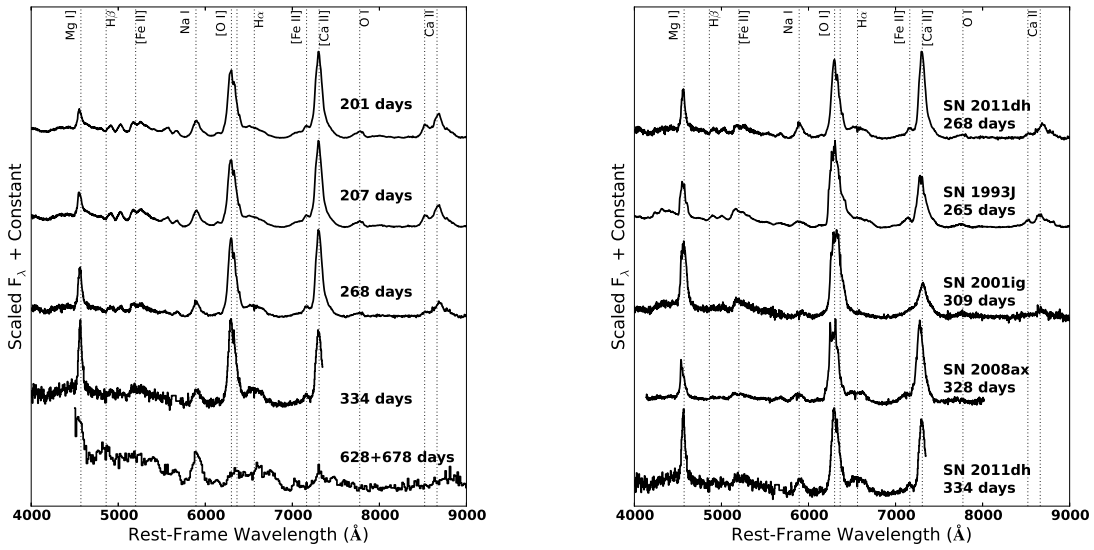

Figure 2.2: Nebular spectra of SN 2011dh (left) and comparison spectra of SN 1993J, SN 2001ig, and SN 2008ax (right). All spectra have been deredshifted. All displayed SNe are at low redshift and time-dilation effects are negligible; listed phases are days since explosion in Earth's reference frame. The spectra of SN 2011dh from 628 and 678 days have been coadded and rebinned to increase the signal-to-noise ratio (S/N). The SN 1993J spectrum is from Filippenko et al. (1994) and Matheson et al. (2000b), the SN 2001ig spectrum is from Silverman et al. (2009), and the SN 2008ax spectrum is from Milisavljevic et al. (2010).

producing a sort of pseudocontinuum. Also, note that this type of integrated flux measurement is by no means exact due to line blending and the approximated local continuum, but care was taken to treat each line similarly and these measures should accurately portray the relative-flux trends.

The relative flux of [Ca II] and [O I] has been shown to be a useful indicator of progenitor core mass, with smaller [O I]/[Ca II] ratios generally indicative of a less massive helium core at the time of explosion (e.g., Fransson & Chevalier 1989; Jerkstrand et al. 2012). SN 2011dh displays an [O I]/[Ca II] ratio significantly smaller than that in both SN 1993J and SN 2001ig. The ratio is similar to that in SN 2008ax, which also displayed a similar upward trend throughout the nebular phase (Silverman et al. 2009; Filippenko et al. 1994; Chornock et al. 2011). It therefore appears that SN 2011dh's progenitor He core mass was relatively close to that of SN 2008ax and significantly less than that of both SN 2001ig and SN 1993J. See §2.4 for a more thorough analysis.

There appears to be a weak blue continuum in the 600+ day spectra of SN 2011dh. Maund et al. (2004), in a very high S/N spectrum of SN 1993J taken $\sim$10 yr after explosion, were able to associate a blue continuum (and a detection of the Balmer absorption-line series) with a companion B supergiant, thereby strongly supporting the binary nature of the

Table 2.2: Integrated line fluxes relative to [Ca II] $\lambda\lambda$7291, 7324

Day$^{\alpha}$	[Ca II] + Fe II$^{\beta}$	Mg I]	Na I D	Ca II$^{\gamma}$	O I λ7774	Hα^{δ}	O I$^{\epsilon}$ $\lambda\lambda$6300,6364
201	1.0	0.114	0.151	0.403	0.059	0.196	0.614
207	1.0	0.140	0.147	0.369	0.059	0.222	0.621
268	1.0	0.218	0.135	0.247	0.039	0.253	0.749

Errors are difficult to estimate for these values, as line edges and continuum levels have been estimated by eye. However, care was taken to treat each line similarly. Measurement errors alone (determined through repeated measurements) are $\sim$5%.
$^{\alpha}$Days since explosion (2011 May 31.5).
$^{\beta}$[Ca II] $\lambda\lambda$7291, 7324 and Fe II λ7155 are difficult to deblend, so we present the integrated flux of both. The contribution from Fe II is, however, very much smaller than [Ca II] (see Fig. 2.2).
$^{\gamma}$The Ca II near-infrared triplet.
$^{\delta}$To measure the blended [O I] and Hα lines we assume Hα is symmetric about the rest wavelength (6563 Å). We report the Hα flux as twice the value obtained by integrating from the red continuum to 6563 Å.
$^{\epsilon}$The [O I] line was integrated after subtracting a smoothed Hα profile, again assuming symmetry about 6563 Å in the Hα line.

SN and identifying the components – a K-giant progenitor and a B-giant companion. In the spectrum of SN 2011dh above, however, we cannot attribute the blue continuum to any stellar companion: fitting a Rayleigh-Jeans curve to the apparent continuum yields best-fit temperatures much too hot for a stellar source. The blue continuum in SN 2011dh is instead most likely a pseudocontinuum caused by many blended lines. In addition, our spectra are more noisy at the blue end, and the blue rise may be partially caused by increased noise. *HST* photometry taken near this time provides a slightly redder colour than synthetic photometry from our spectrum: $F555W - F814W = 0.69 \pm 0.03$ mag (641 days; Van Dyk et al. 2013), compared to $\sim$0.34 mag from our spectrum (628+678 days). Thus, we tilt our spectrum to match the *HST* $F555W - F814W$ colour and re-examine the result for evidence of a stellar companion. Our conclusion is essentially unchanged: even after tilting our spectrum, the blue pseudocontinuum yields unreasonably hot best-fit blackbody temperatures.

Interestingly, there is a broad Hα emission line in spectra of SN 2011dh through at least 334 days, similar to the emission seen in SN 1993J, (Filippenko et al. 1994), SN 2007Y (Stritzinger et al. 2009), and SN 2008ax (Milisavljevic et al. 2010) around the same time. There is also some indication of very broad Hα in the spectra of SN 2011dh at 600+ days, though the S/N is low. At late times the Hα emission of SN 1993J was unambiguously identified with interactions between the expanding SN shock wave and circumstellar material produced by mass loss from the progenitor (e.g., Patat et al. 1995; Houck & Fransson 1996;

Matheson et al. 2000b). As we discuss in §2.3.1, SN 2011dh seems to present us with a more complex situation.

SN 2011dh, like SN 2001ig, displayed a relatively strong Mg I] λ4571 line – significantly more prominent than Mg I] in spectra of SN 2008ax (Silverman et al. 2009; Chornock et al. 2011). This is especially apparent around day 334, where Mg I] emission almost matches the emission in [Ca II] and [O I]. At very late times, in the 628+678 day spectrum, the Mg I] is still quite apparent, though [O I] and [Ca II] have faded into the noise. Unfortunately, our 628 and 678 day spectra do not go much blueward of the Mg I] emission peak; this, together with high noise levels at the blue end, prevents us from measuring the integrated flux reliably at these times. The Na I D flux is also remarkably strong in the 600+ day spectra, as discussed below.

2.3.1 The Spectrum of SN 2011dh at 600+ Days

Recent photometry of the site of SN 2011dh taken by *HST* (Van Dyk et al. 2013) and the Nordic Optical Telescope (NOT; Ergon et al. 2014) provide late-time flux measurements of SN 2011dh. Our latest two spectra, taken around the same time, confirm that the optical flux measured by these groups was predominantly from the SN remnant and not, for example, from a binary companion to the progenitor star. 678 days after explosion, SN 2011dh continues to show clear Na I D emission with approximately the same width as at earlier epochs (see Fig. 2.3). [Ca II] emission is present but much reduced relative to Na I D, Mg I] is still relatively strong but is buried in the noise at the blue end of the spectrum, and there is a very broad feature near 6500 Å – most likely a blend of broad Hα and the [O I] doublet.

Ergon et al. (2014) report a slight fading of 2011dh between days 601 and 685: $0.009 \pm 0.0026\,\mathrm{mag\,day^{-1}}$ in V. The V-band decline rate between the last observation reported by Tsvetkov et al. (2012, 19.44 ± 0.12 mag, 2012 Apr. 4, 310 days) and the first observation by Ergon et al. (2014, 22.56 ± 0.10 mag, 2013 Jan. 20, 601 days) is $\sim 0.011\,\mathrm{mag\,day^{-1}}$. Both of these rates are notably less rapid than the $0.021\,\mathrm{mag\,day^{-1}}$ decline rate measured from the 65–310 day photometry by Tsvetkov et al. (2012, see §2.2.4); it seems that the flux decline rate is slowing down at $t \gtrsim 300$ days.

Na I D provides the clearest feature in our 600+ day spectra and is unambiguously associated with the SN (see Fig. 2.3). We measured the integrated flux in the Na I D line for each of our spectra in the nebular phase; the results are shown in Table 2.3 and Figure 2.4. Note that the absolute flux calibrations of long-slit spectra are often unreliable. As described in §2.2.4, we address this by flux calibrating our spectra to published photometry. Quoted uncertainties include estimated error due to spectral noise, reported photometric errors, and estimated measurement errors, all added in quadrature. As Figure 2.4 illustrates, the Na I D line flux mirrors the trends in the photometry, falling at the early R-band decline rate through ~ 300 days but then deviating significantly around 300 or 350 days and fading much more slowly through ~ 600 days.

This slowdown in the flux decay rate is possibly indicating a transition to γ-ray transparency in the ejecta of SN 2011dh. As described in more detail by Arnett (1996), ^{56}Co

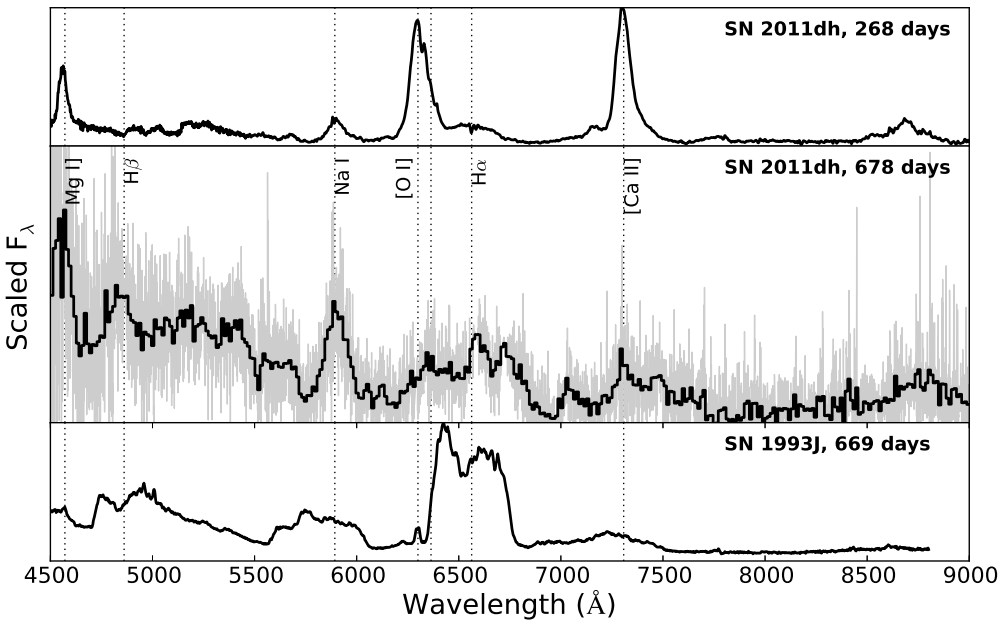

Figure 2.3: SN 2011dh at 268 and 678 days, with SN 1993J at a similar epoch for comparison (SN 1993J spectrum from Matheson et al. 2000b). The later spectrum of SN 2011dh has been rebinned to increase the S/N; the unbinned spectrum is shown in the background. In both SNe, the broad Hα emission likely comes from interaction between an expanding shockwave and the circumstellar medium, but the Na I D line emission in SN 2011dh is most likely powered by ^{56}Co decay while SN 1993J has a Na I D line powered by circumstellar interaction.

radioactivity ($^{56}\mathrm{Co} \rightarrow {}^{56}\mathrm{Fe}$ with a half-life of $\sim$77 days) is the dominant source of energy for SNe at these epochs. ^{56}Co decay produces both γ-rays and high-energy positrons. The kinetic energy of the positrons is very likely to be deposited into the ejecta (and therefore contribute to the nebular line flux), while the fraction of γ-ray energy that gets deposited depends upon the optical depth of the ejecta to γ-rays. As the ejecta expand and the optical depth drops, a larger fraction of the γ-rays escape, carrying their energy with them.

As the γ-ray energy deposition fraction drops, the SN fades away faster than the ^{56}Co rate (0.0098 mag day^{-1}), until such time as the ejecta are transparent to γ-rays and approximately all of them escape. At that point, positron energy deposition dominates the energy input of the ejecta and the bolometric flux decline rate is expected to follow the ^{56}Co rate closely. Broadband photometry should exhibit roughly the same behaviour. Assuming that the ejecta's abundance of neutral sodium is constant and that the exposure to heating does not change significantly, so should the Na I D line flux. The flux decline rates for both the late-time V-band photometry and the Na I D line flux in SN 2011dh are consistent with a transition to a positron-powered ejecta sometime between 300 and 350 days. Because

Table 2.3: Photometric normalisations

Day$^{\alpha}$	Passband	Mag $\pm 1\sigma$	Na I D flux$^{\beta}$
201	R	16.46 ± 0.06	36.26 ± 2.10
207	R	16.58 ± 0.07	31.95 ± 2.24
268	R	17.76 ± 0.10	9.69 ± 1.14
334	R	19.04 ± 0.14	4.22 ± 2.45
628	V	22.80 ± 0.26	0.338 ± 0.171
628+678$^{\gamma}$	$F555W$	23.198 ± 0.019	0.315 ± 0.098
628+678$^{\gamma}$	$F814W$	22.507 ± 0.022	0.439 ± 0.137
678	V	23.32 ± 0.38	0.368 ± 0.243

Photometric normalisations applied to our nebular spectra and resultant absolute flux in the Na I D line. See §2.2.4 for a description of how we calculated the photometric estimates. We measured the integrated line flux in the manner described in §2.3, and the quoted errors include photometric normalisation errors, spectral noise, and estimated measurement errors added in quadrature.
$^{\alpha}$Days since explosion (2011 May 31.5).
$^{\beta}$Units: $10^{-15}\,\mathrm{erg\,s^{-1}\,cm^{-2}}$.
$^{\gamma}$To estimate the spectrum near the *HST* observations, we produce an average of the 628 and 678 day spectra. We flux calibrate both spectra to $R = 0.0$ mag, coadd them, and renormalise the result to the *HST* photometry. This produces an equally weighted average between the two spectra – we assume the SN is changing slowly at this epoch and that this averaged spectrum is a good measure of the relative flux near the average time (653 days).

positrons deposit their energy locally (near the decaying ^{56}Co) but γ-rays deposit energy throughout the ejecta, the transition to a positron-dominated energy input is likely to correspond to a change in the dominant emission lines. In SN 2011dh, we see that Na I D and Mg I] emission stays strong in the positron-dominated epoch while [O I] and [Ca II] fade away. More detailed modeling is necessary to test this scenario, however.

Note that the above discussion assumes the bolometric light curve is completely powered by ^{56}Co. Any additional energy input could be a confounding factor; most importantly, there may be a flux contribution from shockwave interactions with circumstellar gas. The progenitors of SNe IIb are stars that have lost much of their hydrogen envelope, either through radiative winds or through stripping by a binary companion. If a significant amount of that material remains nearby in a cloud of circumstellar matter, the expanding SN ejecta will impact it and form a shock boundary. This shocked region produces high-energy photons which are then reprocessed down to optical wavelengths by material in the outer shells of the ejecta, thereby producing broad emission lines and (possibly) a blue pseudocontinuum (for a more complete description of this process, see, e.g., Chevalier & Fransson 1994; Fransson

1984). Late-time emission from circumstellar interaction (CSI) is common in SNe IIn (e.g., Fox et al. 2013), which have lost a majority of their envelope in the years prior to explosion, and it has been observed in other SNe IIb (e.g., Matheson et al. 2000b).

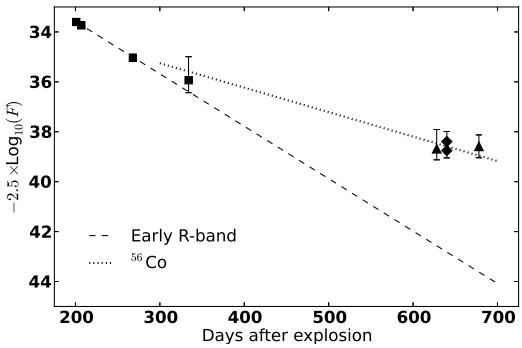

Figure 2.4: Integrated Na I D flux in nebular spectra of SN 2011dh. All values plotted here are presented in Table 2.3. The dashed line shows the early-time decline rate for the R band (see §2.2.4) and the dotted line shows the decline rate of ^{56}Co (0.0098 mag day^{-1}). Boxes are used for spectra normalised to Tsvetkov et al. (2012) photometry, triangles for spectra normalised to Ergon et al. (2014) photometry, and diamonds for spectra normalised to Van Dyk et al. (2013) photometry. The positron-dominated epoch appears to begin somewhere between 300–350 days.

CSI could be augmenting the Na I D flux discussed above through either Na I D or He I λ5876 emission. As Figure 2.3 shows, SN 1993J clearly displayed a shockwave-powered Na I D + He I blend with $\sim 1/3$ the flux of the Hα line (Matheson et al. 2000b). In the Chevalier & Fransson (1994) model, approximately all of the shockwave-powered Na I D flux is emitted from a thin shell at the boundary between the unshocked circumstellar material and the shocked ejecta, while the Hα flux comes from both the thin shell and the shocked ejecta. This would imply a more boxy line profile for Na I D than Hα (see below for further discussion of the nebular Hα line in SN 2011dh). However, the late-time Na I D emission of SN 2011dh has a relatively narrow profile with no evidence of the box-like shape that would be expected if it were mostly CSI-powered, and the profile does not appear to change significantly between the spectra taken at <1 yr and those taken at >1 yr. It seems clear that, at 600+ days, the dominant source of Na I D flux remains radioactive decay and not CSI, though there may well be some small amount of shockwave-powered He I and Na I D emission buried in the noise. If SN 2011dh's CSI-powered Na I D + He I flux were a factor of 3 less than the Hα flux (as was the case in SN 1993J), we would not expect to be able to distinguish it from the noise in our spectra.

Note that the V-band data may, in addition, include flux contributions from a CSI-powered blue pseudocontinuum at these late times – the 600+ d spectra do indicate a faint continuum blueward of 6000 Å. Because of the large time gap between our spectra at 334 d and 628 d, we do not know exactly when this blue pseudocontinuum emerged. It does not seem to evolve significantly between our spectra taken at 628 and 678 days, and so we believe that the flux decline measured around this time by Ergon et al. (2014) (0.009 ± 0.0026 mag day^{-1}) is dominated by the fading ^{56}Co contribution and not by any evolving CSI-powered flux. Note that V-band photometry likely also includes contributions from the

Na I D, [O I], [Fe II], and Hα lines, whether they are powered by radioactivity or CSI — a rather complex puzzle to decode. However, this complexity does not affect the measurement of individual line fluxes. As described above, the Na I D line indicates that the ejecta of SN 2011dh became fully γ-ray transparent (and therefore powered through positron energy deposition) between 300 and 350 days after core collapse.

In contrast with the Na I D line, the nebular Hα line appears to be fueled entirely through CSI. Assuming the broad feature near 6563 Å in the 678 day spectrum of SN 2011dh (see Fig. 2.3) is a broad and boxy Hα feature, it exhibits a full width at half-maximum intensity (FWHM) of roughly 21,000–26,000 km s^{-1} (there are large errors when measuring the line width, as this spectrum has a low S/N and the line is weak). Spectra taken the first month after core collapse show a blueshifted Hα absorption component around 15,400 km s^{-1} to 12,500 km s^{-1} (velocities at 4 to 14 days; Marion et al. 2014). These measurements mesh with the CSI scenario described above, wherein the unslowed outer ejecta impact the circumstellar material and produce a shell of emitting gas that continues to move outward at its initial expansion velocity.

The scenario that SN 2011dh presents to us in its late-stage evolution is notably different than that of SN 1993J or SN 1987A. As shown by Suntzeff et al. (1992), the peculiar Type II-P SN 1987A exhibited a continuously declining (yet nonzero) γ-ray opacity until the slowly decaying isotope ^{57}Co became the dominant source of energy around 800–900 days after explosion (^{57}Co $\rightarrow$ ^{57}Fe with a half-life of $\sim$272 days). This indicates that SN 1987A had a significantly higher γ-ray opacity than SN 2011dh. In contrast, CSI became the dominant flux source in SN 1993J around 350 days, when the spectrum became dominated by broad and boxy emission lines (Matheson et al. 2000b), and it is impossible to tell when (or if) the radioactive energy deposition entered the ^{56}Co positron-powered phase. Of course, several questions remain about SN 2011dh and its late-time evolution. Unless it rebrightens, however, the SN is too faint to hope for a significantly higher S/N spectrum than those presented here (our spectrum at 678 days represents an hour of integration time on a clear night with the 10 m Keck II telescope). Continued photometric monitoring should provide more information as the SN evolves.

2.3.2 The Oxygen Line Profile and the Ejecta Geometry

Fransson & Chevalier (1989) showed that, given the reasonable assumptions of homologous expansion and optically thin emission, the profiles of forbidden lines in nebular SN spectra can be used as tracers of the geometry and density profile of the emitting material. The [O I] $\lambda\lambda$6300, 6364 doublet, specifically, has been used as a diagnostic of ejecta asphericity in Type Ibc/IIb SNe by many studies (e.g., Mazzali et al. 2005; Taubenberger et al. 2009; Milisavljevic et al. 2010; Modjaz et al. 2008a; Maurer et al. 2010; Maeda et al. 2008). The [O I] doublet is generally used because it is consistently one of the strongest lines in nebular SN spectra and is largely isolated and unblended, and oxygen is one of the most abundant elements in stripped-envelope core-collapse SNe. The structure apparent in the [O I] doublet has often been attributed to either a jet or torus geometry in the ejecta with the diversity of

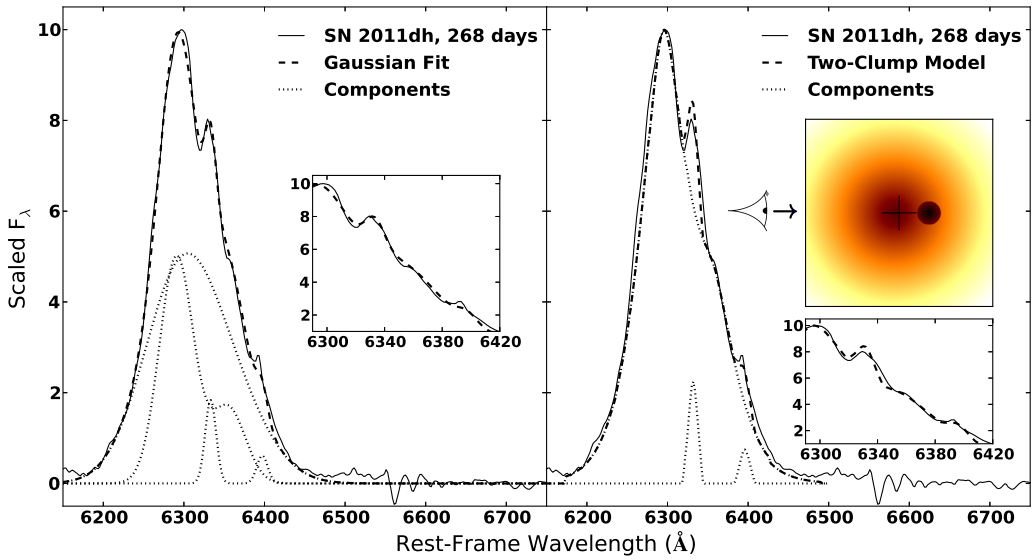

Figure 2.5: The left panel shows a multi-Gaussian decomposition of SN 2011dh's [O I] $\lambda\lambda$6300, 6364 doublet 268 days after explosion. Each component is a doublet with a flux ratio of 3:1 and a wavelength separation of 64 Å. Our best fit includes three such components: a broad central component, a large blueshifted clump, and a small redshifted clump. The inset shows a magnified view of the profile's red side. The right panel shows the same observed line profile with our best-fit two-component model overlaid. The box on the upper right shows a crosscut through the emissivity profile in velocity space, where the colour gradient represents $\log_{10}$ of emissivity density and the cross marks the rest velocity of M51. The box on the lower right is a magnified view of the right side of the line profile. See §2.3.2 for a complete description.

line profiles explained through viewing-angle dependencies (e.g., Mazzali et al. 2005; Maeda et al. 2008; Modjaz et al. 2008a), though other explanations have been presented for some SNe (e.g., Maurer et al. 2010; Milisavljevic et al. 2010).

The [O I] profile of SN 2011dh prominently displays multiple peaks and troughs. We explore the geometrical implications of this line profile in two ways. Several studies have previously explored [O I] line profiles by decomposing the profile into a set of overlapping Gaussian curves, effectively assuming a multi-component Gaussian spatial distribution (e.g., Taubenberger et al. 2009). We performed a similar fit for comparison, but the spatial distribution of emissivity is not necessarily Gaussian; the choice to decompose the profile this way is mainly for convenience. We also ran three-dimensional (3D) nebular radiative transfer models for a variety of geometries, attempting to fit the observed line profile with a simple and physically plausible ejecta geometry. [O I] $\lambda\lambda$6300, 6364 is a doublet with two peaks separated by 64 Å, with their relative intensities determined by the local density of neutral oxygen. The intensity ratio reliably approaches 3:1 in nebular SN spectra (e.g., Chugai 1992;

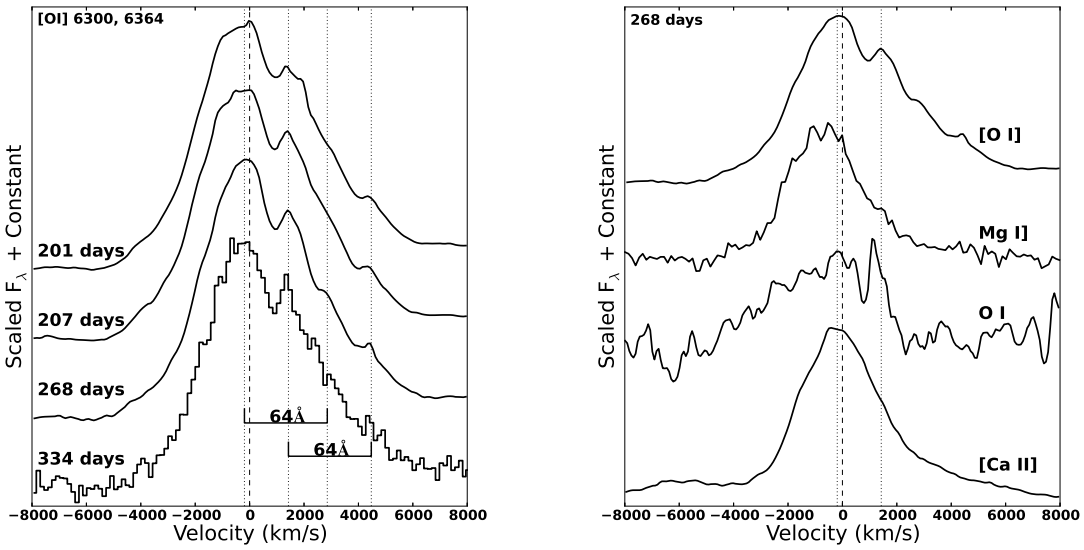

Figure 2.6: The [O I] $\lambda\lambda$6300, 6364 doublet line profile during the early nebular phase of SN 2011dh (left) and the [O I] $\lambda\lambda$6300, 6364, Mg I] λ4571, O I λ7774, and [Ca II] $\lambda\lambda$7291, 7324 profiles of SN 2011dh 268 days after core collapse (right). The components described in §2.3.2 persist throughout the nebular phase with similar relative fluxes and wavelength offsets, and similar profiles are apparent in the [O I], Mg I], and O I lines. The vertical dotted lines show the best-fit velocities of the two components of the [O I] $\lambda\lambda$6300, 6364 line as described in §2.3.2 and shown in Figure 2.5. The dashed line at 0 km s^{-1} marks the rest frame of M51.

Li & McCray 1992), and we assume this holds true for SN 2011dh at these epochs. Before analysing the [O I] profile we remove the Hα emission by assuming it is symmetric about the rest wavelength (6563 Å) and subtracting a smoothed profile. Note that this nebular spectral analysis is not a well-posed inverse problem; many different geometries could produce the same spectral profile.

The results of our Gaussian decomposition of the line profile are shown in the left panel of Figure 2.5. For each component in our fit we specify the amplitude, position, and width of the 6300 Å line; the properties of the 6364 Å line are then forced. In the spectrum at 268 days past core collapse, our best fit to the [O I] line requires three such components. There is a broad component blueshifted by $\sim$250 km s^{-1}, a narrow component blueshifted by $\sim$400 km s^{-1}, and a second narrow component redshifted by $\sim$1600 km s^{-1}. Note, however, that the broad component is only needed because the overall line profile is distinctly non-Gaussian. A more nuanced approach (below) provides a good fit to the profile with only two components.

The results of our 3D modeling analysis are shown in the right panel of Figure 2.5. In our models, we specify the emissivity of the [O I] doublet in each spatial zone and integrate the transfer equation using the Sobolev approximation under the assumption that the ejecta are

optically thin (see, e.g., Jeffery & Branch 1990). We decompose the 3D emission into multiple overlapping spherical clumps, each with an exponentially-declining emissivity profile. The primary peak is well fit by a sphere with an emissivity profile characterised by an exponential falloff with e-folding velocity $v_e = 950\,\mathrm{km\,s^{-1}}$. To match the position of the peak, we need to offset the entire sphere from the origin toward the observer by $\sim 250\,\mathrm{km\,s^{-1}}$. The secondary peak is well fit by placing a second smaller spherical clump along the observer's line of sight but moving away at $\sim 1500\,\mathrm{km\,s^{-1}}$. The emissivity profile of this second clump has an e-folding velocity of $v_e = 300\,\mathrm{km\,s^{-1}}$ which terminates at $600\,\mathrm{km\,s^{-1}}$. The integrated emission from the primary sphere is ~ 24 times greater than the integrated emission of the smaller clump, though the peak local emissivity of the smaller clump is a factor of ~ 4 higher than that of the primary sphere.

The right panel of Figure 2.5 shows that this model does a decent job of fitting all features in the [O I] profile. Though this simple model invokes only two components, the true ejecta geometry could in fact consist of multiple clumps of similar or smaller spatial dimensions. This is because it is only the larger inhomogeneities located along the line of sight that produce noticeable and well-separated features in the line profile.

It is unclear whether the clump-like structures we infer from the [O I] doublet correspond to inhomogeneities in the distribution of the oxygen itself or the ^{56}Ni that excites it. In 3D core collapse simulations, convective motions during neutrino heating act as seeds for Rayleigh-Taylor instabilities that develop when the shock passes through compositional interfaces (e.g., Hammer et al. 2010). This results in fingers of heavier elements, such as ^{56}Ni, punching out into the overlying layers of lighter elements. Such a picture could explain the irregular line profiles seen in several core-collapse SNe at late times (e.g., Filippenko & Sargent 1989; Matheson et al. 2000b), and has been explicitly considered previously for the asymmetry seen in SN 1987A. In particular, the substructure noted in the Hα line profile of SN 1987A (the "Bochum event"; Hanuschik et al. 1988) has been interpreted as resulting from a relatively high velocity ($\sim 4700\,\mathrm{km\,s^{-1}}$) "bullet" of ^{56}Ni (Utrobin et al. 1995). A similar geometry could potentially be applicable to SN 2011dh, assuming a sizable (but slower) clump of ^{56}Ni was mixed into the oxygen layer. More sophisticated 3D nebular spectral modeling will be needed to constrain the geometry in more detail. For example, extending the secondary clump of our model by adding more material to the extreme redshifted edge (making the clump aspherical) would fill in the discrepancies apparent in the line profile near 6340 Å and 6420 Å, and would also more closely resemble the extended structures apparent in the models of Hammer et al. (2010, see their Fig. 2).

Though the primary emitting sphere in our model is slightly offset from the origin, this may be due to uncertainty in the true SN Doppler velocity rather than an actual asymmetry of the ejecta. Though M51 is almost face-on, Tully (1974) show that the southeast quadrant of M51 (where SN 2011dh occurred) is rotating toward us. The line-of-sight motion is significantly less than $250\,\mathrm{km\,s^{-1}}$ but the true Doppler velocity of M51 may be lower than the value we used to deredshift our spectra. Adopting $z = 0.00155 \pm 0.0002$ (Falco et al. 1999) instead of the $z = 0.002$ used in the rest of this paper places the primary emitting component at a blueshift of $\sim 120\,\mathrm{km\,s^{-1}}$, within a factor of 2 of the expected line-of-sight rotational

velocity of M51 at the SN position. In addition, there are narrow Hα lines from the host galaxy superimposed on our spectra (slight oversubtractions are apparent in both the 268 and 334 d spectra; see Figure 2.2). Assuming the strongest of these lines in our 268 d spectrum was emitted in the rest frame of the SN, we measure a Doppler velocity of $550 \pm 160\,\mathrm{km\,s^{-1}}$. Adopting this value places the primary component at a blueshift of $\sim 200\,\mathrm{km\,s^{-1}}$ relative to rest. It appears that the primary emitting component of SN 2011dh is either symmetric with respect to the rest frame or nearly so. Note, as well, that these relatively low Doppler velocities lie near the resolution limit of our spectra. As described by Silverman et al. (2012), our spectra have characteristic wavelength errors of 1 – 2 Å ($\lesssim$90 $\mathrm{km\,s^{-1}}$). The positions of most other nebular lines are consistent with this scenario (with widths of several thousand $\mathrm{km\,s^{-1}}$ and irregular profiles, it is difficult to determine the centres of nebular SN lines to high precision). The Mg I] λ4571 line is an exception, displaying a strong asymmetry and a blueshifted peak (see below).

As Figure 2.6 shows, the components described above persist from 201 to 334 days, and similar components at similar relative positions are apparent in the O I λ7774 profile and the Mg I] λ4571 profile, though the primary component appears to be more blueshifted in Mg I]. The [Ca II] $\lambda\lambda$7291, 7324 profile, however, exhibits a simple and singly-peaked profile. Other studies have shown that it is common for Mg I] and [O I] to display similarly asymmetric line profiles while [Ca II] remains relatively symmetric (e.g., Modjaz et al. 2008a; Milisavljevic et al. 2010).

SN 2011dh's nebular [O I] profile is not consistent with the often-proposed simple torus model of emitting material. An emission trough due to an overall torus-like geometry of emitting material would fall at the rest wavelength of the line (in the SN rest frame). As Figure 2.5 shows, SN 2011dh instead displays an emission peak at roughly the rest wavelength; if the main trough in the line profile were associated with the centre of a torus, it would have to be offset from the rest frame of M51 by $\sim 1000\,\mathrm{km\,s^{-1}}$, an offset inconsistent with the centres of other nebular emission lines. To explore this further we ran several models similar to the two-clump model described above but with a toroidal component at various viewing angles, and we found no physically plausible toroidal geometries that matched the profile well.

Maurer et al. (2010) showed that foreground Hα absorption was a reasonable explanation for the double [O I] peak in SN 2008ax. It is possible that foreground hydrogen absorption is also affecting the oxygen profile in SN 2011dh: early-time spectra indicate a hydrogen expansion velocity of 12,500–15,400 $\mathrm{km\,s^{-1}}$ (velocities at 14 and 4 days; Marion et al. 2014), and the peak of [O I] emission is $\sim$12,000 $\mathrm{km\,s^{-1}}$ (265 Å) blueward of Hα. However, explaining all three bumps in the profile through foreground absorption would require three well-placed hydrogen overdensities, at $\sim$8100, 9600, and 11,100 $\mathrm{km\,s^{-1}}$, and would not account for the line profiles of Mg I] λ4571 and O I λ7774. It seems apparent that the [O I] line-profile asymmetries in SN 2011dh come from distinct emitting components moving relative to each other, each displaying the doublet nature of the line. Additionally, the lack of obvious Hα absorption features may indicate a very low hydrogen shell mass.

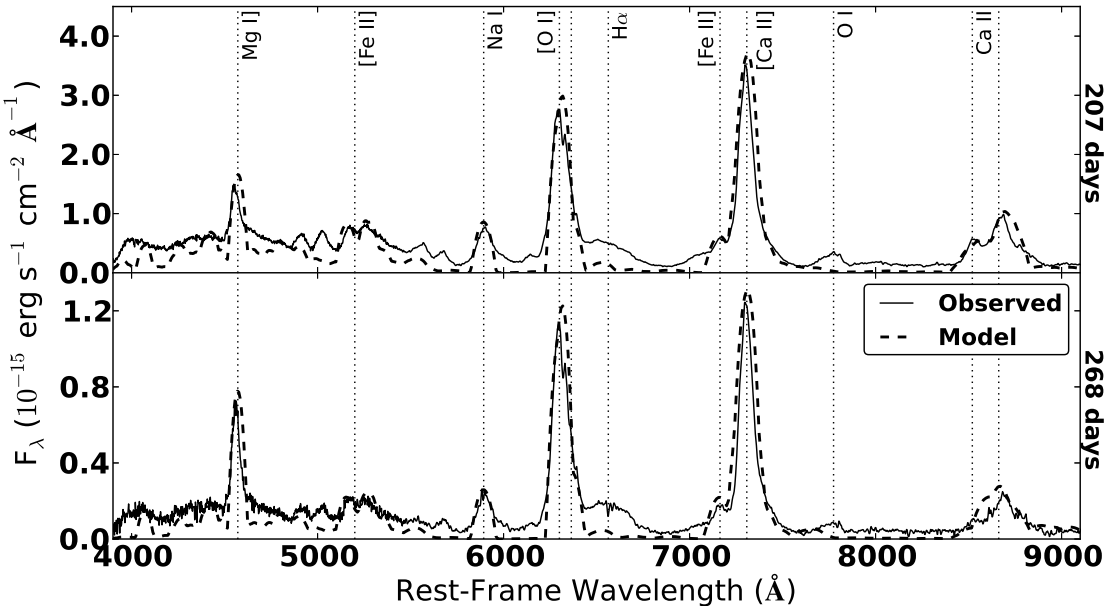

Figure 2.7: Comparison between our best-fit nebular models and the observed spectra of SN 2011dh at 207 and 268 days after core collapse. See §2.4 for details.

2.4 Nebular Models

We use a spherically symmetric single-zone non-LTE (local thermodynamic equilibrium) nebular modeling code to further explore SN 2011dh. The code tracks the heating of the nebular ejecta through deposition of γ-rays and positrons produced by radioactive decay. This heating is balanced by line emission to determine both the temperature and ionization state of the nebula. Following methods and ideas first outlined by Axelrod (1980) and Ruiz-Lapuente & Lucy (1992), the code was developed by Mazzali et al. (2001), and has been described in greater detail by, for example, Mazzali et al. (2010) and Mazzali & Hachinger (2012).

The code is available in a one-zone version, a stratified version, and a three-dimensional version. The one-zone model provides a rough estimate of the properties of a SN nebular spectrum (e.g., mass and elemental abundances). The stratified model is preferred when comparing a detailed model of the explosion with the data (Mazzali et al. 2007), and the three-dimensional model is useful for strongly asymmetric events (Mazzali et al. 2005). Here, since the profiles of the emission lines do not deviate significantly from the theoretically expected parabolic profiles and developing a complete explosion model is beyond the scope of this paper, we restrict ourselves to the one-zone approach. Mass-estimate differences between the one-zone and the stratified model are relatively small in cases where the ejecta do not display strong asphericity ($\sim 20\%$; Mazzali et al. 2001). The code does not include recombination emission, and therefore neither Hα nor the O I λ7774 recombination line are

reproduced. While hydrogen is located outside the carbon-oxygen core and ignoring Hα does not affect our result, ignoring the oxygen recombination line can introduce an error, though it should be small (Maurer et al. 2010). Another element of uncertainty is introduced by the fact that silicon does not have strong lines in the optical range. The strongest line, [Si I] λ6527, is about one third as strong as Na I D and is swamped by the Hα emission. All these effects could lead to an overestimate of the mass. Finally, a major source of uncertainty is the subtraction of the background pseudocontinuum.

Our best-fit models to the day 207 and 268 spectra are shown in Figure 2.7. The spectrum of SN 2011dh changes only slightly between these two epochs, and the two (independent) models are very similar. These models are powered by $\sim 0.07\,M_\odot$ of ^{56}Ni and exhibit an outer envelope velocity of $\sim 3500\,km\,s^{-1}$ with a total enclosed mass of $\sim 0.75\,M_\odot$. See Table 2.4 for a detailed listing of the mass composition of the models. Note that these values are sensitive to errors in the determination of the distance to SN 2011dh and errors in the absolute flux calibration of our spectra. Most of the major features of these spectra are matched by the models, including the prominent [Ca II] $\lambda\lambda$7291, 7324, [O I] $\lambda\lambda$6300, 6364, Na I D, and Mg I] λ4571 lines.

Bersten et al. (2012) derived a similar but slightly lower ^{56}Ni mass of $\sim 0.065\,M_\odot$ from bolometric light curve modeling through the first 80 days, while Sahu et al. (2013) derived a slightly higher mass of $\sim 0.09\,M_\odot$ through an analytic treatment of the bolometric light curve peak. Several other SNe IIb have been modeled in their nebular phase with similar codes, providing a useful set for comparison. Our models of SN 2011dh include $\sim 0.26\ M_\odot$ of oxygen, much less than was needed for SNe 2008ax, 2001ig, and 2003bg ($\sim$0.51, 0.81, and $1.3\,M_\odot$, respectively; Maurer et al. 2010; Silverman et al. 2009; Mazzali et al. 2009). The ^{56}Ni mass required is also relatively low. SN 2011dh had $\sim 0.067\,M_\odot$ of nickel, but as the above authors have shown, SNe 2008ax, 2001ig, and 2003bg required ~ 0.10, 0.13, and $0.17\,M_\odot$, respectively. This indicates a relatively low-mass progenitor for SN 2011dh.

On the other hand, it is unclear whether the nebular spectra capture all of the carbon-oxygen core. The lowest velocity of the He lines is $\sim$5000 km s^{-1}, while the width of the emission lines is only $\sim$3500 km s^{-1}. Material between these two velocities may not be captured by the nebular modelling. Although this would go in the direction of compensating for the overestimate described above, we conservatively assign an error of $\sim \pm 50\%$ in our mass estimates. It would be interesting to test the data against realistic explosion models in order to narrow down this uncertainty. This will be the subject of future work.

Multiple groups have modeled the nucleosynthetic yields of core-collapse SNe of various zero-age main sequence masses (e.g., Woosley et al. 1995; Thielemann et al. 1996; Nomoto et al. 2006). Though there are some discrepancies between our nebular model and the nucleosynthetic models (and some disagreements between different nucleosynthetic modeling efforts), our models are most consistent with a progenitor mass of 13–15 $M_\odot$. For example, Thielemann et al. (1996) predict carbon yields of 0.06, 0.08, and $0.115\,M_\odot$ and oxygen yields of 0.218, 0.433, and $1.48\,M_\odot$ for 13, 15, and $20\,M_\odot$ progenitors, respectively. The values required by our best-fit model, $0.07\,M_\odot$ of carbon and $0.26\,M_\odot$ of oxygen, indicate a 13–$15\,M_\odot$ progenitor. Note that not all elements are in such good agreement.

Table 2.4: Nebular model mass composition

Element	Mass Day 207 ($M_\odot$)	Mass Day 268 ($M_\odot$)
C	7.0×10^{-2}	6.0×10^{-2}
O	2.6×10^{-1}	2.8×10^{-1}
Na	1.3×10^{-4}	1.7×10^{-4}
Mg	1.6×10^{-3}	4.2×10^{-3}
Si	3.0×10^{-1}	3.0×10^{-1}
S	2.3×10^{-2}	2.5×10^{-2}
Ca	9.1×10^{-3}	1.0×10^{-2}
Fe	1.0×10^{-2}	1.0×10^{-2}
^{56}Ni	6.7×10^{-2}	7.0×10^{-2}
Total	7.4×10^{-1}	7.6×10^{-1}

Mass composition of non-LTE nebular models fit to spectra of SN 2011dh at 207 and 268 days after core collapse.

This result corroborates the findings of several other groups: the progenitor of SN 2011dh was a relatively low-mass ($\sim$13–17 $M_\odot$) yellow supergiant that likely had its outer envelope stripped away by a binary companion (e.g., Bersten et al. 2012; Benvenuto et al. 2013; Maund et al. 2011; Van Dyk et al. 2013; Murphy et al. 2011). SN 2011dh has provided a powerful test of the accuracy of SN progenitor studies through nebular spectra. The clear agreement between the nebular modeling and the results of such varied studies indicates that models of nebular SN spectra provide real and powerful constraints of the progenitor's properties. There is, however, work to be done to understand the discrepancies between modeled nucleosynthetic yields and nebular-spectra models.

2.5 Conclusions

SN 2011dh was a very nearby SN IIb discovered in M51 in early June 2011, providing observers with a valuable opportunity to track the evolution of one of these relatively rare SNe in detail. The nature of SN 2011dh's progenitor star has been much debated. In this paper, we present nebular spectra from 201 to 678 days after explosion as well as new modeling results. We confirm that the progenitor of SN 2011dh was a star with a zero-age main sequence mass of 13–15 $M_\odot$, in agreement with the photometric identification of a candidate YSG progenitor.

In addition, our spectra at $\sim$2 yr show that photometric observations taken near that time are dominated by the fading SN and not, for example, by a background source or a binary companion. We present evidence pointing toward interaction between the expanding SN blastwave and a circumstellar medium, and show that the SN enters the positron-dominated

phase by ~ 1 yr after explosion. Finally, we explore the geometry of the ejecta through the nebular line profiles at day 268, concluding that the ejecta are well fit by a globally spherical model with dense aspherical components or clumps. In addition to the data presented here we have obtained several epochs of spectropolarimetry of SN 2011dh as it evolved. The analysis of those data is beyond the scope of this paper, but they will provide additional constraints on any asymmetry in the explosion of SN 2011dh.

Chapter 3

Early Emission from the Type IIn Supernova 1998S at High Resolution

First published in the Astrophysical Journal: Shivvers et al. (2015).
Co-Authors: Jose H. Groh, Jon C. Mauerhan, Ori D. Fox, Douglas C. Leonard, Alexei V. Filippenko

Chapter Abstract

The well-studied Type IIn supernova (SN) 1998S is often dubbed the prototypical SN IIn, and it provides a unique opportunity to study its progenitor star from within as the SN lights up dense circumstellar material (CSM) launched from the progenitor. Here we present a Keck HIRES spectrum of SN 1998S taken within a few days after core collapse — both the earliest high-resolution ($\Delta\lambda < 1.0$ Å) spectrum published of a SN IIn and the earliest published spectrum of SN 1998S. Modern SN studies achieve impressively short turn-around times between SN detection and the first observed spectrum, but high-resolution spectra of very young supernovae are rare; the unique spectrum presented here provides a useful case study for observations of other young SN systems including SN 2013cu, which displayed a remarkably similar spectrum when very young. We examine the fully resolved emission-line profiles of SN 1998S, finding evidence for extreme mass loss from the progenitor at velocities much less than those characteristic of Wolf-Rayet (WR) stars. We model our high-resolution SN 1998S spectrum using the radiative-transfer code CMFGEN and explore the composition, density, and velocity gradients within the SN system. We find a mass-loss rate of $6.0 \times 10^{-3}\,M_\odot\,yr^{-1}$ during the ~ 15 yr before core collapse, while other studies indicate a much lower rate at earlier times (>15 yr before core collapse). A comparison with a spectrum of SN 2013cu indicates many similarities, though SN 2013cu was of Type IIb — indicating that very different supernovae can arise from progenitors with extreme mass loss in the last few years before explosion.

3.1 Introduction

Type IIn supernovae (SNe) provide unique observational windows into the end stages of evolution in massive stars. Though they are somewhat rare (making up $\sim 9\,\%$ of all core-collapse SNe; Li et al. 2011b; Smith et al. 2011b), SNe IIn display a large diversity in observed properties. The class is identified by the presence of narrow or intermediate-width emission lines (full width at half-maximum intensity [FWHM] $\lesssim 1000\,\mathrm{km\,s^{-1}}$), created by radiative recombination and electron scattering in relatively slow-moving circumstellar material (CSM) exterior to the expanding ejecta (e.g., Schlegel 1990; Filippenko 1991; Chugai 1991; Filippenko 1997; Fransson et al. 2002). The presence of this CSM around SNe IIn strongly affects many of their observational traits (e.g., Chugai et al. 2002; Chevalier & Irwin 2011; Fransson et al. 2014). To give just a few examples, the development of a dense shell of swept-up material in the post-shock medium can suppress or mask the underlying broad ejecta features typically seen in normal SN spectra; if the CSM is optically thick, the light-curve shape can be altered and the radiation of the developing SN must diffuse outward through the CSM; and the ejecta-wind interaction can contribute luminosity to the SN (especially at late times).

The commonly accepted explanation for the relatively dense CSM around SNe IIn requires significant mass loss from the progenitor stars in the years and decades before they undergo core collapse. A broad range in mass-loss rates from a diversity of possible progenitors yields a wide variety in observed properties (e.g., Kiewe et al. 2012). SNe IIn can be some of the most luminous SNe in the Universe, efficiently converting the kinetic energy of the expanding SN ejecta into light through shock interaction with the CSM (e.g., Ofek et al. 2007; Smith et al. 2010), and they appear to create large amounts of dust compared to other SN classes (e.g., Fox et al. 2011).

SN 1998S was discovered in NGC 3877 on 1998 March 2.68 (UTC dates and times are used throughout this article), with a nondetection $\sim 3\,\mathrm{d}$ earlier (Li et al. 1998; Qiu et al. 1998). This indicates that SN 1998S was discovered within a few days of core collapse (Leonard et al. 2000), though the exact age of the SN is uncertain. Accordingly, all epochs used here are relative to the discovery date. SN 1998S is one of the best-studied examples of the SN IIn class, with well-sampled optical and infrared light curves (e.g., Fassia et al. 2000; Gerardy et al. 2002), low-resolution optical spectroscopic and spectropolarimetric observations (e.g., Leonard et al. 2000; Anupama et al. 2001; Wang et al. 2001), very late-time spectroscopic observations (e.g., Mauerhan & Smith 2012), space-based UV spectroscopy (Fransson et al. 2005), X-ray and radio observations (Pooley et al. 2002), and high-resolution optical spectroscopy (e.g., Bowen et al. 2000; Fassia et al. 2001), as well as modeling efforts (e.g., Chugai 2001; Lentz et al. 2001; Chugai et al. 2002).

In this paper, we present a single epoch of high-resolution echelle spectroscopy of SN 1998S observed on 1998 March 4 — the earliest spectrum of this object yet published (1.86 d after discovery), and (we believe) the earliest high-resolution ($\Delta\lambda < 1.0\,\text{Å}$) spectrum of a SN IIn ever taken. We also perform a detailed radiative-transfer model using the CMFGEN code (Hillier & Miller 1998), following the methodology described by Groh (2014). This allows us

to explore the temperature, density, composition, and ionization structure of the SN system based on the high resolution spectrum.

Capturing a spectrum of a SN while it is very young is a serious challenge, but recent technical advances have begun to push the envelope for what are called "early" spectra of core-collapse SNe — in some cases perhaps even probing the fading emission attributed to shock breakout from the progenitor star ("flash spectroscopy"; Gal-Yam et al. 2014). Though there are significant differences between the physical environment of SN 1998S and the environs of other SNe not of Type IIn, there are also many similarities, especially when considering the spectral signatures of progenitor winds illuminated by shock breakout from the star or by ongoing shock interaction with a dense CSM. We believe that the spectrum and model given here can serve as a useful case study when interpreting early-time spectra of many core-collapse SNe. In § 3.2 we discuss our data and reduction techniques, in § 3.3 we describe our modeling techniques and the best-fit CMFGEN model of the young SN 1998S system, while § 3.4 synthesizes these results with other studies of SN 1998S and additional objects. We summarize and conclude in § 3.5.

3.2 Observations and Data Reduction

Between 12:45 and 13:20 on 1998 March 04 (UT), we obtained a set of spectra of SN 1998S with the Keck High-Resolution Echelle Spectrometer (HIRES; Vogt et al. 1994), exposing for 2×500 s in each of two setups, *h03* and *h07*. Setup *h03* covers a wavelength range of 3875–6270 Å with a measured resolution of ~ 0.3 Å, while setup *h07* covers 5065–7480 Å at a resolution of ~ 0.2 Å. (Quoted resolutions are averaged FWHM measures from Gaussian fits to narrow Milky Way Na I D lines and telluric absorption lines in our reduced spectra.)

At this time, SN 1998S exhibited a visual magnitude of ~ 13.5 (Li et al. 1998). Photometry of NGC 3877 at the location of the SN, performed with g-band images from the Sloan Digital Sky Survey, indicates that the explosion site has a surface brightness of ~ 20–$21\,\mathrm{mag\,arcsec^{-2}}$. Our observations were obtained with a slit width of ~ 1.0 arcsec, comparable to the seeing, and so any contamination of the SN spectrum by host-galaxy light is quite small. For each setup the two 500 s exposures were reduced using the MAKEE program[1] and coadded. Unfortunately, obtaining an accurate flux normalization and calibration is quite difficult for echelle spectrographs like HIRES. However, because the continuum of SN 1998S is remarkably smooth and well-defined during the first several days (Leonard et al. 2000; Fassia et al. 2001), we are able to remove the convolved SN continuum and flatfield imperfections by fitting for and dividing by a smooth pseudo-continuum both across orders and within each individual order of our HIRES spectra.

We first fit a smooth nonparametric function to the median values of each order to determine the response function along the y axis of the CCD (the axis along which echelle orders are spread). To account for the few prominent broad-wavelength features in our spectra, we do not include the values from orders heavily affected by these emission features.

[1] www2.keck.hawaii.edu/inst/common/makeewww

After dividing our spectrum by the CCD's y-axis response function, we fit another smooth nonparametric function within each individual order, and again divide our spectrum by it, thereby accounting for the variations of the SN continuum and flatfield along the x axis of the CCD (the axis along which each individual order is dispersed). As above, we must be concerned about the few broad features, so we interpolate the response functions of neighboring orders onto those orders with known broad emission lines. The x-axis response functions change slowly with order number and this procedure appears to approximate the true response function well. The C III λ5696 emission line was clearly detected in both setups *h03* and *h07* and provides a quick check that our wavelength and relative-flux procedures produce a well-calibrated spectrum: fitting a simple Gaussian to the line in each setup yields line centers that match to within 0.05 Å and amplitudes that match to within 0.2%. All narrow features and the major broad emission features are preserved with this process, but note that subtle broad features are very difficult to disentangle from the individual echelle order responses and are therefore likely to be subtracted out of our spectrum.

The result of the above procedure is a spectrum in units of $F_\lambda/F_{\lambda,c}$, where $F_{\lambda,c}$ is the flux of the SN continuum per unit wavelength. To get a spectrum in units of F_λ we must determine $F_{\lambda,c}$. We approximate $F_{\lambda,c}$ for the March 4 spectrum by measuring it from a well-calibrated Keck Low-Resolution Imaging Spectrometer (LRIS) observation taken on March 6 (Leonard et al. 2000). At these early times the SN continuum is smooth, there are no broad absorption features, and the SN exhibits an ultraviolet (UV) excess compared to a simple blackbody; we choose to define the continuum with a smooth nonparametric spline function. We assume that the continuum shape is changing only slowly at early times (as implied by spectra from days 3, 4, and 5; Leonard et al. 2000), and that the continuum shape on day 2 is similar to that shown on day 4. Regardless, the largest source of uncertainty in this relative flux calibration is attributable to the unknown color evolution of SN 1998S between days 2 and 4.

Though the color evolution at these times was small, the total-flux evolution was not. SN 1998S was rapidly increasing in brightness over this timespan, so we perform an additional absolute-flux correction by matching the spectrum to the unfiltered photometry observed by the Katzman Automatic Imaging Telescope (KAIT; Filippenko et al. 2001b) the same night (~ 13.5 mag; Li et al. 1998). Though the uncertainty on our absolute-flux calibration procedure is large, this photometric data point falls smoothly between the unfiltered magnitude from the discovery image a little more than one day before (~ 15.2 mag; Qiu et al. 1998) and the later, more densely sampled unfiltered and filtered observations (e.g., Fassia et al. 2000; Anupama et al. 2001). We estimate that the uncertainty of the calibrated absolute-flux level is $\sim 20\%$.

Regardless of the significant uncertainties in the flux calibrations, the widths, positions, and shapes of all emission lines are well determined. Figure 3.1 shows our final HIRES spectrum alongside the well-calibrated LRIS spectrum for comparison. Note that our spectral coverage is not complete over the full 3875–7480 Å range; there are gaps between many of the spectral orders (complete coverage at the blue end spreads out to a ~ 50 Å gap between the two reddest orders). Our final composite spectrum includes coverage from setup *h03* over the

range 3875–6265 Å and from setup *h07* over the range 6275–7480 Å; upon publication it will be made available in electronic format on WISeREP (the Weizmann Interactive Supernova data REPository; Yaron & Gal-Yam 2012).[2]

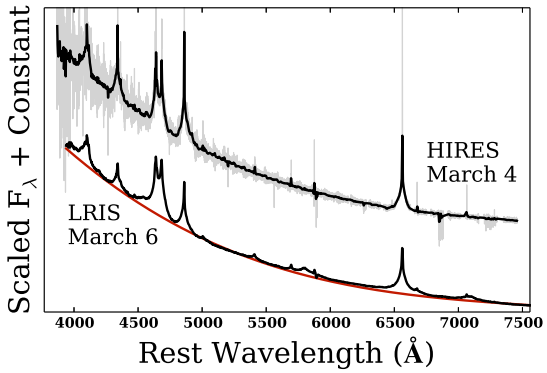

Figure 3.1: Our approximately flux-calibrated HIRES spectrum of SN 1998S observed 1998 March 4 (day 2) and a well-calibrated LRIS spectrum taken 2 d later (day 4); both are shown before application of any dust reddening correction. The full HIRES spectrum is shown in gray, with a spectrum binned to the approximate resolution of the LRIS spectrum overlain in black. The LRIS spectrum is shown at bottom along with the measured SN continuum (red), which has been applied to the HIRES spectrum during the approximate flux-normalization procedure (see §3.2). Note that our HIRES flux calibration procedure may have removed weak and broad features present in the March 4th spectrum — e.g. the wings of the weaker helium lines or the features near 5801 and 7115 Å visible on March 6.

Previous authors present total interstellar reddening values toward SN 1998S of $E(B-V) \approx 0.23 \pm 0.1$ mag (Leonard et al. 2000; Fassia et al. 2000), but recent studies have re-evaluated and improved upon the procedures used to calculate that value. Using the scaling relations published by Poznanski et al. (2012) and equivalent widths measured from our flux-normalized HIRES spectrum (both components of the host galaxy's Na D line are well resolved), we calculate that $E(B-V)_{\rm host} = 0.128^{+0.040}_{-0.028}$ mag. Including the Schlafly & Finkbeiner (2011) measurement of $E(B-V)_{\rm MW} = 0.0202 \pm 0.0009$ mag, we derive that the total interstellar reddening toward SN 1998S is $E(B-V) = 0.148^{+0.040}_{-0.028}$ mag. As described in greater detail in §3.3, we adopt a redshift of $z = 0.00286$. Note that this is slightly at odds with the best-fit value of $z = 0.002824 \pm 0.0000097$ presented by Fassia et al. (2001), and is slightly different from the measured value for the host galaxy NGC 3877 (0.002987 ± 0.000013; Verheijen & Sancisi 2001). We apply appropriate redshift and reddening corrections to all spectra before analysis, assuming a Cardelli et al. (1989) dust law and $R_V = 3.1$. However, we allow the host-galaxy reddening to vary when fitting a model of the system to the spectrum; see the extended extinction discussion in §3.4.5.

[2] http://wiserep.weizmann.ac.il

3.2.1 Young SN 1998S in High Resolution

Figure 3.2 shows our 1998 March 4 HIRES spectrum in high resolution with all identified emission lines labeled. All line identifications have been confirmed with the help of the CMFGEN model. Uncorrected telluric absorption features are apparent in our spectrum; we make sure they do not overlap with the features of interest and otherwise ignore them. For each identified line we either fit a single Gaussian profile or, for the strongest few Balmer lines which clearly display prominent extended wings, the sum of a Gaussian profile and a modified Lorentzian profile (where the exponent is allowed to deviate from 2.0). For each line we perform a maximum-likelihood fit and estimate our parameter errors using Markov-Chain Monte Carlo methods; the results are listed in Table 3.1.

3.3 Modeling

3.3.1 CMFGEN

We use the radiative-transfer code CMFGEN (Hillier & Miller 1998) to analyze the high-resolution spectrum of SN 1998S. The setup of the code for a SN interacting with its CSM follows that of Groh (2014), so here we only briefly recall the main features. CMFGEN computes the radiative transfer in spherical symmetry, simultaneously solving for the level populations and radiation field under nonlocal thermodynamic equilibrium conditions. The effects of line blanketing are taken into account following a super-level approach and, for each element in the model, the most significant species are included.

The properties of our model are determined by the radius of the inner boundary ($R_{\rm in}$), bolometric luminosity ($L_{\rm SN}$), and the chemical abundances of the elements listed in Table 3.2. Since no hydrodynamical modeling is performed, we assume a constant velocity ($v_{\rm wind}$) and mass-loss rate ($\dot{M}$) for the progenitor wind. The wind density structure is determined according to the equation of mass continuity, assuming $\rho \propto r^{-2}$. At the inner boundary, we assume a steep density gradient with a scale height of $0.007\,R_{\rm in}$, as theoretically expected for interacting SNe (e.g., Chugai 2001; Chevalier & Irwin 2011). This ensures that the inner boundary has high optical depths (Rosseland optical depth $\tau_{\rm ross} = 50$ at $R_{\rm in}$) and that the diffusion approximation holds at the inner boundary. Our models also assume that all energy is generated at distances $r < R_{\rm in}$, that time-dependent effects are negligible, and that the medium is unclumped.

3.3.2 A Model of SN 1998S in High Resolution

Table 3.2 lists the parameters of our best-fit CMFGEN model, Figure 3.3 plots the radial profiles of several model parameters, and Figure 3.4 shows the model compared to the observed spectrum of SN 1998S. The CMFGEN model does an excellent job and qualitatively matches the observed spectrum, predicting the appearance of almost all observed lines with

the correct morphology. The quantitative agreement is relatively good, although some discrepancies are apparent. For each species, we endeavored to fit our model to all identified lines in an averaged sense; in practice, of course, this produces slight overestimates for some lines and underestimates for others. We include these uncertainties in our error estimates for model parameters — the best-fit model described here is a compromise taking into account the various diagnostics we have, and small changes in the input parameters (within the error range given) may provide a better fit to individual spectral lines but the overall fit would deteriorate. This can be seen in Figure 3.4. For example, our model fits Hγ well, though the electron-scattering wings of Hβ are underestimated and the narrow component of Hα is overestimated (discussed in more detail below), while for He I our model overestimates He I λ5875 and very slightly underestimates He I λ4713. Note that, to obtain a better fit, we have allowed the total amount of dust reddening to vary, and we find that the models prefer a smaller amount of host-galaxy dust than discussed in §3.2 — see §3.4.5.

The value of $R_{\rm in}$ and $L_{\rm SN}$ determines the temperature at the inner boundary ($T_{\rm in}$), which is the primary regulator of the ionization structure of the illuminated progenitor wind. Our main diagnostic for the ionization structure is the ratio of He I and He II lines, which are very sensitive to $R_{\rm in}$ and $L_{\rm SN}$ in this parameter range. To minimize the confounding effect of the uncertainties in the flux calibration and dust reddening, we use neighboring lines when setting these parameters: He I $\lambda\lambda$4471, 4713 and He II λ4686, all of which are fit reasonably well by the final model. Our best-fit values for $R_{\rm in}$ and $L_{\rm SN}$ are in extremely good agreement with predictions for this epoch by Chugai (2001, see their Fig. 2), which are based upon light-curve model fits to bolometric flux estimates from March 14 and onward (Fassia et al. 2000). Additional constraints on the ionization structure come from the absence of N IV λ4057 and N IV λ7123. To fit the absolute-flux level, we assume a distance of $d = 17.00$ Mpc (Tully 1994) and, as explained in §3.4.5, a standard Milky Way dust-extinction law ($R_V = 3.1$, Cardelli et al. 1989), finding a best-fit total dust reddening of $A_{\rm V} = 0.15$ mag or $E(B-V) = 0.05$ mag.

Given the high spectral resolution, we are able to fully resolve both the narrow and broad components of the features. This allows us to independently determine $v_{\rm wind}$ and $\dot{M}$. We find a progenitor wind speed of $v_{\rm wind} = 40 \pm 5\,{\rm km\,s^{-1}}$. To constrain this value, we use the width of the narrow component of the emission lines and the P-Cygni absorption component of N III λ4097 and He I λ5876. We obtain a progenitor mass-loss rate of $\dot{M} = (6 \pm 1) \times 10^{-3}\,{\rm M_\odot\,yr^{-1}}$, using the strength of Hγ, Hβ, and He II λ4686 lines as diagnostics. The advantage of using these lines rather than the stronger Hα line is that they are formed in the inner parts of the outflow (Fig. 3.3) and thus are less affected by time-dependent effects such as a variable progenitor $\dot{M}$, the changing radiation field from the SN, or light-travel time. Our model overestimates Hα, which may indicate either that part of the extended region responsible for the Hα emission (Fig. 3.3) has not yet been illuminated by the SN, or that the density structure is steeper than r^{-2}, or both. Our best-fit value for $\dot{M}$ is within the range of previously-published estimates for the mass loss rate from SN 1998S's progenitor ($\dot{M} \approx 10^{-4}$–$10^{-2}\,{\rm M_\odot\,yr^{-1}}$, e.g., Lentz et al. 2001; Chugai 2001; Pooley et al. 2002; Moriya et al. 2014).

Table 3.1: Detected Spectral Lines

Ion	Rest wavelength (Å)	Observed wavelength±1σ (Å)	Doppler velocity±1σ (km s^{-1})	FWHM±1σ (km s^{-1})
H I	3889.06	3889.03±0.035	-2.2±2.70	29.76±2.783
H I	3970.08	3970.16±0.122	5.8±9.19	60.18±7.853
He I	4026.19	4026.43±0.017	17.4±1.29	29.93±3.291
N III‡	4097.36	4097.59	16.7	31.97
N III‡*	4097.36	4096.95	-29.9	78.2
H I	4101.73	4101.82±0.013	6.2±0.91	43.93±1.031
N III‡	4103.39	4103.63	17.7	39.31
N III‡*	4103.39	4102.94	-32.8	79.4
Si IV	4116.10	4115.69±0.130	-30.2±9.50	102.70±15.827
H I	4340.47	4340.55±0.004	5.2±0.29	52.63±7.542
H I†	4340.47	4338.73±0.371	-120.4±25.62	3533.02±36.013
[O III]	4363.21	4363.28±0.044	4.9±3.03	33.60±4.356
He I‡	4388.15	4387.88	-18.4	72.49
He I	4471.48	4471.72±0.006	16.4±0.43	29.90±0.898
S IV	4485.64	4485.61±0.055	-2.2±3.65	49.86±7.024
S IV	4504.11	4503.86±0.084	-16.6±5.57	52.98±11.734
He II	4541.49	4540.86±0.044	-41.3±2.88	75.32±10.595
N III	4634.14	4633.86±0.045	-18.1±2.92	76.98±9.911
N III	4640.64	4640.41±0.107	-14.8±6.93	90.31±8.120
C III	4647.42	4647.52±0.015	6.7±0.98	40.45±2.084
C III	4650.25	4650.35±0.057	6.4±3.69	38.23±5.538
He II	4685.80	4685.35±0.015	-28.7±0.98	122.71±3.173
He I	4713.15	4713.30±0.037	9.7±2.38	34.73±3.931
He II‡	4859.32	4858.72	-36.9	50.16
H I	4861.35	4861.32±0.002	-1.9±0.10	43.72±3.626
H I†	4861.35	4860.44±0.026	-56.0±1.58	2241.28±62.489
He I	4921.93	4922.00±0.016	4.5±0.98	36.30±1.535
[O III]	4958.91	4958.85±0.031	-3.7±1.86	29.62±4.329
[O III]	5006.84	5006.33±0.052	-30.9±3.10	32.51±4.197
He I‡	5015.68	5015.90	13.2	20.32
He II	5411.52	5410.65±0.061	-48.0±3.40	116.45±9.634
C III	5695.92	5695.69±0.021	-11.9±1.13	73.26±1.353
C IV‡*	5801.31	5799.03	-117.6	125.3
C IV‡*	5811.97	5810.25	-88.6	86.9
He I	5875.62	5876.01±0.082	19.9±4.16	39.44±5.623
N II	6482.05	6482.37±0.083	14.8±3.84	43.15±2.900
He II‡	6560.09	6559.25	-38.2	44.56
H I	6562.82	6563.18±0.001	16.4±0.06	42.57±3.467
H I†	6562.82	6562.21±0.023	-27.7±1.03	1388.78±13.718
N II	6610.56	6609.89±0.046	-30.3±2.07	26.76±4.336
He I	6678.15	6678.19±0.007	1.8±0.34	36.32±0.584
Si IV	6701.21	6700.54±0.102	-30.0±4.54	75.74±13.493
He I	7065.19	7065.46±0.045	11.3±1.93	41.07±2.758
C II	7231.32	7231.31±0.044	-0.4±1.82	37.98±5.398
C II	7236.42	7236.42±0.036	-0.2±1.50	25.73±2.299
He I	7281.35	7281.48±0.076	5.4±3.15	33.64±4.743

Note. — Identified absorption and emission lines and measures of the velocity offset and full width at half-maximum intensity (or half-minimum intensity, for absorption lines). Lines were fit with a Gaussian profile unless otherwise noted, and all errors are 1σ confidence levels estimated by Markov-Chain Monte-Carlo sampling, but do not include any systematic errors due, for example, to biases imparted by the instrument or reduction method. Note that our error estimation method fails for lines with confounding features very nearby. Line identifications made with the assistance of our CMFGEN model and the NIST Atomic Spectral Database.

† Broad line fit by a modified Lorentzian profile with a variable exponent.

‡ MCMC error analysis failed or not applicable.

* Absorption feature.

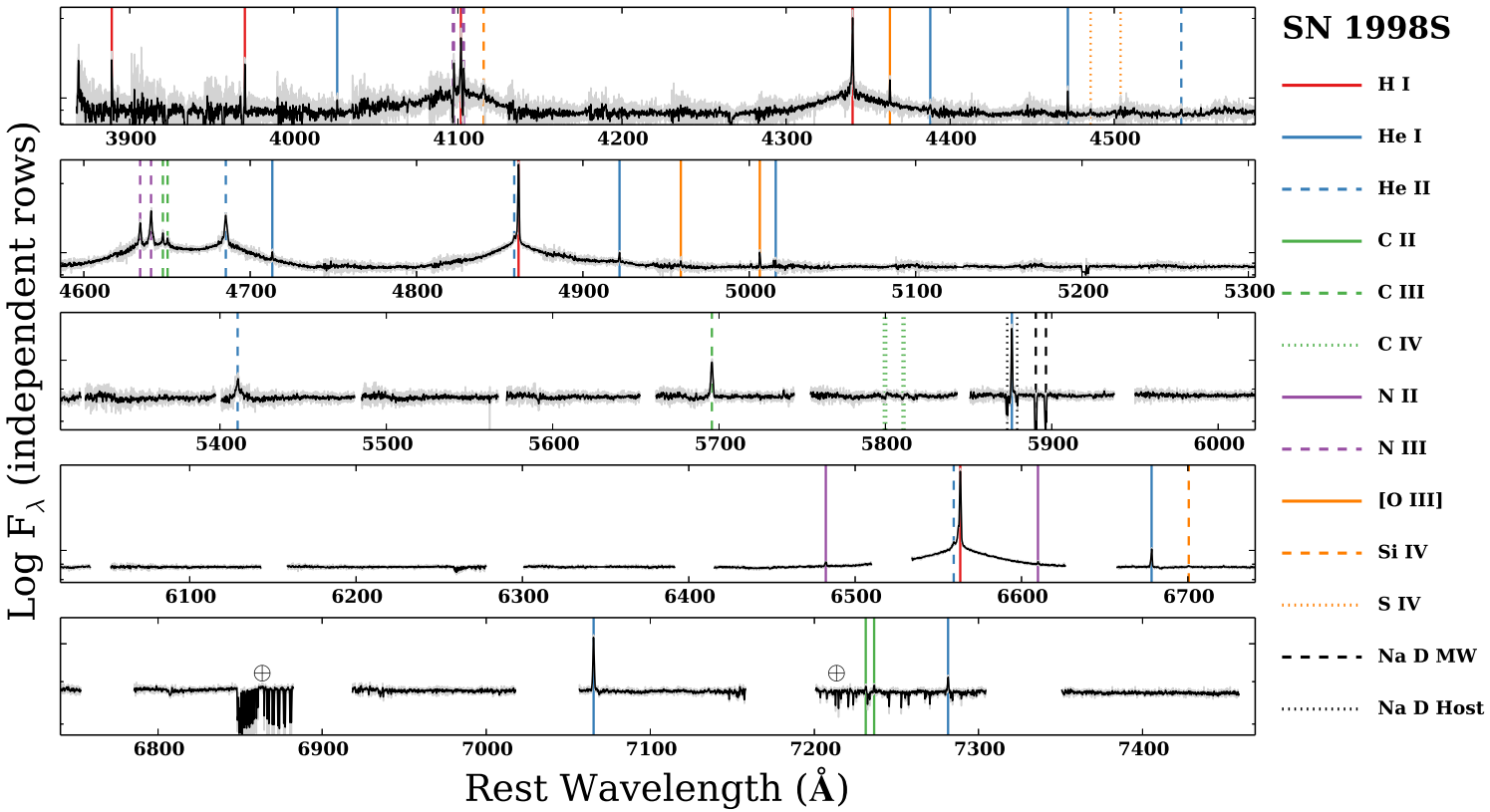

Figure 3.2: A HIRES spectrum of SN 1998S taken on 1998 March 4 (day 2), with all identified lines marked. Full spectrum shown in gray, overlain by a spectrum smoothed to a resolution of ~ 0.5 Å in black. A continuum fit has been subtracted and each row has been individually scaled along the ordinate axis for clarity.

CMFGEN Model Parameters			
	$L_{\rm SN}$	$(1.5 \pm 0.5) \times 10^{10}\,{\rm L}_{\odot}$	
	$R_{\rm in}$	$(6.0 \pm 1.0) \times 10^{14}\,{\rm cm}$	
	$v_{\rm wind}$	$40 \pm 5\,{\rm km\,s^{-1}}$	
	$\dot{M}$	$(6.0 \pm 1.0) \times 10^{-3}\,{\rm M}_{\odot}\,yr^{-1}$	
	Y	0.49 ± 0.10	
	$E(B-V)$	$0.05\,{\rm mag}$	
Element	Species	Mass Fraction (χ)	$\chi/\chi_{\odot}$
H	I	0.4953	0.70
He	I-II	0.4928	1.8
C	II-IV	5.0×10^{-4}	0.16
N	II-V	7.2×10^{-3}	6.5
O	II-VI	1.6×10^{-4}	0.017
Si	II,IV	7.0×10^{-4}	1.0
P	IV,V	6.1×10^{-6}	1.0
S	IV-VI	3.7×10^{-4}	1.0
Fe	III-VII	1.4×10^{-3}	1.0

Table 3.2: The best-fit CMFGEN model parameters. Listed error estimates are obtained by varying the input model parameters and comparing the result to our observed spectra, and they include variance in the overall continuum shape and in the relative line intensities within a species.

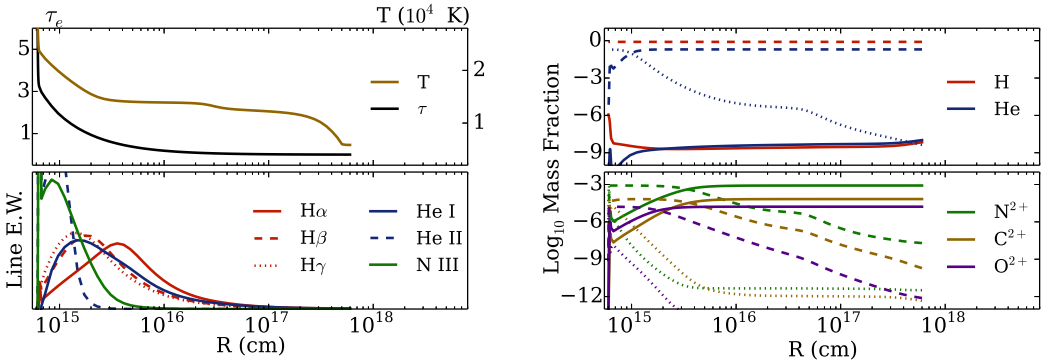

Figure 3.3: Radial profiles of our best-fit CMFGEN model. The top-left panel shows electron optical depth and temperature, the bottom left shows emission for several prominent lines, the top right shows the ionization structure of H and He, and and the bottom right shows the ionization structure of carbon, nitrogen, and oxygen. In the two right-hand panels, dashed lines indicate one ionization state higher and dotted lines indicate two ionization states higher. In all profiles, the edge of the cool dense shell is apparent near $6 \times 10^{14}\,{\rm cm}$, with the CSM continuing out to very large radii.

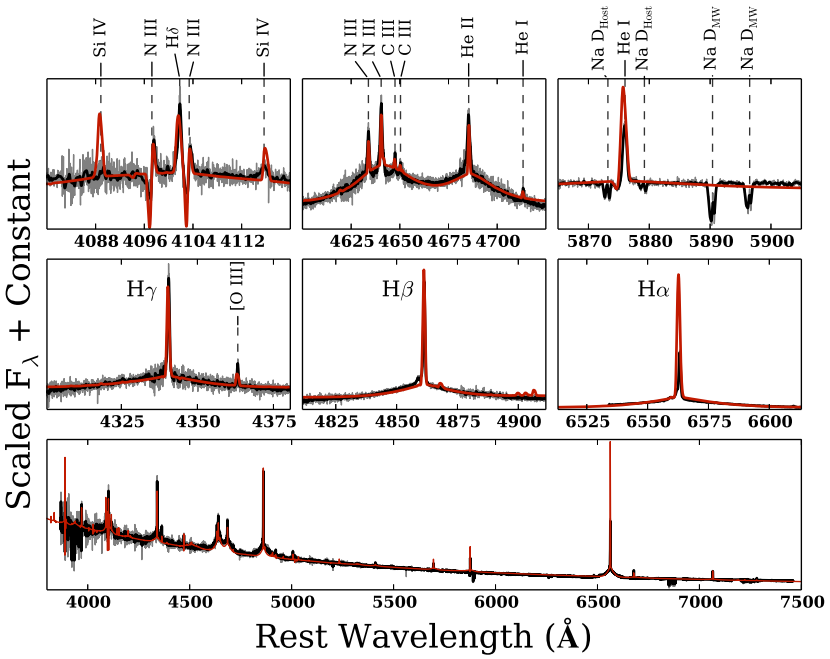

Figure 3.4: Comparison between the observed spectrum of SN 1998S (black, smoothed to 0.5 Å resolution) with the best-fitting CMFGEN model (red). The full-resolution spectrum is shown in the background (gray). Upper panels show individual lines of interest, while the lower panel illustrates the outstanding agreement over the full wavelength range. Note that arbitrary vertical shifts are included in the model in the upper panels to match the observed local continuum, for clarity, and (as described in the text) that the degree of host-galaxy dust absorption was fit as a free parameter.

Figure 3.3 indicates that (except for the Hα line) material between approximately 6×10^{14} cm and 2×10^{15} cm dominates the CMFGEN spectrum. Assuming a constant $v_{\rm wind}$ of 40 km s^{-1}, this corresponds to material launched from the progenitor $\sim$ 5–15 yr before core collapse. As shown in Table 3.2, our model indicates that the progenitor wind presents material mildly enriched by the CNO cycle, with He and N being enhanced and H, C, and O being depleted. The He mass fraction Y is relatively well constrained since the spectrum of SN 1998S has strong H, He I, and He II lines. We use the relative strengths of the He and H lines as diagnostics and find $Y = 0.49 \pm 0.1$. The N abundance is constrained using N III $\lambda\lambda$4634, 4640 and the O abundance is determined from [O III] $\lambda\lambda$4363, 4959, 5007. We employ C III $\lambda\lambda$4647, 4750, 5696 to constrain the C abundance, but the absolute value there should be taken with care given the well-known dependence of these C lines on details of the model atoms (Martins & Hillier 2012). We estimate uncertainties of 50%, 30%, and 50% on the C, N, and O abundances, respectively. We assume solar abundances for the other elements, noting that several Fe IV lines that are predicted by the model are not observed. The absence of these lines could be reconciled with the observations either by decreasing $R_{\rm in}$ (i.e. increasing $T_{\rm in}$) or by decreasing the Fe abundance to 1/3–1/2 of the solar value.

3.4 Discussion

3.4.1 A Cartoon

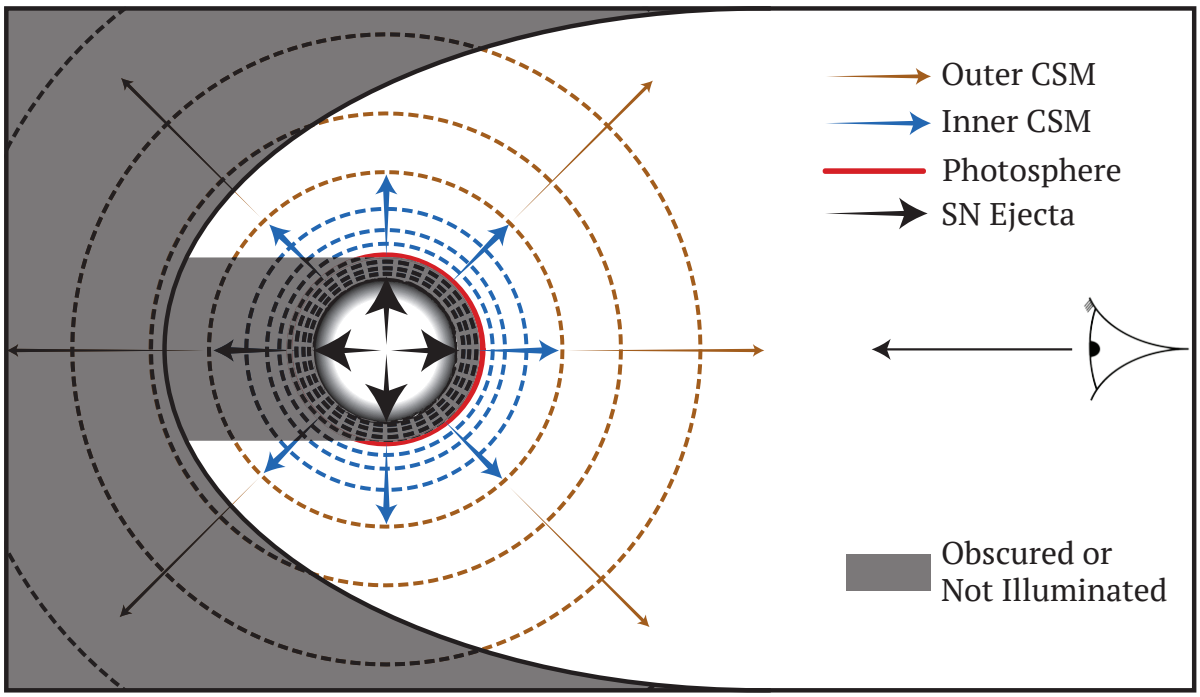

Figure 3.5: A cartoon representation of SN 1998S and its circumstellar environment at the time of observation. For the purposes of this discussion, we define three zones: the SN ejecta (shown in black), the inner CSM region (blue), and the outer CSM region (orange). The photosphere of the system, which falls in the CSM, is shown in red. A fraction of the CSM is obscured by the photosphere and some regions have not yet received any SN radiation owing to nonzero light-travel time; these effects are illustrated by the gray mask, assuming the observer is to the right (figure not to scale).

Figure 3.5 displays a simple cartoon of SN 1998S and its CSM at the time of our HIRES observation. SN 1998S was a hydrogen-rich core-collapse SN, and the expanding SN ejecta exhibited radial velocities of $v \approx 7000\,\mathrm{km\,s^{-1}}$ (Leonard et al. 2000). As indicated by our CMFGEN modeling (§3.3.2), the circumstellar material surrounding SN 1998S was quite dense. On day 2, when this HIRES spectrum was taken, the photosphere was outside the expanding SN ejecta and within the extended progenitor wind. In Figure 3.5 the photosphere is drawn in red, the SN ejecta and swept-up CSM is shown at the center with black arrows, the inner CSM is shown in blue, and the outer CSM is shown in orange. This scenario is informed and supported by several previous studies of SN 1998S in addition to our CMFGEN model (e.g., Leonard et al. 2000; Chugai 2001; Fassia et al. 2001; Mauerhan & Smith 2012).

An Earth-bound observer is shown to the right. The regions of the system that are either obscured by the photosphere or are not yet illuminated to the observer owing to the nonzero travel time of light have been masked in gray.

Note that Figure 3.5 is not drawn to proportion. To orient the reader, here are rough scales for the system at this time, based upon the CMFGEN model outlined in §3.3.2: the outer radius of the expanding ejecta is $\sim 6 \times 10^{14}$ cm, the radius at which $\tau_e = 1.0$ is $\sim 2 \times 10^{15}$ cm, and SN radiation has diffused through the optically thick CSM region and traveled $\sim 5 \times 10^{15}$ cm into the far hemisphere of the wind, while the entirety of the near hemisphere has been illuminated.

To understand the effect of nonzero light-travel time on the observed spectrum, consider the system immediately after the shock traverses the progenitor, as SN radiation is diffusing through the optically thick CSM and ionizing it. Radiative recombination emission from the CSM along the line of sight between SN and observer will follow the first SN light immediately, but an Earth-bound observer will not begin to detect recombination emission from material along other lines of sight until the ionizing radiation has reached that material and the recombination emission has then had time to propagate back to the observer. For a system like SN 1998S, which has a significant amount of material extending to at least 10^{17}–10^{18} cm ($\sim$ 10–100 light days; Mauerhan & Smith 2012), this effect may be important when interpreting early-time observations. For example, CSM located at a radius of $\sim 2 \times 10^{15}$ cm on the far side of the SN (but not obscured by the photosphere) would contribute flux to the observed spectrum at a time lag of about 36 hr relative to CSM located at the same radius on the near side of the SN.

To further confound the issue, the density profile (and therefore ionization potential) is a strong function of radius, and the ionizing radiation field is evolving rapidly as the ejecta/CSM boundary moves outward and the shock interaction fades over time. Any observed spectrum will therefore include emission from material ionized at different times by different radiation fields, emitting material will continue to produce recombination radiation for different timescales after ionization, and this material will be located at a diversity of radii and Doppler shifts relative to the observer. These effects are usually negligible when considering SN spectra, but because of the very young age and high resolution of this spectrum these complications are worth keeping in mind, especially for the Hα line emission, which arises at relatively large radii (see Fig. 3.3).

This cartoon assumes (as does our CMFGEN model) that the progenitor system had a more-or-less spherically symmetric CSM surrounding it, but evidence to the contrary was presented by Leonard et al. (2000) based upon spectropolarimetry from 1998 March 7. Wang et al. (2001) also present spectropolarimetry obtained March 30 and later. The interpretation of the spectropolarimetric data is obfuscated by the uncertain degree of interstellar polarization within the host galaxy, and Leonard et al. (2000) present three distinct physical scenarios consistent with the data. In agreement with Chugai (2001), we prefer the second interpretation of Leonard et al. (2000): the narrow emission features (dominated by unscattered recombination emission) are unpolarized, and the continuum and broad emission wings are both polarized at the few-percent level.

This can be understood in a scenario with a CSM that exhibits a nonspherical but axisymmetric geometry with the axis of symmetry roughly orthogonal to our line of sight. This CSM configuration could be the result of axisymmetrically-enhanced mass loss from the progenitor star (e.g., Bjorkman & Cassinelli 1993; Ignace et al. 1996), an effect which is regularly observed in massive stars (e.g., Coyne & McLean 1982; Zickgraf et al. 1985; Schulte-Ladbeck et al. 1992), or perhaps the result of gravitational interaction with a binary companion (e.g., Smith et al. 2011a). In such a CSM the mean free path of an ionizing photon is greater where the density is lower, and so the ionization front will be elongated in those directions, thereby imparting a significant polarization signal on the continuum and broad-wing flux. The narrow (unscattered) lines are unaffected, regardless of the geometry.

Of course, our quantitative CMFGEN results are dependent upon the assumption of spherical symmetry, but a moderate axisymmetric CSM density enhancement could impart a clear spectropolarimetric signal without affecting the qualitative results from our CMFGEN modeling, and we emphasize that these early-time observations do not probe any possible asphericity of the SN ejecta itself but only the dense CSM. It is difficult to address this issue further without detailed modeling and a more complete dataset, but here we summarize a few additional points: (1) at early times the lack of broad ejecta lines implies that the covering fraction of optically thick CSM is ~ 1 (though it may still be aspherical); (2) the CSM may exhibit different degrees of asphericity at different radii (as would be expected from explosive mass loss from the progenitor, a scenario discussed later), which would mean that a time series of observations is required to fully understand the system; and (3) understanding the effects of asphericity is a persistent difficulty in our efforts to constrain and understand the mass-loss properties of massive stars.

3.4.2 The SN Ejecta and Opaque CSM

The broad P-Cygni features usually observed in SN spectra were not apparent in SN 1998S until about 15 d after discovery and they remained remarkably weak throughout the SN's photospheric phase (Leonard et al. 2000; Fassia et al. 2001). The early absence of ejecta lines is easily explained: as we show in §3.3.2, the photosphere is exterior to the expanding ejecta. The presence of significant CSM also explains the weakness of the SN signatures, once they do appear — as Branch et al. (2000) explain, a significant amount of "toplighting" owing to the ongoing CSM/ejecta interaction effectively mutes the SN lines relative to the continuum even after the photosphere has receded into the ejecta. In addition, Chugai (2001) describes the opaque (in the Paschen continuum) "cool dense shell" (CDS) between the outer shock boundary (where the ejecta are sweeping up CSM) and the inner shock boundary (where the reverse shock is propagating into the expanding ejecta). He argues that this CDS stays optically thick out to 40–50 d and continues to obscure the SN ejecta — a transition from an inner CSM with covering fraction ~ 1 to an outer CSM with covering fraction < 1 could explain the emergence of weak ejecta lines between days 15 and 50.

Regardless, Leonard et al. (2000) and Fassia et al. (2001) argue that the weak ejecta features, once they do emerge from the continuum, are characteristic of a SN II with H and

He features alongside those from Fe, Si, and O. Figure 3.10 shows the spectral evolution of SN 1998S alongside the CMFGEN model. The velocity of the expanding ejecta is $\sim 7000\,\mathrm{km\,s^{-1}}$ as measured by the blue edge of the SN features on day 25 (Leonard et al. 2000).

The time delay between core collapse and shock breakout can be significant in systems with a dense CSM — following Chevalier & Irwin (2011), the diffusion time for the CSM surrounding SN 1998S is $t_\mathrm{d} \approx 0.85\,\mathrm{d}$. This means that core collapse of the progenitor would have occurred almost a full day before any radiation escaped the system. If SN 1998S underwent core collapse 5 d before this HIRES spectrum was taken, the date of the latest nondetection from Li et al. (1998), and assuming v_ejecta is roughly constant, the outer edge of the expanding ejecta would be at $\sim 3 \times 10^{14}\,\mathrm{cm}$. However, note that the ejecta are slowed significantly as they sweep up the CSM, which implies that the early expansion velocity would be faster than $7000\,\mathrm{km\,s^{-1}}$ and therefore that the true radius of the outer ejecta edge is likely a bit larger — in better agreement with our modeled value of $\sim 6 \times 10^{14}\,\mathrm{cm}$.

3.4.3 The Inner CSM

As mentioned in §3.2.1, and as other authors have noted (Leonard et al. 2000; Anupama et al. 2001; Fassia et al. 2001), the strong H emission lines observed in SN 1998S's early-time spectra are well represented by the sum of a narrow Gaussian profile and a broad modified Lorentzian profile. Chugai (2001) has shown that these line profiles are created in regions with τ of a few, where the narrow recombination emission lines are "diffused" through multiple electron-scattering events. The end result is a narrow line core (with a Doppler width indicative of the emitting material's velocity) with broad, symmetric wings (which provide a measure of the optical depth in the emitting region). This electron-scattering process has been observed to produce similar broad, symmetric line profiles in several SNe IIn (e.g., SNe 2010jl, 2011ht; Fransson et al. 2014; Mauerhan et al. 2013a), and our CMFGEN model reinforces this scenario in SN 1998S.

The model further explains why some emission lines in the early SN spectrum exhibit these broad electron-scattering wings while others do not. Figure 3.3 shows the best-fit model's radial profiles of the line-formation regions for Hα, Hβ, Hγ, He II λ4686, He I λ5876, and N III λ4640. The model indicates that Hα is formed over an extended region of the illuminated progenitor wind, with the bulk of the emission coming from 10^{15} to 2×10^{16} cm ($1.6 \gtrsim \tau_e \gtrsim 0.06$), while the higher-ionization lines like He II λ4686 and N III λ4640 are formed in the inner region of the progenitor wind, from 6×10^{14} to (2–3)$\times 10^{15}$ cm ($3 \gtrsim \tau_e \gtrsim 0.8$). Figure 3.6 displays the line profiles of several of these lines normalized to their peak intensity, clearly showing that emission lines which form primarily in the inner wind region (where there is a large electron-scattering optical depth) have strong, broad wings, while lines that form primarily at larger radii (lower τ_e) have relatively weak or no broad wings. A similar result has been found for the Type IIn SN 1994W (Dessart et al. 2009), to which we refer the interested reader for an extensive discussion on the formation of electron-scattering wings and its computation by CMFGEN. In SN 1998S, lines that arise in the inner region

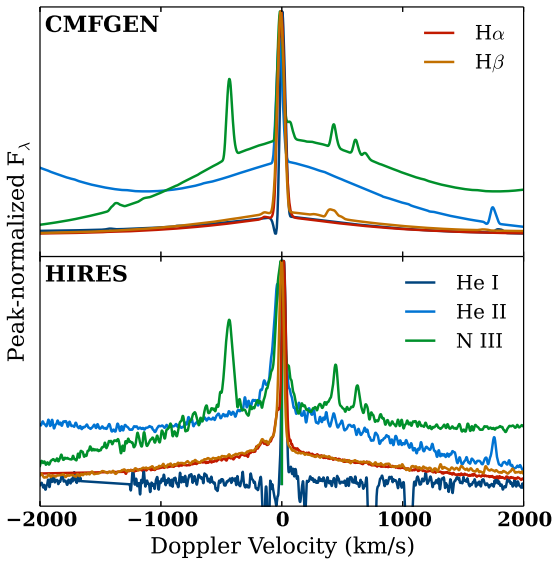

Figure 3.6: A few notable line profiles normalized to their peak emission, shown for the CMFGEN model (top) and in the HIRES data (bottom, smoothed to a resolution of 0.5 Å). We display Hα (red), Hβ (orange), He I λ5876 (dark blue), He II λ4686 (light blue), and N III λ4640 (green).

exhibit more broad emission than lines that arise farther out in the CSM. Note that the N III complex likely includes overlapping flux from the other nearby N III and C III lines. In addition, any weak broad emission associated with the He I line was likely below the noise threshold for detection in our raw spectrum — if it exhibited a broad/narrow ratio comparable to that of the Hα broad emission (as the CMFGEN model implies), it would have been indistinguishable from the echelle order-response function and therefore subtracted out by our flux-normalization routine (see §3.2).

The HIRES spectrum presented here illustrates a further wrinkle: in all two-component lines, the broad wings are systematically blueshifted from the narrow cores by $\sim 50\,\mathrm{km\,s^{-1}}$. Figure 3.7 shows the first three lines of the Balmer series and their best-fit profiles, including a narrow Gaussian profile, a broad modified Lorentzian profile, and a linear background. Unfortunately, deconvolving all of the overlapping line profiles near the N III/C III/He II complex around 4650 Å is difficult and the simple two-component fitting procedure we used for the H lines is not feasible for these ions, but a rough analysis indicates that a similar offset between the central wavelengths of the broad wings and narrow cores exists.

We interpret these broad-wing blueshifts as evidence that the inner wind region exhibits higher wind velocities than the outer region. The opaque photosphere preferentially obscures redshifted material more than blueshifted material, and the effect is more significant for emission arising at small radii than at large radii — as Figure 3.3 shows, the broad H emission (which depends upon the τ_e profile) preferentially arises at lower radii than the narrow H emission.

Similarly, the narrow emission-line cores that arise at low radii are both broader and more blue than the lines arising at large radii. Figure 3.8 displays histograms of the observed line widths and line-center shifts for the emission lines in Table 3.1. Emission arising from

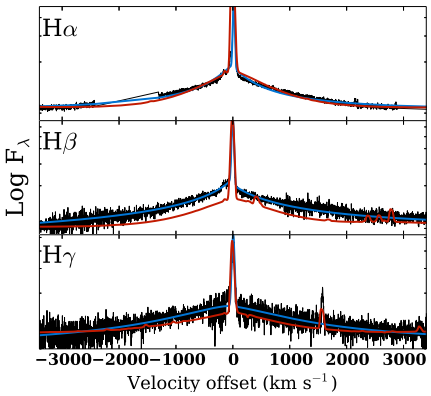

Figure 3.7: A close-up view of the H emission lines on March 4 with the data in black, simple two-component fits shown in blue, and our CMFGEN model in red. All three H lines are well described by the sum of a narrow Gaussian and a broad modified Lorentzian, with the latter blueshifted by $\sim 50\,\mathrm{km\,s^{-1}}$. The CMFGEN model does not show this blueshift trend, as explained in the text. Note that there is a weak helium emission line apparent $\sim 180\,\mathrm{km\,s^{-1}}$ blueward of both Hα and Hβ, as well as other emission lines in the wings of all three lines.

higher-ionization states for C, N, and He display broader line widths than their low-ionization counterparts do, as well as line centers that are significantly blueshifted from those of the low-ionization lines. This reiterates that the CSM at small radii, which exhibits a higher ionization state and more significant obscuration from the photosphere, is moving more rapidly than the CSM at large radii. Note that our CMFGEN model does not include hydrodynamical evolution and assumes a constant velocity profile in the CSM; the observed trend in the line widths and centers is thus not captured in the model.

The line-center effect is significantly smaller than the line-width effect, as expected, and the He I and He II lines illustrate the effect nicely — see Figure 3.9. We estimate the velocity of inner wind material by mirroring the blue wings of the He II lines about $0\,\mathrm{km\,s^{-1}}$, which yields $v \approx 140$–$180\,\mathrm{km\,s^{-1}}$, a factor of ~ 4 higher than the outer wind material.

Evidence for two distinct wind velocity components was also found in spectra 2+ weeks after explosion by Bowen et al. (2000) and Fassia et al. (2001), with the same velocity for the slow component ($\sim 40\,\mathrm{km\,s^{-1}}$) but with a significantly broader fast component ($\sim 350\,\mathrm{km\,s^{-1}}$) — Fassia et al. (2001) proposed that the faster wind was due to something like a blue supergiant phase in the progenitor shortly before core collapse. However, Chugai et al. (2002) presented models indicating a negative velocity gradient in the CSM directly exterior to the photosphere, and proposed that the observations are better explained by the acceleration of a steady (slow) wind through radiation pressure from the SN rather than an increase in wind velocity shortly before core collapse. This idea has been invoked to explain observations of other SNe IIn as well (e.g., SN 2010jl, Fransson et al. 2014).

Our observations are consistent with the latter scenario — radiative acceleration naturally explains the observed increase in inner wind velocity (observations from March 20 indicate a velocity a factor of 2 greater than we observe on March 4, Fassia et al. 2001). To explore this further, we adopt an approximation from Chugai et al. (2002): the maximum velocity to which the SN could accelerate a slow wind through Thomson scattering alone is $v \approx 80\,E_{49} r_{15}^{-2}\,\mathrm{km\,s^{-1}}$, where E_{49} is the time-integrated energy released through radiation in units of $10^{49}\,\mathrm{erg}$ and r_{15} is the radius in units of $10^{15}\,\mathrm{cm}$. We estimate E_{49} by assuming that the luminosity of the young SN roughly follows a power law in time: $L_{\mathrm{SN}} \approx \alpha(t - t_0)^n$. We

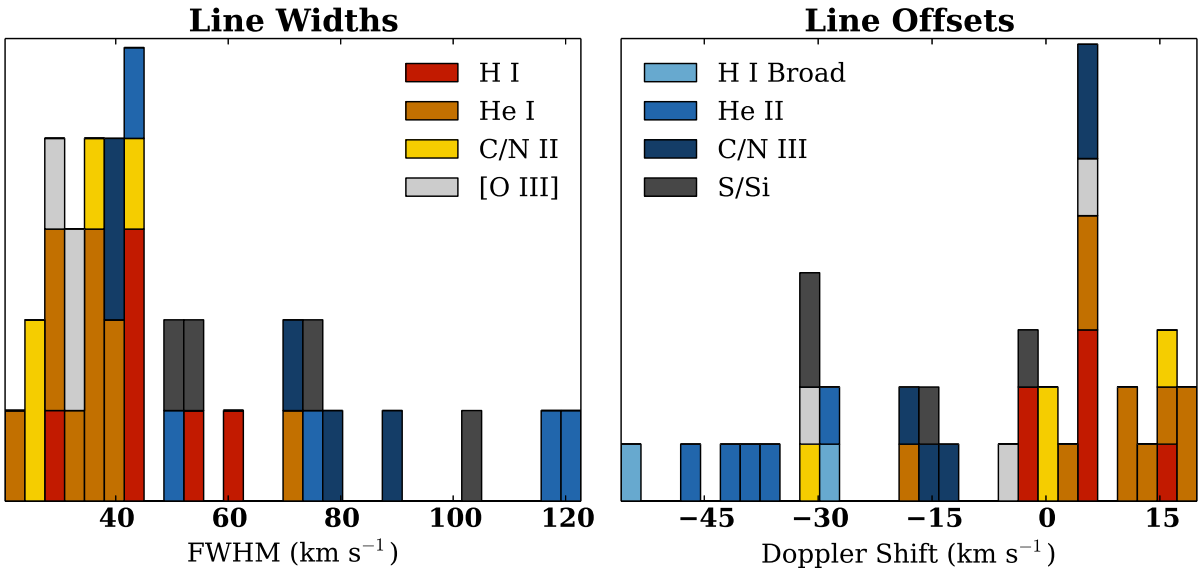

Figure 3.8: A stacked histogram of line widths and line-center shifts for narrow emission lines in the HIRES spectrum of SN 1998S. Lines arising in the inner CSM are shown in red/orange/yellow, and lines arising predominantly in the outer CSM are shown in various shades of blue. Inner CSM lines are, in general, broader and blueshifted from the outer CSM lines. A complete list of lines and their properties is in Table 3.1.

assume the time since explosion $(t - t_0)$ is $\sim 5\,\mathrm{d}$ and we determine $n \approx 3.25$ from early photometry reported by Li et al. (1998) and Qiu et al. (1998). Adopting our modeled values for the luminosity and radius of the photosphere, we calculate that $E_{49} \approx 0.6$ at the time of our HIRES spectrum. This yields a maximum v of $\sim 130\,\mathrm{km\,s^{-1}}$. As Chugai et al. (2002) notes, including UV line-absorption effects increases the maximum velocity by $\sim 50\,\%$ in SN 1998S, and including the original wind velocity adds another $\sim 40\,\mathrm{km\,s^{-1}}$. This more than accounts for the full He II velocity of $\sim$ 140–180 $\mathrm{km\,s^{-1}}$ measured from our HIRES spectrum.

In §3.3.1 we adopt a $\rho \propto r^{-2}$ wind profile for the CSM beyond the CDS. This provides a good fit for most emission lines, but as Figure 3.2 demonstrates, our model overestimates the narrow Hα line. The $\dot{M}$ parameter of the model adjusts the strengths of all hydrogen emission lines. When fitting, we chose to match the Hβ, Hγ, and Hδ lines accurately, but the Hα line is better fit by a lower value. As Fig. 3.3 shows, the Hα line in the model includes flux at larger radii than the other lines do — our inability to match the entire Balmer series with a single $\dot{M}$ is evidence that the true density profile in SN 1998S was steeper than r^{-2}. As we discuss in more detail in §3.4.4, this is in good agreement with other studies of SN 1998S (Chugai 2001; Lentz et al. 2001). Note, however, that a significant fraction of the large-radii material is not yet illuminated owing to light-travel-time effects (Fig. 3.5), and this may also contribute to the observed effect.

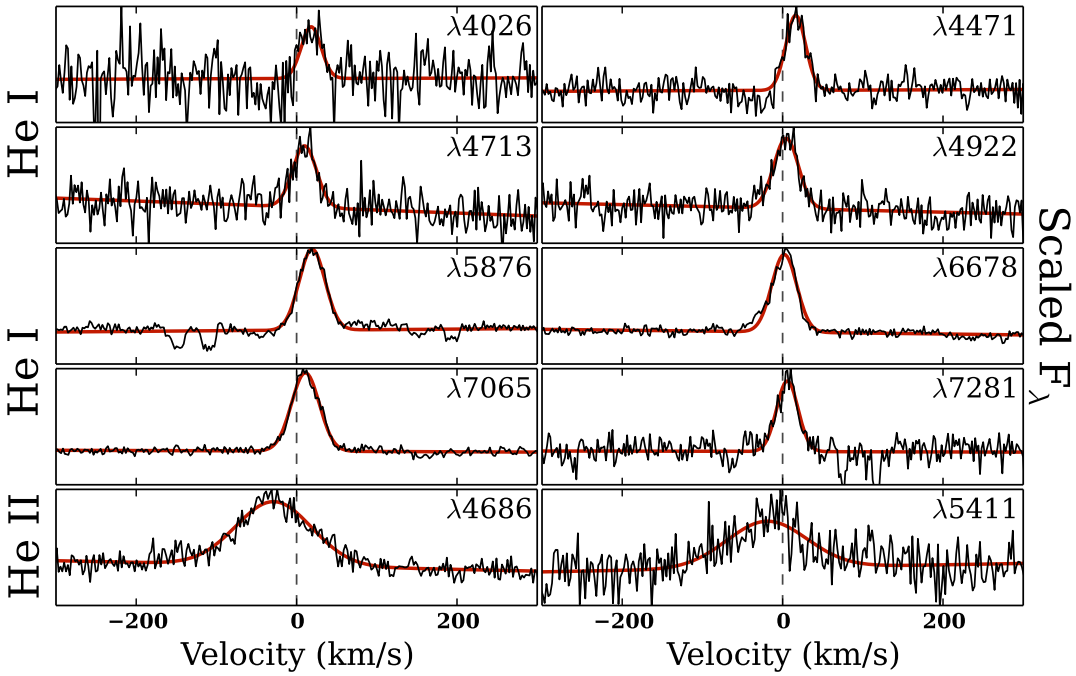

Figure 3.9: Velocity structure of helium lines in the early HIRES spectrum of SN 1998S. He I lines are shown in the top eight panels while He II lines are in the bottom two. The HIRES spectrum is shown in black, red lines illustrate simple Gaussian fits to the data, and the vertical ashed lines indicate the rest frame. The He II lines are significantly broader and blueshifted compared to the He I lines. A complete list of lines and their properties is in Table 3.1.

Our best-fit value of the progenitor's $\dot{M}$ is $6 \times 10^{-3}\,\mathrm{M}_\odot\,\mathrm{yr}^{-1}$. This value, though remarkably high for most massive stars, is in good agreement with previous studies. Chugai (2001) estimates the wind density parameter of SN 1998S through a combination of the bolometric light curve and the line profiles, and Moriya et al. (2014) re-examine the bolometric light curve with an updated model — both estimate $\dot{M} \approx 10^{-2}\,\mathrm{M}_\odot\,\mathrm{yr}^{-1}$. To put this high $\dot{M}$ in perspective, the nearby red supergiant (RSG) Betelguese exhibits a steady mass-loss rate of $(3-4) \times 10^{-6}\,\mathrm{M}_\odot\,\mathrm{yr}^{-1}$ (e.g., Glassgold & Huggins 1986; Harper et al. 2001), and luminous blue variables (LBVs) often have (variable) mass-loss rates a factor of 10–100 higher (Humphreys & Davidson 1994), as do yellow hypergiants (YSGs; Lobel et al. 2003). However, note that some rare RSGs can also exhibit extreme mass loss — VY CMa is a nearby RSG undergoing variable and asymmetric mass loss at a rate of $(2-4) \times 10^{-4}\,\mathrm{M}_\odot\,\mathrm{yr}^{-1}$ at velocities up to $40\,\mathrm{km\,s}^{-1}$(Smith et al. 2009).

The radiative diffusion timescale and light-travel time across the inner CSM region are both less than 1 d, and the recombination times in this region are on the order of seconds

to minutes (assuming the density and temperature profiles from §3.3; Osterbrock & Ferland 2006; Chevalier & Irwin 2011). Thus, by the time our HIRES spectrum was taken, the inner CSM had already entered into photoionization equilibrium with the SN flux and the flux coming from the ejecta/CSM shock boundary.

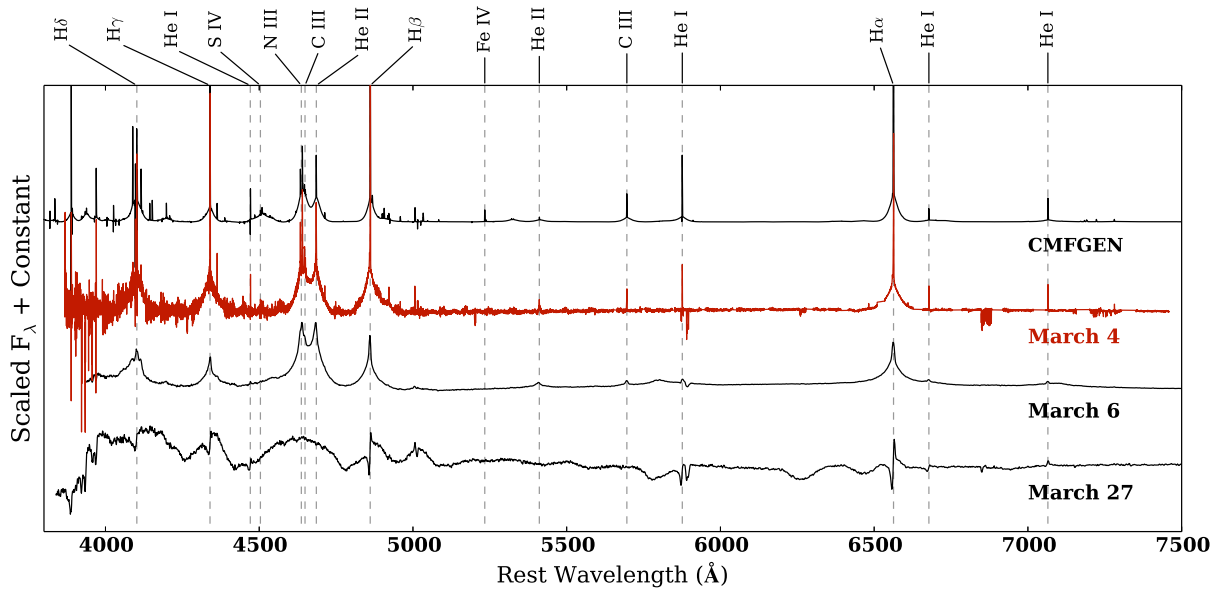

Figure 3.10: The HIRES spectrum of SN 1998S and our CMFGEN model alongside low-resolution spectra taken at later phases (Leonard et al. 2000). A continuum fit has been subtracted from all spectra and notable features are marked with dotted lines. The transition from narrow emission lines to narrow P-Cygni profiles is apparent in the strong hydrogen and He I lines, as all other narrow features fade away. The mismatch in iron abundance between model and data is apparent (§3.3.2) — see the Fe IV λ5234 feature. In addition, it is probable that our flux-normalization procedure (§3.2) removes some weak broad features — e.g. see the Si IV λ4504, C III λ5696, and He I λ5876 lines.

3.4.4 The Outer CSM

Several studies have established that the CSM around SN 1998S extends out to very large radii (e.g., Gerardy et al. 2000; Leonard et al. 2000; Fassia et al. 2001) and in observations taken $\sim$ 3–14 yr after core collapse (when the expanding ejecta is at $r \gtrsim 6 \times 10^{16}$ cm) the Hα emission indicates ongoing interaction with a relatively vigorous RSG progenitor wind ($\dot{M} \approx 10^{-4}\,M_\odot$; Mauerhan & Smith 2012). Note that this mass-loss rate is $\sim$ 1.5 orders of magnitude less than that inferred from our CMFGEN model. Lentz et al. (2001) model UV/optical spectra of SN 1998S from March 16 (day 14), indicating that the CSM exterior to $r_{\rm phot} \approx 10^{15}$ cm exhibits an integrated τ of ~ 0.2. This implies a steeper density gradient than r^{-2}, or a precipitous drop in wind density near $r \approx 10^{15}$ cm (as proposed by Chugai

2001), though as Figure 3.10 shows, narrow P-Cygni profiles of H and He I persist beyond March 25 — strong evidence for at least some CSM at large radii. Assuming the wind velocity remained constant at $40\,\mathrm{km\,s^{-1}}$, a density drop in the CSM at $r = 10^{15}\,\mathrm{cm}$ would correspond to a dramatic increase in the mass-loss rate off of SN 1998S's progenitor $\sim 10\,\mathrm{yr}$ before core collapse. We note that the relative strengths of the Balmer emission lines in our early HIRES spectrum qualitatively support this scenario (see §3.4.3) and our model is dominated by emission from material that left the star 5–15 yr before core collapse (see §3.3.2) — a lower mass-loss rate 15+ yr before core collapse is consistent with our model.

This timescale for increased mass loss is reminiscent of Galactic LBVs, which have been observed to undergo extreme mass-loss events over timescales of 10–40 yr (e.g., Humphreys & Davidson 1994), with one recent example exhibiting an eruption only a few years before core collapse (SN 2009ip; Mauerhan et al. 2013b; Graham et al. 2014). Alternatively, there could be a wind geometry transition near $r \approx 10^{15}\,\mathrm{cm}$ — if the inner wind region were roughly spherical while the outer region were in a disky or equatorial belt configuration, the drop in CSM interaction luminosity could simply be caused by a drop in the CSM covering fraction. See §3.4.1 for further discussion of asphericity in the SN 1998S system.

As Figure 3.8 shows, the outer CSM emission lines in the HIRES spectrum have a median Gaussian FWHM of $\sim$ 35–40 $\mathrm{km\,s^{-1}}$, consistent with the velocities of winds from extreme RSGs (e.g., Smith et al. 2009). These narrow lines are fully resolved here, which was not the case for the low-resolution early-time spectra previously published (e.g., Leonard et al. 2000; Fassia et al. 2001).

Unlike the inner CSM, which has had time to come into photoionization equilibrium, at this time the first radiation from the SN was still propagating through the extended CSM region. With a characteristic outer CSM recombination timescale of hours to days (Osterbrock & Ferland 2006), the observed spectrum must include emission arising from material ionized by the evolving radiation field at various time lags. These effects are mitigated by the radial density profile in the CSM — in an optically thin medium, emission roughly traces the density of material, so CSM at smaller radii (where light-travel-time effects are less important) should contribute most to the narrow-line emission in our spectrum. However, our model indicates that an appreciable amount of the Balmer and He I line flux arises at $r > 10^{16}\,\mathrm{cm}$, and Mauerhan & Smith (2012) have shown that a significant amount of material is present even at $R \approx 2 \times 10^{17}\,\mathrm{cm}$. At $\sim 5\,\mathrm{d}$ after core collapse (assuming a short diffusion time), only $\sim 5\%$ of a sphere of material with that radius would be illuminated ($\sim 84\%$ for $r \approx 10^{16}\,\mathrm{cm}$), so we must keep the light-travel effects in mind when considering the influence of material at large radii on the early-time spectra of SN 1998S.

Note that, as described in §3.2, our best-fit recession velocity is slightly less than that from Fassia et al. (2001), which was determined by fitting for the line centers of forbidden emission lines in a high-resolution spectrum from day 36. Though the discrepancy is only $\sim 10\,\mathrm{km\,s^{-1}}$, it is significant given the very high resolution data and the narrow line features. Fassia et al. (2001) find that the P-Cygni peak of the Hα line moves from a redshift of +8 to $+17\,\mathrm{km\,s^{-1}}$ between days 17 and 36, while our spectrum on day 2 shows the peak of Hα emission at a redshift of $+16\,\mathrm{km\,s^{-1}}$ (or $+26\,\mathrm{km\,s^{-1}}$, adopting their value of z). The cause

of this line velocity evolution is unclear.

3.4.5 Dust Extinction of SN 1998S

Both Leonard et al. (2000) and Fassia et al. (2001) have observed a blue ($\lambda \lesssim 5000\,$Å) flux excess in the very early spectra of SN 1998S, beyond what can be accounted for with a blackbody continuum. Because the early-time spectrum of Leonard et al. (2000) provides the overall flux calibration for the HIRES data presented here, the same issue remains.

However, the ionization states of lines in our detailed non-LTE CMFGEN model provide an independent measure of the temperature, allowing us to compute a spectral energy distribution that can be compared to the observations. We find remarkable agreement between the model and data if the total dust reddening toward SN 1998S is quite small: $E(B-V) \approx 0.05\,$mag, assuming $R_V = 3.1$. Adopting $E(B-V) = 0.148^{+0.040}_{-0.028}\,$mag and the standard Milky Way dust-extinction law, as derived in §3.2, all CMFGEN models include a significant mismatch between the relative line fluxes and the continuum level in the blue region. Leonard et al. (2000) explore reddened blackbody fits with $E(B-V)$ and R_V as free variables and find reasonable fits with total $0.08 \lesssim E(B-V) \lesssim 0.15\,$mag and $R_V \gtrsim 4.0$; our results are in rough agreement, though we only vary $E(B-V)$ and hold R_V constant.

Significant variance in the properties of dust extinction toward extragalactic SNe has been observed before (e.g., Foley et al. 2014), likely owing to obscuration from the CSM of the SN or from anomalous dust laws in the host galaxy. Perhaps a similar situation presents itself here in SN 1998S — there certainly is a large amount of CSM in the immediate vicinity of the SN. Regardless, this uncertainty in the reddening only somewhat affects our determination of $R_{\rm in}$, $L_{\rm SN}$, and $\dot{M}$ using CMFGEN, while values for $v_{\rm wind}$ and the abundances are unaffected. For instance, with $E(B-V) = 0.148\,$mag and $R_V = 3.1$, our model indicates $\dot{M} \approx (7.5 \pm 1) \times 10^{-3}\,{\rm M}_\odot\,{\rm yr}^{-1}$, $R_{\rm in} \approx 7.0 \times 10^{14}\,$cm, and $L_{\rm SN} \approx 3 \times 10^{10}\,{\rm L}_\odot$. These values are 17%, 25%, and 50% different from the best-fit values when adopting the reduced value of $E(B-V) = 0.05\,$mag (see Table 3.2). Note also that in §3.4.1 we adopt an interpretation of the spectropolarimetric data from Leonard et al. (2000) that implies a relatively large amount of host-galaxy reddening based upon empirical relations between $E(B-V)$ and the degree of interstellar polarization from Milky Way dust, though Wang et al. (2001) present an alternative interstellar dust polarization interpretation. Adopting $E(B-V)_{\rm total} = 0.05\,$mag indicates that the polarimetric properties of the host galaxy's dust likely differ significantly from those of the Milky Way.

3.4.6 Wolf-Rayet, Luminous Blue Variable, Red Supergiant?

As other authors have noted (e.g., Leonard et al. 2000), the low-resolution early emission-line spectrum of SN 1998S shows remarkable similarities to the spectra of Wolf-Rayet (WR) stars. However, as also found for SN 2013cu (Groh 2014) and PTF11iqb (Smith et al. 2015), this does not necessarily indicate that the progenitor of SN 1998S was a WR star. We find that the emission lines observed in the early-time spectra of SN 1998S are a result

of the photoionization of a pre-existing progenitor wind after the SN explosion, and are physically unrelated to WR stars — in good agreement with other analyses of SN 1998S and other SNe IIn. Regardless, WR spectra generally fall within a well-accepted and physically understood classification scheme (e.g., Smith 1968; Smith et al. 1996) which can provide a useful framework for comparison (e.g., Gal-Yam et al. 2014). Groh (2014), in an effort to clarify the distinction between WR spectra and young SN spectra, suggests prepending an "X" to the WR spectral types when discussing spectra of post-explosion objects that exhibit WR-like spectra but are not WR stars. In this spirit, we apply the Smith et al. (1996) classification criteria to our spectrum of SN 1998S to explore the similarities and differences between this spectrum of the young SN 1998S system and the spectra of WR stars.

First, the SN spectrum is nitrogen rich, similar to the WN class of WR stars. After applying the flux and reddening corrections described in §3.2, the He II λ5411 / He I λ5875 line ratio ("ionization criterion"; Smith 1968) and the relative strengths of the N III and N IV lines in our HIRES spectrum indicate similarities to the WN7 or WN8 spectral classes. There is, of course, very strong hydrogen emission in the SN 1998S spectrum, with a "hydrogen criterion" (Smith et al. 1996) greater than 1.3. WR stars with a hydrogen criterion greater than 0.5 are given the "h" postfix, but the value for our SN 1998S spectrum is well outside the range generally seen even in WNh stars.

Note that the WR classification scheme assumes that the major emission lines are fully resolved; for our HIRES spectrum that requirement is satisfied, but it may not be for lower-resolution spectra of SN 1998S or other similar objects. Note, also, that both the ionization criterion and the hydrogen criterion are defined based upon the ratio of the narrow emission line peak to the local continuum and, when examined in detail, the line profiles in our HIRES spectrum display systematic differences from those of WR stars. For the ionization criterion this does not appear to be important, but if one compares integrated flux ratios rather than peak flux ratios, thereby accounting for the broad wings of the H and the He I lines, the hydrogen criterion is even larger than is given above — highlighting again that the physical conditions in this post-explosion spectrum of SN 1998S are actually quite different from those found in WN stars. The "strength-width" criterion of Smith et al. (1996) is also not very informative when applied to the SN 1998S spectrum.

In summary, the early-time spectrum of SN 1998S is similar to WR spectra of spectral classes WN7h and WN8h, although clear differences are apparent and they indicate a very different physical picture than in a WR star. Following Groh (2014), our SN 1998S spectrum would be classified as an XWR7h or XWN8h, but this classification scheme breaks down when one examines the details.

Our analysis of the early spectrum of SN 1998S provides three major clues to the nature of the progenitor — its chemical composition ($Y = 0.49$, N-enhanced material), mass-loss rate ($6 \times 10^{-3}\,M_\odot\,yr^{-1}$), and wind velocity ($40\,km\,s^{-1}$). Given the extreme mass-loss rate and the evidence for an increased mass loss soon before core collapse, the LBV interpretation becomes quite attractive, although RSGs like VY CMa (Smith et al. 2009) and YHGs like ρ Cas (Lobel et al. 2003) also show evidence of outbursts with extreme and variable mass-loss rates. In addition, our CMFGEN model indicates that the progenitor wind was only mildly

enriched by the CNO cycle, while the spectra of Milky Way LBVs generally indicate strong CNO enrichment (e.g., Davidson et al. 1986). Our physical interpretation is that the CSM around SN 1998S was created by mass loss from an SN progenitor that was compositionally consistent with theoretical predictions of RSGs, YHGs, and LBVs at the pre-SN stage (Groh et al. 2013b; see Groh et al. 2013c and their Table 3).

Continued monitoring of SN 1998S over the years since explosion has not indicated any evidence for an older shell of very-high-density CSM, as one might expect if there were previous outbursts. However Mauerhan & Smith (2012) publish spectroscopy of the Hα line as late as ~ 5000 d, powered by interaction with a steady RSG-like progenitor wind at $r \approx 3 \times 10^{17}$ cm — material that (assuming $v_{\rm wind}$ is steady at 40 km s^{-1}) left the progenitor a few thousand years prior. Of course, coverage is very spotty over those 5000 d, and increased interaction with a CSM shell caused by a short-lived high-mass-loss episode may have gone by unnoticed. Variable and extreme mass loss in the few years before core collapse was recently observed in detail in the SN 2009ip system (e.g., Mauerhan et al. 2013b; Graham et al. 2014); perhaps the SN 1998S system underwent a similar process. Exactly how eruptive mass loss and the evolution toward core collapse are (or are not) coupled in massive stars is poorly understood at best, and we look forward to further studies of this topic.

3.4.7 SN 2013cu

In a remarkable spectrum of the Type IIb SN 2013cu taken less than a day after explosion, Gal-Yam et al. (2014) discovered emission features very much like those observed in our HIRES spectrum of SN 1998S. The lower resolution of their SN 2013cu spectrum makes the two-component emission features more difficult to analyze, but the Hα profiles of the two SNe are almost identical and most of the same emission lines are present in both (see their Extended Data, Figure 3). Gal-Yam et al. (2014) interpret the SN 2013cu spectrum within the context of a WR-like wind and consider the possibility that it provides a long-sought observational connection between massive H-deficient WR stars and the progenitors of stripped-envelope core-collapse SNe.

However, as shown in Figure 2 of Gal-Yam et al. (2014), most of the emission-line profiles in the early SN 2013cu spectrum are unresolved and therefore must have widths $\lesssim 100$ km s^{-1}, much slower than those expected for a WR wind. The spectrum of SN 2013cu is similar to that of a WN6(h) star (Gal-Yam et al. 2014), but WN6 stars in the Milky Way have terminal wind velocities of ~ 1800 km s^{-1} (Crowther 2007). The wings of the strongest few lines in the SN 2013cu spectrum do extend out to WR-like velocities if one interprets them as the result of a Doppler shift ($v \approx 2500$ km s^{-1}). On the other hand, it is then difficult to understand why the line cores (and the complete profiles of the weaker lines) are so remarkably narrow.

It instead seems likely that the broad wings of the emission lines in SN 2013cu were created by Thomson scattering in an optically thick CSM moving at a low velocity, the same process that created the characteristic emission-line profiles of SN 1998S. Gal-Yam et al. (2014) note this scenario as a possibility, though they adopt $v_{\rm wind} \approx 2500$ km s^{-1} in their analysis. Groh (2014) presents a CMFGEN analysis of SN 2013cu, indicating that the broad-

line profiles are indeed created by Thomson scattering, that $v_{\rm wind}$ is low ($\lesssim 100\,{\rm km\,s^{-1}}$), and that the progenitor was likely an LBV or YHG. Gal-Yam et al. (2014) also note that the progenitor mass-loss rate indicated by their spectrum of SN 2013cu is very much greater than the rates from known WR stars and models, which may be an indication that the mass-loss rate increased markedly in the year or so before core collapse — quite similar to the irregular mass-loss scenario we ascribe to the progenitor of SN 1998S. The detailed emission-line profiles and the strong similarities between the early-time spectra of SN 1998S and SN 2013cu cast further doubt on this particular connection between WR progenitors and stripped-envelope SNe. Rather than a persistent WR-like wind, it seems likely that a short-lived epoch of extreme mass loss from the progenitor of SN 2013cu created the CSM whose flash-ionized lines populate the spectrum seen in the first hours after explosion (also suggested by, e.g., Groh 2014).

There is no evidence for an extended outer CSM region in SN 2013cu. The early-time emission features fade quickly, unlike those of SN 1998S which are sustained by the ejecta/CSM shock front, and the narrow P-Cygni H and He features seen in the spectra of SN 1998S do not appear. Unlike SN 1998S, SN 2013cu was hydrogen poor, exhibiting spectral features characteristic of a Type IIb SN. The progenitors of these two SNe were therefore quite different, with differing masses or, perhaps, with different evolutionary histories owing to the effects of a nearby binary companion star, present in one progenitor system but not the other. If both objects did indeed undergo extreme mass-ejection episodes in the 1–10 yr before core collapse, it seems that these episodes can occur in a variety of progenitor systems (see also PTF11iqb, Smith et al. 2015). The rapid "flash spectroscopy" technique described by Gal-Yam et al. (2014) will be a powerful tool to explore this issue further, enabling the study of the CSM immediately surrounding SNe of various types before it is swept up by the expanding ejecta.

3.5 Conclusion

In this article we present what we believe to be the earliest high-resolution ($\Delta\lambda < 1.0\,$Å) spectrum ever taken of a Type IIn supernova and the earliest published spectrum of SN 1998S: a Keck HIRES spectrum taken only a few days after core collapse. We present a CMFGEN model of the entire SN+CSM system and we explore the physical implications of this remarkable spectrum in detail. We discuss the connections between the progenitor of SN 1998S and massive stars in the Milky Way Galaxy that are undergoing extreme mass loss and show that the progenitor of SN 1998S shared many properties with Galactic examples of high-mass stars — LBVs, YHGs, and some extreme RSGs. We compare the spectrum of SN 1998S to that of the recent Type IIb SN 2013cu and find remarkable similarities, indicating that the progenitors of qualitatively different SNe may exhibit similarly extreme mass loss shortly prior to explosion.

The spectrum published herein offers a new window into the complex circumstellar environment of a prototypical and well-studied SN IIn, and we hope it can be of some use

as a case study as many more SNe are observed at very early epochs in the coming era of autonomous spectroscopic studies, which will be capable of observing SNe within mere hours of discovery (e.g., the Spectral Energy Distribution Machine; Ben-Ami et al. 2012).

Chapter 4

SN 2015U: A Rapidly Evolving and Luminous Type Ibn Supernova

First published in the Monthly Notices of the Royal Astronomical Society:
Shivvers et al. (2016).
Co-Authors: WeiKang Zheng, Jon Mauerhan, Io K. W. Kleiser, Schuyler D. Van Dyk, Jeffrey M. Silverman, Melissa L. Graham, Patrick L. Kelly, Alexei V. Filippenko, Sahana Kumar

Chapter Abstract

Supernova (SN) 2015U (also known as PSN J07285387+3349106) was discovered in NGC 2388 on 2015 Feb. 11. A rapidly evolving and luminous event, it showed effectively hydrogen-free spectra dominated by relatively narrow helium P-Cygni spectral features and it was classified as a SN Ibn. In this paper we present photometric, spectroscopic, and spectropolarimetric observations of SN 2015U, including a Keck/DEIMOS spectrum (resolution ≈ 5000) which fully resolves the optical emission and absorption features. We find that SN 2015U is best understood via models of shock breakout from extended and dense circumstellar material (CSM), likely created by a history of mass loss from the progenitor with an extreme outburst within ~ 1–$2\,\mathrm{yr}$ of core collapse (but we do not detect any outburst in our archival imaging of NGC 2388). We argue that the high luminosity of SN 2015U was powered not through ^{56}Ni decay but via the deposition of kinetic energy into the ejecta/CSM shock interface. Though our analysis is hampered by strong host-galaxy dust obscuration (which likely exhibits multiple components), our dataset makes SN 2015U one of the best-studied Type Ibn supernovae and provides a bridge of understanding to other rapidly fading transients, both luminous and relatively faint.

4.1 Introduction

Core-collapse supernovae (SNe) are luminous explosions that mark the end of a massive star's life. These SNe are differentiated from their thermonuclear counterparts (Type Ia SNe) and are grouped into classes via spectral and photometric analyses (e.g., Filippenko 1997). The major core-collapse subclasses include SNe IIP and IIL, events which show strong hydrogen throughout their evolution and respectively do or do not exhibit a hydrogen-recombination plateau in their light curves (though the distinction between SNe IIP and IIL may be less clear than previously thought; e.g., Arcavi et al. 2012; Anderson et al. 2014; Sanders et al. 2015). SNe Ib and Ic (often called stripped-envelope SNe) are core-collapse events that show no hydrogen in their spectra and (for SNe Ic and broad-lined SNe Ic) no helium; they (along with the intermediate SNe IIb, which exhibit very little hydrogen) are commonly understood to arise from progenitor stars that have lost all or most of their hydrogen (and perhaps helium) envelopes prior to core collapse, though the detailed connections between progenitors and SN observables remain somewhat uncertain (e.g., Matheson et al. 2001; Drout et al. 2011; Bianco et al. 2014; Modjaz et al. 2014; Liu et al. 2016; Dessart et al. 2015).

A subset of SNe reveal signatures of a dense shroud of circumstellar material (CSM) surrounding their progenitors at the time of explosion. For hydrogen-rich events, relatively narrow lines (full width at half-maximum intensity [FWHM] $\lesssim 1000\,\mathrm{km\,s^{-1}}$) from this interaction with the CSM are often detected; these objects have been dubbed SNe IIn (e.g., Schlegel 1990; Filippenko 1991). This interaction can provide a significant luminosity boost (as has been observed for superluminous SNe IIn; e.g., Gal-Yam 2012). CSM interaction occurs in some hydrogen-poor SNe as well. SNe Ia-CSM are thermonuclear events that exhibit relatively narrow features (usually Hα emission) caused by interaction with hydrogen-rich CSM (though the underlying SN ejecta are hydrogen-poor; e.g., Silverman et al. 2013a,b). A small number of stripped-envelope SNe have been found to exhibit the spectral signatures of CSM interaction. SNe Ibn (e.g., Foley et al. 2007; Pastorello et al. 2008a) show relatively narrow helium lines in their spectra but no hydrogen, and they can be quite heterogeneous in their photometric evolution (e.g., Pastorello et al. 2016), while the remarkable SN 2014C appeared to be a normal SN Ib at peak brightness but then began interacting with hydrogen-rich CSM only a few months later (Milisavljevic et al. 2015).

In addition to the examples of interaction with dense CSM described above, indications of very short-lived interaction with CSM have been discovered through "flash spectroscopy" of very young SNe of various types (e.g., Gal-Yam et al. 2014; Shivvers et al. 2015; Khazov et al. 2016). These examples exist on a continuum of CSM densities with the strongly interacting events described above; they require much less CSM and their observables at peak brightness generally align with those of "normal" events.

Here we present the results of our observational campaign to study SN 2015U, a remarkable and very well-monitored SN Ibn. It was discovered in NGC 2388 by the Lick Observatory Supernova Search (LOSS) with the 0.76 m Katzman Automatic Imaging Telescope (KAIT; Filippenko et al. 2001b) on 2015 Feb. 11 (all dates and times reported herein

are UTC). Note that, because the official International Astronomical Union name was not assigned until November 2015 (Kumar et al. 2015), this event has also been discussed in the literature under the name PSN J07285387+3349106. Ochner et al. (2015) classified it as a young SN Ibn based upon spectra obtained on Feb. 18, which showed a blue continuum and relatively narrow He I emission features (see also Kumar et al. 2015). Tsvetkov et al. (2015) present *BVRI* photometry of SN 2015U starting Feb. 17, showing that it has one of the fastest decline rates known (similar to those of SNe 2002bj, 2005ek, and 2010X) and is remarkably luminous (though SN 2015U is significantly obscured by an uncertain amount of dust in the host galaxy). Pastorello et al. (2015c) present additional photometry and low-resolution spectra of this event and describe SN 2015U within the context of SNe Ibn (e.g., Foley et al. 2007; Pastorello et al. 2008a, 2016).

In this paper we present photometric, spectroscopic, and spectropolarimetric observations of SN 2015U, including one epoch of relatively high-resolution Keck DEIMOS spectroscopy ($R = \lambda/\delta\lambda \approx 5000$), enabling us to study the narrow-line features in detail. We show that SN 2015U is similar to several other SNe from the heterogeneous SN Ibn class, and that it shares many features with the rapid and luminous transients discovered in the Pan-STARRS1 (PS1) archives (Drout et al. 2014), those found in the SuperNova Legacy Survey (SNLS) archives (Arcavi et al. 2016), and a few other rapidly fading SNe from the literature. SN 2015U offers valuable insights into the physics of the poorly observed class of rapidly fading SNe.

4.2 Observations

4.2.1 Photometry

SN 2015U was first detected by KAIT on Feb. 11.24 at 18.06 ± 0.15 mag in an unfiltered image.[1] An unfiltered image taken the night before (Feb. 10.30) shows no source to a limit of ~ 18.4 mag. We began acquiring multiband photometry (*BVRI* and *clear*) starting Feb. 14 with KAIT and the 1 m Nickel telescope at Lick Observatory. We used a set of 50 Nickel and KAIT images with strong detections of SN 2015U and with good astrometric solutions for the field to calculate an updated position: $\alpha = 07^h28^m53.90^s$, $\delta = +33^\circ49'10.56''$ (J2000), offset from the centre of the galaxy by $\sim 6''$. We believe this position to be accurate within $0.15''$ or better — the positions we measured for the SN exhibit a scatter of $0.09''$ in both right ascension and declination across 50 images.

Ganeshalingam et al. (2010) describe our photometric observing program at Lick in detail, along with our KAIT and Nickel image-reduction pipeline. Point-spread-function (PSF) photometry was performed using DAOPHOT (Stetson 1987) from the IDL Astronomy User's Library.[2] Instrumental magnitudes were calibrated to several nearby stars from the Sloan

[1] The KAIT *clear* passband is similar to the *R* band but broader. For more details and transformations to standard passbands, see Riess et al. (1999) and Li et al. (2003).

[2] http://idlastro.gsfc.nasa.gov/

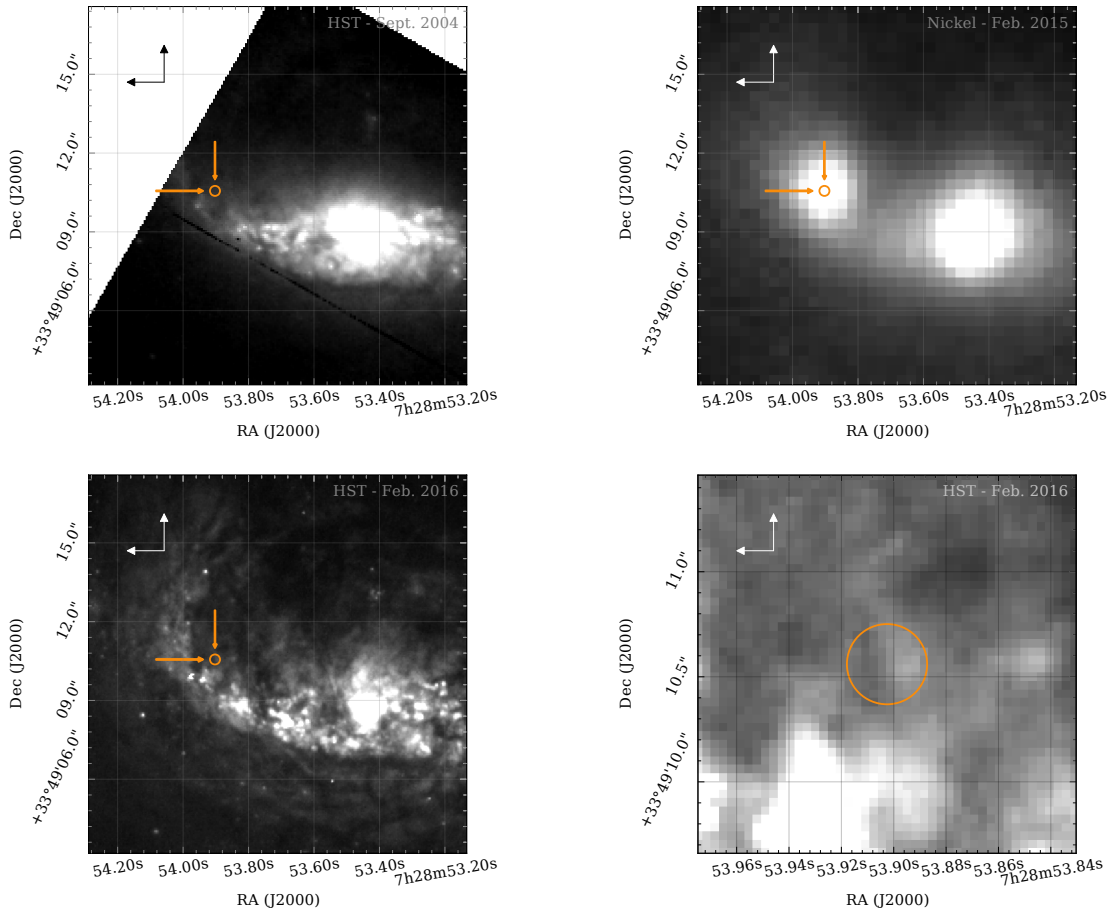

Figure 4.1: Top left: a pre-detection *HST* NICMOS image of NGC 2388 through the *F110W* filter. Top right: a detection of SN 2015U by the Lick Nickel 1 m telescope through the V-band filter. Bottom left: an *HST* WFC3 image of SN 2015U's location through the *F555W* filter at ~ 1 yr post-explosion. Bottom right: a zoom-in of SN 2015U's location in the *HST* *F555W* filter. All images show the location of the SN with orange arrows, and the size of our 3σ position error is marked with a circle.

Digital Sky Survey, transformed into the Landolt system using the empirical prescription presented by Robert Lupton.[3]

We measure SN 2015U's date of peak of brightness in each passband of our Nickel+KAIT photometry by fitting a low-order polynomial to the light curve within the first week (first 10 days for the I band) and use Monte Carlo Markov Chain (MCMC) methods to estimate our uncertainties. In Modified Julian Day (MJD), we find $t_V^{\max} = 57071.1 \pm 0.2$, $t_R^{\max} = 57071.6 \pm 0.5$, and $t_I^{\max} = 57072.4 \pm 0.2$ (our data do not constrain the B-band peak well). Throughout our analysis we present phases relative to the V-band peak. NGC 2388 is at a

[3] http://www.sdss.org/dr7/algorithms/sdssUBVRITransform.html

redshift of $z_{\rm host} = 0.013790 \pm 0.000017$ (NED; de Vaucouleurs et al. 1991), which (assuming cosmological parameters $H_0 = 71\,{\rm km\,s^{-1}\,Mpc^{-1}}$, $\Omega_m = 0.27$, and $\Omega_\Lambda = 0.73$) translates into a luminosity distance of 58.9 Mpc (Wright 2006) and a distance modulus of 33.85 mag that we adopt for all absolute-magnitude corrections.

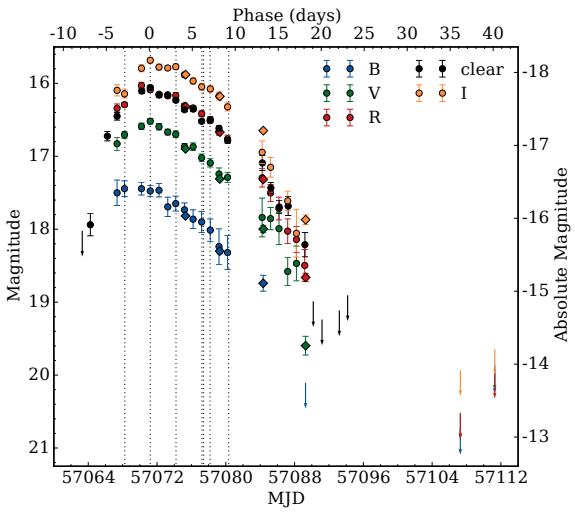

Figure 4.2: The *BVRI* and *clear* passband light curves of SN 2015U after correcting for MW dust absorption but not for the host absorption. KAIT data are indicated by circles and Nickel data by diamonds. The dates of our spectral observations are marked by dotted vertical lines. The phase relative to the V-band peak is shown along the top while the absolute magnitude is shown on the right. Because these absolute magnitudes have not been corrected for significant but uncertain dust absorption arising within the host galaxy, they can be taken as lower limits on the luminosity of SN 2015U.

NGC 2388 and the SN site (pre-explosion) were imaged on 2004 Sep. 10 with the *Hubble Space Telescope (HST)* and the Near-Infrared Camera and Multi-Object Spectrometer (NICMOS) with the NIC2 aperture (scale $0\farcs076$ pixel^{-1}) in bands *F110W*, *F160W*, *F187N*, and *F190N*. We determined the SN position in each band's mosaic data products based on the absolute SN position and the world coordinate system of the image — no stellar object was detected at this position in any of the mosaics. We quantified these nondetections in the *F110W* and *F160W* mosaics using DAOPHOT by assuming a PSF constructed from the brightest isolated star in the mosaics and inserting an artificial star at the SN position. The artificial star was measured with ALLSTAR within DAOPHOT using photometric calibrations established from the online cookbook[4] and with parameters appropriate for NIC2, and then reduced in luminosity until it was detected at a signal-to-noise ratio (S/N) of ~ 3. The corresponding upper limits are > 26.0 and > 25.2 mag in *F110W* and *F160W*, respectively.

Under our Cycle 23 Snapshot program with *HST*'s Wide Field Camera 3 (WFC3; GO-14149, PI Filippenko), we obtained images of the SN location on 2016 Feb. 14 (1 yr post explosion) through the *F555W* (710 s) and *F814W* (780 s) filters (scale $0\farcs04$ pixel^{-1}). Figure 4.1 shows a Nickel detection of SN 2015U alongside the pre-explosion NICMOS *F110W* image and the 1 yr WFC3 *F555W* image of the SN location. We find that SN 2015U exploded on the trailing edge of NGC 2388's spiral arm, in a region with several probable dust

[4] www.stsci.edu/hst/nicmos/performance/photometry/cookbook.html; corrections to infinite aperture and zeropoints at zero magnitude were obtained from www.stsci.edu/hst/nicmos/performance/photometry/postncs_keywords.html.

Table 4.1: KAIT and Nickel Photometry of SN 2015U

UT Date	MJD	*B* (1σ)	*V* (1σ)	*R* (1σ)	*I* (1σ)	*clear* (1σ)	Instrument
2015-02-10	57063.30	-	-	-	-	>18.4	KAIT
2015-02-11	57064.24	-	-	-	-	18.06 (0.15)	KAIT
2015-02-13	57066.22	-	-	-	-	16.85 (0.06)	KAIT
2015-02-14	57067.35	17.71 (0.17)	16.98 (0.09)	16.46 (0.06)	16.18 (0.08)	16.57 (0.05)	KAIT
2015-02-15	57068.22	17.65 (0.11)	16.86 (0.05)	16.41 (0.03)	16.23 (0.06)	-	KAIT
2015-02-17	57070.19	17.65 (0.09)	16.74 (0.04)	16.15 (0.05)	15.88 (0.05)	16.23 (0.03)	KAIT
2015-02-18	57071.21	17.69 (0.08)	16.67 (0.04)	16.21 (0.03)	15.77 (0.04)	16.18 (0.03)	KAIT
2015-02-19	57072.23	17.68 (0.09)	16.75 (0.04)	16.27 (0.03)	15.87 (0.04)	16.28 (0.03)	KAIT
2015-02-20	57073.24	17.90 (0.13)	16.82 (0.04)	16.29 (0.03)	15.88 (0.04)	16.28 (0.02)	KAIT
2015-02-21	57074.18	17.86 (0.10)	16.85 (0.05)	16.29 (0.04)	15.86 (0.04)	16.35 (0.02)	KAIT
2015-02-22	57075.20	17.94 (0.09)	17.02 (0.04)	16.43 (0.03)	15.97 (0.04)	16.48 (0.02)	KAIT
2015-02-22	57075.32	18.03 (0.02)	17.05 (0.01)	16.44 (0.01)	15.97 (0.01)	-	Nickel
2015-02-23	57076.20	18.07 (0.13)	17.02 (0.05)	16.46 (0.04)	16.06 (0.04)	16.48 (0.03)	KAIT
2015-02-24	57077.19	18.11 (0.14)	17.18 (0.05)	16.54 (0.04)	16.13 (0.05)	16.64 (0.02)	KAIT
2015-02-25	57078.19	18.22 (0.15)	17.24 (0.06)	16.62 (0.04)	16.16 (0.04)	16.63 (0.03)	KAIT
2015-02-26	57079.21	18.45 (0.24)	17.40 (0.08)	16.79 (0.05)	16.26 (0.06)	16.74 (0.03)	KAIT
2015-02-26	57079.30	18.51 (0.04)	17.47 (0.02)	16.79 (0.01)	16.27 (0.02)	-	Nickel
2015-02-27	57080.21	18.53 (0.23)	17.44 (0.07)	16.89 (0.05)	16.41 (0.06)	16.91 (0.04)	KAIT
2015-03-03	57084.23	-	17.99 (0.27)	17.42 (0.13)	17.03 (0.16)	17.21 (0.10)	KAIT
2015-03-03	57084.35	18.95 (0.11)	18.15 (0.05)	17.44 (0.03)	16.74 (0.02)	-	Nickel
2015-03-04	57085.22	-	18.01 (0.15)	17.63 (0.12)	17.24 (0.13)	17.56 (0.08)	KAIT
2015-03-05	57086.19	-	18.15 (0.22)	17.84 (0.16)	-	17.82 (0.09)	KAIT
2015-03-06	57087.20	-	18.73 (0.19)	18.15 (0.17)	17.70 (0.13)	-	KAIT
2015-03-06	57087.25	-	-	-	-	17.81 (0.13)	KAIT
2015-03-07	57088.21	-	18.62 (0.24)	18.26 (0.18)	18.14 (0.33)	-	KAIT
2015-03-08	57089.19	-	-	18.62 (0.22)	-	18.33 (0.17)	KAIT
2015-03-08	57089.28	>20.5	19.75 (0.13)	18.78 (0.06)	17.96 (0.07)	-	Nickel
2015-03-09	57090.17	-	-	-	-	>19.3	KAIT
2015-03-10	57091.19	-	-	-	-	>19.6	KAIT
2015-03-12	57093.20	-	-	-	-	>19.5	KAIT
2015-03-13	57094.17	-	-	-	-	>19.3	KAIT
2015-03-26	57107.28	>21.1	>20.9	>20.9	>20.3	-	Nickel
2015-03-30	57111.28	>20.3	>20.2	>20.3	>20.0	-	Nickel

lanes and a generally clumpy appearance. One of those clumps falls within the 3σ position error circle in both the *F555W* and *F814W* images and is not detected in the pre-explosion NICMOS images. However, this clump appears to be extended and smoothly connected with other bright regions, not point-like, and we therefore attribute it to the host galaxy and not to SN 2015U.

Table 4.1 presents our photometry of SN 2015U before applying any dust reddening corrections, and Figure 4.2 shows the light curves after correcting for Milky Way (MW) dust absorption. The data are also available for download from the Berkeley SuperNova DataBase (SNDB; Silverman et al. 2012).[5]

[5] http://heracles.astro.berkeley.edu/sndb/

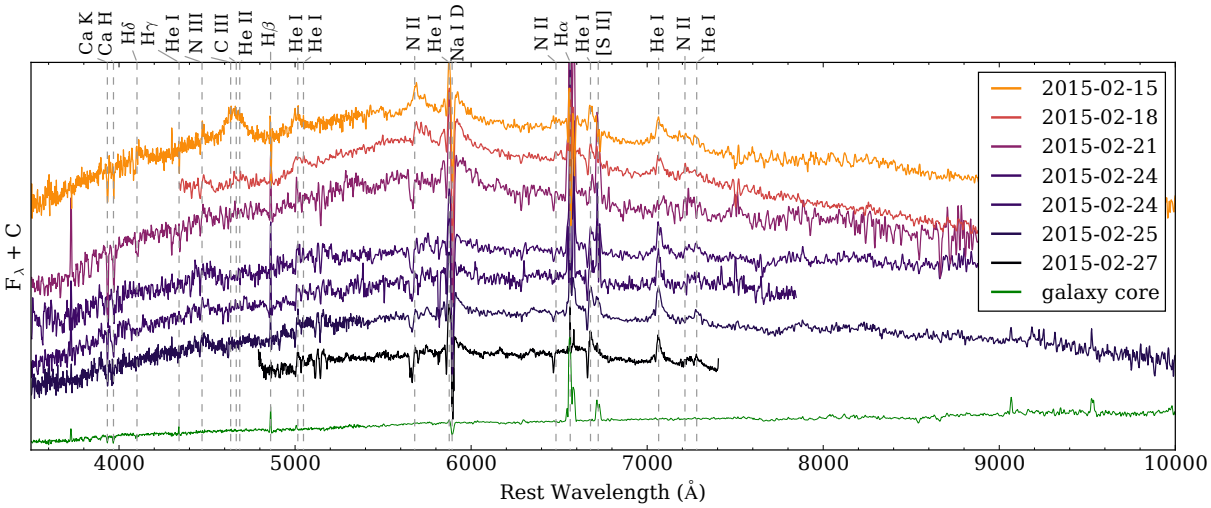

Figure 4.3: The spectral sequence of SN 2015U. This figure shows the spectral evolution after dereddening to correct for MW dust absorption but not for the host-galaxy absorption. On the bottom, we show an extraction of NGC 2388's nucleus, taken from a Kast spectrum obtained on Feb. 15. Contamination from the host galaxy's strong emission lines is apparent in some spectra; we indicate Hα, Hβ, and [S II] $\lambda\lambda$6716, 6731, as well as the host's Na ID absorption.

4.2.2 Spectroscopy

We began a spectral monitoring campaign of SN 2015U on 2015 Feb. 15, obtaining six spectra with the Kast double spectrograph (Miller & Stone 1993) on the Shane 3 m telescope at Lick Observatory and one spectrum with the DEIMOS spectrograph (Faber et al. 2003) on the Keck-II 10 m telescope. Details of our spectral observations are listed in Table 4.2, and all reductions and calibrations were performed with standard tools and methods, including IRAF routines and custom Python and IDL codes[6] (e.g., Matheson et al. 2000b; Pérez & Granger 2007; Silverman et al. 2012).

All spectra were taken at or near the parallactic angle (Filippenko 1982), and the amount of galaxy flux falling into the slit varied as a function of seeing and the slit orientation on the sky. For the spectra which included a large amount of host-galaxy flux (Feb. 18, 21, and 24), we extract a spectrum from a region of the galaxy that does not include any SN 2015U flux, perform a median-filter smoothing to obtain the galaxy continuum, and then subtract it from our spectra, after determining a best-fit galaxy scaling coefficient by comparing synthetic photometry to the multiband photometry observed the same night. We do not attempt to remove the narrow (unresolved) galaxy emission features, so our spectra show varying degrees of narrow-line contamination from the host (including Hα, Hβ, and [S II]).

We renormalise each spectrum to match our template-subtracted V or R-band pho-

[6] https://github.com/ishivvers/TheKastShiv

tometry (depending on the spectral wavelength coverage) after linearly interpolating the photometry to the time of spectral observation. Figure 4.3 shows our total-flux spectra of SN 2015U. All spectra are available to download from the Berkeley SNDB and the Weizmann Interactive Supernova Data REPository (WiseREP; Yaron & Gal-Yam 2012).[7]

Using narrow Hα host-galaxy emission in our DEIMOS spectrum, we measure a line-of-sight redshift at the SN's location: $z_{\rm SN} = 0.013161 \pm 0.000005$, a difference of $\sim 200\,{\rm km\,s^{-1}}$ from the published redshift of the host galaxy — consistent with the SN's position on the approaching arm of this spiral galaxy.

4.2.3 Spectropolarimetry

Three epochs of spectropolarimetry were obtained of SN 2015U near peak brightness utilising the dual-beam polarimetry mode of the Lick 3 m Kast spectrograph. The orientation of the slit on the sky was always set to a position angle of 180° (i.e., aligned north-south), and exposures of 900 s were obtained at each of four waveplate positions (0.°0, 45.°0, 22.°5, and 67.°5). On each night, several waveplate sequences were performed and coadded. Flatfield and arc-lamp spectra were obtained immediately after each sequence without moving the telescope.

For polarimetric calibrations, the low-polarization standard stars BD+32°3739 and BD+05°2618 were observed to verify the low instrumental polarization of the Kast spectrograph. We constrained the average fractional Stokes Q and U values to $< 0.1\%$. By observing the above unpolarized standard stars through a 100% polarizing filter we determined that the polarimetric response is so close to 100% that no correction was necessary. Finally, we obtained the instrumental polarization position-angle curve and used it to correct the data. We observed the high-polarization stars HD 19820, BD +59°389, and V1Cyg12 to obtain the zeropoint of the polarization position angle on the sky (θ) and to determine the accuracy of polarimetric measurements, which were generally consistent with previously published values within $\Delta P < 0.05\%$ and $\Delta\theta < 1°$. All spectropolarimetric reductions and calculations were performed using the methods described by Mauerhan et al. (2015, and references therein), and we define the polarimetric parameters in the same manner as those authors (Stokes parameters q and u, debiased polarization P, and sky position angle θ).

To probe the Galactic component of interstellar polarization (ISP) along the line of sight toward SN 2015U, we used the method of spectroscopic parallax to select three stars within 1° of separation from the source and measured their integrated V-band polarization (P) and position angle (θ). For HD 58221 we obtained $P = 0.28\%\pm0.01\%$, $\theta = 13.0° \pm 0.6°$; for HD 58726, $P = 0.50\%\pm0.01\%$, $\theta = 24.8° \pm 0.3°$; and for HD 59291, $P = 0.24\%\pm0.01\%$, $\theta = 16.3°\pm0.7°$ (uncertainties are statistical). We interpret the significantly higher value of P for HD 58726 (A0 V spectral type) as being caused by some intrinsic polarization for that star, so we used the average values of the other two stars (0.25%, 14.3°) to calculate the associated Serkowski-Whittet form (Serkowski et al. 1975; Whittet et al. 1992), assuming a total-to-

[7] http://wiserep.weizmann.ac.il/

Table 4.2: Journal of Spectroscopic Observations

UT Date	Type[α]	Tel./Instr.	Wavelength (Å)	Resolution (Å)	Exp. (s)	Observer[β]	Reducer[β]
2015-02-15.256	F	Shane/Kast	3440–10,870	2	1200	IS	IS
2015-02-18.211	F	Shane/Kast	4400–9880	2	2400	WZ	IS
2015-02-21.207	F	Shane/Kast	3500–10,500	2	1200	WZ	IS
2015-02-21.313	S	Shane/Kast	4500–10,000	16	$4 \times 4 \times 900^{\gamma}$	WZ	JM
2015-02-24.224	F	Shane/Kast	3500–10,500	2	1200	WZ	IS
2015-02-24.322	S	Shane/Kast	4500–10,000	16	$3 \times 4 \times 900^{c}$	WZ	JM
2015-02-24.414	F	Shane/Kast	3500–7875	1	1800	WZ	IS
2015-02-25.171	F	Shane/Kast	3500–10,500	2	1200	MG	MG
2015-02-25.301	S	Shane/Kast	4500–10,000	16	$5 \times 4 \times 900^{c}$	MG	JM
2015-02-27.34	F	Keck/DEIMOS	4850–7510	0.3	1200	PK	IS
2010-03-022.17[δ]	F	Shane/Kast	3450–10,790	3	2100	IK	JS

[α]F: total flux; S: spectropolarimetry.
[β] Observers and data reducers are indicated with their initials. IS: Isaac Shivvers; WZ: WeiKang Zheng; JM: Jon Mauerhan; MG: Melissa Graham; PK: Patrick Kelly; IK: Io Kleiser; JS: Jeffrey Silveman.
[γ]All spectropolarimetry was obtained by rotating multiple times through four wave-plate positions; see §4.2.3. [δ]A previously unpublished observation of SN 2010al; see Figure 4.13.

selective extinction ratio of $R_V = 3.1$ and that the polarization peaks at 5500 Å, values appropriate for the MW. The resulting curve was subtracted from the SN 2015U data to remove the small but nonnegligible Galactic component of ISP. The above observations (along with calibration observations of the low-polarization standard star HD 14069 and the high-polarization standards HD 245310 and HD 25443) were taken with the Kast spectrograph on 2015 Sep. 21.

4.3 Analysis

4.3.1 Dust Corrections

All observations of SN 2015U are heavily affected by an obscuring screen of dust present in the host galaxy, NGC 2388. Because the treatment of dust corrections affects much of the following discussion, we start by describing our efforts to understand, characterise, and correct for the effects of the host-galaxy dust. First, however, we correct for MW dust along the line of sight using the dust maps of Schlafly & Finkbeiner ($E(B-V) = 0.0498$ mag; 2011) and assuming $R_V = 3.1$ (Cardelli et al. 1989).

Ochner et al. (2015) note that a significant amount of host-galaxy reddening is apparent in their classification spectrum, with an estimated $E(B-V) = 1.0$ mag based upon the Na ID feature. Our higher-resolution DEIMOS spectrum from Feb. 27 reveals complex Na ID absorption near the host redshift (we examine the structure of this feature in §4.3.2).

We measure the equivalent width (EW) of the entire absorption complex to be 9.1 ± 0.15 Å — well outside the empirical relations of Poznanski et al. (2012) and similar previous efforts, which show that the Na ID lines saturate and lose their predictive power above a total EW of ~ 2 Å and $E(B-V) \approx 1.0$ mag. This indicates that the reddening toward SN 2015U likely exhibits $E(B-V) > 1.0$ mag, if the dust in NGC 2388 is similar to that in our MW.

Pastorello et al. (2015c) measure an Na ID EW of 6.5 ± 0.5 Å from their spectra; we tentatively suggest that the discrepancy between their value and ours is caused by different choices made when defining the local continuum. Figure 4.6 shows that the Na ID components fall on the red wing of the He I emission line, even at early times. However, if one instead defines the local continuum based upon the overall flux-density level (a reasonable choice if the emission-line wings were not detected), one obtains Na ID EW values similar to those of Pastorello et al. (2015c).

We next examined the 5780.5 Å diffuse interstellar band (DIB). This feature is one of the strongest DIBs; it has long been known to correlate with extinction in the MW when the Na ID feature is saturated (e.g., Herbig 1995; Friedman et al. 2011; Lan et al. 2015; Baron et al. 2015), and Phillips et al. (2013) show a clear correlation between this feature and the reddening toward SNe Ia produced by host-galaxy dust. We do not detect this feature, and our spectra have insufficient S/N to place strong constraints on the dust using our nondetection. We also examined modeled estimates for the amount of dust obscuring the bulk of stars in the host galaxy NGC 2388 (Pereira-Santaella et al. 2015), and we determined the same value at the location of the SN (within $\sim 1''$ on the sky) by measuring the Balmer ratio implied by the Hα and Hβ galaxy lines present in our DEIMOS spectrum (e.g., Brocklehurst 1971). We estimate $E(B-V) \approx 0.56$ and 1.1 mag, respectively, toward the average star in NGC 2388's core and the average star near the explosion site of SN 2015U. Although this does not provide a measure of the line-of-sight reddening toward SN 2015U specifically, it does provide valuable context about the dust content of NGC 2388.

Additional information is available to us through the spectropolarimetry: as we describe in §4.3.2, the peak of the polarization spectrum ($\lambda_{\rm max}$) of NGC 2388's ISM is blueward of 4600 Å. The shapes of the polarization law and the dust-extinction law are related within the MW (e.g., Serkowski et al. 1975; Clayton & Mathis 1988). Using $R_V = (-0.29 \pm 0.74) + (6.67 \pm 1.17)\,\lambda_{\rm max}$ from Clayton & Mathis (1988, with $\lambda_{\rm max}$ in μm), our measurement of $\lambda_{\rm max} < 0.46\,\mu$m implies $R_V < 2.8 \pm 0.9$. However, note that Patat et al. (2015) show the polarization properties of the host-galaxy dust obscuring several well-studied and reddened SNe Ia to be remarkably different from those of the dust in our MW.

Finally, we model SN 2015U as a blackbody emitter obscured behind a simple screen of dust in the host galaxy and fit for the parameters of that dust via comparisons with our multiband photometry at three epochs (pre-maximum, maximum, and post-maximum brightness). Our spectra show that the emission from SN 2015U is roughly that of a blackbody obscured by dust, at least at optical wavelengths (unlike most SNe, which display spectra consisting of prominent and overlapping features with sometimes strong line blanketing), and in §4.3.5 we discuss why one would expect roughly blackbody emission from

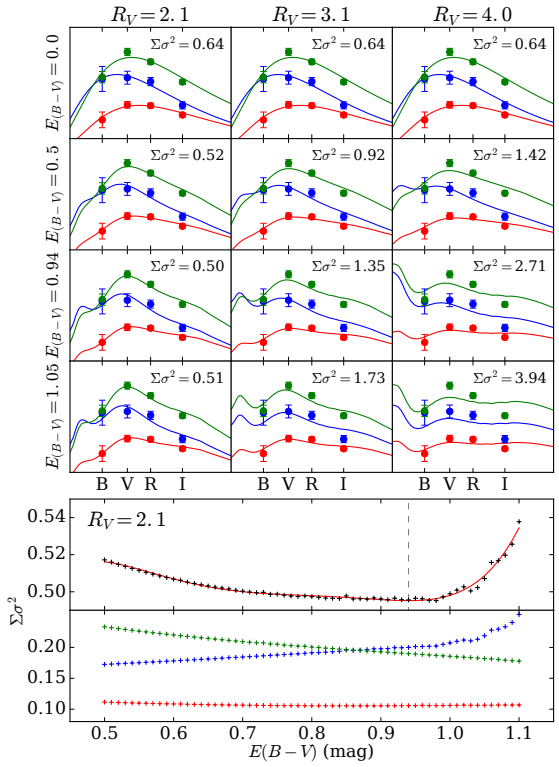

Figure 4.4: In the top panel, we fit reddened blackbodies to our photometry of SN 2015U at three epochs (blue, Feb. 14.35; green, Feb. 18.21; red, Feb. 27.21) after correcting for MW absorption and assuming various values for R_V and $E(B-V)$ within NGC 2388. For many data points, the measurement errors are smaller than the plotted symbol. The weighted sum of squared differences ($\Sigma\sigma^2$) between observed photometric points and synthetic photometry of a blackbody is shown in the upper right of each plot; lower values indicate a better agreement across all epochs. In the bottom panel, we show $\Sigma\sigma^2$ as a function of $E(B-V)$ for $R_V = 2.1$ in black as well as $\Sigma\sigma^2$ broken down by individual epochs, coloured as above. $R_V = 2.1$ and $E(B-V) = 0.94^{+0.1}_{-0.4}$ mag (marked with a dashed line in the bottom panel) are the preferred values. In many panels a blue feature is introduced into the reddened blackbody spectrum by the wavelength dependency of the MW's reddening law, but our spectral data provide no clear evidence for or against such a feature in the spectra of SN 2015U.

SN 2015U. We use PySynphot[8] and assume the dust is described by the empirical extinction law of Cardelli et al. (1989) — by varying the parameters R_V and $E(B-V)$ we are able to explore a wide variety of dust populations and search for the parameters that produce the best blackbody fits to our photometric data.

Figure 4.4 shows a comparison between synthetic photometry from PySynphot and the photometry assuming four different values for $E(B-V)$ ranging from 0.0 mag to 1.0 mag and three different reddening laws parameterised by R_V from 2.1 to 4.0 (note that PySynphot only includes a few built-in options for R_V; we explore the most relevant of them here). For every combination of R_V and $E(B-V)$, we perform a weighted least-squares fit to determine the best-fit temperature and luminosity of the source blackbody and we list the weighted sum of squared differences ($\Sigma\sigma^2$) for each. Figure 4.4 shows that a nonzero amount of host-galaxy reddening correction makes the fits worse for $R_V = 3.1$ and 4.0 — in those cases the photometric data prefer a blackbody with no dust. However, the spectra clearly

[8] http://ssb.stsci.edu/pysynphot/docs/

show a nonthermal rolloff at blue wavelengths (see Figure 4.3), and so there must be a significant amount of dust absorption within NGC 2388. If we instead adopt $R_V = 2.1$, a grid search over $E(B-V)$ values indicates a best fit at $E(B-V) \approx 0.94$ mag. As Figure 4.5 shows, dereddening the spectra for this reddening law appears to correct the blue rolloff. Figure 4.4 shows that $\Sigma\sigma^2$ increases above $E(B-V) = 1.0$ and below $E(B-V) = 0.6$ mag, but between those values $\Sigma\sigma^2$ is only weakly dependent upon $E(B-V)$. We therefore use Figure 4.4 to estimate our error bars: $E(B-V) = 0.94^{+0.1}_{-0.4}$ mag. A similar approach was taken by Pastorello et al. (2015c), who compared the colour curves of SN 2015U to the intrinsic colour curves of other SNe Ibn to obtain $E(B-V)_{\rm tot} = 0.81 \pm 0.21$ mag (assuming $R_V = 3.1$). However, as they note, the SN Ibn subclass is remarkably heterogeneous, and it is not clear whether the physics governing those colour curves is the same for all members.

Given the above discussion, we adopt $R_V = 2.1$ and $E(B-V) = 0.94^{+0.1}_{-0.4}$ mag. The large EWs measured from the Na ID and the odd absorption-feature complex indicate that a simple analysis of those features cannot be trusted. Studies of the integrated galaxy flux and the Balmer decrement measured from our spectrum show that the bulk of NGC 2388's stellar mass is strongly obscured, and our spectropolarimetric data indicate that SN 2015U itself exploded behind a significant dust screen. The low $\lambda_{\rm max}$ value in the polarization spectrum and our blackbody fits to the light curves together prefer a relatively wavelength-dependent dust extinction law for NGC 2388 (i.e., $R_V < 3.1$) and $E(B-V) = 0.94^{+0.1}_{-0.4}$ mag — we find this line of reasoning most convincing. The above result is consistent with the $E(B-V) = 0.99 \pm 0.48$ mag adopted by Pastorello et al. (2015c), though they assume $R_V = 3.1$. Our determination of the dust properties toward SN 2015U remains uncertain, so we consider a range of plausible reddening corrections throughout the rest of this paper. We find that the extinction toward §4.3.2 does not appear to change over the course of our observations, and we discuss and reject the possibility that a significant fraction of the extinction toward SN 2015U arises from the SN's CSM rather than the host galaxy's ISM.

4.3.2 Spectra

The optical spectra of SN 2015U show a strong continuum overlain with narrow and intermediate-width emission features. Though our data cover only 12 days of SN 2015U's evolution, they range from a pre-maximum spectrum to one taken after the SN had faded from peak by ~ 1 mag (see Figure 4.2). No broad ejecta features became apparent in our spectra throughout that timespan — markedly different behaviour from that of the well-observed, rapidly fading SNe 2002bj, 2005ek, and 2010X (Poznanski et al. 2010; Drout et al. 2013; Kasliwal et al. 2010) and similar to that of the interacting SN 2010jl (e.g., Fransson et al. 2014). Though broad features do not emerge, the continuum temperature shows significant evolution, the narrow emission and absorption features evolve, and the relative ionisation states of the detected elements change. While there are no strong H lines, multiple ionisation levels of helium, nitrogen, iron, and perhaps oxygen and carbon are detected, some in both emission and absorption and some in absorption only. Pastorello et al. (2015c) also present a series of spectral observations of SN 2015U. Their data are in good agreement with

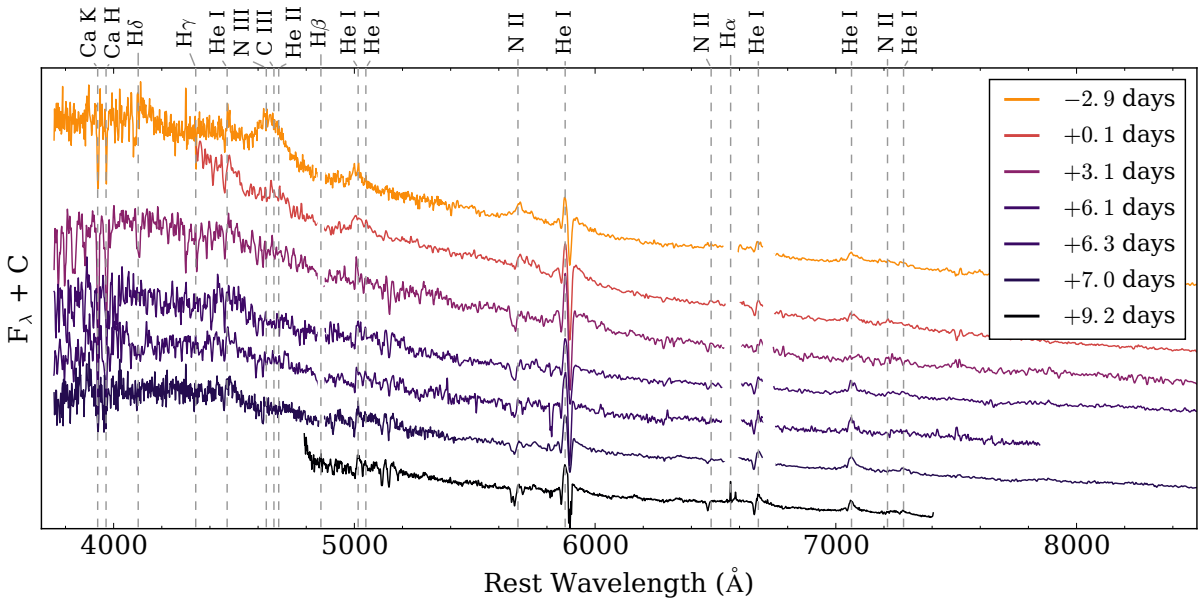

Figure 4.5: The spectral sequence of SN 2015U after dereddening to correct for MW dust absorption and the (uncertain) host absorption. Phases are listed relative to the V-band peak brightness. We have masked regions of our low-resolution spectra where the host's narrow emission lines dominate, but we do not mask the Na ID absorption features from the MW and the host.

ours and extend to later epochs, while our (higher-resolution) spectra illustrate new details not apparent previously.

Evolving Line Profiles

The most obvious features in our spectra are emission lines of He I. These lines are centred at the rest wavelength, exhibit a relatively broad base with a full width near zero intensity (FWZI) of $\sim$ 9000–10,000 km s^{-1}, and are overlain with P-Cygni absorption features blueshifted by $\sim$ 745 km s^{-1} and with widths of 400–500 km s^{-1}. The wavelengths and widths of these features do not significantly change during the $\sim$ 12 days covered by our spectra. We find that the He I line profiles can be parameterised by a "modified Lorentzian" emission component (where the exponent is allowed to vary) with a suppressed blue wing and an overlain Gaussian absorption component, indicative of recombination lines broadened via electron scattering within the CSM. SN 2015U's line profiles are very similar to those observed in many SNe IIn but with a faster inferred CSM velocity (see, e.g., the spectra of SN 1998S; Leonard et al. 2000; Anupama et al. 2001; Fassia et al. 2001; Chugai 2001; Shivvers et al. 2015). Figure 4.6 shows our best fit to the He I λ5876 line using this parameterisation. We also show the unsuppressed Lorentzian feature to emphasise the asymmetry, which arises from the effects of Compton scattering within a wind-like CSM (e.g., Auer & van Blerkom

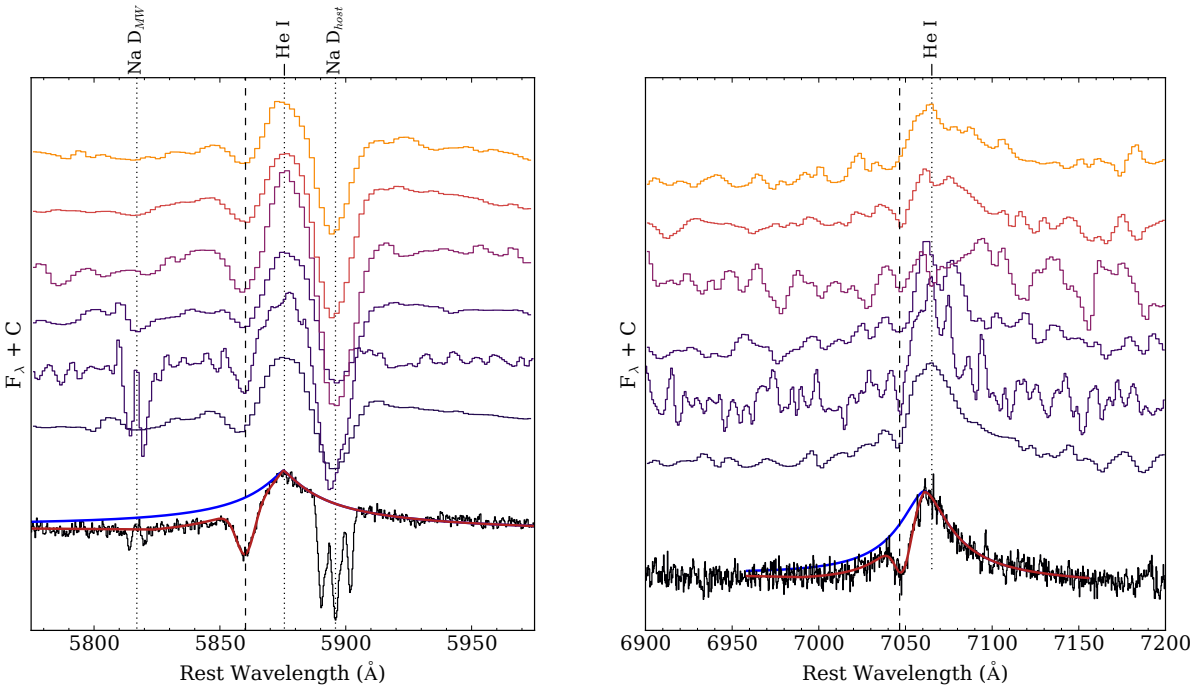

Figure 4.6: The evolution of the He I λ5876 (left) and λ7065 (right) lines. The spectra increase in time downward on the plot as in Figure 4.3. The rest wavelength of each line is shown with a dotted line and the absorption component is marked at a blueshift of $v = 789\,\mathrm{km\,s^{-1}}$ (the mean blueshift of He I lines measured from our DEIMOS spectrum). In the left panel we also mark the host and MW Na ID absorption features (see §4.3.2 for a discussion of the host galaxy's remarkable Na ID absorption complex).

1972; Hillier 1991; Chugai 2001). The magnitude of the effect scales with the expansion velocity, explaining the strongly asymmetric emission lines of SN 2015U compared to those observed in most SNe IIn.

After He I (and host-galaxy Hα and [N II]), the most clearly detected features in our spectra are the N II lines. As Pastorello et al. (2015c) note, SN 2015U appears to be the first SN Ibn to show these features, though they are commonly found in the spectra of hot stars. In our DEIMOS spectrum we are able to identify nine N II absorption lines (see §4.3.2), and for the strongest of these we track their evolution throughout our spectral series. In our -2.9 and $+0.1$ d spectra, the 5667 Å and 5676 Å features are apparent in emission around $v \approx 0\,\mathrm{km\,s^{-1}}$, but they transition into absorption at $v \approx 680\,\mathrm{km\,s^{-1}}$ after maximum light — see Figure 4.7. The same trend is apparent in the N II features at 6482 Å and 7215 Å (Figure 4.3).

We find a strong emission feature centred around 4650 Å in our earliest spectrum. In Figure 4.3 we label it as a blend of N III, C III, and He II, a blend that has been observed and modeled in the spectra of a few other young, interacting SNe (e.g., Gal-Yam et al. 2014;

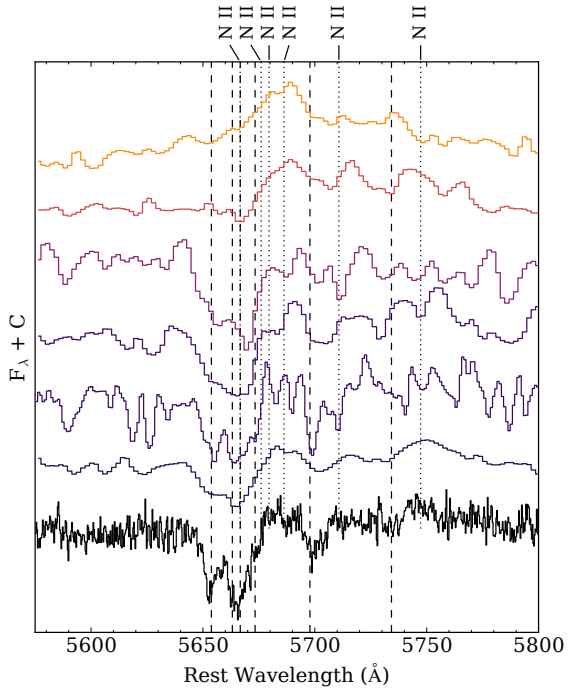

Figure 4.7: The evolution of the N II lines. The spectra increase in time downward as in Figure 4.3. Identified N II lines are marked at rest using dotted lines and with a blueshift of $v = 680\,\mathrm{km\,s^{-1}}$ using dashed lines (the mean blueshift of N II lines measured from our DEIMOS spectrum). The emission features marginally detected at $v = 0\,\mathrm{km\,s^{-1}}$ in our earliest spectra evolve into blueshifted absorption lines post-maximum brightness.

Shivvers et al. 2015; Pastorello et al. 2015a). The 4650 Å emission feature fades rapidly. Given the clear detection of N II at all epochs we believe the identification of N III to be very robust, but whether the blue wing of that emission feature is caused by C III or He II is more difficult to determine. The He II λ5411 line is extremely weak in SN 2015U, which argues that C III must be contributing to the 4650 Å feature, but discerning between these ions likely requires detailed modeling and is beyond the scope of this paper.

A Trace of Hydrogen?

Inspection of our two-dimensional (2D) spectral images reveals host-galaxy emission features at Hα, Hβ, and Hγ, and there is no indication of either absorption or emission features intrinsic to SN 2015U for any of those lines. However, our spectra at -2.1 d and $+3.1$ d do show an absorption feature near the expected wavelength of Hδ, decelerating over those 5 days from $-1060 \pm 75\,\mathrm{km\,s^{-1}}$ (blueshifted) to $160 \pm 65\,\mathrm{km\,s^{-1}}$ (redshifted relative to the rest frame of SN 2015U, consistent with the rest frame of NGC 2388) and then disappearing by $+6.1$ d. Though this feature is difficult to disentangle from the significant noise at these wavelengths, it appears to show weak P-Cygni emission in our first observation.

NGC 2388 shows some Hδ absorption, and the feature from $+3.1$ d is probably associated with the galaxy (this spectrum has undergone host-galaxy subtraction as described in §4.2.2). However, in our -2.1 d spectrum SN 2015U was well-separated from the host and we performed no galaxy subtraction. Along with the $\sim$1000 $\mathrm{km\,s^{-1}}$ Doppler shift and faint P-Cygni feature, this indicates that the weak Hδ feature in the earliest spectrum of

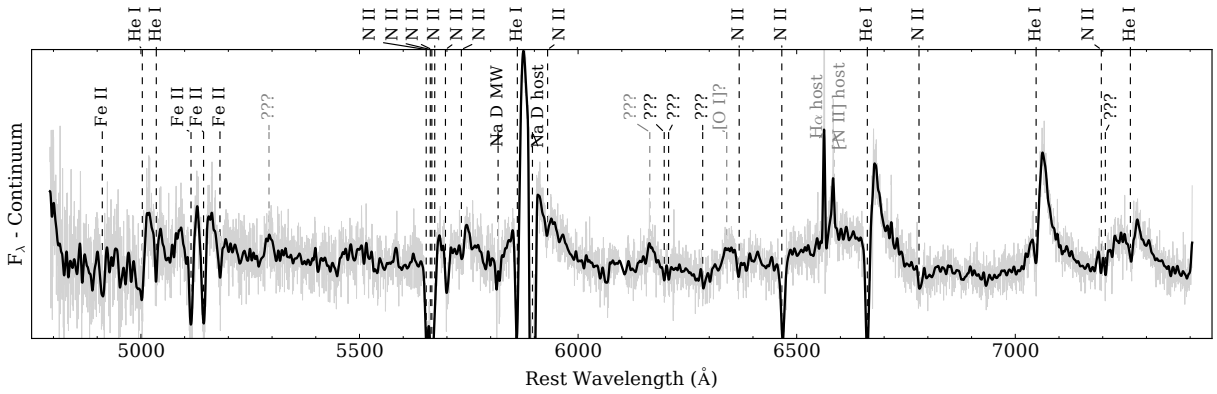

Figure 4.8: The DEIMOS spectrum from Feb. 27 in detail. A simple polynomial continuum fit has been removed. The full spectrum is shown in grey in the background while the black line displays the spectrum smoothed with a 10 Å Gaussian kernel. Identified emission lines are shown with grey dashed lines and text; absorption lines are in black. All absorptions are indicated with a $745\,\mathrm{km\,s^{-1}}$ blueshift but emission lines are marked at rest velocity.

SN 2015U arose within the same CSM as the He I and other features described above.

Several SNe have been found to exist between the IIn and Ibn subclasses, exhibiting weak hydrogen features (e.g., SNe 2005la, 2010al, and 2011hw; Pastorello et al. 2008b, 2015a). Remarkably, SN 2010al had an Hδ feature of comparable strength to its Hα emission while showing only faint traces of Hβ and Hγ emission — perhaps similar physics governs the hydrogen emission lines in SN 2015U. Regardless of this putative Hδ feature, the amount of hydrogen in the CSM surrounding SN 2015U must be vanishingly small.

Higher Resolution

Our DEIMOS spectrum from Feb. 27 ($R \approx 5000$) reveals fully resolved absorption and emission lines from a host of ions in the spectra of SN 2015U; see Figure 4.8 and Table 4.3. We include measured positions and widths for several lines for which we have no good identification; it is especially difficult to differentiate between Fe III ($E_i = 30.651\,\mathrm{eV}$) and Fe II ($E_i = 16.20\,\mathrm{eV}$).[9] In our spectrum we find at least four Fe absorption lines between 4900 and 5200 Å (in the SN rest frame). The strongest two were identified as Fe III by Pastorello et al. (2015c), but several known Fe II lines occur at very similar wavelengths, and we also identify weak features at 4912.5 and 5180.3 Å which are most plausibly interpreted as Fe II λ4924 and Fe II λ5195. However, these identifications are tentative at best, given the nondetection of other expected Fe II lines and the odd relative strengths of these features, and so we caution the reader against overinterpreting the Doppler velocities presented in Table 4.3.

[9] All ionisation energies and line wavelengths were found through the NIST Atomic Spectra Database (ASD): http://www.nist.gov/pml/data/asd.cfm.

Table 4.3: Absorption Lines in the DEIMOS Spectrum

Ion	Rest λ (Å)	Observed λ (Å)	Offset ($\mathrm{km\,s^{-1}}$)	FWHM ($\mathrm{km\,s^{-1}}$)
He I	5015.7	5002.6	778.8	586.4
He I	5047.7	5034.6	783.2	267.8
He I	5875.6	5860.2	789.2	488.7
He I	6678.2	6661.7	737.2	470.1
He I	7065.2	7047.9	733.7	432.9
He I	7281.3	7265.4	655.9	404.0
N II	5666.6	5653.0	721.4	232.5
N II	5676.0	5665.4	559.2	433.1
N II	5710.8	5699.9	570.4	407.2
N II	5747.3	5734.8	651.6	367.5
N II	6482.1	6468.1	643.4	428.1
N II	5941.6	5927.5	711.5	600.7
N II	6796.6	6781.8	654.2	337.9
N II	7214.7	7195.9	783.5	173.7
N II	6384.3	6366.7	829.6	253.7
Fe II$^{\alpha}$	4923.9	4912.5	698.0	677.2
Fe II$^{\alpha}$	5126.2	5114.9	658.1	514.5
Fe II$^{\alpha}$	5157.3	5143.2	819.4	584.9
Fe II$^{\alpha}$	5195.5	5180.3	873.2	545.7
?	—	6197.2	—	166.9
?	—	6207.3	—	152.7
?	—	6285.9	—	153.8
?	—	7206.5	—	190.5

Identifications and properties of the absorption lines identified in our DEIMOS spectrum (after correcting for $z = 0.013161$). All lines were fit by a Gaussian with a linear approximation to the nearby continuum, and rest wavelengths were downloaded from the NIST ASD. Characteristic error bars are ~ 0.6 Å ($30\,\mathrm{km\,s^{-1}}$) for the observed wavelengths and ~ 1.6 Å for the Gaussian FWHM ($85\,\mathrm{km\,s^{-1}}$), as estimated by calculating the 95% confidence intervals for the N II λ5711 line using MCMC techniques.
$^{\alpha}$It is difficult to determine exactly which Fe II or Fe III transition is responsible for these lines, and so the listed Doppler offsets are only tentative.

We also find three unidentified emission features in our DEIMOS spectrum that are not from host-galaxy contamination, falling near 5290, 6165, and 6340 Å and exhibiting widths similar to those of the He I lines. None of these is clearly detected in our other spectra or the spectra published by Pastorello et al. (2015c, though generally they exhibit a S/N too low to rule them out). The feature at 6340 Å is suggestive of the [O I] $\lambda\lambda$6300, 6364 doublet that

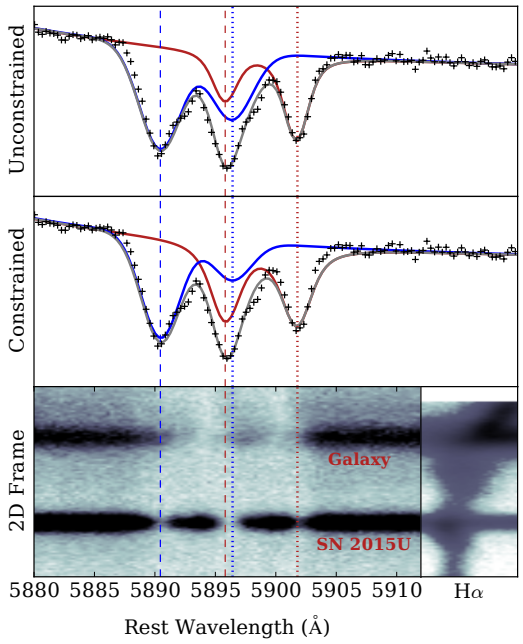

Figure 4.9: The Na D features in our DEIMOS spectrum of SN 2015U and NGC 2388. The top panel plots the observed spectrum of SN 2015U with our best-fit absorption profiles while the middle panel shows the result after introducing the additional constraint that $D_2/D_1 \geq 1.0$ (see §4.3.2). The shorter-wavelength doublet is shown in blue and the longer-wavelength one in red, with the central wavelengths indicated by dashed and dotted vertical lines for D_2 and D_1, respectively. Their sum is given in grey. The bottom panel shows the 2D frame of our DEIMOS observation in this region, including both the light from the host and the SN, as well as a cutout of the Hα emission line (plotted with the same Doppler δv per pixel) to indicate the shape of the galaxy's rotation curve.

regularly arises in nebular spectra of stripped-envelope SNe (Types Ib/c; e.g., Filippenko 1997; Matheson 2001), but this identification is only tentative.

The Na D Lines

Our DEIMOS spectrum of SN 2015U reveals a remarkable set of Na D absorption lines — see Figure 4.9. In addition to the MW doublet we find several overlapping lines from NGC 2388 along our sight line, though as we show below, there is no evidence that any of these lines originate within the CSM immediately surrounding SN 2015U. The astronomical Na D doublet has been studied in great detail (it was one of the original Fraunhofer lines) and the relative strength of the doublet has long been used to measure the interstellar abundance of neutral sodium: the Na D_2 line is generally observed to be stronger than the D_1 line by a factor ranging from 1.0 to 2.0, for high and low column densities of Na I, respectively (e.g., Strömgren 1948; Nachman & Hobbs 1973; Somerville 1988). The MW Na D doublet in our spectra exhibits the expected behaviour, with an EW ratio of $D_2/D_1 \approx 1.2$, but the host-galaxy lines do not.

There are at least two distinct and overlapping Na D absorption doublets near the host-galaxy's rest frame in the spectrum of SN 2015U. Figure 4.9 shows them (as well as model fits) in detail. We model the absorption complex by overlaying the modified Lorentzian emission-line profile (see §4.3.2) with two doublets of Voigt absorption profiles (though we note that some of these lines may be unresolved and saturated). D_1 and D_2 lines from a single doublet are forced to have the same velocity properties and to be separated by 5.97 Å,

but they are allowed independent strengths.

In the top panel of Figure 4.9 we show the result when we allow the relative strengths of the doublet (i.e., D_2/D_1) to vary freely. In the rest frame of the SN, the bluest doublet falls at $\lambda\lambda 5890.45$, 5896.35 ± 0.066 Å. This is a blueshift of only $\sim 25\,\mathrm{km\,s^{-1}}$ from the SN rest frame, and so this doublet is likely to arise from the ISM of NGC 2388 along our sight line to SN 2015U. The second (redder) doublet, however, falls at $\lambda\lambda 5895.80$, 5901.69 ± 0.063 Å — redshifted from the SN by almost $300\,\mathrm{km\,s^{-1}}$, and even redshifted from the galaxy core by more than $100\,\mathrm{km\,s^{-1}}$. This is within the velocity range of NGC 2388's rotation curve, but SN 2015U is located well away from the receding spiral arm and the bulk of the galaxy's receding material (see Figure 4.1). In addition, the second Na D doublet shows a strength ratio of $D_2/D_1 \approx 0.5$, well outside the commonly observed values of ~ 1.0–2.0 (in contrast, the blue doublet exhibits a reasonable $D_2/D_1 \approx 1.5$).

If, instead, we constrain the doublet ratio to $D_2/D_1 \geq 1.0$, we can also obtain a reasonable fit, though this introduces noticeable discrepancies in the reddest part of the feature — see the middle panel of Figure 4.9. In addition, this forces the doublet ratio of the bluer doublet outside of the range of normal values: $D_2/D_1 \approx 2.5$. Adding more components to our model fit will not solve this quandary (though the data do show a shoulder on the bluer doublet, suggesting a third absorption component). The implications for the Na I gas (and the dust) in NGC 2388 are not clear.

Given the spectral signatures of dense CSM surrounding SN 2015U, it is natural to wonder whether some of the Na D absorption arises within the local CSM. Variation in the Na D features over the timescale of the SN evolution would be a clear signature of local absorption (e.g., Patat et al. 2007); however, as Figure 4.6 shows, no such variation is apparent in our data.

The bottom panel of Figure 4.9 displays a cutout of the 2D DEIMOS spectrum around the Na D feature. Both SN 2015U and NGC 2388 are clearly visible, and we also show the rotation curve of the galaxy via a cutout of the Hα emission line. The Na D absorption of NGC 2388's own ISM is seen against the stellar light of the galaxy, and this galactic self-absorption roughly covers the velocity range of the two components observed along the line of sight toward SN 2015U. It appears that the anomalous red component described above obscures the host galaxy as well as the SN, providing further evidence that this component is unlikely to arise within the CSM of SN 2015U.

Spectropolarimetry

We did not observe significant evolution in the polarization of SN 2015U between our three epochs, so we coadded all of the data to increase the S/N; the results are illustrated in Figure 4.10. The polarization spectrum of SN 2015U appears to be dominated by ISP associated with the host galaxy NGC 2388, showing a strong increase in continuum polarization toward shorter wavelengths with a value of $P \approx 2.5\%$ at 4600 Å and decreasing to $P \approx 1.0\%$ near 7000 Å. This behaviour is dissimilar to what is typically observed for the MW ISP, which exhibits a peak and turnover near 5500 Å. Instead, the observed behaviour is

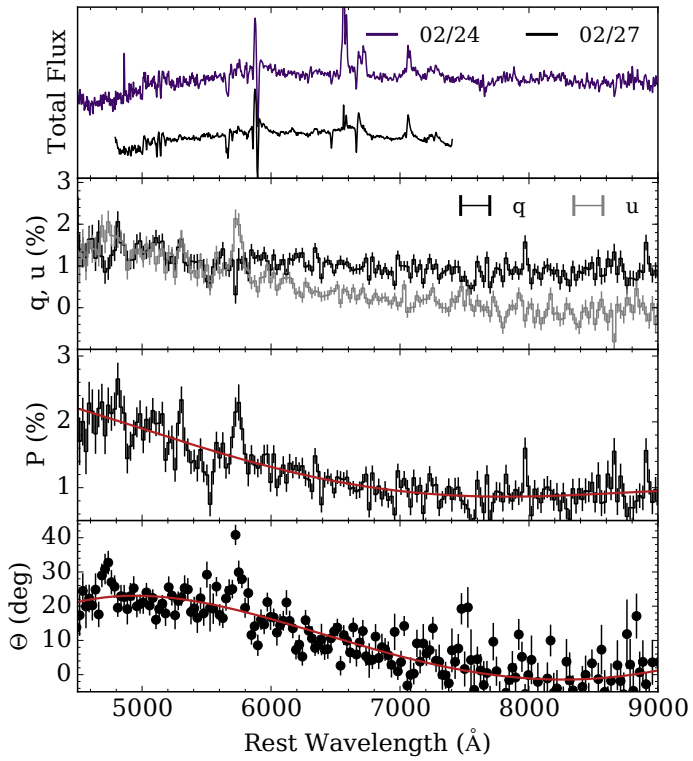

Figure 4.10: Our spectropolarimetric observations of SN 2015U. From top to bottom: total-flux spectra near V-band peak and in higher resolution (for visual comparison), q and u Stokes parameters, P with a fourth-order polynomial fit showing the overall trend, and θ with a similar polynomial fit (after discarding outliers). The spectropolarimetric data from three nights of observations have been coadded and binned to 25 Å.

reminiscent of the ISP produced by the host galaxies of several SNe Ia, including SNe 1986G, 2006X, 2008fp, and 2014J (Patat et al. 2015, see their Figure 2). The continuous rise in P beyond the B and U photometric passbands has previously been interpreted as evidence for scattering by dust grains smaller than those characteristic of the MW disk ISM.

Interestingly, we observe a significant wavelength dependence for the position angle (θ), which has a value of $\sim 25°$ at 4600 Å and monotonically trends toward $\sim 10°$ near 7000 Å. In the MW, the ISP's position angle is generally flat. However, a wavelength dependence in θ has been observed along particular lines of sight toward star-forming regions at distances greater than 0.6 kpc (e.g., Gehrels & Silvester 1965; Coyne & Gehrels 1966), and has been explained as the result of photons traversing multiple clouds or scattering media that exhibit various sizes for the scattering particles as well as various orientations for the interstellar magnetic field.

A similar interpretation is plausible here: along the line of sight within NGC 2388 toward SN 2015U there are likely to be multiple separate components of dusty scattering media having different grain sizes and/or different magnetic field orientations. This possibility is particularly interesting considering the complex superposition of multiple Na I D absorption doublets that we see in our high-resolution DEIMOS spectrum. If the continuum flux spectrum of SN 2015U is devoid of broad SN features because of high optical-depth CSM, then

one might suspect there also to be a separate and distinct scattering component associated with this CSM, if it is dusty. The subsequent re-scattering of this light as it traverses the dusty ISM of the host could provide a means for producing the observed wavelength dependence of θ, if there is a difference in grain sizes between these multiple scattering media. Although this scenario is physically plausible, the spectropolarimetric data cannot discriminate between a CSM+ISM scattering combination and multiple components of host ISM, and our analysis of the total-flux Na I D features indicates that they are likely associated with ISM (see §4.3.2).

Finally, there is a line-like feature near 5820 Å which might naively be interpreted as a signature of intrinsic polarization associated with SN 2015U and with the He I / Na I transition. However, the MW Na I D doublet falls at the same wavelength. Although relatively weak compared to the redshifted host-galaxy Na D absorption, the results of our spectral arithmetic in the vicinity of this poorly resolved doublet profile might have created a spurious artifact in the final coadded dataset mimicking the shape of a polarized line feature. Indeed, in each individual epoch, the polarized spectra near this feature appear to suffer from systematic noise, so we are reluctant to attribute this feature to the SN itself.

4.3.3 Photometry

The optical light curves of SN 2015U show that it was a remarkably luminous and rapidly evolving event — Figure 4.11 shows our photometry corrected for host-galaxy dust reddening. With a peak absolute magnitude of $\lesssim -19$ mag at optical wavelengths, a rise time of $\lesssim 10$ d, a time above half-maximum of $t_{1/2} \approx 12$ d, and a decline rate of nearly 0.2 mag day^{-1} after peak, SN 2015U was more than a magnitude brighter than most stripped-envelope SNe and evolved much more rapidly (e.g., Drout et al. 2011; Bianco et al. 2014).

Though the first unfiltered (*clear*) KAIT detection of SN 2015U was on Feb. 11, and it went undetected by KAIT on Feb. 10 (> 18.4 mag), Pastorello et al. (2015c) present detections from Feb. 9 and 10 at $R = 18.62 \pm 0.26$ and 18.14 ± 0.30 mag, respectively. Unfortunately, the location does not appear to have been observed in the days prior and there are not deep upper limits constraining the explosion date further. SN 2015U rose quite rapidly, so we adopt a tentative explosion date one day before the first detection published by Pastorello et al. (2015c): $t_{\rm exp} \approx 57062$ MJD (Feb. 8). This provides us with a rise time for SN 2015U of $t_{\rm rise} \approx 9$ days. Tsvetkov et al. (2015) note that SN 2015U is among the most rapidly evolving SNe known, with a decline rate similar to those of SNe 2002bj, 2005ek, and 2010X. We measure $\Delta M_{15} \approx 2.0$ mag in the R band, but note that the decline rate increases ever more steeply after ~ 10 days post-peak, and at all times the bluer passbands decline more rapidly than the red. Simple linear fits indicate the following decline rates before and after +10 d (in mag day^{-1}): $B_{\rm early} = 0.110 \pm 0.007$, $V_{\rm early} = 0.099 \pm 0.005$, $V_{\rm late} = 0.28 \pm 0.07$, $R_{\rm early} = 0.080 \pm 0.005$, $R_{\rm late} = 0.267 \pm 0.009$, $I_{\rm early} = 0.067 \pm 0.006$, and $I_{\rm late} = 0.26 \pm 0.04$ (uncertainties are statistical, and our data do not constrain the late B-band decline).

SN 2015U is one of the nearest SNe Ibn to date (Pastorello et al. 2016), but it is still relatively distant for direct progenitor studies (and is obscured by the dust in NGC 2388).

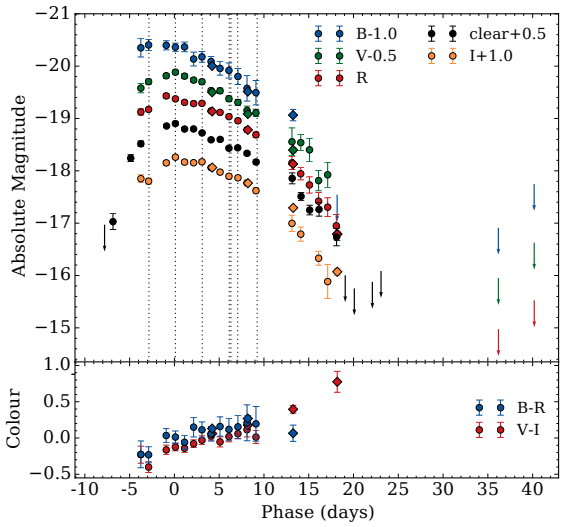

Figure 4.11: The KAIT and Nickel light curves (top) and colour curves (bottom) of SN 2015U, after correcting for MW dust absorption and host absorption. Nickel data are shown with diamonds and KAIT data with circles, and the dates of our spectral observations are indicated in the top panel with dashed vertical lines. Host-galaxy contamination becomes significant in our KAIT photometry around +10 d, and so we only show the Nickel data beyond that date in the lower panel (we include all data in the upper panel). We apply vertical offsets to every passband except R in the top panel, to enable comparisons.

Regardless, the *HST* nondetections presented in §4.2.1 can be used to place interesting constraints on the SN's progenitor. We compared these limits to the MIST stellar evolutionary tracks (Choi et al. 2016) at solar metallicity generated in the WFC3/infrared bandpasses (negligible photometric differences exist between NICMOS/NIC2 and WFC3/IR for *F110W* and *F160W*). Based on these tracks we can eliminate single-star progenitors with initial masses $M_{\rm ini} \gtrsim 9\,{\rm M}_\odot$ and $\lesssim 40\,{\rm M}_\odot$. That is, the progenitor would have been either a low-mass star near the core-collapse limit or a highly massive evolved star, possibly in a luminous blue variable (LBV) or Wolf-Rayet phase at the time of explosion. We did not interpret our upper limits with respect to existing binary evolution models, and we caution that these results are somewhat dependent upon the uncertain properties of NGC 2388's dust population.

The structure near SN 2015U's position in the 1 yr *HST* images (Figure 4.1) may be due to clumpy star-forming regions, perhaps associated with SN 2015U. NGC 2388 is a strongly star-forming and massive galaxy — Pereira-Santaella et al. (2015) calculate an ongoing star-formation rate of $\sim 40^{+9}_{-22}\,{\rm M}_\odot\,{\rm yr}^{-1}$ and a total stellar mass of $10^{11.0\pm0.1}\,{\rm M}_\odot$ — and though SN 2015U is not obviously associated with the brightest star-forming regions of the galaxy, our spectra do show emission lines from nearby H II regions. The clump may also be an artifact of the intervening dust lanes in NGC 2388; unfortunately there is essentially no colour information available from our images as the host-galaxy background dominates.

4.3.4 Comparisons with Other Supernovae

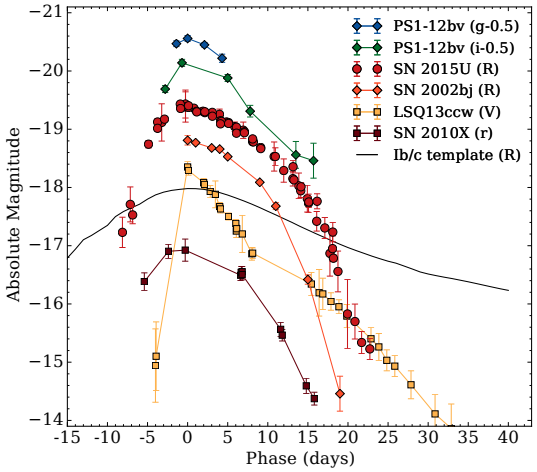

Figure 4.12: The extinction-corrected light curve of SN 2015U compared to light curves of SNe 2002bj and 2010X (Poznanski et al. 2010; Kasliwal et al. 2010), the rapidly evolving SN Ibn LSQ13ccw (Pastorello et al. 2015b), and one of the rapidly evolving events from the PS1 sample (Drout et al. 2014). We also show in black the R-band SN Ib/c template from Drout et al. (2011). For SN 2015U we include data from the R and *clear* passbands published here as well as the r-band photometry from Pastorello et al. (2015c); a vertical offset of -0.25 mag was applied to the r-band data to match the R and *clear* bands, enabling visual comparison.

In Figure 4.12 we compare the light curves of SN 2015U to the R-band light curves of SN 2002bj (Poznanski et al. 2010), which was very similar though $\sim$ 1 mag fainter, and SN 2010X (Kasliwal et al. 2010), which also matches well but was ~ 2.5 mag fainter. SNLS04D4ec and SNLS06D1hc, two of the rapidly rising transients discovered by the Supernova Legacy Survey (SNLS) and presented by Arcavi et al. (2016), also show similar light-curve behaviour but $\sim$ 0.5 mag brighter than SN 2015U (see their Figure 2). In Figure 4.13 we compare the spectra of these events: SN 2002bj was hydrogen deficient (SN IIb-like, though not a good spectroscopic match to normal SNe IIb) with a strong blue continuum and P-Cygni features at higher velocities than observed in SN 2015U, while SN 2010X showed no hydrogen (SN Ib/c-like, though again not a good spectroscopic match to normal SNe Ib/c) with broad absorption features. (Unfortunately, no spectra were obtained of the SNLS events.)

The light curves and spectra of SN 2015U are quite similar to those of the rapidly evolving and luminous transients discovered in the PS1 dataset and presented by Drout et al. (2014). Figure 4.11 includes the g and i-band light curves of the relatively well-observed PS1-12bv from that sample; it was discovered at $z = 0.405$, so the g and i passbands probe rest wavelengths around 3500 Å (about 100 Å shortward of B) and 5350 Å (similar to V), respectively. Without the 0.5 mag offset used in Figure 4.11, the i-band light curve of PS1-12bv would overlie the V band of SN 2015U almost exactly, and the g-band curve would be somewhat brighter than the B band of SN 2015U. There are no clear detections of any emission features in the spectrum of PS1-12bv, but it and the other events from the PS1 sample were discovered at very large distances, and high-S/N spectra do not exist for those events. It is plausible that narrow emission lines of helium (and/or hydrogen) were present but went undetected.

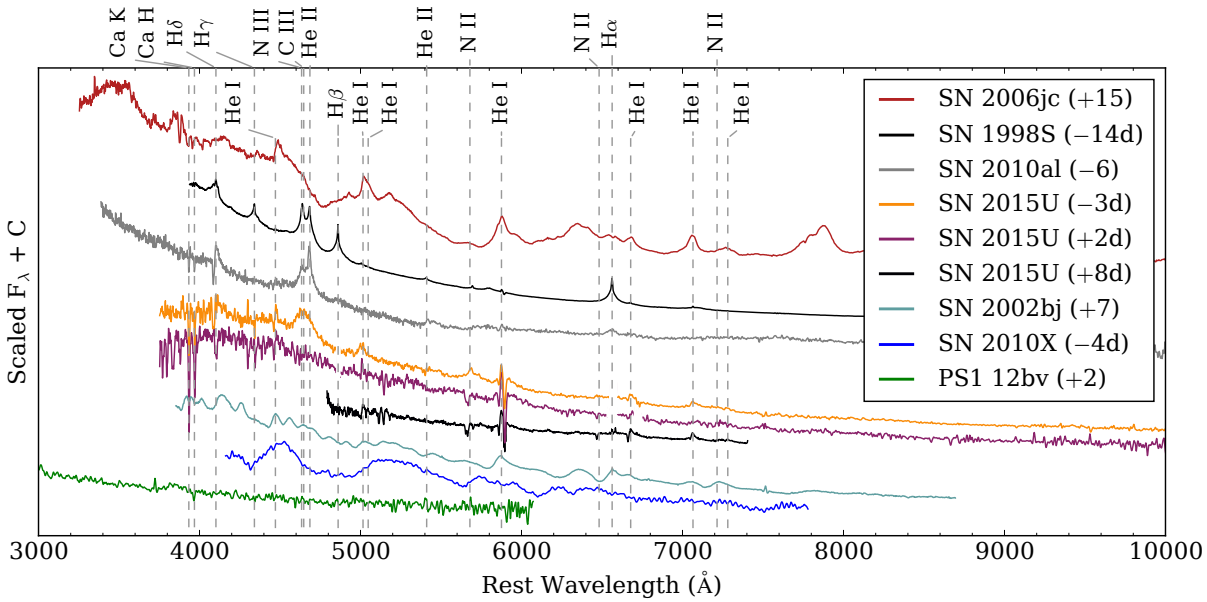

Figure 4.13: Spectra of SN 2015U compared with spectra of the prototypical SN Ibn 2006jc (Foley et al. 2007), the young SN IIn 1998S (Leonard et al. 2000; Shivvers et al. 2015), a previously unpublished spectrum of the transitional SN Ibn 2010al (Silverman et al. 2010; Pastorello et al. 2015a), the rapidly fading SNe 2002bj and 2010X (Poznanski et al. 2010; Kasliwal et al. 2010), and one of the rapidly fading events from the PS1 sample (Drout et al. 2014). Galactic emission features have been masked in the low-resolution spectra of SN 2015U to facilitate comparisons.

Figure 4.13 shows that SN 2015U shares the blue colour and prominent He I emission features of the canonical SN Ibn 2006jc (e.g., Foley et al. 2007; Pastorello et al. 2008a). However, SN 2006jc was discovered post-peak and evolved more slowly than SN 2015U: the earliest extant spectrum of SN 2006jc was taken after the event had faded ~ 1 mag from peak and the spectrum had already transitioned into a nearly nebular phase, though a blue pseudocontinuum was apparent owing to ongoing interaction with the CSM (Foley et al. 2007). At later times, a second red continuum arose in SN 2006jc and the emission features became progressively more asymmetric and blueshifted, evidence for dust formation with the SN system. Increased absorption in the optical passbands by this dust, with re-emission in the infrared, provided an explanation for the rapid increase in the optical decline rate observed for SN 2006jc after $\sim$50 days (Mattila et al. 2008; Smith et al. 2008; Pastorello et al. 2008a).

In contrast, SN 2015U presented a spectrum dominated by a single blue continuum through our last epoch of spectroscopy, also taken after the event had faded ~ 1 mag from peak. The $B - R$ and $V - I$ colour curves of SN 2015U smoothly trend redward from a few days before (optical) maximum brightness to $\sim$2 mag out onto the rapidly fading tail (at which point the SN fades below our detection threshold) — see Figure 4.11. The

accelerating decline rate observed in the SN 2015U light curves does not appear to be due to dust formation: one would expect a redward knee in the colour curves if it were. On the contrary, there is some evidence that the $B-R$ curve of SN 2015U was beginning to flatten in our last few epochs, though note that B-band data become sparse.

We also show the light curve of the peculiar and rapidly fading SN Ibn LSQ13ccw in Figure 4.12 (Pastorello et al. 2015b). LSQ13ccw rose to peak extremely quickly ($t_{\rm rise} \approx 5$ d) and then faded rapidly for ∼10 days, similar to SN 2015U's behaviour. However, it thereafter slowed in its decline, and the spectra of LSQ13ccw (not shown) exhibited both broad and narrow features (as do many, but not all, SNe Ibn). The knee in the light curve of LSQ13ccw is plausibly interpreted as evidence for ongoing energy injection from ejecta/CSM interaction in the system — no such knee is observed in the light curve of SN 2015U, which instead appears to be consistent with a single shock-breakout/diffusion event.

The early-time spectrum of SN 2015U is similar to the very early spectra of the Type IIn SN 1998S and the transitional Type IIn/Ibn SN 2010al, excepting the absence of hydrogen (though see §4.3.2 for a discussion of the tentative Hδ feature in SN 2015U). All three events show a smooth, blue, and (approximately) blackbody continuum. The implied CSM velocity of SN 2015U is higher than in SN 1998S and SN 2010al, and SN 2015U shows strong He I lines while the other two events exhibit stronger He II. The N III/C III complex near 4500 Å is clearly detected in all three events — this feature dominates at very early times and disappears by peak (though that evolution took place over different timescales for these SNe).

Despite the spectral similarities, these three SNe displayed diverse light-curve behaviour. SN 1998S had a SN IIL-like light curve with a long-lasting tail (e.g., Fassia et al. 2000), while the evolution of SN 2010al was more similar to that of SN 2015U though less rapid (Pastorello et al. 2015a, 2016). The $B-R$ colour curve of SN 2015U (as shown in Figure 4.12) is also notably similar to that of SN 2010al, with a slow trend toward redder colours for most of the SN's evolution and then either leveling off or perhaps even becoming more blue again beyond +10 d and +20 d for SNe 2015U and 2010al, respectively (Pastorello et al. 2015a, see their Figure 4).

The ∼ 20-day timescale for SN 2015U's evolution and the increasing decline rate are reminiscent of the light curves expected for low-^{56}Ni explosions in helium-dominated or oxygen-dominated envelopes — see, for example, the models of Dessart et al. (2011) and Kleiser & Kasen (2014). In these models, the recombination of helium or oxygen produces a dramatic and rapid drop in opacity within the ejecta and an inward-moving recombination front. SN 2015U was much more luminous than the objects in these models, but perhaps it was an analogous event wherein a recombination wave in the extended CSM produced a rapid fade from maximum luminosity as the CSM cooled after shock breakout. Similar situations have been observed in hydrogen-rich SNe: there exists a subclass of SNe IIn that shows light curves with a plateau likely produced via hydrogen recombination within their extended CSM (SNe 1994W, 2009kn, and 2011ht; e.g., Chugai et al. 2004; Kankare et al. 2012; Mauerhan et al. 2013a).

The narrow P-Cygni profiles and strong continuua of SN 2015U's spectra are clear indi-

cations of dense CSM. The diversity of ways in which such CSM can affect the light curves of SNe has been explored in detail by several authors motivated by observations of SNe IIn/Ibn, superluminous SNe, and rapidly fading SNe (e.g., Ofek et al. 2010; Chevalier & Irwin 2011; Kleiser & Kasen 2014), and comparisons of SN 2015U's light curve to these models implies that SN 2015U was a shock-breakout event. The high luminosity indicates that shock breakout occurred at a large radius and that a significant fraction of the SN's kinetic energy was converted into light, while the lack of a long-lasting light-curve tail shows that the CSM surrounding SN 2015U was more shell-like than wind-like (there is no interaction-powered tail) and that relatively little ^{56}Ni was produced (there is no radioactively powered tail).

The rapidly fading light curves of SNe 2002bj and 2010X are remarkably similar to those of SN 2015U, and we argue that their spectral differences do not exclude the possibility that these three events were fundamentally quite similar. By varying the radius of a putative opaque CSM shell in a simple model, we can understand events spanning a range of luminosities and timespans for which the opaque CSM reprocesses the SN flux. Under the assumption that their light curves are all shock cooling curves without significant contribution from radioactive nickel, the peak luminosities and timescales of these three SNe should be governed roughly by

$$t_{\rm SN} \propto E^{-1/6} M^{1/2} R^{1/6} \kappa^{1/6} T^{-2/3} \,,$$
$$L_{\rm SN} \propto E^{5/6} M^{-1/2} R^{2/3} \kappa^{-1/3} T^{4/3} \,,$$

following Kleiser & Kasen (2014), adapted from Kasen & Woosley (2009) for hydrogen-free SNe and based on the analytic framework of Popov (1993). E is the energy of the SN explosion, M is the mass ejected, and R is the effective radius (in this case, the radius reached by a significant amount of mass ejected prior to the final explosion).

In particular, consider the peak-luminosity equation, assuming these explosions are similar in all their properties except for the effective pre-SN radius R, which would be determined by the time before explosion and the speed at which any pre-SN material was ejected. Inverting the equation, the pre-SN effective radius $R \propto L_{\rm SN}^{3/2}$. If we assume that the ejecta velocities of all three objects are similar, this means that the ejecta from the SN itself will pass through the surrounding CSM in a time $t_{\rm interact} \propto R$, and the length of time after explosion we expect to see narrow lines from this interaction is proportional to R. Comparing the relative peak luminosities, we find that, since SN 2015U exhibited narrow lines at least up to ~ 16.5 days after explosion, SN 2002bj should have shown narrow lines at least until ~ 5.5 days after explosion and the even dimmer SN 2010X would have shown narrow lines at least until ~ 0.52 days. These times are well before the first spectra were taken of either SN 2002bj or SN 2010X. Typically, we expect that to discover narrow lines in these rapidly fading SNe, we will either need to look at the brightest among them or catch them very early. The luminosity (and timescale) may also depend on the explosion energies, ejected masses, and other properties of the SN, but these must be disentangled with more sophisticated numerical approaches.

4.3.5 Temperature and Luminosity Evolution

The extreme and uncertain degree of host-galaxy dust reddening toward SN 2015U makes estimating bolometric properties quite difficult. In §4.3.1 we assume that the emission from SN 2015U is roughly blackbody in spectral shape; here we further discuss this assumption. It has long been known that the continua of young SNe II exhibit "diluted blackbody" spectral energy distributions (SEDs), which (at optical wavelengths) are similar to the Planck function at a lower temperature (e.g., Hershkowitz et al. 1986; Eastman et al. 1996). Though SN 2015U is certainly not a SN II, it is continuum-dominated, and in the sections above we present evidence that SN 2015U was shrouded in an optically thick CSM. In addition, Moriya et al. (2011) show that modeled shock breakouts from the hydrogen-dominated CSM around red supergiants exhibit roughly blackbody SEDs. Rabinak & Waxman (2011) explore shock breakouts from He or He/CO stellar envelopes in detail; for He-dominated stellar envelopes, they show that the colour temperature of the system deviates from the photosphere's temperature by a (time-dependent) factor of only $\sim 20\%$, largely owing to diffusion effects as a helium recombination wave moves through the material.

Given the above discussion, we assume that SN 2015U's emission was roughly blackbody and we estimate the bolometric properties by fitting a dust-reddened Planck spectrum to our multiband photometry. Using our almost nightly observations of SN 2015U in the $BVRI$ passbands, we assembled the observed optical SEDs from -5 d to $+20$ d and find the best-fit blackbody temperature, radius, and luminosity using MCMC maximum-likelihood methods. As described in §4.3.1, there are large uncertainties in the properties of the host galaxy's dust, and these uncertainties produce similarly large uncertainties in the absolute value of the temperature at any given time. In addition, our optical photometry largely probes the Rayleigh-Jeans tail of SN 2015U's SED, so the implied bolometric corrections are large and uncertain. Our MCMC-produced error bars include these effects, and our photometric data do indicate significant temperature evolution (assuming $E(B-V)$ and R_V do not change). Because our data constrain the evolution of SN 2015U more strongly than they constrain the absolute values of any given parameter, it is useful to consider the implications for a few assumed values of $E(B-V)$.

Figure 4.14 shows the blackbody temperature, bolometric luminosity, and radius evolution of SN 2015U for three different assumed values of $E(B-V)$, adopting $R_V = 2.1$. In all cases, the best-fit temperature decreases over time, with the temperature falling rapidly before (optical) peak and then decreasing slowly thereafter. The effective blackbody radius increases with a photospheric velocity of $v_{\rm phot} \approx 15,000\,{\rm km\,s^{-1}}$ until peak, leveling off thereafter. Though this value of $v_{\rm phot}$ is similar to the characteristic velocities of ejecta in stripped-envelope SNe, our spectra do not show any material moving that quickly and, given our interpretation of SN 2015U as a cooling shock-breakout event, we expect the photospheric radius to be approximately constant throughout these observations. In addition, Figure 4.14 may surprise the reader by indicating that the peak bolometric luminosity occurred several days before the optical peak. Though the bolometric corrections are at their largest and most uncertain at early times, and we unfortunately do not know of any observations constraining

Table 4.4: Bolometric Properties of SN 2015U

$E(B-V)$ (mag)	$L_{\rm peak}$ (erg s^{-1})	$E_{\rm rad}$ (erg)	$T_{\rm peak}$ (K)	$R_{\rm peak}$ (cm)
0.5	7.3×10^{42}	9.3×10^{48}	8400	1.5×10^{15}
0.94	5.9×10^{43}	7.1×10^{49}	19,000	8.7×10^{14}
1.05	2.3×10^{44}	2.9×10^{50}	30,000	6.7×10^{14}

Bolometric luminosity, radiated energy, blackbody temperature, and blackbody radius for the three assumed values of $E(B-V)_{\rm host}$ shown in Figure 4.14.

the ultraviolet emission of SN 2015U, similar behaviour was observed from SN Ibn 2010al with ultraviolet to near-infrared wavelength coverage (Pastorello et al. 2015a).

In addition, we can constrain the temperature evolution of SN 2015U independently of the continuum shape through the relative line strengths of detected emission lines in our spectra. Though detailed modeling is beyond the scope of this paper, the pre-maximum detection and rapid fading of the N III/C III/He II 4500 Å complex in our spectra of SN 2015U brings to mind the spectral evolution of SN 1998S (see Figure 4.13). Detailed CMFGEN models of SN 1998S while the 4500 Å feature was strong were presented by Shivvers et al. (2015), indicating a temperature of ∼30,000 K throughout most of the line-forming region. The agreement between this value and the pre-maximum temperatures found for SN 2015U assuming $E(B-V) = 0.94$ mag are heartening.

In Table 4.4 we present the integrated energy released and various values at V-band peak for three assumed values of $E(B-V)$. Our uncertainty about the host galaxy's dust properties is the dominant source of error in this analysis, and the spread over these three values of $E(B-V)$ indicates the range. All values are estimated through simple polynomial fits to the curves shown in Figure 4.14. To calculate $E_{\rm rad}$, we integrated from day −5 to day +20 (the timespan of our almost nightly multiband photometric coverage), and for the other parameters we list the value at V-band peak. Note that the bolometric luminosity peaks before the optical maximum; again, see Figure 4.14.

4.3.6 Nickel Content

A slowly declining light-curve tail, powered either via CSM interaction or ^{56}Ni decay, has been detected in some SNe Ibn, but many members of this subclass (including SN 2015U) do not show one (e.g., Foley et al. 2007; Gorbikov et al. 2014; Pastorello et al. 2016). For most SNe I, Arnett's law can be used to estimate the total ^{56}Ni synthesized by the explosion (Arnett 1982) based upon observed properties near the time of peak luminosity; however, that approach is not applicable for shock-breakout events. If the opacity of the ejecta is well understood, the luminosity at late times can be used instead. For example, Hamuy (2003a) analyzed Type IIP supernovae and, given a luminosity L_t at time t and an explosion time

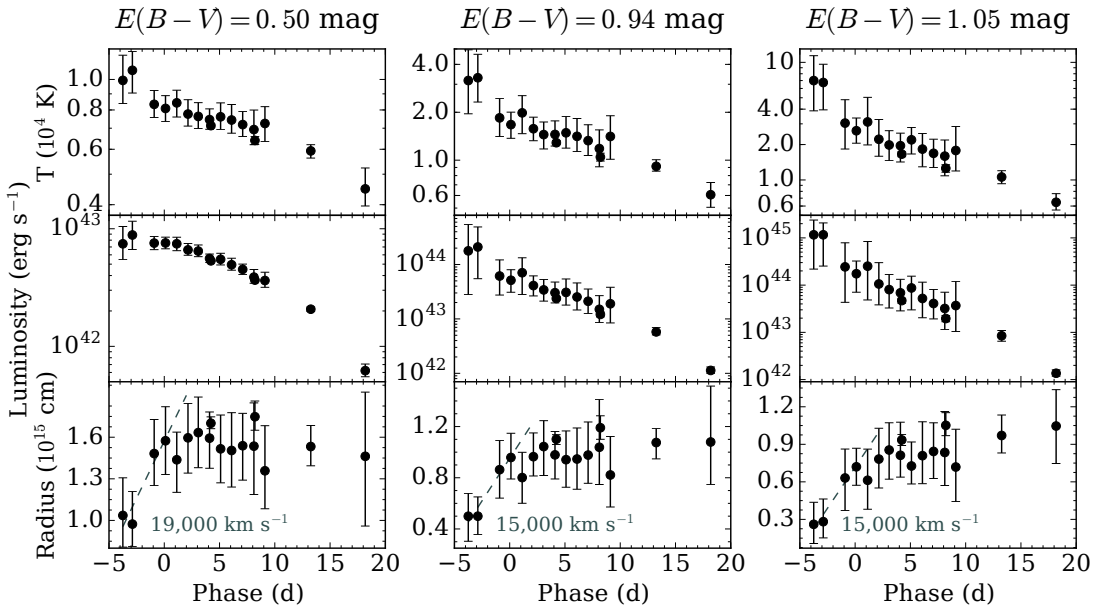

Figure 4.14: The best-fit blackbody temperature, bolometric luminosity, and radius evolution of SN 2015U for three assumed values of $E(B-V)$ as a function of phase relative to V-band peak. The leftmost column shows the evolution assuming a value of 0.5 mag, the middle column assumes our preferred value of 0.94 mag, and the rightmost column corresponds to a value of 1.05 mag. In the lower panels, we show linear fits to the radius evolution up to V-band peak with a grey dashed line. All parameters are fitted using maximum-likelihood MCMC methods and error bars represent 95% confidence intervals (but do not include errors caused by uncertainty in the degree of host-galaxy dust reddening).

t_0, estimated the ^{56}Ni mass to be

$$M_{\rm Ni} = (7.866 \times 10^{44})\, L_t \exp\left(\frac{(t-t_0)/(1+z) - 6.1}{111.26\,{\rm d}}\right) {\rm M}_\odot.$$

This equation assumes that γ-rays produced via radioactive decay are fully trapped and thermalized by the ejecta, an assumption which (though reasonable for SNe IIP) has been shown not to be true for most stripped-envelope SNe (which fade faster than expected for complete trapping; e.g., Wheeler et al. 2015).

The extreme CSM surrounding SN 2015U further complicates the issue, as it may be contributing luminosity via ongoing interaction at late times and perhaps even trapping a higher fraction of the γ-rays than is normal for CSM-free SNe Ib/c. Though a robust measure of the amount of nickel created by SN 2015U would require more sophisticated treatment, we place a rough upper limit on the value by assuming that the ejecta+CSM system of SN 2015U completely traps any radioactively produced γ-rays and that there is no luminosity contribution from ongoing interaction beyond our last detection at ~ 20 days.

Our most constraining observation of a putative radioactively powered tail is a non-detection in the R band at $+36$ d. Our last multiband photometric measurement of the temperature yields $T = 6000 \pm 1000$ K at $+18$ d (see §4.3.5). We adopt that temperature to calculate the blackbody luminosity for a source at our nondetection threshold, but we note that the temperature is still changing at this time, possibly affecting our results. This calculation yields an upper limit of $M_{\rm Ni} \lesssim 0.02\,{\rm M}_\odot$ — quite low for SNe I ($M_{\rm Ni,Ia} \gtrsim 0.4\,{\rm M}_\odot$, $M_{\rm Ni,Ib/c} \approx 0.2\,{\rm M}_\odot$; Contardo et al. 2000; Drout et al. 2011), but within the range of values observed for SNe II ($M_{\rm Ni,II} \approx 0.0016$–$0.26\,{\rm M}_\odot$; Hamuy 2003a).

4.3.7 Progenitor Mass-Loss Rate

We adopt the simple shock-wind interaction model of Chevalier & Irwin (2011) to estimate the properties of the CSM surrounding SN 2015U. We assume that the CSM is spherically symmetric and follows a wind-like density profile ($\rho \propto r^{-2}$), and we use the opacity of helium-dominated material in our calculations ($\kappa = 0.2\,{\rm cm^2\,g^{-1}}$). Margutti et al. (2014) solve the Chevalier & Irwin (2011) model in terms of three observables: break-out radius $R_{\rm bo}$ (the radius at which radiation diffuses forward ahead of the shock), total radiated energy $E_{\rm rad}$, and light-curve rise time $t_{\rm rise}$. We use $t_{\rm rise} = 9$ days and, assuming $E(B-V)_{\rm host} = 0.94$ mag, we adopt $E_{\rm rad} = 7.1 \times 10^{49}$ erg from Table 4.4. For $R_{\rm bo}$ we take the first measured blackbody radius from Figure 4.14: $R_{\rm bo} = 5 \times 10^{14}$ cm. The resultant mass-loss estimate is very large, $\dot{M} \approx 1.2\,{\rm M}_\odot\,{\rm yr^{-1}}$. However, in this model $\dot{M} \propto R_{\rm bo}^{-3}$, and there is reason to believe that our measurement of the blackbody radius before peak brightness does not reflect the true $R_{\rm bo}$ (see §4.3.5). If we instead use $R_{\rm bo} = 9 \times 10^{14}$ cm, the blackbody radius at V-band peak, we calculate $\dot{M} \approx 0.2\,{\rm M}_\odot\,{\rm yr^{-1}}$.

Both of these values are several orders of magnitude above the most extreme mass-loss rates produced by steady winds from stars, but they are not far from the time-averaged eruptive mass-loss rates from LBVs (which may well exhibit much higher instantaneous mass-loss rates; Smith 2014). Observations of iPTF13beo, a recent SN Ibn discovered by the intermediate Palomar Transient Factory (iPTF), implied an even higher (but short-lived) mass-loss rate of $\dot{M} \approx 2.4\,{\rm M}_\odot\,{\rm yr^{-1}}$ immediately before the progenitor underwent core collapse (estimated via similar methods; Gorbikov et al. 2014).

If the CSM around SN 2015U was launched from the surface explosively rather than through a steady wind, the assumption that $\rho_{\rm csm} \propto r^{-2}$ is suspect. In fact, the lack of an interaction-powered tail in the light curve of SN 2015U indicates that the density profile cannot be wind-like: Chevalier & Irwin (2011) show that ongoing interaction with a wind-like CSM powers a tail with $L \propto t^{-0.6}$, and SN 2015U fades more rapidly than that throughout its post-peak evolution. The lack of any high-velocity features in our spectra argues that this outer CSM must be optically thick at least out to the radius of the shock at the time of our last spectrum. Assuming $v_{\rm shock} \approx 20{,}000\,{\rm km\,s^{-1}}$, the velocity of the fastest material in unshrouded stripped-envelope SNe, this produces an estimate for the CSM extent of $R \gtrsim 3 \times 10^{15}$ cm. Adopting the average He I velocity measured from our spectra ($745\,{\rm km\,s^{-1}}$), material at that radius was launched 1–2 yr before core collapse. However, it is likely that

the SN ejecta are slowed by its collision with the CSM, and so it may be more physically relevant to assume the CSM extent to be $R \gtrsim 9 \times 10^{14}$ cm (the blackbody radius at V-band peak); material at that radius was launched < 1 yr before collapse.

It is not clear whether the extreme mass loss from SN 2015U's progenitor was episodic and brief or sustained over a year or more, nor is it known whether the assumption of spherical symmetry is appropriate. We leave a more thorough examination of these questions to future work.

4.3.8 Constraints on Progenitor Variability

The presence of dense CSM suggests a recent history of extreme mass loss and perhaps variability of the progenitor star. SN Ibn 2006jc, for example, underwent a bright outburst ($M = -14$ mag) about 2 yr before becoming a genuine SN (Nakano et al. 2006; Foley et al. 2007; Pastorello et al. 2007), and there are multiple cases where SN IIn progenitors have been detected in outburst in the years prior to core collapse (e.g., Ofek et al. 2014), though such outbursts do not appear to be ubiquitous (e.g., Bilinski et al. 2015). KAIT has been monitoring NGC 2388 for almost 20 yr and we searched this extensive dataset for evidence of pre-explosion variability. We augment our unfiltered KAIT data with the publicly available PTF/iPTF images of the field in the r passband.[10]

Examining 758 images with observed upper limits fainter than 17.0 mag from 1998 Oct. through 2015 Feb. 10, we find no evidence for previous outbursts of the progenitor based upon difference imaging (using one of our deepest single exposures as a template). We stacked our images into rolling-window time bins 20 d wide and subtracted templates to search for evidence of previous outbursts of that timescale, but found none. We also stacked all images together and searched for evidence of a progenitor, but found none. (Note that we stacked the KAIT and PTF/iPTF images separately, and we did not perform difference imaging on these very deep stacks, as we had no templates with which to compare.) Figure 4.15 plots our 1σ single-image nondetections and the observed light curve of SN 2015U.

Though we have regular imaging of NGC 2388 most years since 1998, the field was inaccessible to our telescopes for several months every year, so there are significant gaps, especially compared to the timescale of SN 2015U's light curve (~ 20 d). The orange bars along the bottom of Figure 4.15 mark every night at which more than 20 days had passed since the previous upper limit, indicating timespans when a previous SN 2015U-like event could have occurred undetected.

Unfortunately, even the epochs that were covered by our monitoring campaigns do not yield stringent constraints on the luminosity of a previous outburst, partially owing to the estimated ~ 1.5 mag of host-galaxy dust extinction along the line of sight toward SN 2015U. The detected outburst of SN 2006jc's precursor reached a peak of $M_r \approx -14.1$ mag (Pastorello et al. 2007), and such an outburst in SN 2015U's precursor would have probably remained undetected by our monitoring campaign.

[10] http://irsa.ipac.caltech.edu/applications/ptf/

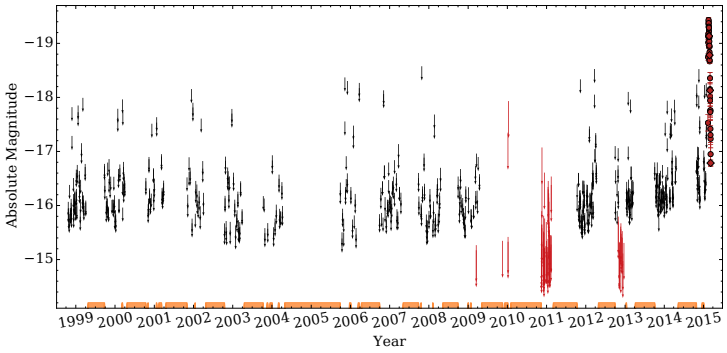

Figure 4.15: Our 1σ nondetections from KAIT unfiltered images (black) and PTF/iPTF R images (red). The light curve of SN 2015U is shown to the far right. Timespans for which no upper limit had been obtained for at least 20 days are marked in orange along the bottom.

4.4 Conclusion

In this paper we presented observations of SN 2015U, a highly extinguished, low-velocity, rapidly evolving, luminous, apparently hydrogen-free SN which exploded in the strongly star-forming galaxy NGC 2388. Though detailed modeling has yet to be performed, and the degree of host-galaxy dust interference is uncertain, our data indicate that SN 2015U was a core-collapse SN with a peak powered by shock breakout from a dense CSM rather than radioactive decay. We suggest that this CSM was not wind-like but was instead created by at least one extreme episode of mass loss ($\dot{M} \approx 0.2$–$1.2\,\mathrm{M}_\odot\,\mathrm{yr}^{-1}$) within a few years of core collapse. The CSM that surrounded SN 2015U was effectively hydrogen-free but was helium-rich; we also detect features from nitrogen, iron, and probably carbon in our spectra. No long-lasting light-curve tail was observed from radioactivity or from ongoing CSM interaction, implying that SN 2015U produced a relatively small amount of ^{56}Ni compared to normal SNe Ib/c.

SN 2015U is a remarkably well-observed SN Ibn, especially among the rapidly fading subset of these events, and we find many similarities between it and other SNe in the literature. Modern surveys indicate the existence of a class of blue, continuum-dominated, hydrogen-deficient, luminous, and rapidly evolving SNe including those found by Drout et al. (2014) and Arcavi et al. (2016); our analysis of SN 2015U implies fundamental similarities between these events, a subset of the SNe Ibn (e.g., Pastorello et al. 2016), and other rapidly fading SNe of lower luminosity (i.e., SN 2002bj and SN 2010X). While the exact progenitors of these events are quite uncertain, it is clear that they demand extreme mass-loss rates from their stripped-envelope progenitor stars.

Chapter 5

The Nearby Type Ibn Supernova 2015G: Signatures of Asymmetry and Progenitor Constraints

Submitted for publication in the Monthly Notices of the Royal Astronomical Society: Shivvers et al. (2017b).
Co-Authors: WeiKang Zheng, Schuyler D. Van Dyk, Jon Mauerhan, Alexei V. Filippenko, Nathan Smith, Ryan J. Foley, Paolo Mazzali, Atish Kamble, Charles D. Kilpatrick, Raffaella Margutti, Heechan Yuk, Melissa L. Graham, Patrick L. Kelly, Jennifer Andrews, Thomas Matheson, W. M. Wood-Vasey, Kara A. Ponder, Peter J. Brown, Roger Chevalier, Dan Milisavljevic, Maria Drout, Jerod Parrent, Alicia Soderberg, Chris Ashall, Andrzej Piascik, Simon Prentice

Chapter Abstract

SN 2015G is the nearest known SN Ibn to date at 23.2 Mpc and it has proven itself a truly remarkable example of this rare subclass. We present the results of an extensive observational campaign including data from radio through ultraviolet wavelengths. SN 2015G was asymmetric, showing late-time nebular lines redshifted by $\sim 1000\,\mathrm{km\,s^{-1}}$. It shared many features with the prototypical SN Ibn 2006jc, including extremely strong He I emission lines and a late-time blue pseudocontinuum. The young SN 2015G showed narrow P-Cygni profiles of He I, but never in its evolution did it show any signature of hydrogen — arguing for a dense, ionized, and hydrogen-free circumstellar medium moving outward from the progenitor with a velocity of $\sim 1000\,\mathrm{km\,s^{-1}}$ and created by relatively recent mass loss from the progenitor star. Ultraviolet through infrared observations show that the fading SN 2015G (which was probably discovered some 20 d post-peak) had a spectral energy distribution that was well described by a simple, single-component blackbody. Archival *HST* images provide upper limits on the luminosity of SN 2015G's progenitor, while nondetections of any luminous

radio afterglow and optical nondetections of outbursts over the past two decades provide constraints upon its mass-loss history.

5.1 Introduction

A basic understanding of core-collapse supernovae (SNe) as luminous displays marking the collapse of a massive stellar core has been in place for at least half a century (e.g., Colgate & White 1966; Arnett 1971). Remarkably, new observations continue to find extreme examples of the process, some of which test the boundaries of our understanding.

For example, binarity within massive-star populations appears to produce complex and only partially understood diversity in supernova (SN) properties via pre-explosion mass exchange and mass loss, likely leading to the population of stripped-envelope SNe (Types IIb/Ib/Ic; e.g., Podsiadlowski et al. 1992; Smith et al. 2011b; Sana et al. 2012; Shivvers et al. 2017a). Evidence is mounting from observations of interacting (Type IIn) SNe that their progenitors undergo extreme episodes of mass loss shortly before core collapse, creating dense circumstellar material (CSM; see review by Smith 2014), but exactly what mechanism is powering these death throes remains unclear. In some cases, enhanced (eruptive) mass loss occurs only a few years to decades before core collapse, which may point to instabilities in late nuclear burning phases triggering mass loss or binary interaction (e.g., Quataert & Shiode 2012; Mauerhan et al. 2013b; Margutti et al. 2014; Smith & Arnett 2014).

Connecting the stripped-envelope and interacting SN populations are the rare Type Ibn SNe (e.g., Matheson et al. 2000a; Foley et al. 2007; Pastorello et al. 2008a). These core-collapse SNe exhibit the narrow spectral emission lines characteristic of an ionized CSM and other key indications of dense CSM (e.g., Chugai 2009); however, spectra of SNe Ibn show little or no hydrogen emission and instead are dominated by strong helium emission lines (most notably He I $\lambda\lambda$5876, 6678, and 7065). Weak-hydrogen examples also exist as intermediate Type IIn/Ibn SNe (e.g., Pastorello et al. 2008b; Smith et al. 2012; Pastorello et al. 2015a), and there are a few known examples of hydrogen-weak explosions (Type Ib SNe) which then interacted with shells of hydrogen-rich material lost by the progenitor tens to thousands of years before core collapse (e.g., SNe 2001em and 2014C; Milisavljevic et al. 2015; Margutti et al. 2017).

Only about 20 SNe Ibn are known at this time, and the properties of this subclass are just beginning to be mapped out (e.g., Sanders et al. 2013; Pastorello et al. 2016; Shivvers et al. 2016; Hosseinzadeh et al. 2017). SN 2015G, which exploded in the outskirts of NGC 6951[1] at a distance of 23.2 Mpc, is the nearest known SN Ibn to date; as such, it has allowed us the opportunity to study a member of this rare subclass in detail. In this paper we present the results of an extensive campaign from radio wavelengths to the ultraviolet (UV) and spanning nearly a year of follow-up observations. In §5.2 we present our observations, in §5.3 we put those data into context and calculate the implied physical properties of the system, and in §5.4 we summarise and conclude.

[1]NGC 6951 has also hosted two other SNe in the past few decades: SN IIn 1999el and SN Ia 2000E.

5.2 Observations

SN 2015G was discovered by Kunihiro Shima at 15.5 mag (unfiltered) on 2015-03-23.778 (we use UT dates and times throughout this article) and spectroscopically classified as a SN Ibn, similar to SN 2006jc, 3 s afterward (Yusa et al. 2015; Foley et al. 2015). We initiated a photometric and spectroscopic follow-up effort for SN 2015G as soon as its nature as a nearby example of the rare Type Ibn subclass was understood. From the ground, this campaign included a regular cadence of imaging through *BVRI* filters, a detailed spectroscopic follow-up campaign at both low and moderate resolution, two epochs of near-IR imaging (*J, H,* and K_s filters), and three epochs of radio-wavelength observations. We also obtained multiple epochs of space-based UV imaging with *Swift* and with the *Hubble Space Telescope (HST)*, three epochs of *HST* UV spectroscopy, and two epochs of *HST* optical imaging. Though some of these observations produced only nondetections, the combination of detections and upper limits forms an extensive dataset on SN 2015G.

Unfortunately, we did not catch SN 2015G before it reached peak brightness — comparisons between the early unfiltered amateur photometry and ours (beginning 4 d later) indicate that the SN was already on the decline at the time of discovery. Because the peak was unobserved, throughout this paper we refer to the time since the *discovery date* as the phase of SN 2015G.

5.2.1 Ultraviolet through Infrared Imaging

Filtered *BVRI* and unfiltered observations of SN 2015 were obtained with the 0.76 m Katzman Automatic Imaging Telescope (KAIT; Filippenko et al. 2001b) at Lick Observatory nearly nightly from days 4 through 37. As the SN faded below KAIT's detection threshold, we began a campaign with the Direct Imaging Camera on the Lick 1 m Nickel telescope. We maintained a regular observing cadence until day 155, at which point SN 2015G faded below our Nickel detection threshold in both the *B* and *V* passbands.

Our images were reduced using a custom pipeline, as discussed by Ganeshalingam et al. (2010). Template subtractions were performed with additional images obtained on 12 July 2016 (day 477), after the SN had faded entirely. Point-spread-function (PSF) photometry was performed with the `DAOPHOT` package (Stetson 1987) in the IDL Astronomy User's Library.[2] Nearby reference stars in our images were calibrated to the APASS[3] catalog, which we transform to the Landolt system[4] and then to the KAIT4 natural systems using the colour terms and equations as calculated by Ganeshalingam et al. (2010, 2013). As the Nickel camera has aged, our best-fit colour terms for the above transformation have changed; we correct the data published here with updated Nickel colour terms recalculated in 2016 ($C_B = 0.041,\ C_V = 0.082,\ C_R = 0.092,\ C_I = -0.043$).

[2] http://idlastro.gsfc.nasa.gov/

[3] http://www.aavso.org/apass

[4] http://www.sdss.org/dr7/algorithms/sdssUBVRITransform.html

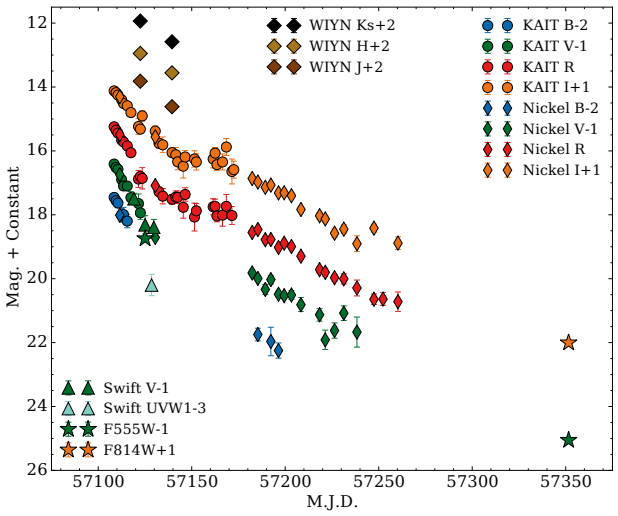

Figure 5.1: Our photometry of SN 2015G, from UV through IR wavelengths. All data are shown after correcting for extinction arising from dust within the Milky Way Galaxy and the SN host galaxy (see §5.2.4).

Table 5.1 presents our photometry of SN 2015G within the natural photometric systems of KAIT4/Nickel. Because our observations show a significant gap in the bluer passbands, after the SN dropped below the sensitivity limits for KAIT in those passbands but before we began our campaign with the larger Nickel telescope, we do not convert these data into a standard photometric system. Ganeshalingam et al. (2010) and Ganeshalingam et al. (2013) provide the colour terms and equations required to perform this conversion, but doing so at all phases would require interpolating the evolution in the bluer passbands, so we provide only the natural photometry and leave any conversion (required for detailed comparisons with observations from other instruments) to future work.

Infrared (IR) imaging through the J, H, and K_s filters was obtained 18 s and 35 d after discovery with the Wisconsin-Indiana-Yale-NOAO (WIYN) 3.5 m telescope using the WIYN High-Resolution Infrared Camera (WHIRC; Meixner et al. 2008). SN 2015G was clearly detected in all three bands at both epochs. The raw images were processed using the methods described by Weyant et al. (2014) to construct the combined stacked images for each visit. We used Source Extractor to obtain aperture photometry, and we calculate photometric zeropoints for these data by cross-matching field stars with the Two Micron All Sky Survey catalog (2MASS; Skrutskie et al. 2006). We do not correct for any colour differences between the WIYN+WHIRC and 2MASS systems.

The Ultraviolet/Optical Telescope (UVOT; Roming et al. 2005) mounted on the *Swift* satellite (Gehrels et al. 2004) was used to observe the field of SN 2015G regularly from day 12 through day 30. Photometric reduction for these data was performed with the pipeline for the *Swift* Optical Ultraviolet Supernova Archive (SOUSA; Brown et al. 2014). For each of these images, a 5″ aperture is used to measure the counts for the coincidence loss correction, and a 3″ or 5″ source aperture (depending on the uncertainty from above) was used for the photometry after subtracting off the galaxy count rate in a template image. We apply aperture corrections (based on the average PSF in the *Swift* CALDB), zeropoint corrections, and time-dependent sensitivity loss corrections to place the magnitudes on the UVOT photometric system as described by Poole et al. (2008) and Breeveld et al. (2011).

Table 5.1: Table of Photometric Observations

Date (UT)	Magnitude	Passband	Telescope
2015-03-27.51	17.07±0.07	B	KAIT
2015-03-27.51	16.61±0.04	V	KAIT
2015-03-27.51	16.20±0.03	R	KAIT
2015-03-27.51	15.81±0.04	I	KAIT
2015-03-28.53	17.17±0.08	B	KAIT
2015-03-28.53	16.71±0.04	V	KAIT
2015-03-28.53	16.30±0.03	R	KAIT
2015-03-28.53	15.86±0.04	I	KAIT
2015-03-29.54	17.25±0.15	B	KAIT
2015-03-29.54	16.77±0.08	V	KAIT
2015-03-29.54	16.40±0.05	R	KAIT
2015-03-29.54	15.94±0.08	I	KAIT
2015-03-30.52	17.63±0.02	B	Nickel
2015-03-30.52	16.94±0.01	V	Nickel
2015-03-30.53	16.44±0.01	R	Nickel
2015-03-30.53	15.99±0.01	I	Nickel
2015-03-31.53	17.63±0.21	B	KAIT
2015-03-31.54	17.10±0.07	V	KAIT
2015-03-31.54	16.61±0.05	R	KAIT
2015-03-31.54	16.09±0.06	I	KAIT
Truncated; full table available digitally.			

Most of these observations produced nondetections of SN 2015G, which prove useful in constraining the luminosity of SN 2015G at UV wavelengths.

The *HST* and its Wide Field Camera 3 (WFC3) was used to obtain optical images of SN 2015G through the *F555W* band on day 20 and the *F555W* and *F814W* bands on day 247, as part of programs GO-14149 (PI A. Filippenko) and GO-13683 (PI S. Van Dyk).[5] We also examine pre-explosion *HST* observations of the SN 2015G explosion site obtained in 2001 through the *F555W* and *F814W* filters with the Wide-Field Planetary Camera 2 (WFPC2) as part of the campaign to monitor SN 1999el (GO-8602 with PI A. Filippenko; see Li et al. 2002a). All of these images were obtained from the *HST* Archive after standard pipeline processing. We performed photometry on these images using `DOLPHOT` (Dolphin 2000). The `DOLPHOT` parameters `FitSky` and `RAper` were set to 3 and 8 (respectively), appropriate for crowded galactic environments, and we set `InterpPSFlib=1`, implemented with the TinyTim PSF library (Krist et al. 2011).

The above data are presented in Table 5.1 and shown in Figure 5.1. Values in the

[5]Another epoch of imaging was attempted on 15 October 2016 as part of GO-14668 (PI A. Filippenko), but unfortunately the observations were set up such that the pointing was toward the center of NGC 6951 and, owing to the orientation of the image array, the SN site itself was missed.

table are given as observed, without applying any dust reddening corrections. Additional UV-wavelength nondetections were obtained with *Swift*; we list only those relevant for this work.

5.2.2 Radio

We obtained three epochs of observations on SN 2015G using the Janksy Very Large Array (VLA), in April, May, and July 2015, all of which were nondetections producing upper limits on the radio flux from the SN.

All data were taken in the standard continuum-observing mode with a bandwidth of $16 \times 64 \times 2$ MHz. The VLA underwent a few configuration changes at various stages during these observations. During the data reductions, we split the data into two side bands of approximately 1 GHz each, centred on 4.8 and 7.1 GHz. We used the radio source 3C286 for flux calibration, and calibrator J2022+6136 for phase referencing. Data were reduced using standard packages within the Astronomical Image Processing System (AIPS). No radio emission was detected from SN 2015G in any of these observations, resulting in the deep flux limits summarised in Table 5.2.

Table 5.2: Table of Radio Observations

Date (UT)	Frequency (GHz)	3σ RMS (μJy)	VLA Configuration
2015-04-04.42	4.8	< 36.6	B
2015-04-04.42	7.1	< 34.8	B
2015-05-14.37	4.8	< 32.1	BnA
2015-05-14.37	7.1	< 37.8	BnA
2015-09-25.19	4.8	< 40.5	A
2015 Jul 25.19	7.1	< 29.8	A

5.2.3 Ultraviolet and Optical Spectra

Regular optical spectra of SN 2015G were obtained with the Kast Double Spectrograph mounted on the 3 m Shane telescope (Miller & Stone 1993) at Lick Observatory, starting day 3 (see Foley et al. 2015) and continuing until the SN was too faint for Kast. A single observation was taken with Kast in the spectropolarimetric mode, on day 4; the details of our spectropolarimetric observing techniques are described by Mauerhan et al. (2015) and Shivvers et al. (2016). During the same time period we obtained additional spectra with the Boller & Chivens Spectrograph mounted on the 2.3 m Bok Telescope and the Spectrograph for the Rapid Acquisition of Transients (SPRAT; Piascik et al. 2014) mounted on the 2.0 m Liverpool Telescope. With these telescopes, we were able to maintain a cadence between observations of 1 week or less for the first 2 months of SN 2015G's evolution.

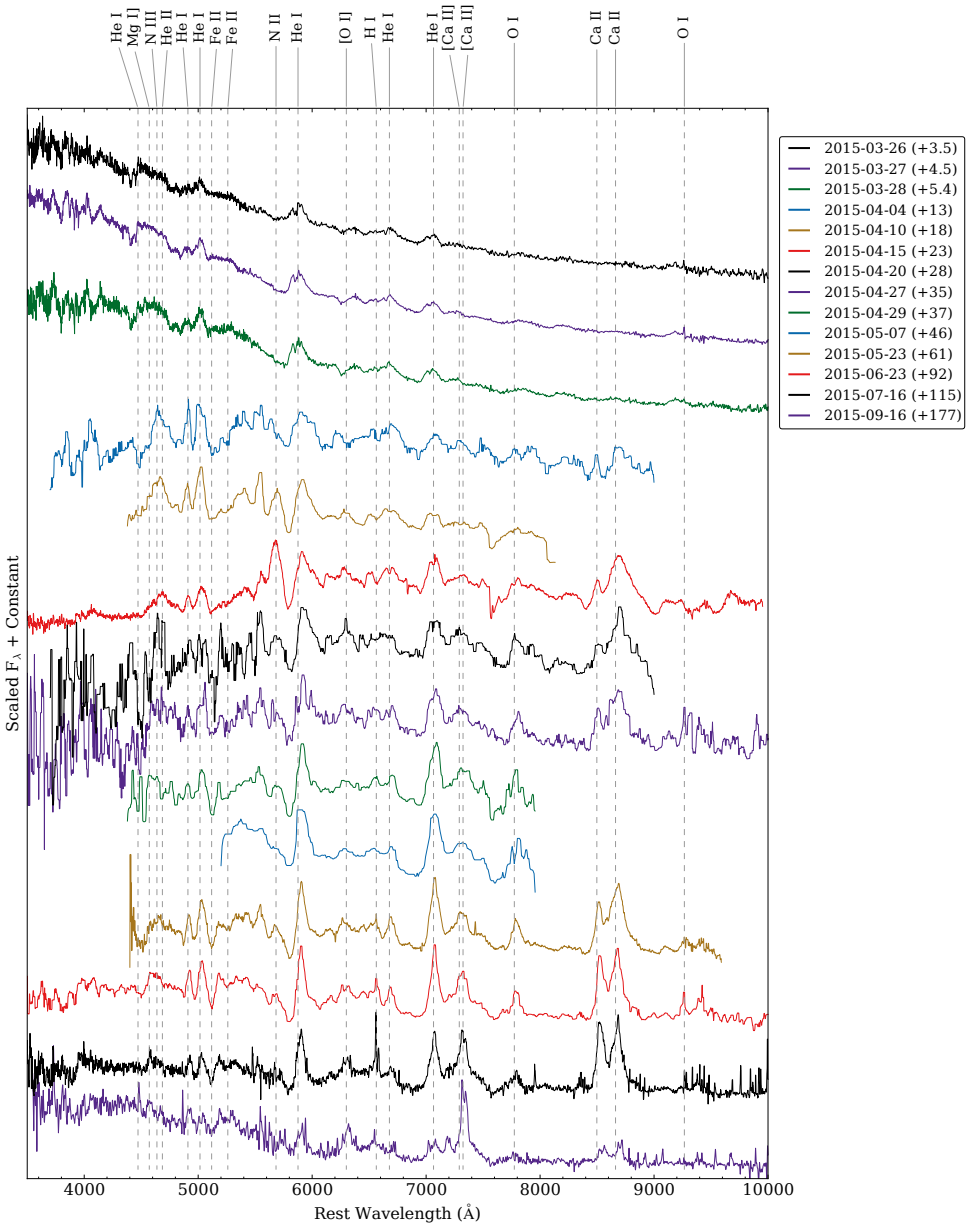

Figure 5.2: Subset of the observed spectral series, showing only the higher-SNR spectra for clarity. Our complete spectral dataset is listed in Table 5.3. Data have been corrected for dust absorption along the line of sight and are presented in the host galaxy's rest frame, and in the legend we state both the UT date of observation and the days since discovery. For some of the later epochs, we plot coadditions of multiple spectra to increase the SNR, and we label these coadditions with the mean date. Spectra at phases $> 10\,\mathrm{d}$ have been smoothed via a moving window median or convolution with a Gaussian kernel. All line labels are plotted at the rest wavelenth of the line ($v = 0\,\mathrm{km\,s^{-1}}$).

Table 5.3: Journal of Spectroscopic Observations

Date (UT)	Tel./Inst.	Wavelength (Å)	Resolution (Å)
2015-03-26.51	Shane/Kast	3,450–10,860	10
2015-03-27.44	Bok/B&C	4,400–8,170	10
2015-03-27.50	Bok/B&C	6,190–7,350	2
2015-03-27.50	Shane/Kast	3,450–10,880	10
2015-03-28.46	Shane/Kast	3,460–10,850	10
2015-03-28.48	Shane/Kast	3,450–7,960	6
2015-03-28.50	Shane/Kast (SpecPol)	4,550–9,940	10
2015-04-04.64	HST/STIS/MAMA	1,570–10,230	10
2015-04-09	Liverpool/SPRAT	4,010–7,950	18
2015-04-10.49	Bok/B&C	5,700–6,870	2
2015-04-10.43	Bok/B&C	4,400–8,170	10
2015-04-11	Liverpool/SPRAT	4,010–7,950	18
2015-04-11.50	HST/STIS/MAMA	1,570–10,230	10
2015-04-15.44	LBT/MODS	3,500–10,000	7
2015-04-16.49	Shane/Kast	3,450–10,860	10
2015-04-17	Liverpool/SPRAT	4,010–7,950	18
2015-04-19.52	Shane/Kast	5,000–10,000	10
2015-04-20.31	HST/STIS/MAMA	1,570–10,230	10
2015-04-27	Liverpool/SPRAT	4,000–7,950	18
2015-04-27.43	Shane/Kast	3,500–10,500	10
2015-04-28.43	Bok/B&C	4,400–8,060	10
2015-04-29	Liverpool/SPRAT	4,020–7,990	18
2015-04-30.38	MMT/Blue Channel	5,710–7,000	2
2015-05-01	Liverpool/SPRAT	4,020–7,990	18
2015-05-05	Liverpool/SPRAT	4,020–7,990	18
2015-05-08	Liverpool/SPRAT	4,020–7,990	18
2015-05-10	Liverpool/SPRAT	4,020–7,990	18
2015-05-13	Liverpool/SPRAT	4,000–7,960	18
2015-05-20.56	Keck-2/DEIMOS	4,410–9,640	4
2015-05-26.48	Shane/Kast	3,460–10,880	10
2015-06-22.43	Shane/Kast	3,440–10,860	10
2015-06-23.47	Shane/Kast	3,450–10,850	10
2015-06-24.46	Shane/Kast	3,440–10,860	10
2015-07-16.53	Keck-1/LRIS	3,100–10,330	7
2015-07-20.37	Shane/Kast	3,430–10,820	10
2015-08-12.32	Shane/Kast	3,420–10,830	10
2015-09-16.38	Keck-1/LRIS	3,560–10,320	7

Several additional optical spectra were obtained after the SN had significantly faded using the DEep Imaging Multi-Object Spectrograph (DEIMOS; Faber et al. 2003) and the Low Resolution Imaging Spectrometer (LRIS; Oke et al. 1995; Rockosi et al. 2010) mounted on the Keck 10 m telescopes, the Multi-Object Double Spectrograph (MODS; Byard & O'Brien 2000) mounted on the 8.4 m Large Binocular Telescope (LBT), and the Bluechannel spectrograph on the 6.5 m Multiple Mirror Telescope (MMT), extending our spectroscopic sequence out until 16 September, some 6 months after SN 2015G was discovered.

All ground-based spectra were observed at the parallactic angle to minimise slit losses from atmospheric refraction (Filippenko 1982). We reduced and calibrated our Keck and Lick observations following the procedures detailed by Silverman et al. (2012), utilising IRAF[6] routines and custom Python and IDL codes.[7] For all Arizona facility telescopes (Bok, LBT, MMT), we performed standard reductions in IRAF. We use the standard reductions of SPRAT data as provided by the Liverpool automated pipeline. All data were flux calibrated via spectrophotometric standards observed through an airmass similar to that of SN 2015G, each night. We performed the spectropolarimetric reduction in the manner described by Mauerhan et al. (2015, and references therein), producing the reduced polarimetric parameters of q and u (Stokes parameters), P (debiased polarization), and θ (sky position angle).

As part of program GO-13797, we obtained three epochs of *HST*/Space Telescope Imaging Spectrograph (STIS) spectroscopy of SN 2015G (on 4, 11, and 20 April 2015) covering UV through near-IR wavelengths. We use the reduced spectra as provided by the Space Telescope Science Data Analysis System (STSDAS) pipeline.

Table 5.3 lists our spectra, and Figure 5.2 illustrates the spectral evolution of SN 2015G. All spectra will be made available for download through WISeREP[8], the Open Supernova Catalog[9] (Guillochon et al. 2017), and the UC Berkeley Supernova Database[10] (SNDB; Silverman et al. 2012).

5.2.4 Line-of-Sight Extinction

SN 2015G lies behind a moderate amount of dust extinction arising from the intestellar medium (ISM) within the Milky Way (MW): $E(B-V)_{\rm MW} = 0.3189$ mag (Schlafly & Finkbeiner 2011). In our spectra that exhibit sufficient signal-to-noise ratio (SNR) and resolution, we observe an Na I D absorption doublet from gas within the MW, as well as Na I D from gas within the host galaxy NGC 6951 (see Figure 5.3).

We use these sodium doublets to estimate the extinction toward SN 2015G arising within the host galaxy. We measure the equivalent widths of the (separately resolved) D_1 and

[6] IRAF is distributed by the National Optical Astronomy Observatory, which is operated by AURA, Inc., under a cooperative agreement with the NSF.

[7] https://github.com/ishivvers/TheKastShiv

[8] wiserep.weizmann.ac.il

[9] sne.space

[10] heracles.astro.berkeley.edu/sndb

D_2 lines in both the MMT spectrum from 30 May and the Keck spectrum from 20 June, averaging multiple measurements from both spectra. We obtain 0.20 ± 0.06 and 0.37 ± 0.02 Å for D_1 and D_2, respectively. Assuming the dust and gas properties within NGC 6951 are well approximated by their properties within the MW ($R_V = 3.1$), we use the relations of Poznanski et al. (2012) to infer $E(B-V) = 0.053 \pm 0.028$ mag (using the D_1 line) and $E(B-V) = 0.076 \pm 0.028$ mag (using the D_2 line).

Given these measures, we estimate that NGC 6951 contributes $E(B-V) \approx 0.065$ mag, for a total line-of-sight dust reddening of $E(B-V) \approx 0.384$ mag. Our major results are not dependent upon the exact level of dust reddening, and we caution that our calculation of the internal host galaxy's reddening is only an estimate; the line-of-sight Na ID and dust within the hosts of some previous SNe have been observed to be dissimilar from those of the MW (e.g., Phillips et al. 2013; Shivvers et al. 2016).

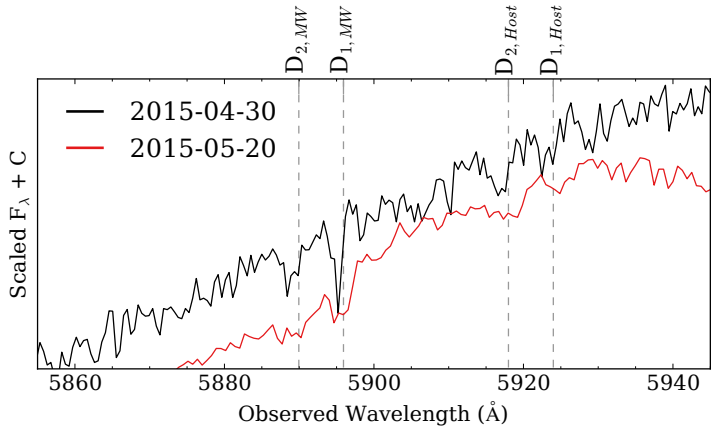

Figure 5.3: Na ID absorption lines observed in two of our higher-resolution spectra of SN 2015G, with the wavelengths of the doublet indicated in the Milky Way rest frame and in the rest frame of the host, NGC 6951.

5.3 Analysis

We analyze all data in the rest frame of the host galaxy NGC 6951, adopting $z = 0.00475 \pm 0.000005$ (Haynes et al. 1998) and a distance of 23.2 Mpc ($\mu = 31.83$; median of 13 distances to NGC 6951 as reported on the Nasa Extragalactic Database[11]). Before our analysis we correct for absorption arising from dust both within our MW galaxy and within NGC 6951 (see §5.2.4).

5.3.1 SN 2015G's Spectral Evolution

Figure 5.2 illustrates the spectral evolution of SN 2015G. Hosseinzadeh et al. (2017) present four other spectra, providing additional coverage of the SN evolution between days 18 and 40. The early-time spectra of SN 2015G show the signatures observed in many young

[11] ned.ipac.caltech.edu/

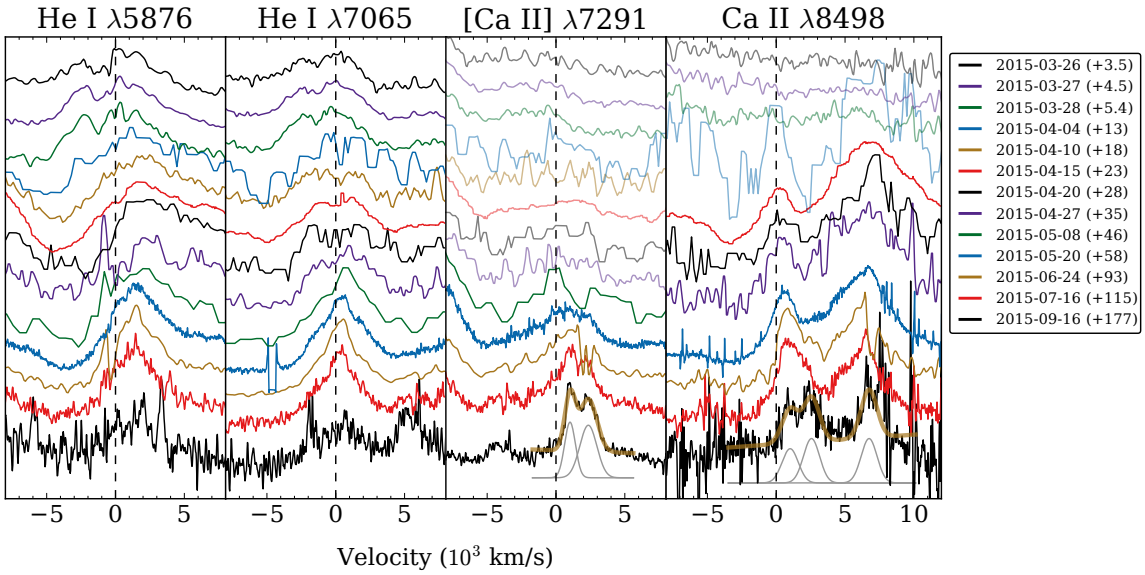

Figure 5.4: Evolution of He I, [Ca II], and Ca II lines in velocity space. All late-time lines are strongly offset redward from $0\,\mathrm{km\,s^{-1}}$, most clearly the Ca II. Note that we calculate velocities in both calcium panels relative to the blue-most line in each blend. Our best-fit line profiles of calcium features in the last spectrum are shown overlying that spectrum on the bottom, with the profile components shown below in grey.

and intermediate-age SNe Ibn (e.g., Foley et al. 2007; Pastorello et al. 2008a; Hosseinzadeh et al. 2017). They have a strong continuum and relatively narrow P-Cygni helium lines (absorption minima blueshifted by $\sim 1000\,\mathrm{km\,s^{-1}}$) atop broader emission. By our third epoch of spectroscopy ($+5\,\mathrm{d}$), the broader emission lines formed a blueshifted absorption component, transforming into a P-Cygni line profile with absorption minima blueshifted by $\sim 8000\,\mathrm{km\,s^{-1}}$. These broader P-Cygni lines persisted throughout the photospheric phase and into the nebular phase, at which point the continuum had faded and the P-Cygni absorption components had disappeared, leaving behind the emission lines of helium and calcium which dominate our spectra out to the last observations.

SN 2015G's spectral features undergo a remarkable wavelength evolution over the course of our campaign, implying a similarly remarkable change in the velocity of the material contributing most to those features. Figure 5.4 shows this evolution for two He I lines, for the forbidden doublet of [Ca II] $\lambda\lambda$7291, 7324 (which only becomes apparent starting $\sim 100\,\mathrm{d}$, but is prominent at late phases), and for the Ca II $\lambda\lambda$8498, 8542, 8662 near-IR triplet.

In the He I feature we see early P-Cygni absorption around $-1000\,\mathrm{km\,s^{-1}}$ sitting atop broader emission lines with widths of $\sim 5000\,\mathrm{km\,s^{-1}}$. Both the narrow and broad profiles at first show emission components centred near velocity $v = 0\,\mathrm{km\,s^{-1}}$. By $\sim 10\,\mathrm{d}$, the major lines at wavelengths $\lambda \lesssim 6500\,\text{Å}$ (where the continuum is strongest) show broad, blueshifted P-Cygni absorption, as is normal in SN spectra. By $\sim 20\,\mathrm{d}$ time the narrow P-Cygni features

have faded from our spectra.

The SN then progresses toward the nebular phase and the continuum drops away below the emission lines. As it does so, the peaks of those emission lines clearly trend redward through our final observation. We model the near-IR calcium triplet in our last spectrum (+177 d) to measure its implied Doppler velocity. Our model consists of three Gaussian profiles separated by the triplet's intrinsic spacings and forced to have the same width, and we fit it to the data via Monte Carlo Markov Chain (MCMC) maximum-likelihood methods. Our best-fit profile is shown at the bottom right of Figure 5.4, and we find a velocity offset of $\sim 1000\,\mathrm{km\,s^{-1}}$ receding (relative to the host-galaxy rest frame) and a full width at half-maximum intensity (FWHM) of $\sim 1400\,\mathrm{km\,s^{-1}}$ (for each component line in the triplet). The forbidden calcium doublet can also be fit quite well by a doublet profile with an offset velocity forced to match that of the near-IR triplet, though we were required to allow the two components of the doublet to exhibit different FWHMs; perhaps the [O II] λ7320 blend is contributing some flux to the [Ca II] feature.

5.3.2 Comparisons with Other SNe

Figure 5.5 shows spectra of SN 2015G compared to those of other SNe Ibn and normal SNe Ib, with early-time spectra plotted on the left, late-time spectra on the right, and those taken at intermediate ages in the middle. We ran our +5 d spectrum of SN 2015G through the SuperNova Identification code (SNID; Blondin & Tonry 2007) with the updated template sets of Silverman et al. (2012) and Liu & Modjaz (2014). Note that none of these template sets includes SN Ibn spectra, but SNID identified the +27 d SN Ib 2007C spectrum as a reasonable match. Broad features arising from many of the same ions are apparent in both SNe, though of course the SN 2007C spectrum (which is reasonably characteristic of normal SN Ib spectra at photospheric phases) does not exhibit the strong blue continuum and narrow emission features of SNe Ibn. The presence of a similar set of broad features between these two SNe suggests that SN 2015G could have been a relatively normal SN Ib if its dense CSM were not present.

The pre-maximum spectrum of SN 2015U showed emission lines of N II $\lambda\lambda$5680, 5686 and N III $\lambda\lambda$4634, 4642/C III λ4647 (Pastorello et al. 2015c; Shivvers et al. 2016). Neither of these is apparent in our early spectra of SN 2015G. However, probable N II $\lambda\lambda$5680, 5686 and N III $\lambda\lambda$4634, 4642 emission features do become prominent by day 23 (see Figure 5.2).

During its transition from the photospheric phase to the nebular (see the middle panel of Figure 5.5), SN 2015G followed an evolution not so dissimilar from that of normal SNe Ib, as the previously dominant continuum faded away to leave only the nebular emission lines behind. However, the "broad" nebular features of SN 2015G are less broad than those shown by normal SNe Ib throughout, and the strong He I emission lines of SN 2015G do not appear in normal SN Ib spectra.

This strong He I emission is usually interpreted as a result of ongoing interaction between the outer layers of the ejecta and a helium-rich CSM (e.g., Matheson et al. 2000a). Because the excitation energy of He I is so large, thermal excitation in the freely expanding and

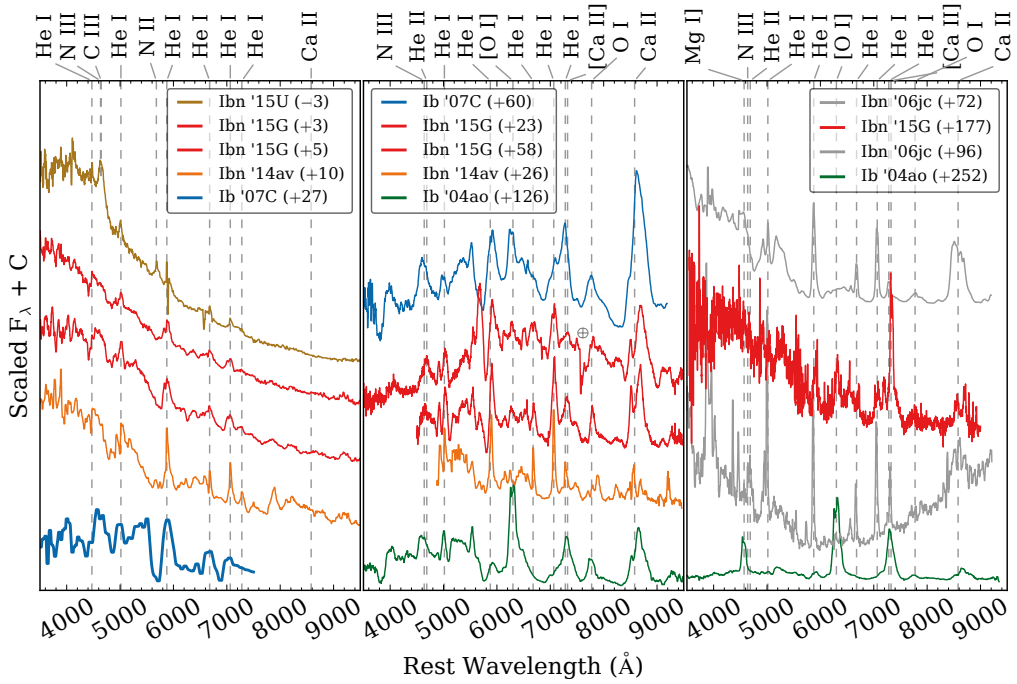

Figure 5.5: The spectra of SN 2015G at early, middling, and nebular phases (left, middle, and right panel, respectively). We compare to spectra of SNe Ibn 2006jc, 2014av, and 2015U (Foley et al. 2007; Smith et al. 2008; Pastorello et al. 2016; Shivvers et al. 2016); to the SN Ib 2007C SNID template presented by Liu & Modjaz (2014) along with previously unpublished spectra of the event, and to previously unpublished spectra of SN Ib 2004ao. For each SN, spectra are presented in the SN rest frame and have been corrected for dust reddening along the line of sight. The phases of the spectra are given in days after discovery for SNe 2004ao, 2006jc, and 2015G, and days after optical peak for SNe 2007C, 2014av, and 2015U. All line labels are plotted at the rest wavelength of the line ($v = 0\,\mathrm{km\,s^{-1}}$).

cooling SN ejecta cannot account for features like these. Instead, the ongoing shock between the ejecta and the helium-rich CSM is usually invoked to explain the strong helium lines in SNe Ibn. Normal SNe Ib, which show strong He I absorption lines at peak but no nebular He I emission lines, are often argued to arise via a different process: "mixed" SNe (e.g., Lucy 1991). In this scenario, radioactive nickel is mixed well out into the helium envelope and the γ rays from the decay process are therefore able to excite the helium nonthermally.

Hosseinzadeh et al. (2017) propose the existence of two spectroscopic subclasses of SNe Ibn: those that show narrow ($v \approx 1000\,\mathrm{km\,s^{-1}}$) He I P-Cygni features within $\sim 20\,\mathrm{d}$ of peak and those that do not. They group SN 2015U into the first class and they group both SNe 2006jc and 2015G into the second (SN 2014av, also shown in Figure 5.5, they label as intermediate between the classes). The spectra presented here show that the similarities between SNe 2015G and 2006jc are manyfold and robust, but that SN 2015G actually did

have narrow P-Cygni He I lines at early phases. SN 2015G therefore appears to span the differences between the two proposed subclasses (as SN 2014av does).

This adds evidence to the argument that either SNe Ibn exhibit a continuum of spectral properties between the two extremes exemplified by the Hosseinzadeh et al. (2017) subclasses, or that the issue of interest is not the presence or absence of narrow P-Cygni lines but instead their longevity or our viewing angle. Perhaps all SNe Ibn show these features but they quickly disappear from the spectra of SN 2006jc-like events, as those authors speculate, or perhaps SNe Ibn often exhibit strong asymmetries (in their CSM distributions or in their explosions) and the narrow lines are only apparent from certain perspectives.

SN 2015G exhibited much stronger calcium (both allowed and forbidden) than did SN 2014av, though comparisons to SN 2006jc indicate that the strength of these calcium features are quite variable among different objects. As the SNe Ibn shown in Figure 5.5 enter the nebular phase, their oxygen emission lines are weak compared to those of normal SNe Ib. The oxygen line strengths of SN 2015G are between those of the very oxygen-weak SN 2006jc and the oxygen-strong (normal) Type Ib SN 2004ao, at both mid-nebular and fully-nebular phases.

Note that the late-time spectra of SN 2015G show some similarities to those of the "calcium-rich" class of SNe Ib (see, e.g., Filippenko et al. 2003; Perets et al. 2010; Kasliwal et al. 2012; Foley 2015; Lunnan et al. 2017), with very strong calcium emission lines relative to those of oxygen. There are several important differences between SN 2015G and the calcium-rich SNe Ib, however, most notably the strong iron features (calcium-rich events show none in their spectra; Kasliwal et al. 2012).

As SN 2015G aged a blue continuum became apparent, similar to those observed in the Type Ibn SNe 1999cq and 2006jc (Matheson et al. 2000a; Foley et al. 2007) and the transitional IIn/Ibn SN 2011hw (Smith et al. 2012), and visible in the right panel of Figure 5.5. The late-time blue continuua of SNe 1999cq and 2006jc were attributed to a forest of blended Fe II lines; we believe the same process to be at work in the SN 2015G system. The density of features at these wavelengths makes individual lines difficult to isolate, but we identify clear Fe II features by comparing our 15 April spectrum to synthetic models calculated with SYN++ (Fisher 2000; Thomas et al. 2011). We are unable to converge upon a SYN++ model that reproduces all of the major spectral features, most especially the strong He I emission, but our best-fit model does argue for significant near-UV line blanketing from iron as well as multiple overlapping absorption features in the blue, the two most obvious and isolated of which are indicated in Figure 5.2.

This blue pseudocontinuum arose later in SN 2015G's evolution than it did for SN 2006jc. Though the peak dates of both SNe passed by unobserved, the relative strengths of the Ca II and [Ca II] lines, as well as the O I and [O I] features, provide another indicator of the age. As the SN aged, forbidden emission lines became prominent while those lines arising from allowed transitions faded. The right-most panel of Figure 5.5 shows that the blue pseudocontinuum of SN 2006jc formed while the near-IR triplet of Ca II was strong, but the blue pseudocontinuum of SN 2015G did not become apparent until the near-IR triplet had faded and [Ca II] emission had become dominant (see also Figure 5.2). This enhanced blue

continuum is generally understood to arise via nonthermal excitation of iron via an ongoing shock as ejecta collide with CSM (e.g., Foley et al. 2007), and normal SNe Ib do not show it.

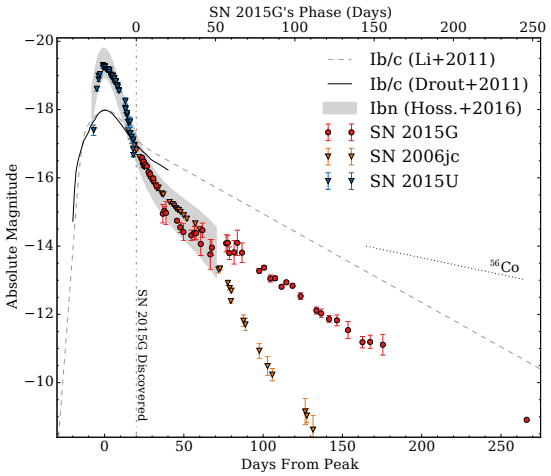

Figure 5.6: Absolute R-band light curve of SN 2015G, compared with absolute R light curves of SNe Ibn 2006jc (Foley et al. 2007; Maund et al. 2016) and 2015U (Shivvers et al. 2016). We compare to the template light curves of Li et al. (2011b, dashed line), Drout et al. (2011, solid line), and Hosseinzadeh et al. (2017, shaded region). We offset the SNe 2006jc and 2015G light curves so as to best match with the SN Ibn template, and we show the phase of SN 2015G relative to its discovery date on the top axis with the inferred phase relative to optical peak on the bottom axis. We also show the ^{56}Co $\rightarrow$ ^{56}Fe decline rate for comparison.

SN 2006jc, at extremely late phases, developed a red/near-IR continuum as dust formed in the shocked shell of material created by the SN ejecta's collision with the CSM (Smith et al. 2008; Sakon et al. 2009). This red continuum is apparent in the +96 d spectrum of SN 2006jc; our spectra of SN 2015G show that no such late-time red continuum formed in SN 2015G during our 6 months of spectroscopic follow-up observations.

Interestingly, Smith et al. (2008) identified transient He II λ4686 and N III $\lambda\lambda$4634, 4642 emission with the rise of the red hot dust continuum of SN 2006jc, tying these phenomena to observations of the colliding winds in η Carinae (Smith 2010). The middle and right panels of Figure 5.5 show that the same transient emission feature of ionized helium and nitrogen was temporarily present in SN 2015G but at a much earlier phase, and it does not appear to be associated with the formation of dust in this event. Perhaps dust was able to form behind the shock in the SN 2006jc system, but not in SN 2015G, because the interaction occured in SN 2006jc only after the equilibrium temperature had dropped substantially. The spectra of SN 2015G showing He II and N III emission still exhibit a best-fit blackbody temperature of $\sim$ 4000 K — likely too hot to allow any dust formation in the system at that phase.

Figure 5.6 shows the light curve of SN 2015G compared to template light curves for SNe Ib/c and Ibn (Li et al. 2011b; Drout et al. 2011; Hosseinzadeh et al. 2017) and to the light curves of SNe Ibn 2006jc and 2015U (Foley et al. 2007; Shivvers et al. 2016). The date of maximum brightness is unknown for both SNe 2006jc and 2015G; for this comparison we infer the dates of maximum for these two SNe by comparing their observed light curves to the template of Hosseinzadeh et al. (2017) while respecting the limits imposed by what constraints we have on their explosion dates. We estimate that SN 2006jc was discovered

some 6 d after peak and SN 2015G was discovered 20 d after peak.

The photometric evolution of SN 2015G is similar to that of other SNe Ibn (e.g., Pastorello et al. 2008a; Hosseinzadeh et al. 2017). Note, however, the steepening of SN 2006jc's R-band light curve around 75 d, likely caused by obscuration from a newly formed dust shell (Smith et al. 2008). In good agreement with our spectra, the light curve of SN 2015G shows no evidence for a forming dust shell at least out to $\sim$ 8 months after discovery. Instead, the SN's optical light curve continues to decline approximately linearly and slightly more rapidly than the ^{56}Co $\rightarrow$ ^{56}Fe decline rate, as do those of normal SNe Ib.

Very few SNe Ibn have been monitored out to such late phases, so it is difficult to know how common the formation of a dust shell is among these events. However, enough have been observed to note that they show remarkable similarities in their post-peak light curves and, like SN 2015G, most SNe Ibn are subluminous at late phases compared to normal stripped-envelope SNe (Hosseinzadeh et al. 2017). If the luminosity of SNe Ibn on the post-peak decline is driven by radioactive decay, as is the case for normal stripped-envelope SNe, this implies that a significantly smaller amount of ^{56}Ni is present in the ejecta of SNe Ibn than in those of normal SNe Ib/Ic.

5.3.3 Spectropolarimetry

Our spectropolarimetric observation of the young SN 2015G is shown in Figure 5.7. SN 2015G shows strong continuum polarization ($P \approx 2.7\%$), with some small but apparently significant variations across the strong He I line features.

It is possible that the continuum polarization level is substantially affected or perhaps even dominated by interstellar polarization (ISP) along the line of sight. The host galaxy's contribution to interstellar dust absorption is relatively low and the SN appears to be in a rather remote environment, so we do not expect the host ISP to be dominant. Nonetheless, the maximum polarization from the host could be up to 0.6% (following Serkowski et al. 1975), with an entirely unknown position angle. The larger MW dust absorption toward SN 2015G indicates that our Galaxy's ISP contribution could be as high as 2.9% (Serkowski et al. 1975). Indeed, SN 2015G is at a low Galactic latitude of 14.8°, and substantial Galactic cirrus is present in this region of the sky.

The MW ISP can be estimated by measuring the polarization of stars that (1) are along the line of sight toward the SN (ideally within 1°); (2) are suspected to have negligible intrinsic polarization (ideally spectral types A5 through F5; Leonard et al. 2002a); and (3) lie at sufficient distances such that all ISM along the line of sight and within a scale height of 150 pc above the Galactic disk is sampled. For the line of sight near SN 2015G this minimum required probe distance is 675 pc. Unfortunately, there are no stars in the literature of known spectral type with polarization measurements satisfying all of these criteria. Loosening these constraints to allow stars of any spectral types within 5°, we identify two stars in the catalog of Heiles (2000) — HD 197911 (B5 V; 1043 pc) and HD 198781 (B0.5 V; 712 pc) — which exhibit an average (1σ) polarization and position angle of 1.36% (0.03%) and 150° (16°). This position angle value is consistent with that measured for SN 2015G, while the level of

polarization is about half that of the SN. However, we are reluctant to trust these values as accurrate measures of the ISP because at least one of those stars (HD 197911) has been associated with a dusty interstellar bow shock that is likely to scatter the star's light and exhibit its own polarization (Peri et al. 2015). The existence of a star at that distance (well beyond the 675 pc limit we imposed above) with shocked ISM in its vicinity suggests that the scattering and polarizing effect of the ISM could extend to distances larger than expected in this region of the sky, and may be highly spatially variable.

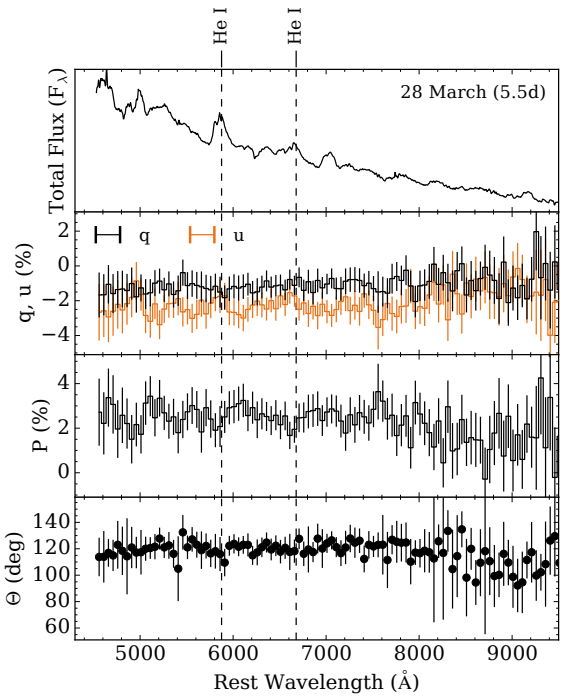

Figure 5.7: A single epoch of spectropolarimetry obtained 5.5 d after the discovery of SN 2015G. The top panel illustrates the total-flux spectrum smoothed with a 50 Å Gaussian kernel, while the middle panels show the Stokes parameters (q, u) and total polarization (P) binned to 50 Å, and the bottom panel gives the measured position angle, also binned to 50 Å.

To improve our census of the ISP, we obtained new Lick/Kast observations (on 2017 March 3) of two additional probe stars of known spectral types that have smaller angular separations, $< 2°$: BD 661309 (A5 V) exhibits $P_V = 0.22\,(0.01)\%$ and $\theta_V = 54.7°\,(1.0°)$, and HD 197344 (B8 V) exhibits $P_V = 0.22\,(0.01)\%$ and $\theta_V = 64.6°\,(1.2°)$. These stars have spectroscopic parallaxes that indicate distances of 525 and 575 pc, respectively — close to, but slightly below, the minimum suggested distance to effectively probe the bulk of intervening ISM. Nonetheless, the measured values are very low, which indicates that either the ISP is small near the SN's line of sight or that there is substantial ISP originating from greater distances than we are currently able to probe.

In conclusion, the complexity of the ISM in this region of the sky and the lack of excellent probe stars has proven problematic for our efforts to obtain a reliable estimate of the ISP toward SN 2015G. However, we note that none of the ISP estimates we have considered come close in strength to the very strong $\sim 2.7\%$ measured for the SN. It appears that, if the SN is not intrinsically polarized, then the ISP vector components of the MW and the host must be constructively interfering (i.e., have similar position angles, or at least be in similar quadrant of the $q-u$ plane) to give us such a strong polarization measure. For this reason, it seems plausible that the intrinsic polarization of the SN is significant and, therefore, that the electron-scattering photosphere of the explosion is substantially aspherical, consistent with the other proxies for explosion asymmetry we consider in this paper. Without better constraints on the ISP,

however, it is difficult to quantify the degree of asphericity.

5.3.4 The Ultraviolet Spectra

Figure 5.8 shows the full STIS UV+optical spectrum from day 13, rebinned and median-averaged in wavelength bins ~ 50 Å wide to increase the SNR and reduce the effects of cosmic rays. Continuum emission is detected from ~ 2300 Å out to $\sim 1\,\mu$m, overlain by the broad and narrow P-Cygni features described above. We find one emission line in the near-UV, labeled Mg II $\lambda\lambda$2796, 2803 in Figure 5.8. This feature is also observed in our spectrum from 11 April, but not in the spectrum from 20 April (at which point the continuum has faded below detectability at these wavelengths as well). Between the first two spectra it evolves from a wavelength of 2764 ± 2 Å to 2784 ± 6 Å (uncertainty estimated via MCMC fits of two Gaussian profiles separated by the spacing of this doublet, 7.16 Å). Assuming our line identification is correct, and that both lines of the doublet contribute equally to the line flux, this implies velocity blueshifts for this feature of about 3800 km s^{-1} and 1600 km s^{-1} on 4 and 11 April (respectively), so the slowdown is ~ 300 km s^{-1} d^{-1}. No other narrow emission lines in our dataset on SN 2015G show this sort of behaviour and we note that it is peculiar. However, the SNR is low in our UV spectra and, though inspection of the raw two-dimensional frames shows them to be clean with no obvious artifacts, we are hesitant to infer too much from this putative Mg II line.

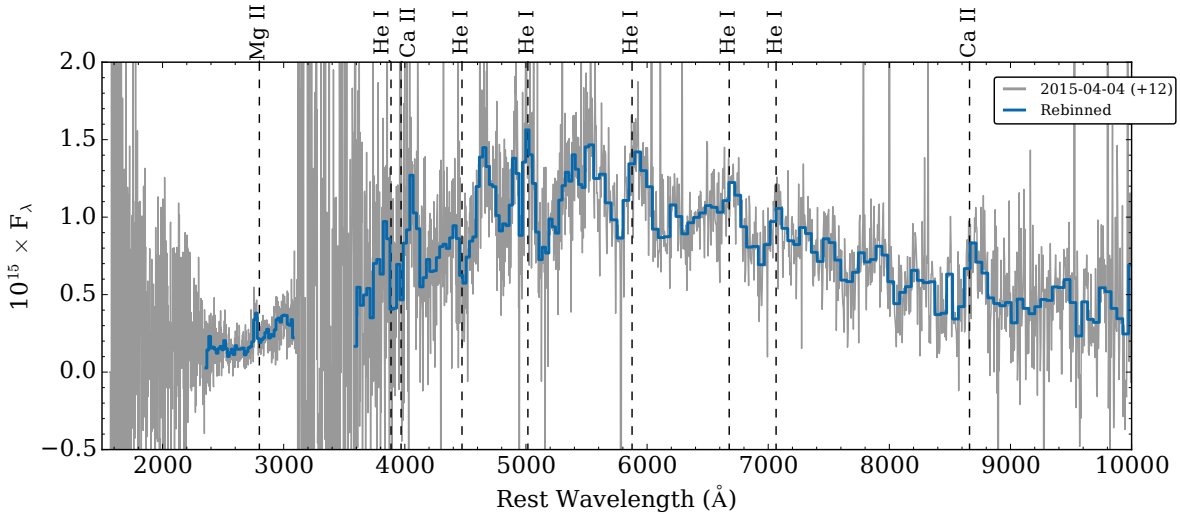

Figure 5.8: The UV through near-IR spectrum of SN 2015G, as observed by *HST*. Data have been corrected for dust absorption along the line of sight and are presented in the host galaxy's rest frame. The full spectrum is shown in grey and a rebinned spectrum with bins ~ 50 Å wide is shown in blue.

5.3.5 The Spectral Energy Distribution

Our observations of SN 2015G cover radio through UV wavelengths, and we are able to reconstruct a broad-wavelength spectral energy distribution (SED) at several phases. Figure 5.9 shows the UV through IR SED of SN 2015G as observed at 5 epochs between 12 d and 35 d after discovery. For the two phases at which we have IR photometry, we interpolate the optical light curves to the time of the IR observations using a Gaussian process regression. At the earlier epoch, the *Swift* satellite observed the location of SN 2015G nearly concurrently (within a few hours), and we plot the 3σ upper limits from the resulting UV nondetections. For the later epoch we plot the last UV nondetection from *Swift*, which was observed 5 d before the listed phase (when the optical+IR images were taken).

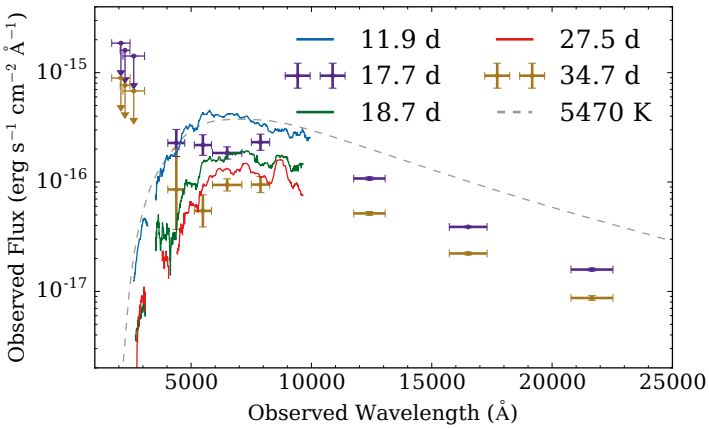

Figure 5.9: UV through IR observations of SN 2015G, including three UV-optical spectra observed by *HST*, which have been trimmed and smoothed with a wide (~ 500 Å) median box filter to illustrate the overall SED, alongside two epochs of UV–IR photometry. All data are shown in the observer frame, with no corrections for extinction applied. For comparison, a blackbody at 5470 K is shown in dashed grey, redshifted into the observer's frame and obscured by the dust populations described in §5.2.4. Phase (days) or $T_{\rm BB}$ (K) are given in the legend.

Our *HST* spectra strongly constrain the wavelength of peak flux, and we show a best-fit model blackbody spectrum in Figure 5.9, for comparison. Fitting a redshifted and dust-reddened blackbody (assuming the dust properties presented in §5.2.4) to the first *HST* spectrum, we find that the SED of SN 2015G is approximated quite well by a single-component blackbody with a temperature of $T_{\rm BB} \approx 5470 \pm 250$ K. Our uncertainties about the dust reddening arising within the host galaxy likely dominate our temperature errors, so we estimate the above error bars on $T_{\rm BB}$ by ranging $E(B-V)_{\rm host}$ from 0.0 mag to twice our best-guess value of 0.065 mag and refitting. For Figure 5.9 we have converted our photometric observations into flux units using PySynphot and the published filter curves for each instrument, assuming a 5470 K blackbody spectrum.

Between 12 d and 35 d after discovery, the SED qualitatively behaves like a cooling blackbody, fading in both temperature and luminosity. Our IR photometry argues for a steeper Rayleigh-Jeans tail than do our fits to the UV/optical peak, but (given our uncertainties

about the degree and wavelength dependence of the dust obscuration toward SN 2015G) we are hesitant to assign much significance to that discrepancy. We estimate the bolometric energy output of SN 2015G and the implied blackbody radius at 11.9 d after discovery, based upon our blackbody fit to the *HST* spectrum: $L \approx 10^{42}\,\mathrm{erg\,s^{-1}}$ and $R \approx 10^{15}\,\mathrm{cm}$.

5.3.6 Limits on Radio Luminosity

Radio emission from SNe predominantly arises via the synchrotron mechanism as the forward shock ploughs through the CSM. The narrow emission features in our early-time optical spectra provide clear evidence for a dense CSM near the progenitor at the time of core collapse. However, the density profile of the CSM at larger radii is quite uncertain, so the radio flux expected from the SN at intermediate and late phases is similarly uncertain. Though our attempts to observe radio emission SN 2015G yielded only upper limits, they do provide some interesting constraints on the extended CSM surrounding the SN.

We argue elsewhere in this paper that the dense CSM that made SN 2015G a SN Ibn was likely not created by wind-like mass loss from the progenitor, but rather was built up through one or more extreme mass-loss events $\lesssim$1 yr before core collapse. However, we find it plausible (in the absence of evidence to the contrary) to assume a history of more stable wind-like mass loss from the progenitor at earlier times before core collapse, as is normal for the progenitors of stripped-envelope SNe (e.g., Chevalier 1998; Kamble et al. 2014, 2016).

Our mid-phase spectra show broad lines with absorption edges falling at blueshifts of $\sim 8000\,\mathrm{km\,s^{-1}}$ (see Figure 5.4), placing a lower limit on the velocity of the forward shock ($v_{\mathrm{shock}} \gtrsim 8000\,\mathrm{km\,s^{-1}}$), while the narrow P-Cygni features in our early-time spectra have characteristic velocities of $1000\,\mathrm{km\,s^{-1}}$. We construct a simple model of the SN 2015G system by assuming a history of mass loss with $v_{wind} \approx 1000\,\mathrm{km\,s^{-1}}$ and adopting $v_{\mathrm{shock}} = 10,000\,\mathrm{km\,s^{-1}}$. We further estimate that the SN took ~ 5 d to rise to maximum (SN 2015G's rise time is effectively unconstrained, but other SNe Ibn for which the rise has been observed exhibit values of ~ 5 d; Hosseinzadeh et al. 2017), giving a best-guess date of explosion of 2015-02-27. Our naive blackbody model from §5.3.5 showed that our data are described rather well by a cooling blackbody of $R \approx 10^{15}$ cm. If we take this value to be the outer extent of the low-radii dense CSM, the forward shock would have taken ~ 10 d to traverse this inner CSM and emerge into the hypothesised larger-radii, lower-density CSM. If this scenario is correct, our radio observations at 36, 76, and 148 d after explosion should therefore probe ongoing CSM interaction between the fastest-moving ejecta and material lost from the star around 1, 2, and 4 yr before explosion, respectively.

Following Kamble et al. (2014) and Kamble et al. (2016), we adopt the models of Chevalier (1998) to describe the radio flux from SN 2015G at the observed epochs, assuming that the radial density profile of the CSM goes as $\rho \propto r^{-2}$ at large radii. We parameterise the energy distribution of the shocked electrons as a power law in the electron Lorentz factor with index p, $n_e(\gamma_e) \propto \gamma_e^{-p}$; we assume that the fractional energy densities in the relativistic electrons and in the magnetic field are equivalent (i.e., the shocked material is in equipartition), $\epsilon_e = \epsilon_B$; and we assume that $\epsilon_e = 0.1$. These models include both the effects of synchrotron

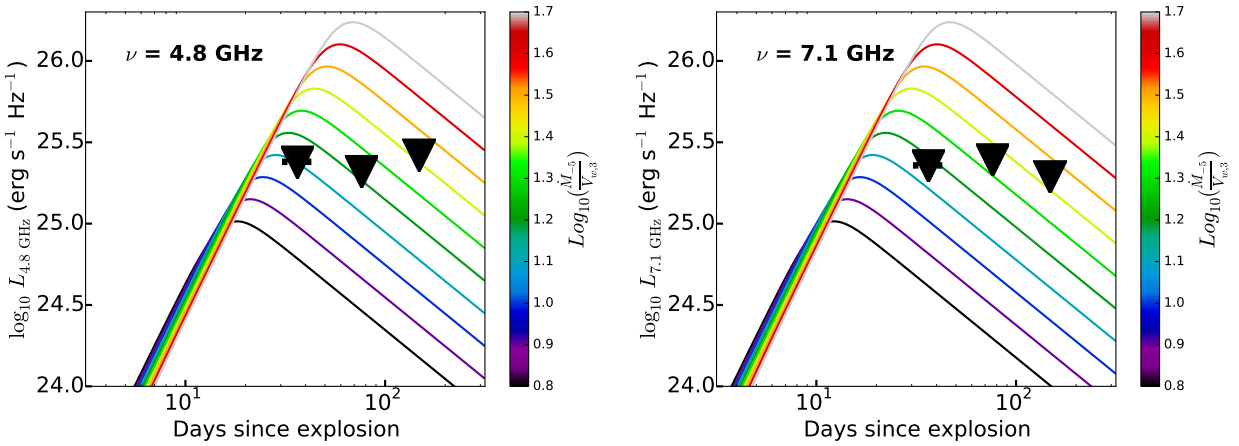

Figure 5.10: Our 3σ nondetections of SN 2015G at 4.8 and 7.1 GHz, plotted against modeled light curves assuming a range of values for the wind parameter. These models were constructed assuming $v_{\rm shock} = 10,000\,{\rm km\,s^{-1}}$and $v_{\rm wind} = 1000\,{\rm km\,s^{-1}}$. We adopt an explosion date of 57080 MJD, and we show horizontal error bars of ± 5 d to illustrate our uncertainty about the exact date of explosion (the plotted data points are often wider than those error bars).

self-absorption and free-free absorption from the CSM.

In Figure 5.10 we plot our 3σ nondetections against modeled radio light curves assuming $v_{\rm wind} = 1000\,{\rm km\,s^{-1}}$ and $v_{\rm shock} = 10,000\,{\rm km\,s^{-1}}$. We show models for a range of values for the wind parameter, $10^{0.8} \leq A_* \leq 10^{1.7}$, where

$$A_* \equiv \frac{\dot{M}/10^{-5}\,{\rm M_\odot\,yr^{-1}}}{v_{\rm wind}/10^{3}\,{\rm km\,s^{-1}}}$$

Our first epoch of observations produces the strongest constraint on the wind mass-loss rate from SN 2015G's progenitor: $\dot{M} \lesssim 1 \times 10^{-4}\,M_\odot\,yr^{-1}$. Assuming a slower wind velocity produces a more stringent constraint (we find $\dot{M} \lesssim 10^{-5}\,{\rm M_\odot\,yr^{-1}}$ if $v_{\rm wind} = 100\,{\rm km\,s^{-1}}$), while assuming a slower shock velocity relaxes the constraint (we find $\dot{M} \lesssim 10^{-3}\,{\rm M_\odot\,yr^{-1}}$ if $v_{\rm shock} = 5000\,{\rm km\,s^{-1}}$).

Radio emission from SNe Ibn is still uncharted territory, and it is difficult to know whether the assumptions (and therefore the models) outlined above are fully appropriate. Similar assumptions have been shown to be reasonable for stripped-envelope SNe with detected radio light curves, but the diversity of radio signatures found for these events is remarkable, especially among the SNe with evidence for unsteady pre-explosion mass loss from their progenitor. See, for example, PTF 11qcj, a radio-bright SN Ic that may have had a SN 2006jc-like outburst from its progenitor ~ 2 yr before core collapse (Corsi et al. 2014), or SN 2014C, a SN Ib that began to interact with an H-rich dense shell a year after explosion and showed extreme variability in its radio light curve (Margutti et al. 2017).

Our radio flux limits and the resultant CSM density limits shown in Figure 5.10 are surprising, given the strong signatures of a dense CSM at low radii — SNe Ib/c with radio detections generally have peak luminosities in the range 10^{26}–10^{28} erg s^{-1} Hz^{-1} at these frequencies (e.g., Soderberg 2007). If the CSM around SN 2015G had a structured density profile at large radii, perhaps with shells of material created by episodes of eruptive mass loss rather than the steady wind-driven profile we model above, the radio emission powered by ongoing interaction could be entirely obscured via free-free absorption within the CSM exterior to the shock. Type IIn SNe in very dense environments, for example, sometimes exhibit radio light curves with rise times of ~ 1000 d because of this effect (e.g., Chandra et al. 2012, 2015). These SNe sustain the optical signatures of ongoing interaction, however, while SN 2015G's narrow spectral features disappear and its interaction-powered optical brightness fades away — differences which argue that the radial profile of the CSM surrounding SN 2015G must be quite dissimilar from the (relatively) smooth density profiles inferred for the SNe IIn above. A further worry is that our models do not account for any CSM clumpiness or global asymmetry, though our optical observations argue that the SN 2015G system is strongly asymmetric. Without clear detections and lacking a true radio light curve, many uncertainties remain.

5.3.7 Progenitor Constraints

SN 2015G is the nearest known SN Ibn to date, and as such it provides us a unique opportunity to study the progenitor star and local environment for a member of this rare subclass. A preliminary search for the progenitor in the *HST*/WFPC2 images from 2001 was presented by Maoz & Poznanski (2015). They established the SN position in these archival pre-SN data using a ground-based I-band image and did not detect a progenitor candidate there. Neglecting any extinction within the host galaxy, they estimate upper limits on the luminosity of a progenitor at $M_I > -6.4$ mag and $M_V > -7.1$ mag.

We initially used our *HST* Target of Opportunity (ToO) WFC3 images from GO-13683 to provide a better position for the SN in the 2001 WFPC2 *F555W* data. However, since the individual frame times for the ToO observations were only 10 s each (for a total of 240 s) and we observed in subarray mode, there were only 7 stars in common between the two image datasets. Consequently, we could only register the images with a 1σ uncertainty of 0.61 WF pixel (the SN site is on the WF2 chip of the WFPC2 array). We therefore registered the pre-SN images to the much deeper WFC3 full-array data from GO-14149 (total exposure times of 780 s in *F555W*, 710 s in *F814W*). We found 30 star-like objects in common between the images and were able to achieve an astrometric registration that was somewhat better, with a 1σ uncertainty of 0.38 WF pixel. We note that the positions for the SN in the pre-SN data estimated from the two different WFC3 image sets agree to 0.49 pixel. We also do not see a progenitor candidate at this position, nor does `DOLPHOT` detect any object there. In Figure 5.11 we present the *HST*/WFC3 image of SN 2015G from November 2015, a close-up view of the SN and its local environment, and a close-up view of the progenitor nondetection from 2001 (all in the *F814W* band).

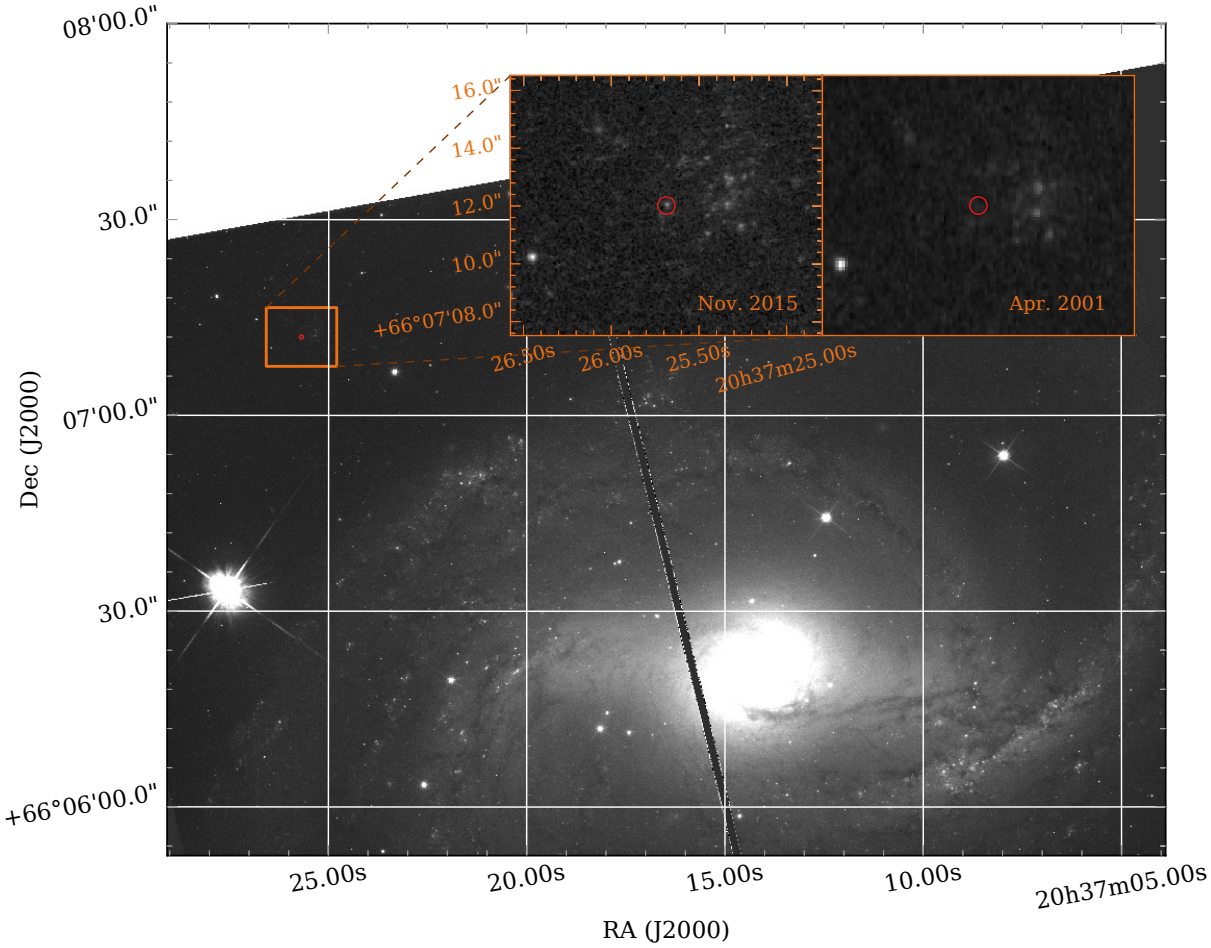

Figure 5.11: *HST* image of SN 2015G taken ~ 8 months after discovery and a pre-explosion image of the SN site from 2001, both observed through the *F814W* filter. The main frame shows the large offset between SN 2015G and its host, while the two inset frames display close-up views of the fading SN (left) and the pre-explosion progenitor nondetection (right). We indicate the location of the SN with a red circle 0.3″ in diameter (larger than our 3σ uncertainty in the SN location).

As Figure 5.11 shows, SN 2015G exploded far from the bulk of the stellar mass in NGC 6951 and far from the major star-forming regions. As noted by Maoz & Poznanski (2015), however, there is a small but conspicuous clump of bright and blue stars near that location. The centre of this clump is $\sim 2''$ west of SN 2015G, a distance of ~ 200 pc. Most of the stars in the clump are within ~ 100 pc of the centre — if SN 2015G's progenitor formed as a part of this clump, it appears to have traveled an appreciable distance from its birthplace. Alternatively, the progenitor may have formed within a smaller stellar subgroup,

possibly at a different time.

Our final spectrum of SN 2015G was observed with this cluster along the slit, and a narrow H I line arising from this small star-forming region was detected. The redshift as measured from this emission line is in good agreement with the published redshift of the host galaxy, with an observed wavelength of 6592.33 ± 0.06 Å (as measured via maximum-likelihood MCMC fitting, assuming a Gaussian line profile). This implies a redshift of 0.00450, or a line-of-sight velocity within $100\,\mathrm{km\,s^{-1}}$ of that of NGC 6951.

We attempted artificial-star tests with `DOLPHOT` on the images from 2001, injecting an artificial star at the exact SN position, and found the following nondetection upper limits: $F555W \gtrsim 26.7$ mag and $F814w \gtrsim 25.4$ mag. These are consistent with the formal 3σ source detections by `DOLPHOT` at the SN's location, and they translate into absolute upper limits of $\mathrm{M}_{F555W} \gtrsim -6.4$ mag and $\mathrm{M}_{F814W} \gtrsim -7.1$ mag. These limits are essentially the same as those found by Maoz & Poznanski (2015), though their assumptions of the distance and reddening to the SN differed from ours.

Assuming the progenitor of SN 2015G was a single supergiant, and that it exploded at the terminus of its evolutionary track as something other than a hydrogen-rich supergiant, we compared our detection upper limits with the MESA Isochrones and Stellar Tracks (MIST; Paxton et al. 2011, 2013, 2015; Choi et al. 2016) at solar and slightly subsolar ([Fe/H] $= -0.25$) metallicities, adjusted for the distance and reddening to SN 2015G as described above. We find the following limits on the zero-age main sequence mass by comparison with our $F555W$ limit (the more constraining of the two): $M_0 \lesssim 18\,\mathrm{M}_\odot$ (solar) and $M_0 \lesssim 20\,\mathrm{M}_\odot$ (subsolar). These limits effectively rule out a single massive ($M_0 \gtrsim 30\,\mathrm{M}_\odot$) Wolf-Rayet star progenitor (assuming that the luminosity at the time of collapse is similar to the luminosities observed for Wolf-Rayet stars in the MW). Comparisons, instead, with the interacting binary models of Kim et al. (2015) show that some configurations are disallowed by our upper limits but a variety of possible binary models remain viable. Note that *HST* images of the field were obtained in 1994 through the *F218W* and *F547M* filters, but they do not provide deeper constraints.

Maund et al. (2016) have recently reported the likely detection of a binary companion to the progenitor of SN 2006jc in *HST* images obtained 4 yr after the SN explosion. The pre-explosion upper limits we find for the progenitor system of SN 2015G are marginally consistent with a similarly luminous source, depending upon the assumed properties of the extinction along the line of sight within the host galaxy.

We also considered the stellar environment of SN 2015G to constrain the properties of the progenitor. We analyzed objects within a 43-pixel (~ 200 pc) radius of the SN detected by `DOLPHOT` in the WFC3 *F555W* and *F814W* images from GO-14149 that had a `DOLPHOT` object type of "1" (i.e., star-like). The resulting colour-magnitude diagram is shown in Figure 5.12. We again compared the stellar photometry to the MIST tracks and found that, assuming that the population of stars in this region are coeval and that the SN progenitor itself was not rejuvenated in its evolution as a result of binary interaction, the highest initial mass the progenitor star could have had was $\sim 18\,\mathrm{M}_\odot$, consistent with the upper limits calculated from our progenitor nondetection.

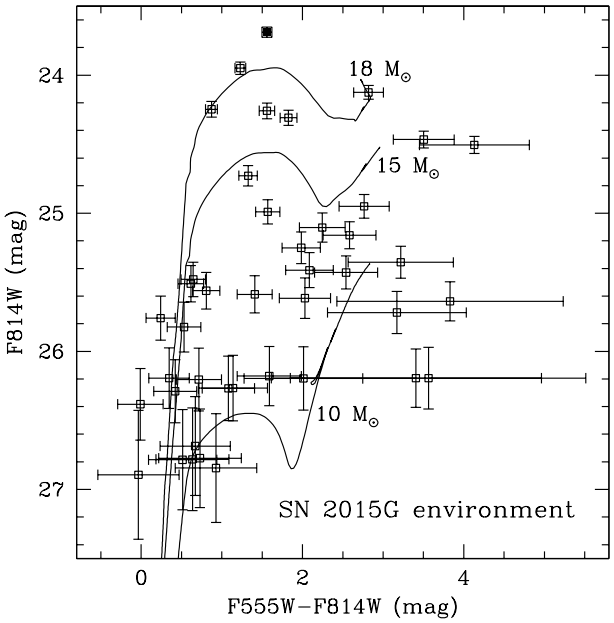

Figure 5.12: Colour-magnitude diagram of star-like objects (open squares) detected by DOLPHOT within a 43-pixel ($\sim$ 200 pc) radius of SN 2015G's position in *HST*/WFC3 images obtained in 2015 by program GO-14149. The SN itself is shown as a filled square. For comparison we plot MIST stellar evolutionary tracks at slightly subsolar ([Fe/H] = -0.25) metallicity and initial masses of 10, 15, and 18 $M_\odot$, adjusted to the assumed distance and reddening of SN 2015G.

Comparing our Figure 5.11 to Figure 1 of Maund et al. (2016), we note the remarkable similarity between SN 2006jc's local environment and that of SN 2015G: both SNe exploded in sparse areas of their hosts near clumps of young, massive stars but offset from them by $\gtrsim$ 100 pc. The Type IIn SN 2009ip was also quite isolated (Smith et al. 2016), and Smith & Tombleson (2015) show that luminous blue variables (LBVs) in the MW, often proposed to be Galactic analogues for the progenitors of strongly interacting SNe, are as well. They interpret the isolation of LBVs as evidence that they are mass gainers in binary pairs which get rejuvenated by mass exchange and receive a kick when their (more massive) companion explodes, allowing them to travel far from their birth sites before their own deaths (note that these results are under some debate; e.g., Humphreys et al. 2016).

The presence of a dense CSM surrounding SN 2015G suggests a recent history of extreme mass loss from, and therefore variability of, the progenitor star. An LBV-like bright outburst from SN Ibn 2006jc's progenitor was observed some 2 yr before the SN itself ($M_r \approx -14.1$ mag; Nakano et al. 2006; Foley et al. 2007; Pastorello et al. 2007). There have also been a few SN IIn progenitors detected in outburst in the years prior to core collapse (e.g., Mauerhan et al. 2013b; Margutti et al. 2014; Smith 2014; Ofek et al. 2014), though similar outbursts have, in other cases, been ruled out (e.g., Bilinski et al. 2015). KAIT has been monitoring NGC 6951 for almost 20 yr and we searched this extensive dataset for evidence of pre-explosion variability.

Examining 1248 unfiltered images taken between 1998 and 2015 with detectability thresholds deeper than 17.0 mag, we find no detections at the SN location and no evidence for previous outbursts of the progenitor brighter than -13.3 ± 0.5 mag (median and standard deviation of the detection thresholds among all images). Figure 5.13 plots our 1σ non-detections and the observed light curve of SN 2015G, with the luminosity of SN 2006jc's

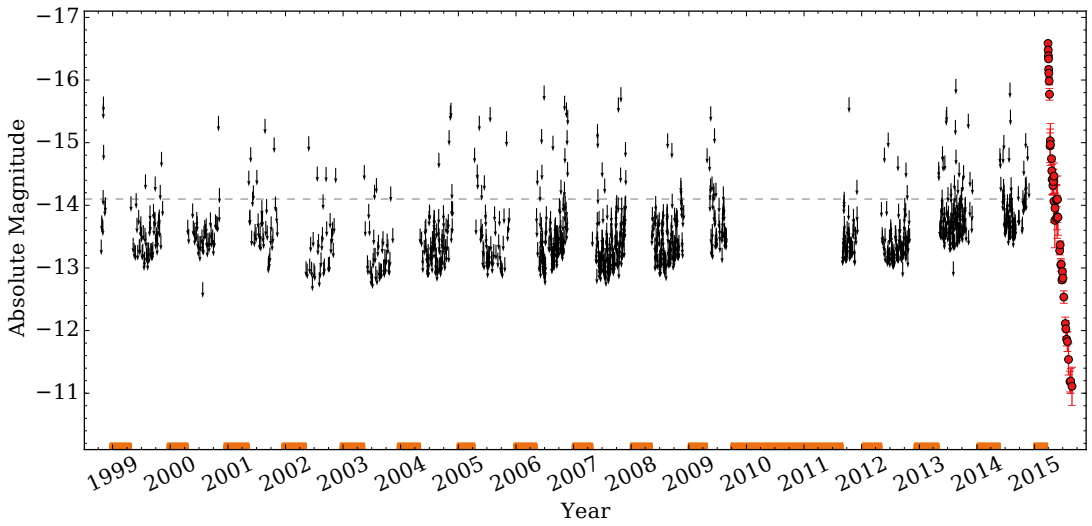

Figure 5.13: Our 1σ pre-explosion nondetections from KAIT unfiltered images. The R-band light curve of SN 2015G is shown at the far right. Timespans for which no upper limit had been obtained for at least 1 month are marked in orange along the bottom, and a dashed line indicates the absolute magnitude of SN 2006jc's pre-explosion outburst (Foley et al. 2007).

pre-explosion outburst indicated for comparison. (The *HST* nondetections described above provide additional extremely strong constraints in 2001 May, off the bottom of the scale of Figure 5.13.) The SN field was inaccessible to our telescopes for several months every year, so there are significant gaps; the orange bars along the bottom of Figure 5.13 mark every night on which more than 1 month had passed since the previous upper limit. Approximately 45% of the nights between October 1998 and the SN discovery in March 2015 fall into such a gap.

Though these observations rule out any long-lasting luminous outbursts in the last 20 yr, the outburst from SN 2006jc's progenitor was observed to fade rapidly after discovery ($\sim 0.16\,\mathrm{mag\,d^{-1}}$ over the 9 d it was detected, Pastorello et al. 2007); thus, our nondetections argue neither for nor strongly against a SN 2006jc-like outburst from SN 2015G's progenitor (Nakano et al. 2006; Pastorello et al. 2007).

5.3.8 A Rough Schematic of the SN 2015G System

Based upon the above observations, we interpret SN 2015G to be a Type Ib SN explosion modified by additional luminosity arising via the collision between explosive ejecta and dense CSM, with the collision between SN ejecta and the CSM converting the kinetic energy of the ejecta into radiative luminosity (e.g., Chugai & Danziger 1994; Chevalier & Fransson 1994; Chevalier & Irwin 2011).

The luminous yet rapidly fading light-curve peak settles into a slower decline rate, while

either ongoing (weaker) interaction or a (relatively small amount of) radioactive material powers the luminosity of the late-time light-curve tail. Our spectroscopic monitoring of SN 2015G began after shock breakout and peak luminosity, and the early-time spectra of the event show a cooling blue continuum topped by relatively broad emission lines (arising from the ejecta and perhaps the shocked and accelerated CSM) and narrow P-Cygni lines (arising from the unshocked and extended CSM at larger radii which has been ionized by the shock breakout). The spectral lines at early phases are centred at a velocity of $0\,\mathrm{km\,s^{-1}}$, and therefore the CSM in which these early lines formed likely exhibited a range of velocity vectors more or less symmetrically distributed around the progenitor.

These narrow P-Cygni features disappeared from our spectra $\sim 10\,\mathrm{d}$ after the discovery of SN 2015G, or $\sim 35\,\mathrm{d}$ after our roughly estimated explosion date. Coupled with our radio nondetections (the first of which was observed 36 d post-explosion), this argues that the dense CSM was predominantly located at small radii and was therefore likely lost from the surface of the progenitor in the last year or so before core collapse.

As the light curve settles into its late-time decline rate, the broader features transition from pure emission into a P-Cygni profile, likely arising from some mixture of the swept-up CSM and the ejecta. The light curve then continues to decline steadily as the continuum, and therefore the absorption features, fade away. As the ejecta and accelerated CSM continue to expand and the density drops, forbidden emission lines become prominent. The evolution of all emission lines redward argues that the line flux at late times arises predominantly within receding material, unlike the early emission-line flux.

Whether ongoing weak CSM interaction or a relatively small amount of ^{56}Ni powers the late-time light curves of SNe Ibn is still a difficult question. SN 2015G's late-time decline at redder wavelengths (the *I* and *F814W* passbands) appears to be very similar to that at bluer wavelengths (*V* and *F555W*), arguing that the blue pseudocontinuum and the (mostly red) emission lines are powered by the same process. The blue pseudocontinuum is generally understood to be powered via CSM interaction, and so this argues that the line emission also arises from CSM interaction.

In contrast, the linear decline of the late-time light curve and the homogeneity of light-curve shapes among SNe Ibn argue for the radioactively powered interpretation. If SN Ibn light curves are interaction-powered on the tail, the diversity of late-time light-curve properties should reflect the diversity of CSM configurations around the progenitors; it would be surprising if these CSM configurations (and therefore the progenitor pre-explosion mass-loss histories) were so similar across different SNe (e.g., Pastorello et al. 2008a; Hosseinzadeh et al. 2017). The light curves of SNe IIn (which assuredly are powered largely by interaction) are very heterogeneous, as expected (e.g., Kiewe et al. 2012), though comparisons with hydrogen-rich SNe must be made with caution; the lack of hydrogen in SNe Ibn may force the continuum opacity significantly lower. Note that the late-time luminosities of SNe Ibn are low compared to those of normal SNe Ib/Ic — if they are radioactively powered at late times, it seems they must produce a relatively small amount of ^{56}Ni.

The systemic redshift of the Ca II and He I lines implies a severe (and peculiar) asymmetry of the system, likely due to an asymmetry of the CSM with which SN 2015G's ejecta

are interacting at these phases (assuming these lines are interaction-powered). However, we do observe some polarization intrinsic to SN 2015G at early times, and a less-than-spherical explosion itself may also be playing a role. Not only are asymmetric geometries often invoked to understand the observed properties of core-collapse SNe (e.g., Mazzali et al. 2005; Maeda et al. 2008; Modjaz et al. 2008a; Taubenberger et al. 2009; Milisavljevic et al. 2010), but both the analysis of some SN remnants and the results of modern 2- and 3-dimensional modeling efforts of the core-collapse mechanism itself argue that asymmetric (sometimes unipolar) explosions are possible and may even be common.

The Puppis A SN remnant (Petre et al. 1996), for example, shows a compact neutron-star remnant with a systemic velocity of some $1000\,\mathrm{km\,s^{-1}}$ along a vector opposite that of the bulk ejecta velocity, arguing that the neutron star received a substantive kick from the core-collapse event and that the ejecta received a similar kick in the opposite direction. Explosion asymmetries of lesser degree have also been observed (e.g., the so-called "Bochum" event of SN 1987A; Phillips & Heathcote 1989). From the modeling side, several teams have shown that low-order spherical harmonics of the exploding core may well manifest themselves in large-scale asymmetries of the explosion (e.g., Suwa et al. 2010; Hanke et al. 2012; Couch & Ott 2014; Couch & O'Connor 2014).

5.4 Conclusion

SN 2015G, which exploded in NGC 6951 at a distance of 23.2 Mpc, is the nearest known SN Ibn to date. Though it was discovered after peak brightness, we have been able to accrue a remarkable dataset on this event, making it one of the best-studied SNe of this rare type and highlighting both strong similarities with and differences from the archetypical SN Ibn 2006jc.

Hosseinzadeh et al. (2017) argue for two spectroscopically defined subclasses of SNe Ibn, but our observations of SN 2015G show that it exhibited properties of both proposed subclasses. Rather than two physically distinct subclasses, perhaps a continuum of CSM properties surrounding the SN produces a continuum of spectroscopic properties; this question should be investigated further as more SNe Ibn are identified and studied.

Archival *HST* images of the resolved SN explosion site argue against a single massive WR-like progenitor for SN 2015G. Given the recent likely detection of a binary companion to SN 2006jc's progenitor, the isolation of SN 2015G's explosion site and the well-determined position of the SN in multiple *HST* images makes SN 2015G an excellent candidate for a similar study in the future.

Extreme mass loss from the progenitor of SN 2015G occurred soon ($\sim 1\,\mathrm{yr}$) before core collapse, and the SN 2015G system was asymmetric. Asymmetries in stripped-envelope SNe are common, but the degree of asymmetry shown by the late-time spectra of SN 2015G has not been observed in a SN Ibn before now. A dedicated effort to obtain more high-resolution spectra and better late-time coverage of SNe Ibn is called for to understand whether severe asymmetry is characteristic of SNe Ibn or a unique trait of the SN 2015G system.

Chapter 6

Revisiting the Lick Observatory Supernova Search Volume-Limited Sample: Updated Classifications and Revised Stripped-Envelope Supernova Fractions

First published in the Proceedings of the Astronomy Society of the Pacific: Shivvers et al. (2017a).
Co-Authors: Maryam Modjaz, WeiKang Zheng, Yuqian Liu, Alexei V. Filippenko, Jeffrey M. Silverman, Thomas Matheson, Andrea Pastorello, Or Graur, Ryan J. Foley, Ryan Chornock, Nathan Smith, Jesse Leaman, Stefano Benetti

Chapter Abstract

We re-examine the classifications of supernovae (SNe) presented in the Lick Observatory Supernova Search (LOSS) volume-limited sample with a focus on the stripped-envelope SNe. The LOSS volume-limited sample, presented by Leaman et al. (2011) and Li et al. (2011b), was calibrated to provide meaningful measurements of SN rates in the local universe; the results presented therein continue to be used for comparisons to theoretical and modeling efforts. Many of the objects from the LOSS sample were originally classified based upon only a small subset of the data now available, however, and recent studies have both updated some subtype distinctions and improved our ability to perform robust classifications, especially for stripped-envelope SNe. We re-examine the spectroscopic classifications of all events in the LOSS volume-limited sample (180 SNe and SN impostors) and update them if necessary. We discuss the populations of rare objects in our sample including broad-lined Type Ic SNe, Ca-rich SNe, SN 1987A-like events (we identify SN 2005io as SN 1987A-like here for the

first time), and peculiar subtypes. The relative fractions of Type Ia SNe, Type II SNe, and stripped-envelope SNe in the local universe are not affected, but those of some subtypes have changed due to this analysis. Most significantly, after discussing the often unclear boundary between SNe Ib and Ic when only noisy spectra are available, we find a higher SN Ib fraction and a lower SN Ic fraction than calculated by Li et al. (2011b): spectroscopically normal SNe Ib occur in the local universe 1.7 ± 0.9 times more often than do normal SNe Ic.

6.1 Introduction

The Lick Observatory Supernova Search (LOSS) has been a long-running project at the University of California, Berkeley, using the Katzman Automatic Imaging Telescope at Lick Observatory (KAIT; e.g., Li et al. 2000; Filippenko et al. 2001b; Filippenko 2003, 2005), with many spectroscopic follow-up observations obtained with the 3 m Shane telescope at Lick and the 10 m telescopes at Keck Observatory. LOSS/KAIT has been discovering and observing SNe since first light in 1996; these data have contributed to several PhD theses and formed the foundation of many research projects on SNe. A detailed examination of the relative rates of nearby SNe was one of those projects, and was published as a series of papers in 2011 (Leaman et al. 2011; Li et al. 2011a,b; Maoz et al. 2011; Smith et al. 2011b). The second of these, Li et al. (2011b, L11 hereafter), presents a sample of 180 events that occurred within 80 Mpc (for Type Ia SNe) or 60 Mpc (for core-collapse SNe), all of which were spectroscopically classified (the classes of SNe are differentiated primarily via spectroscopy; e.g., Filippenko 1997). Most SN classifications from this time period were performed via visual inspection and comparisons with spectra of a few SNe of well-understood types and subtypes.

Over time we have found that a small fraction of the objects in L11 deserve reclassification; in some cases this is because the original classifications were made using only a subset of the now-available data on the objects, while in other cases our more modern classification methods are less prone to errors than the methods used at the time of classification. Independent of data quality or cadence, there is a history of debate in the literature over the exact distinction (if any) between SNe Ib and SNe Ic and whether transitional events showing weak helium lines exist (e.g., Filippenko et al. 1990a; Wheeler & Harkness 1990; Wheeler et al. 1994; Clocchiatti et al. 1996; Matheson et al. 2001; Branch et al. 2006).

The results of recent efforts by Liu & Modjaz (2014), Modjaz et al. (2014), and Liu et al. (2016) argue that the distinction between SNe Ib and SNe Ic is useful, and they offer a clearly defined scheme for discriminating between them alongside updated software tools to perform those classifications in a repeatable manner. Modjaz et al. (2014) identify as SNe Ib all events with detections of both the He I λ6678 and He I λ7065 lines at phases between maximum light and $\sim$50 days post-maximum, regardless of line strengths (the stronger He I λ5876 line is also present, but overlaps with Na I). They find that at least one good spectrum observed at these phases is necessary and sufficient to detect the helium lines, which are often absent at pre-maximum and nebular phases even for helium-rich events. Using this classification

scheme, they find evidence for a transitional population of "weak helium" SNe Ib (Valenti et al. 2011; Modjaz et al. 2014; Liu et al. 2016).

Clarifying the distinction between SNe Ib and SNe Ic is important given the surprising ratio of population fractions for these subtypes found by LOSS (SNe Ic/SNe Ib = $14.9^{+4.2}_{-3.8}\%/7.1^{+3.1}_{-2.6}\%$; Smith et al. 2011b), which has proven difficult to reproduce with stellar modeling efforts (e.g., Georgy et al. 2009; Yoon et al. 2010; Yoon 2015), though see also Groh et al. (2013a). Modjaz et al. (2014) show that a subset of the objects originally labeled SNe Ic in their sample in fact do qualify for the SN Ib label according to the definition above, and so they relabel these events as SNe Ib (see their discussion of all such cases, in their §4.2).

For some of those SNe, the spectra that were used to classify them and thus announce their types were obtained before the helium lines became prominent; for some, applying proper telluric corrections made the He I λ6678 or λ7065 lines more apparent; for others the spectra show clear helium but the exact division between SNe Ib and SNe Ic was under debate in the literature at the time of classification (e.g., SN 1990U; Filippenko et al. 1990b; Filippenko & Shields 1990; Matheson et al. 2001). We explore these issues within the LOSS sample and also find that some events with helium lines were systematically labeled as SNe Ic — we update the classifications for these events and recalculate the relative fractions of core-collapse events.

In this article we re-examine the classifications of the 180 events in the volume-limited sample of L11 and we make public all spectra of them we have been able to locate. This work was performed in conjunction with Graur et al. (2017a,b), who re-examine correlations between SN rates and galaxy properties. Note that much of the spectroscopy discussed herein has already been described in the literature and made publicly available by, for example, Silverman et al. (2012, SNe Ia), Faran et al. (2014a,b, SNe II), Matheson et al. (2001, SNe IIb/Ib/Ic). We collect these spectra, light curves obtained by LOSS, as-yet unpublished spectra from our archives, and as-yet unpublished spectra contributed from other SN research groups' archives, and analyze the complete set.

We present 151 newly published spectra of 71 SNe and 20 rereduced KAIT light curves. In §6.2 we describe these data, in §6.3 we detail our methods for classification, in §6.4 we present all updated classifications and discuss notable events within the sample, in §6.5 we calculate updated core-collapse SN rates in the local universe, in §6.6 we discuss the implications these updates have for our understanding of the progenitors of stripped-envelope SNe, and in §6.7 we conclude.

6.2 Data

Spectra were collected from our own UC Berkeley Supernova Database (UCB SNDB; Silverman et al. 2012),[1] from the literature, and from WISeREP (the Weizmann Interactive

[1]The SNDB was updated in 2015 and is available online at http://heracles.astro.berkeley.edu/sndb/.

Supernova Data REPository; Yaron & Gal-Yam 2012).[2] We do not include any results from spectropolarimetric or nonoptical observations; we know of no such observations that would help for the few events we cannot robustly classify using optical data. We made an effort to track down as-yet unpublished spectra for all objects with sparse or no spectral data in our database or in the public domain. All objects in this sample were classified in the Central Bureau of Electronic Telegrams (CBETs), and we contacted original authors to request data whenever possible. Contributions were made by the Center for Astrophysics (CfA) SN group (Matheson et al. 2008),[3] the Padova-Asiago SN group (Tomasella et al. 2014),[4] the Carnegie Supernova Project (CSP; Hamuy et al. 2006),[5] and the National Astronomical Observatories, Chinese Academy of Sciences (NAOC) SN group (Qui et al. 1999; Li et al. 1999).

We publish spectra from the following observatories and instruments:

- the Kast double spectrograph (Miller & Stone 1993) mounted on the Shane 3 m telescope at Lick Observatory;
- the Low Resolution Imaging Spectrometer (LRIS; Oke et al. 1995) and the Echellette Spectrograph and Imager (ESI; Sheinis et al. 2002) on the 10 m Keck I & II telescopes at Keck Observatory;
- the FAST spectrograph (Fabricant et al. 1998) on the Tillinghast 60 inch telescope and the Blue Channel spectrograph (Schmidt et al. 1989) on the 6.5 m Multiple Mirror Telescope (MMT) at the Fred Lawrence Whipple Observatory (FLWO);
- the European Southern Observatory (ESO) Faint Object Spectrograph and Camera (EFOSC; Buzzoni et al. 1984) on the ESO 3.6 m telescope, the Danish Faint Object Spectrograph and Camera (DFOSC, modeled after EFOSC; Andersen et al. 1995) on the Danish 1.54 m telescope, and the ESO Multi-Mode Instrument in medium resolution spectroscopy mode (EMMI; Dekker et al. 1986) on the ESO 3.58 m New Technology Telescope, all at La Silla Observatory;
- the Asiago Faint Object Spectrograph and Camera (AFOSC, modeled after EFOSC) on the 1.82 m Copernico telescope and the Boller and Chivens spectrograph (B&C$_{1.2}$) on the 1.2 m Galileo telescope at Asiago Observatory;
- the Boller and Chivens spectrograph (B&C$_{2.5}$) and the Wide Field Reimaging CCD Camera in long-slit spectroscopy mode (WFCCD, described by Hamuy et al. 2006) on the 2.5 m du Pont telescope and the Low Dispersion Survey Spectrograph (LDSS-2; Allington-Smith et al. 1994) on the 6.5 m Magellan Clay telescope at Las Campanas Observatory;

[2] http://wiserep.weizmann.ac.il/
[3] https://www.cfa.harvard.edu/supernova/
[4] http://sngroup.oapd.inaf.it/
[5] http://csp.obs.carnegiescience.edu/

- and the Optomechanics Research, Inc.[6] spectrograph (OMR) mounted on the NAOC 2.16 m telescope at Xinglong Observatory near Beijing, China.

Details of the spectral reduction pipeline used by the UCB team are described by Silverman et al. (2012). Matheson et al. (2008), Blondin et al. (2012), and Modjaz et al. (2014) discuss the reduction process performed on the CfA spectra, and Hamuy et al. (2006) outline the reduction process performed on the CSP spectra. Standard IRAF[7] reduction packages were used by the Padova-Asiago and NAOC groups. Most spectra presented here have resolutions of $\sim$10 Å, were observed at or near the parallactic angle (Filippenko 1982), and were flux calibrated with bright standard stars observed at similar airmasses. Most spectra have also been corrected for wavelength-dependent telluric absorption. Details of the observations and data-reduction methods vary from group to group, and we discuss any possible data-quality issues for the spectra most vital to our classification effort in the text.

All photometry used by L11 and in this effort was observed at Lick Observatory with KAIT or the Nickel 1 m telescope, and all SNe discussed here were discovered by LOSS/KAIT (e.g., Li et al. 2000; Filippenko et al. 2001b). KAIT photometry is generally performed on unfiltered images (the *clear* band), though filtered *BVRI* KAIT images of some events are available. Nickel data are observed through a *BVRI* filter set. Details for both instruments and for our photometry reduction pipeline are given by Ganeshalingam et al. (2010), and we present these light curves as observed, without correcting for Milky Way (MW) or host-galaxy dust absorption, unless otherwise stated. All of the spectra and photometry used in this project will be made public through the UCB SNDB, WiseREP, and the Open Supernova Catalog (Guillochon et al. 2017).[8] See Appendix 6.8 for logs of the data released publicly here for the first time.

6.3 Classification Methods

Following Silverman et al. (2012) and Modjaz et al. (2014), we use the SN IDentification code[9] (SNID; Blondin & Tonry 2007) as our primary classification tool. SNID classifies SNe by cross-correlating an input (optical) spectrum against a library of template spectra (Tonry & Davis 1979). Updated sets of template spectra have been released since the original release of SNID — for this study we use the BSNIP v7.0 templates (Silverman et al. 2012) augmented by the Liu & Modjaz (2014) stripped-envelope templates (and following all suggestions from their Table 4). When running SNID, we set the SN redshift with the *forcez* keyword using observed host-galaxy redshifts from the NASA/IPAC Extragalactic Database (NED).[10] For those SNe that SNID alone cannot identify, we incorporate results from two other spectral

[6] http://www.echellespectrographs.com/about.htm
[7] http://iraf.noao.edu/
[8] https://sne.space/
[9] http://people.lam.fr/blondin.stephane/software/snid/index.html
[10] https://ned.ipac.caltech.edu/

identification codes, Superfit[11] (Howell et al. 2005) and GELATO[12] (Harutyunyan et al. 2008), and for some stripped-envelope SNe we also compare to the average spectra of Liu et al. (2016).

As shown by (for example) L11, the light curves of SNe Ic, Ib, and IIb are similar to each other, but are generally distinguishable from those of SNe Ia and hydrogen-rich core-collapse SNe. We incorporate light-curve information in our classifications when it proves useful, comparing the light curves of individual objects to the *clear*-band templates from L11 and providing constraints on the phases of spectra. Recent studies have advanced our understanding of stripped-envelope SN light-curve evolution (e.g., Drout et al. 2011; Cano 2013; Bianco et al. 2014; Taddia et al. 2015; Lyman et al. 2016; Prentice et al. 2016). Drout et al. (2011) present template SN Ib/c light curves in the R and V bands assembled from 25 events and Lyman et al. (2016) give template bolometric light curves assembled from 38 events, while L11 produce four template light curves for stripped-envelope SNe: "Ibc.fast," "Ibc.ave," "Ibc.slow," and "IIb." The Ibc.ave template is very similar to the R-band SN Ibc template of Drout et al. (2011) and the SN Ib and SN Ic templates of Lyman et al. (2016). The SN IIb templates from L11 and Lyman et al. (2016) are also in good agreement, and both show cooling envelope emission followed by a dip and a rise to a second radioactively-powered peak, with a post-peak evolution basically indistinguishable from that of SNe Ib/c. L11 do not produce a template for broad-lined Type Ic SNe (labeled SNe Ic-BL here), but other authors show that SN Ic-BL light curves are quite similar to those of other SNe Ib/c though trending toward higher absolute luminosities (e.g., Drout et al. 2011; Taddia et al. 2015; Prentice et al. 2016).

Several recent large-scale SN data releases have relied on SNID classifications using relatively stringent requirements for a robust identification, requiring a high *rlap* value for the top match (*rlap* is a quality parameter used by SNID — a higher value corresponds to a more trustworthy classification) and that the first few matches be of the same subtype (e.g., Silverman et al. 2012; Graur & Maoz 2013; Modjaz et al. 2014; Graur et al. 2015). We follow these methods whenever possible, and for most of the SNe in our sample they clearly indicate a single type and subtype.

All of the SNe Ia in this sample have been examined in detail by other authors (e.g., Blondin et al. 2012; Silverman et al. 2012; Folatelli et al. 2013). We follow the methods of Silverman et al. (2012) to determine SN Ia subtypes, and we do not attempt to identify subpopulations within the normal SNe Ia — i.e., high-velocity events (Wang et al. 2009a) or the subgroups defined by Benetti et al. (2005). We discuss the more peculiar SNe Ia from this sample in §6.4.3.

We do not attempt to sort the hydrogen-rich SNe II into the IIP and IIL subtypes. Type II SNe have long been sorted into those that exhibit a clear plateau phase and those that decline linearly in magnitudes (IIP and IIL, respectively; e.g., Barbon et al. 1979; Filippenko 1997). L11 used spectra to identify H-rich SNe, and then labeled as Type IIL those that decline more than 0.5 mag in the R band during the first 50 d after explosion and the rest

[11] http://www.dahowell.com/superfit.html
[12] https://gelato.tng.iac.es/

as IIP, but recent work has shown that the issue may be more complex. While Arcavi et al. (2012) find there to be distinct SN IIP and SN IIL subclasses among the R-band light curves of 21 H-rich noninteracting Type II SNe, Anderson et al. (2014) show that their sample of V-band light curves for 116 SNe II indicate that there is a continuous distribution of properties for these events. Rubin et al. (2016) present an analysis of the early light curve rise for 57 events finding only a weak correlation between rise times and decline rates, Sanders et al. (2015) and Valenti et al. (2016) argue that there exists a continuous distribution of properties for SNe II and that there is no evidence for separate SNe IIP and SNe IIL subclasses, while Rubin & Gal-Yam (2016) argue for a type II subclassification system based upon both the rise and the fall of the light curves and Faran et al. (2014a) argue that a simple subclass definition based upon the light curve decline alone remains reasonable. Throughout this article, we group the SN IIP-like and SN IIL-like events under the label "SNe Type II," but when comparing to data from other sources we preserve the SN IIP/SN IIL labels if given by the original authors.

Though we do not differentiate between SNe IIL and SNe IIP, we do identify other H-rich subclasses. We identify the H-rich SNe with narrow spectral emission lines indicative of interaction with dense circumstellar material (SNe IIn; e.g., Schlegel 1990; Chugai 1991; Filippenko 1991) and the SN impostors, thought to be nonterminal ejections or explosions from the surface of massive stars (labeled "IIni" in L11; e.g., Van Dyk et al. 2000; Maund et al. 2006; Smith et al. 2011c). We also identify three slow-rising (SN 1987A-like) Type II SNe in our sample (e.g., Arnett et al. 1989; McCray 1993).

Our main focus is on the stripped-envelope SNe. We divide this class into those with some hydrogen features (SNe IIb), those without hydrogen features (or with only very weak hydrogen features; Liu et al. 2016) but with clear helium features (SNe Ib), and those exhibiting neither clear hydrogen nor clear helium features (SNe Ic). The exact distinction between SNe Ib and Ic has been an issue of some debate in the literature; we follow Modjaz et al. (2014) and Liu et al. (2016) to define the differences between these subclasses. We differentiate between Type Ic SNe and Ic-BL SNe (see Modjaz et al. 2016), and we identify the "calcium-rich" SNe separately (included in the Ibc-pec category by L11, this class of events has been described by, e.g., Filippenko et al. 2003; Perets et al. 2010; Kasliwal et al. 2012).

For events with spectra that match both the SN Ib and SN Ic SNID templates equally well, we discuss the available data in detail and assign the label "Ib/Ic" (i.e., unsure) if we remain unable to determine a single best classification. Figure 6.1 shows that this classification scheme tends to move events that were previously labeled SNe Ic into the Ib or Ib/Ic categories (there are no SNe Ib that we reclassify as SNe Ic in this work).

We follow Smith et al. (2011b) and group the SNe IIb with other stripped-envelope SNe in our sample, although L11 included them with the Type II SNe. SNe IIb show a strong Hα line at early times, as do normal SNe II, but then the hydrogen fades and the later spectra of SNe IIb resemble those of SNe Ib (e.g., Filippenko 1988; Filippenko et al. 1993; Filippenko 1997; Pastorello et al. 2008c; Chornock et al. 2011; Milisavljevic et al. 2013). Several authors have claimed the detection of weak high-velocity hydrogen features in SNe

Ib and Ic (e.g., Branch et al. 2006; Parrent et al. 2007, 2016; Liu et al. 2016). However, Liu et al. (2016) argue that the putative weak Hα absorption line often present in SNe Ib is, at all phases, weaker than the Hα line in SNe IIb, and that SNID capably distinguishes between SNe Ib and SNe IIb even after the strong Hα feature of the SNe IIb has faded, so long as spectra were obtained during the photospheric phase. The nebular spectra of SNe IIb and SNe Ib, on the other hand, are often very similar and are not well separated by SNID. When discriminating between Types IIb and Ib, we trust the SNID result if obtained from spectra of the photospheric phase.

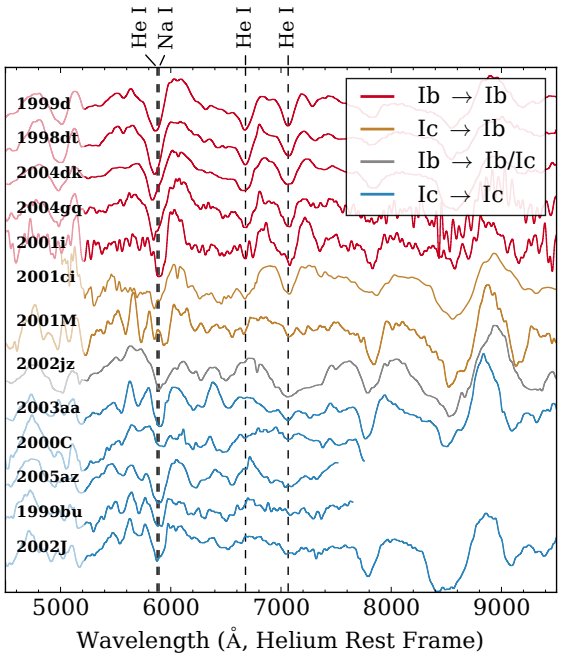

Figure 6.1: Representative sample of spectra of the SNe Ib and Ic in our sample, observed between 5 and 20 days after peak brightness, as well as spectra of three SNe for which we provide updated classifications (SNe 2001M, 2001ci, and 2002jz). We have subtracted a spline continuum from these spectra, smoothed them with a 50 Å Gaussian kernel, and shifted them in velocity space to align their He I features (or Na I λ5892 if no helium is detected).

To examine possible biases SNID may introduce when classifying stripped-envelope subtypes, we ran a series of trials introducing wavelength restrictions, noise, and artificial dust reddening to spectra of Type IIb, Ib, and Ic SNe at two different phases in their evolution (near maximum brightness and 2–4 weeks post-maximum). We classified the degraded spectra with the methods described above and compared the results to those obtained from the original data. We chose events that are not included in the SNID template set and for which we have relatively high signal-to-noise ratio (S/N) spectra (S/N $>$ 30) at these phases covering $\sim$ 3500–10,000 Å: SN IIb 2003ed, SN Ib 1998dt, and SN Ic 2003aa. The spectra used in this study either cover a similar wavelength range or $\sim$ 3500–7500 Å; we test the efficacy of SNID using both the full spectra and spectra trimmed to match the smaller wavelength range.

We find that, regardless of subtype or which of the two wavelength ranges is used, SNID capably classifies events in the presence of strong reddening ($E(B-V) \sim 2.0$ mag and $R_V = 3.1$), so long as the spectra exhibit a S/N $\gtrsim$ 1–3. This is to be expected, as SNID divides input spectra by a pseudo-continuum fit and discards the spectral color information before performing cross-correlation (Blondin & Tonry 2007). In contrast, classifications performed via visual comparison may be prone to error when strong reddening is present.

At moderate and high noise levels (S/N $\lesssim 3$), the post-maximum spectrum of SN Ic 2003aa could be confused with a SN Ib spectrum while the near-maximum-light spectrum is still identified as that of a SN Ic (the He I lines in SNe Ib fade as the event nears the nebular phase; e.g., Modjaz et al. 2014). At extremely high noise levels (S/N $\lesssim 1$) SNID prefers a SN Ic-BL classification for SN 2003aa, especially when examining the post-maximum spectrum or using spectra covering only the smaller wavelength range, which does not capture the strong Ca II near-infrared (IR) triplet feature.

We also find that, if the SN redshift is uncertain and the S/N is low, SN Ic spectra can be confused with SN Ia spectra (as shown by Blondin & Tonry 2007), and so incorporating an independently measured redshift is helpful. Though SN 2004aw is not in the sample discussed here, it offers a nice illustration of the sometimes-confounding similarities between spectra of Type Ia and Type Ic SNe (e.g., Matheson et al. 2004a; Benetti et al. 2004; Filippenko et al. 2004).

Examining SN 1998dt, we find that SNID correctly identifies it as a SN Ib at both phases using spectra with S/N $\gtrsim 1$, and though the classification becomes very uncertain using only spectra with S/N $\lesssim 1$ and a restricted wavelength range, SNID never prefers an incorrect label.

SN 2003ed was correctly identified as a Type IIb SN so long as we examined spectra with S/N $\gtrsim 1$. Unlike SN 1998dt, however, including spectra covering an extended wavelength range did not significantly affect the results even at low S/N, since the He I λ5876 and Hα features proved the most useful and they are captured by all of our spectra.

Based on the above discussion, we adopt the following guidelines to avoid systematic biases when using SNID for our stripped-envelope classifications. First, it is difficult to discriminate between SNe Ib and Ic or between SNe IIb and Ib if only noisy (S/N $\lesssim 3$) spectra observed at more than a few weeks post-maximum are available. Second, SNe Ic can be mislabeled as SNe Ic-BL when only low-S/N spectra are available.

6.4 Updated Classifications

For the bulk of the SNe in the sample, especially the SNe Ia, our methods robustly confirm the L11 classifications.[13] Table 6.1 lists all SNe in this sample, the type and subtype labels used by L11, and our updated labels. In the ensuing subsections, we discuss each changed classification individually as well as the rare subtypes and the uncertain and peculiar events we find. Many of the comparison spectra used in this section were drawn from the updated SNID template set; citations to the original publications are given.

[13]Note that, in a small number of cases, L11 reclassified some events from the original type announced in the CBETs; in this article we only discuss differences relative to the L11 labels.

Table 6.1: Updated Classifications of SNe in the LOSS Volume-Limited Sample

Name	Previous (L11)	This Work	Ref.	Name	Previous (L11)	This Work	Ref.
SN 1998de	Ia-91bg	Ia-91bg	1,2,2	SN 1998dh	Ia-norm	Ia-norm	2,3
SN 1998dk	Ia-norm	Ia-norm	2,3	SN 1998dm	Ia-norm	Ia-norm	2,3
SN 1998dt	Ib	Ib	4	SN 1998ef	Ia-norm	Ia-norm	3
SN 1998es[1]	Ia-91T	Ia-99aa	2,3	SN 1999D	IIP	II	5
SN 1999aa[1]	Ia-91T	Ia-99aa	2,3,6	SN 1999ac[1]	Ia-91T	Ia-99aa/Ia-norm	2,3,7
SN 1999an	IIP	II	-	SN 1999bg	IIP	II	5
SN 1999bh[1]	Ia-02cx	Ia-02es	8,9	SN 1999br	IIP	II	-
SN 1999bu	Ic	Ic	-	SN 1999bw	*impostor*	*impostor*	10
SN 1999by	Ia-91bg	Ia-91bg	3	SN 1999cd	IIb	IIb	-
SN 1999cl	Ia-norm	Ia-norm	2,3	SN 1999cp	Ia-norm	Ia-norm	3
SN 1999da	Ia-91bg	Ia-91bg	3	SN 1999dk	Ia-norm	Ia-norm	3
SN 1999dn	Ib	Ib	4	SN 1999dq[1]	Ia-91T	Ia-99aa	2,3
SN 1999ej	Ia-norm	Ia-norm	2	SN 1999ek	Ia-norm	Ia-norm	3
SN 1999el	IIn	IIn	-	SN 1999em	IIP	II	5,11
SN 1999gd	Ia-norm	Ia-norm	2,3	SN 1999gi	IIP	II	12
SN 1999go	IIL	II	13	SN 2000C	Ic	Ic	-
SN 2000H	IIb	IIb	14	SN 2000L	IIP	II	-
SN 2000N	**IIb/IIL**	**II**	-	SN 2000cb[2]	IIP	II-87A	15
SN 2000ch	*impostor*	*impostor*	10,16	SN 2000dc	IIL	II	17
SN 2000dm	Ia-norm	Ia-norm	3	SN 2000dr	Ia-norm	Ia-norm	3
SN 2000el	IIP	II	-	SN 2000eo	IIn	IIn	-
SN 2000ex	IIP	II	-	SN 2001E	Ia-norm	Ia-norm	3
SN 2001J	**IIP**	**II/IIb**	-	SN 2001K	IIP	II	-
SN 2001L	Ia-norm	Ia-norm	3	**SN 2001M**	**Ic**	**Ib**	-
SN 2001Q	IIb	IIb	-	SN 2001V[1]	Ia-91T	Ia-99aa	2,3
SN 2001ac	*impostor*	*impostor*	10	SN 2001bq	IIP/IIL	II	5
SN 2001ci	**Ic**	**Ib**	-	SN 2001cm	IIP	II	5,18
SN 2001dc	IIP	II	19	SN 2001dn	Ia-norm	Ia-norm	3
SN 2001do	IIL	II	17	SN 2001en	Ia-norm	Ia-norm	3
SN 2001ep	Ia-norm	Ia-norm	3,20	SN 2001fh	Ia-norm	Ia-norm	3
SN 2001fz	IIP	II	-	SN 2001hf	IIL	II	-
SN 2001is	Ib	Ib	-	SN 2002J	Ic	Ic	-
SN 2002an	IIL	II	5	SN 2002ap	Ic-pec	Ic-BL	21
SN 2002bo	Ia-norm	Ia-norm	3	SN 2002bu[3]	IIn	*impostor*	10
SN 2002bx	IIP	II	5	SN 2002ca	IIP	II	5
SN 2002ce	IIP	II	-	SN 2002cf	Ia-91bg	Ia-91bg	3
SN 2002cr	Ia-norm	Ia-norm	3	SN 2002dj	Ia-norm	Ia-norm	3
SN 2002dk	Ia-91bg	Ia-91bg	3	SN 2002do	Ia-norm	Ia-norm	3
SN 2002dq	IIP	II	-	SN 2002ds[4]	IIP	II	-
SN 2002er	Ia-norm	Ia-norm	3	SN 2002es[1]	Ia-02cx	Ia-02es	22
SN 2002fb	Ia-91bg	Ia-91bg	3	SN 2002fk	Ia-norm	Ia-norm	3
SN 2002gd	IIP	II	5	SN 2002gw	IIP	II	-
SN 2002ha	Ia-norm	Ia-norm	3	SN 2002hh	IIP	II	5
SN 2002hw	Ia-norm	Ia-norm	3	SN 2002jg	Ia-norm	Ia-norm	3
SN 2002jj	**Ic**	**Ic/Ic-BL**	-	SN 2002jm	Ia-91bg	Ia-91bg	3
SN 2002jz	**Ic**	**Ib/Ic**	-	SN 2002kg	*impostor*	*impostor*	23,24
SN 2003E	IIP	II	-	SN 2003F	Ia-norm	Ia-norm	3
SN 2003G	IIn	IIn	-	SN 2003H[5]	Ibc-pec	Ca-rich	25
SN 2003Y	Ia-91bg	Ia-91bg	3	SN 2003Z	IIP	II	5
SN 2003aa	Ic	Ic	-	SN 2003ao	IIP	II	-
SN 2003bk	IIP	II	-	**SN 2003br**	**IIP**	**II/IIb**	-
SN 2003bw[4]	**IIP**	**II/IIb**	-	SN 2003cg	Ia-norm	Ia-norm	26
SN 2003dr[5]	Ibc-pec	Ca-rich	25	SN 2003du	Ia-norm	Ia-norm	3,27
SN 2003dv	IIn	IIn	28	SN 2003ed	IIb	IIb	-

Table 6.1 (cont'd): Updated Classifications of SNe in the LOSS Volume-Limited Sample

Name	Previous (L11)	This Work	Ref.	Name	Previous (L11)	This Work	Ref.
SN 2003ef	IIP	II	-	SN 2003gm	*impostor*	*impostor*	23
SN 2003gt	Ia-norm	Ia-norm	3	SN 2003hg	IIP	II	13
SN 2003hl	IIP	II	5	**SN 2003id**	**Ic-pec**	**Ic-pec**	-
SN 2003iq	IIP	II	5	SN 2003kf	Ia-norm	Ia-norm	3
SN 2003ld	IIP	II	-	**SN 2004C**	**Ic**	**IIb**	-
SN 2004ab	Ia-norm	Ia-norm	9	**SN 2004al**	**IIb/IIL**	**II**	-
SN 2004aq	IIP	II	-	SN 2004bd	Ia-norm	Ia-norm	3
SN 2004be	IIb	IIb	-	SN 2004bl	Ia-norm	Ia-norm	3
SN 2004bm	**Ibc-pec/IIb**	**IIb/IIb-pec**	-	SN 2004bv	Ia-91T	Ia-91T	3
SN 2004ca	Ia-norm	Ia-norm	3	**SN 2004cc**	**Ic**	**Ib/Ic**	13
SN 2004ci	IIP	II	-	SN 2004dd	IIP	II	-
SN 2004dk	Ib	Ib	-	SN 2004er	IIP	II	-
SN 2004et	IIP	II	5	SN 2004fc	IIP	II	-
SN 2004fx	IIP	II	29	SN 2004gq	Ib	Ib	14
SN 2005A	Ia-norm	Ia-norm	3,30	SN 2005E[5]	Ibc-pec	Ca-rich	25,31
SN 2005H	**IIb**	**II/IIb**	13	SN 2005J	IIL	II	-
SN 2005U	IIb	IIb	14	SN 2005W	Ia-norm	Ia-norm	3,30
SN 2005ad	IIP	II	-	SN 2005am	Ia-norm	Ia-norm	3,30
SN 2005an	IIL	II	-	SN 2005aq	IIn	IIn	-
SN 2005as	Ia-norm	Ia-norm	3	SN 2005ay	IIP	II	5
SN 2005az	Ic	Ic	14	SN 2005bb	IIP	II	-
SN 2005bc	Ia-norm	Ia-norm	3	SN 2005bo	Ia-norm	Ia-norm	3,30
SN 2005cc	Ia-02cx	Ia-02cx	9	SN 2005cf	Ia-norm	Ia-norm	32
SN 2005ci[2]	IIP	II-87A	15	SN 2005de	Ia-norm	Ia-norm	3
SN 2005el	Ia-norm	Ia-norm	3,30	SN 2005hk	Ia-02cx	Ia-02cx	3,33,34
SN 2005io[2]	**IIP**	**II-87A**	-	SN 2005kc	Ia-norm	Ia-norm	3,30
SN 2005ke	Ia-91bg	Ia-91bg	3,30	**SN 2005lr**	**Ic**	**IIb**	-
SN 2005mg	**IIP**	**II/IIb**	-	SN 2005mz	Ia-91bg	Ia-91bg	9
SN 2006F	Ib	Ib	-	SN 2006T	IIb	IIb	-
SN 2006X	Ia-norm	Ia-norm	3,30	SN 2006ax	Ia-norm	Ia-norm	3,30
SN 2006be	IIP	II	-	SN 2006bp	IIP	II	-
SN 2006bv[3,4]	IIn	*impostor*	10	SN 2006ca	IIP	II	-
SN 2006cm[1]	Ia-91T	Ia-99aa/Ia-norm	3	SN 2006dy	Ia-norm	Ia-norm	3
SN 2006ef	Ia-norm	Ia-norm	3,30	**SN 2006eg**	**Ic**	**S.E.**[6]	-
SN 2006ke	Ia-91bg	Ia-91bg	3	SN 2006le	Ia-norm	Ia-norm	3
SN 2006lf	Ia-norm	Ia-norm	3	SN 2006qr	IIP	II	-

This table lists the previous classifications for all objects in L11 and our confirmed or updated classifications. Notable objects, discussed individually within the text, are printed in boldface. We also list references to the original publishers for all data already in the literature that were used in this effort. When we cannot confim a single clear classification, we list more than one possible type or subtype. See §6.3 for a detailed description of each type and subtype label.

References: [1] Modjaz et al. (2001); [2] Matheson et al. (2008); [3] Silverman et al. (2012); [4] Matheson et al. (2001); [5] Faran et al. (2014b); [6] Garavini et al. (2004); [7] Garavini et al. (2005); [8] Li et al. (2001); [9] Blondin et al. (2012); [10] Smith et al. (2011c); [11] Leonard et al. (2002c); [12] Leonard et al. (2002b); [13] Harutyunyan et al. (2008); [14] Modjaz et al. (2014); [15] Kleiser et al. (2011); [16] Wagner et al. (2004); [17] Faran et al. (2014a); [18] Poznanski et al. (2009); [19] Pastorello et al. (2004); [20] Sauer et al. (2008); [21] Foley et al. (2003); [22] Ganeshalingam et al. (2012); [23] Maund et al. (2006); [24] Van Dyk et al. (2006); [25] Perets et al. (2010); [26] Elias-Rosa et al. (2006); [27] Leonard et al. (2005); [28] Bilinski et al. (2015); [29] Hamuy et al. (2006); [30] Folatelli et al. (2013); [31] Foley et al. (2009); [32] Wang et al. (2009b); [33] Chornock et al. (2006); [34] Phillips et al. (2007)

[1]See §6.4.3
[2]See §6.4.5
[3]See §6.4.7
[4]See §6.4.8
[5]See §6.4.6
[6]Data on SN 2006eg are consistent with all stripped-envelope subtype classifications; see §6.4.2

6.4.1 Reclassified Objects

SN 2000N (IIb/IIL → II)

SN 2000N was discovered in MCG-02-34-054 (Sato et al. 2000) and classified as a Type II SN from a spectrum with a low S/N (Jha et al. 2000). However, because the data they had on this object were quite sparse, L11 could not determine if SN 2000N was a Type IIb or a Type II SN. We were able to obtain the spectrum originally used to classify the SN as well as additional spectra, including one near peak brightness when the spectra of SNe IIb and II are more clearly differentiable; see Figure 6.2. SNID identifies SN 2000N as a Type II SN, and our rereduced light curve indicates that the SN IIL template from L11 is a better match than the SN IIb one.

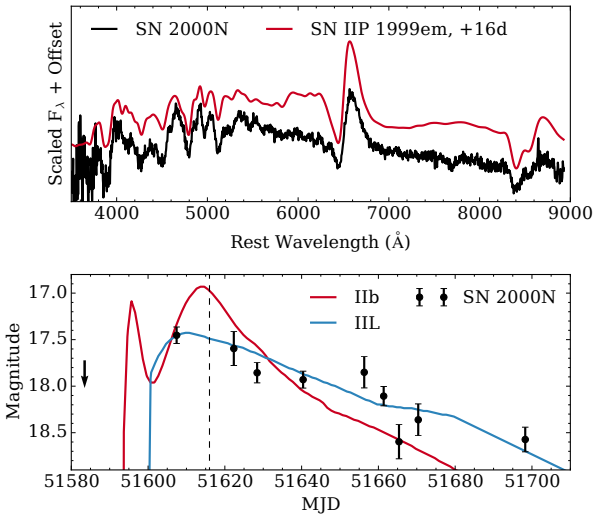

Figure 6.2: Top: the near-maximum-light spectrum of SN 2000N alongside that of the Type IIP SN 1999em (Leonard et al. 2002c). Bottom: the light curve of SN 2000N, with a vertical line showing the date the spectrum shown was observed, and colored lines showing the template light curves from L11.

SN 2001M (Ic → Ib)

SN 2001M was discovered in NGC 3240 and classified as a SN Ic (Aazami & Li 2001; Suntzeff et al. 2001; Filippenko et al. 2001a). SNID identifies reasonably good cross-correlations with spectra of both SNe Ib and SNe Ic. We have been able to locate only a single spectrum of this object and our light curve is sparse, so the phase of our spectrum is somewhat uncertain; see Figure **??**. Narrow, unresolved Hα emission from the star-forming host galaxy partially obscures the He I λ6678 absorption line, but we do identify probable weak He I λ6678 and He I λ7065 lines at $v \approx 8500\,\mathrm{km\,s^{-1}}$. The region around He I λ5876 is complex, with what must be several overlapping absorption lines; we believe it to be consistent with He I λ5876 absorption but not dominated by it.

We compare our spectrum to the +10 day average SN Ib and SN Ic spectra of Liu et al. (2016), after estimating a date of peak of 24 January 2001 from the light curve (implying a phase of +7.5 d for our spectrum). This comparison shows many similarities between

SN 2001M and both classes, but reinforces our identifications of the He I lines. Given our detections of both He I λ6678 and He I λ7065, we relabel SN 2001M as a Type Ib SN, though we note that the helium lines are weak compared to those in most SNe Ib.

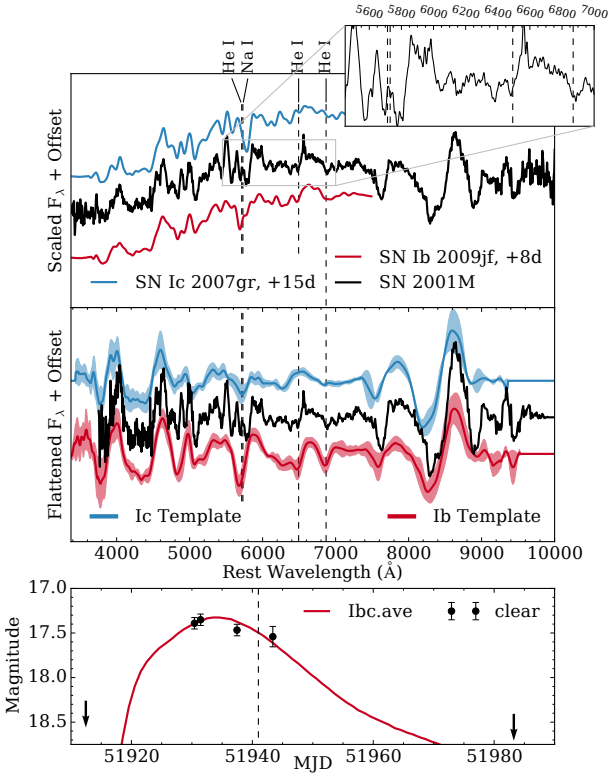

Figure 6.3: Top: spectrum of SN 2001M smoothed with a 20 Å Gaussian kernel, and with weak helium features identified. We also show spectra of SN Ic 2007gr and SN Ib 2009jf (Modjaz et al. 2014), and the wavelengths of He I and Na I features are marked at $v = 8300\,\mathrm{km\,s^{-1}}$. The inset shows the He I lines we identify in the SN 2001M. Middle: the continuum-normalized spectrum of SN 2001M compared to the +10 d average spectra of Ib and Ic SNe from Liu et al. (2016), with the standard deviation shown as shaded regions. Bottom: light curve of SN 2001M compared to the average Ib/c template light curve from L11, with the date of spectrum shown with a dashed line.

SN 2001ci (Ic → Ib)

SN 2001ci was discovered in NGC 3079 (Swift et al. 2001) and announced as a SN Ic heavily obscured by host-galaxy dust absorption (Filippenko & Chornock 2001). A re-examination of the spectrum cited therein (observed UT 2001-05-30; we were not able to locate any other spectra of this object) confirms that it is heavily reddened by host-galaxy dust. The MW contribution to the reddening is only $E(B-V) = 0.0097\,\mathrm{mag}$ (Schlafly & Finkbeiner 2011, used for all subsequent MW reddening measures), but the spectrum clearly shows narrow Na I absorption features from the host galaxy indicating significant reddening produced by host-galaxy dust. The spectrum is of sufficiently high resolution to resolve both components of the Na I D doublet, but their equivalent widths (EWs) are well outside the range of the empirical relations of Poznanski et al. (2012): $EW_{D1} \approx 2.4$ Å and $EW_{D2} \approx 2.2$ Å. This implies that $E(B-V) \gtrsim 3.0\,\mathrm{mag}$.

Note that SNID, by construction, is insensitive to color information and to uncertainties in the reddening corrections or flux calibrations (Blondin & Tonry 2007). Throughout this paper we apply (often uncertain) reddening corrections to spectra to facilitate visual comparisons, but they do not appreciably affect the SNID classifications.

Adopting $E(B-V) = 2.0\,\mathrm{mag}$ and a MW-like dust law is good enough to achieve a robust identification: SN 2001ci is a Type Ib SN, with a spectrum that is most similar to those of SNe Ib with weak helium lines. See Figure 6.4 for a comparison to the He-weak SN Ib 1999ex (Hamuy et al. 2002). Filippenko & Chornock (2001) drew attention to a similarity with SN 1990U, which was (at the time) classified as a SN Ic, but Modjaz et al. (2014) have subsequently reclassified SN 1990U as a SN Ib.

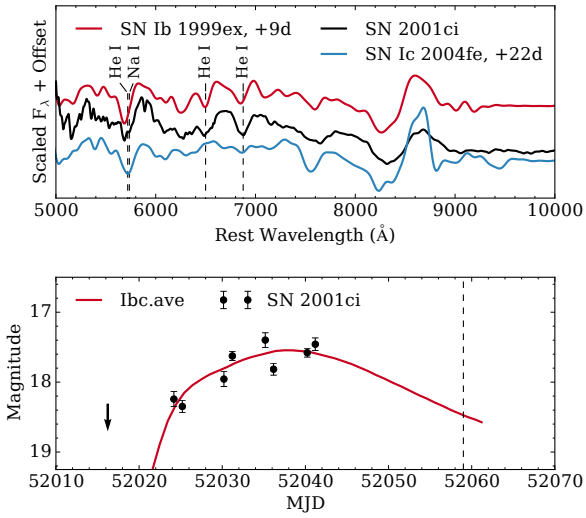

Figure 6.4: Top: spectrum of SN 2001ci (corrected for a reddening of $E(B-V) = 3.0\,\mathrm{mag}$ and smoothed with a Gaussian kernel 50Å wide), compared with that of the Type Ib SN 1999ex (Hamuy et al. 2002) and the Type Ic SN 2004fe (Modjaz et al. 2014). Bottom: the light curve compared to a L11 template with the date of the spectrum marked by a vertical line.

SN 2004C (Ic → IIb)

SN 2004C was discovered in NGC 3683 (Dudley & Fischer 2004) and classified as a heavily reddened SN Ic (Matheson et al. 2004b), spectrally similar to SN 1990U (see §6.4.1: SN 1990U was a SN Ib). The MW reddening along the line of sight is only $E(B-V) = 0.0133\,\mathrm{mag}$, but (unresolved) Na I D absorption in our spectra indicates strong host-galaxy obscuration. As with SN 2001ci, the Na I D EW is well beyond the empirical relations of Poznanski et al. (2012), but the spectra do not appear to be as reddened as those of SN 2001ci. Correcting for a total reddening of $E(B-V) = 1.0\,\mathrm{mag}$ produces a reasonable result.

Here we publish several spectra of SN 2004C which indicate that SN 2004C was a Type IIb SN. Figure 6.5 shows a comparison between the spectrum announced by Matheson et al. (2004b) and the Type IIb SN 2008ax, as well as a later spectrum with broader wavelength coverage compared to a spectrum of the Type IIb SN 1993J.

SN 2004al (IIb/IIL → II)

SN 2004al was discovered in ESO 565-G25 (Singer et al. 2004) and classified as a Type II SN (Matheson et al. 2004c). As L11 show, SN 2004al had a light curve consistent with either a SN IIb or a SN IIL classification, and so they assign it a 50% weight in each class. Although we have no additional spectra to examine, we were able to obtain the classification

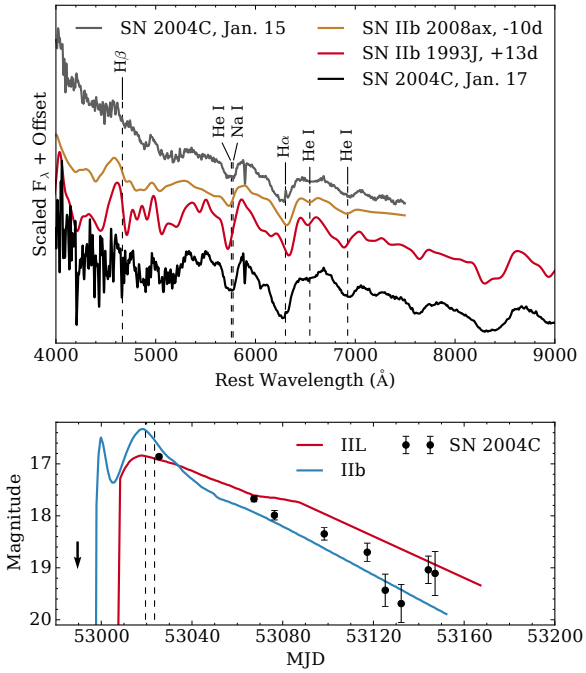

Figure 6.5: Top: spectra of SN 2004C observed on UT 2004-01-15 and on UT 2004-01-17, alongside a premaximum spectrum of the Type IIb SN 2008ax (Modjaz et al. 2014) and a post-maximum spectrum of the Type IIb SN 1993J (Matheson et al. 2000b). Both spectra of SN 2004C have been dereddened by $E(B-V) = 1.0$ mag and smoothed by a 20 Å Gaussian kernel, and galaxy emission lines have been subtracted by hand. Bottom: light curve of SN 2004C compared to templates from L11 with the date of the spectra marked by vertical lines.

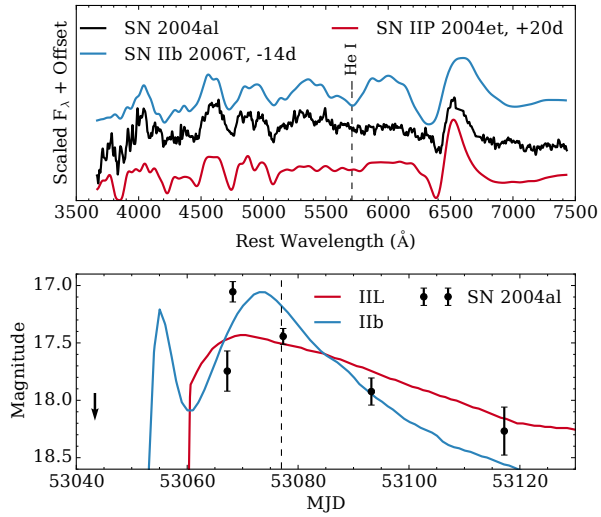

Figure 6.6: Top: spectrum of SN 2004al smoothed with a 20 Å Gaussian kernel and compared to spectra of the Type IIP SN 2004et a few weeks after maximum (Sahu et al. 2006) and the premaximum SN IIb 2006T (the top non-IIP SNID template, Modjaz et al. 2014). Bottom: the light curve compared to templates from L11 with the date of the spectrum marked by a vertical line.

spectrum and SNID clearly identifies it as a Type II SN, not a SN IIb, mostly owing to the absence of He I λ5876. Figure 6.6 shows that our spectrum was observed $\sim$1 week post-maximum; though He I lines are often weak in young SNe IIb, they become pronounced by maximum light. In good agreement with L11, our rereduced light curve exhibits a relatively rapid decline and is better fit by the SN IIb template; see Figure 6.6. Despite this tension, we consider the spectroscopic classification robust and we label SN 2004al a Type II event.

SN 2005io (IIP → II-87A)

SN 2005io was discovered in UGC 3361 (Lee et al. 2005) and reported as a young Type II SN (Filippenko & Foley 2005) based upon a Keck LRIS spectrum. The photometry of SN 2005io shows a peculiar evolution, however — see Figure 6.7. The light curve initially follows the Type IIP template almost exactly, but after peaking at an absolute magnitude of -15.2 mag SN 2005io goes into a slight decline and then a very slow rise (over $\sim$100 days) to a second maximum (< -15.75 mag; the peak itself went unobserved). This is similar to the photometric behavior of SN 1987A and other related events, though in SN 1987A the early peak was only visible in bluer passbands and the rise to its second, more luminous, peak occurred more rapidly. The spectrum is similar to that of a normal young Type II SN with hydrogen P-Cygni profiles dominated by the emission component and with an absorption Doppler velocity of $\sim$8,000 km s^{-1}, slower than the velocity found for hydrogen in SN 1987A.

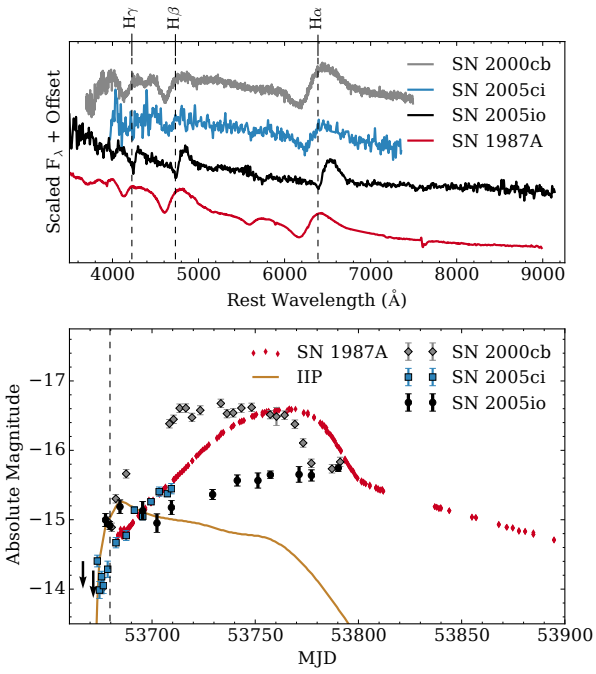

Figure 6.7: Top: spectrum of SN 2005io compared to spectra of the young SNe 2000cb, 2005ci, and 1987A (SNe 2000cb and 2005ci are also included in the LOSS volume-limited sample; Blanco et al. 1987; Kleiser et al. 2011). The spectra of SNe 2005io and 2005ci have been smoothed by a Gaussian kernel 20 Å wide. We mark prominent hydrogen features at 8000 km s^{-1}. Bottom: light curve of SN 2005io (with a vertical line showing the date the spectrum was observed) compared to the light curves of the other SN 1987A-like events after correcting for distance and MW dust absorption along the line of sight, and then offset in time to align their initial rises (Hamuy & Suntzeff 1990; L11). Also shown is the template Type IIP light curve from L11, offset to match the early evolution of SN 2005io.

Based primarily upon the light-curve evolution, and noting that the subclass is heterogeneous (Pastorello et al. 2005b; Kleiser et al. 2011; Taddia et al. 2012; Pastorello et al. 2012; Taddia et al. 2016b), we classify SN 2005io as a SN 1987A-like event alongside the two other SN 1987A-like events already identified within the L11 sample (SNe 2000cb and 2005ci; Kleiser et al. 2011). It unfortunately appears that the peculiarity of SN 2005io was not recognized while it was bright: we believe that Figure 6.7, which shows the classification spectrum and the KAIT photometry, includes all extant observations of the event. Though the central wavelength of unfiltered KAIT photometry is quite similar to that of the R band,

the effective passband is significantly wider (Ganeshalingam et al. 2010). Our early-time spectrum of SN 2005io shows that it was quite blue while young, and it's likely that the rapid rise to the first photometric peak was powered by cooling envelope emission, as was observed in SN 1987A via photometry in bluer passbands.

The second peak of SN 2005io lasts longer than that of SN 1987A, and the fade from peak was not observed. We have upper limits showing that the object had faded to $\gtrsim 19.7$ mag (absolute mag -14.2) by Sep. 18, but we have no data obtained between the last detection on Feb. 24 (shown in Figure 6.7) and then. SN 2005io shares some similarities with SN 2009E (Pastorello et al. 2012), including a slow rise and faint peak compared to the prototypical SN 1987A. The early peak and slow rise to second maximum is also reminiscent of SN 2004ek (Taddia et al. 2016b), although that SN was a great deal more luminous ($R \approx -18.5$ mag) than SN 2005io ($clear \lesssim -15.75$ mag), further illustrating the heterogenous nature of these slow-rising SNe II.

SN 2005lr (Ic → IIb)

SN 2005lr was discovered in ESO 492-G2 (Baek & Li 2005) and was spectroscopically classified as a SN Ic, with spectra similar to those of SN 1990B (Hamuy et al. 2005). We obtained a copy of the classification spectrum for SN 2005lr from the CSP archives (observed 2005 Dec. 18) as well as a second (higher S/N) spectrum taken two days later.

The spectra of SN 2005lr show that this SN was strongly reddened by host-galaxy dust — the Na ID line in these low-resolution spectra exhibits a total EW of $\sim$2.4 Å, just beyond the limits of the relations from Poznanski et al. (2012). We again deredden the spectrum by an arbitrary value of $E(B-V) = 1.0$ mag to facilitate visual inspection.

SNID identifies SN 2005lr as either a SN Ib or IIb, with matches to examples of either class. Distinct He I, O I, and Ca II lines are detected alongside an Hα absorption feature; see Figure 6.8. Our spectra appear to be taken well after peak brightness (although the light curve is extremely sparse) and the detection of a relatively strong Hα feature at this phase identifies SN 2005lr as a Type IIb SN.

6.4.2 Low-Certainty Classifications and Peculiar Events

We have made an effort to track down spectra of every object in the volume-limited sample, especially those spectra originally used for classification in the CBETs, and re-examine the classifications of each. Unfortunately, however, there are several objects in our sample for which robust classifications are simply not possible given the peculiarity of the object or the quality of the data.

SN 2001J (IIP → II/IIb)

SN 2001J was discovered in UGC 4729 (Beckmann & Li 2001) and classified as a Type II SN (Jha et al. 2001). SNID identifies the SN 2001J spectrum as that of a young SN IIb, similar to the spectrum of SN 2008ax. L11 list SN 2001J as a SN IIP with poor light-curve

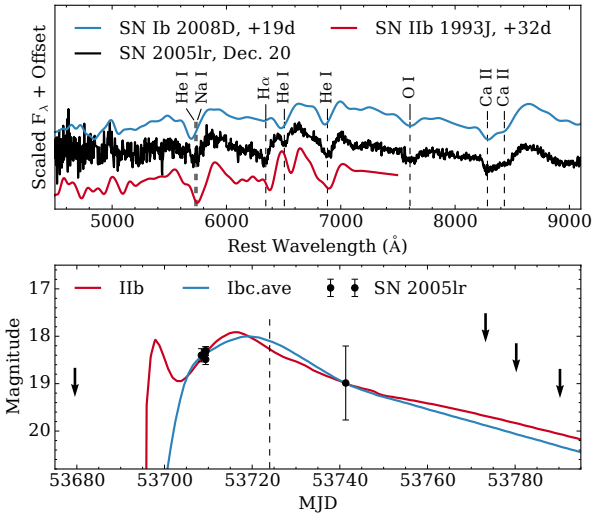

Figure 6.8: Top: the higher S/N spectrum of SN 2005lr smoothed with a Gaussian kernel 10 Å wide and compared to spectra of the SN Ib 2008D and SN IIb 1993J (Matheson et al. 2000b; Modjaz et al. 2009). Bottom: light curve of the SN compared to templates from L11 with date of spectrum shown by a vertical line.

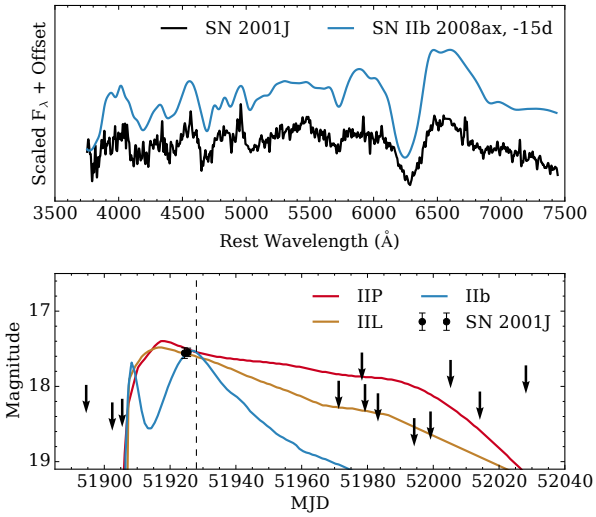

Figure 6.9: Top: the spectrum of SN 2001J (smoothed by a 20 Å Gaussian kernel) compared to that of the Type IIb SN 2008ax (Modjaz et al. 2014). Bottom: the light curve compared to the Type IIL, IIP, and IIb templates from L11. Upper limits from nondetections are shown as arrows, and the date of the spectrum is marked with a dashed vertical line.

coverage, but Figure 6.9 shows our rereduced KAIT light curve (including nondetection upper limits) indicating there was no bright hydrogen recombination plateau phase. Taking into account both the SNID result and the rapid light-curve decay, we prefer the SN Type IIb classification, but cannot rule out the possibility that SN 2001J was a hydrogen-rich Type II SN with a relatively rapid decline rate.

SN 2002jj (Ic → Ic/Ic-BL)

SN 2002jj was discovered in IC 340 (Hutchings & Li 2002) and classified as a SN Ic (Foley & Filippenko 2002), with a spectrum similar to that of SN 1994I. We have three spectra of SN 2002jj, all of moderate quality. SNID prefers a SN Ic-BL classification, as do comparisons

with the average spectra of Liu et al. (2016), but the data are not good enough to be sure. The light curve (though it is sparse) indicates that all of our spectra were taken well past peak brightness. SN 2002jj showed a peak absolute magnitude of -17.66 ± 0.23 (L11), a value in the normal range for both SNe Ic and SNe Ic-BL (SNe Ic-BL are, on average, more luminous than other stripped-envelope SNe; e.g., Drout et al. 2011; Lyman et al. 2016), and so it is not clear whether this SN was a bona-fide SN Ic-BL.

In addition, the He I lines used to distinguish SNe Ic from Ib are most apparent around the time of peak brightness and then fade, in most cases disappearing entirely by $\sim$ 50–70 days (Modjaz et al. 2014; Liu et al. 2016). The spectroscopic coverage of SN 2002jj did not begin until $\sim$1 month post-peak and we cannot rule out the possibility of weak helium features near peak, but we prefer the SN Ic or SN Ic-BL classification; see Figure 6.10.

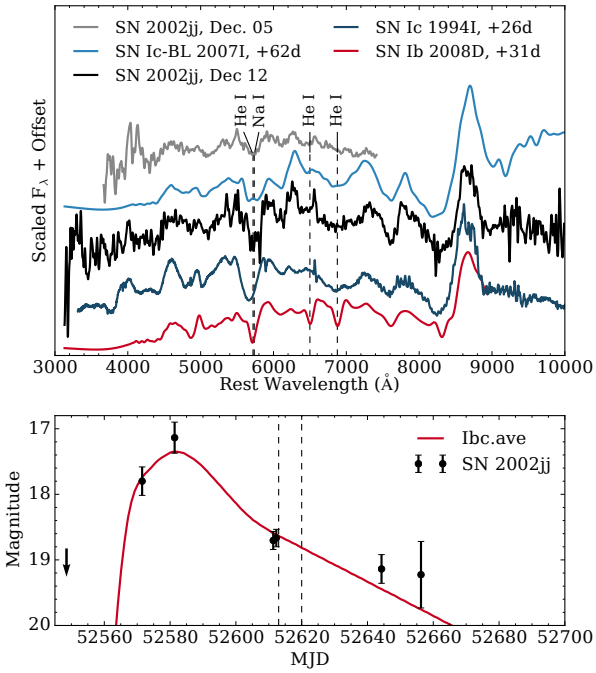

Figure 6.10: Top: spectra of SN 2002jj, smoothed by a 40 Å Gaussian kernel and compared to spectra of the Type Ic-BL SN 2007I (Modjaz et al. 2014), the Type Ic SN 1994I (Filippenko et al. 1995), and the Type Ib SN 2008D (Modjaz et al. 2009). Bottom: light curve of SN 2002jj compared to the average SN Ib/c template from L11, with the dates of the spectra marked by vertical lines.

SN 2002jz (Ic $\rightarrow$ Ib/Ic)

SN 2002jz was discovered in UGC 2984 and classified as a SN Ic with a resemblance to SN 1994I (Puckett et al. 2002). We present three spectra of this object, the most useful of which was observed on UT 2003-01-07. There is significant MW dust reddening along the line of sight ($E(B-V) = 0.4846$ mag), and the unresolved Na I D absorption in our spectra indicates a similar amount of host-galaxy dust obscuration.

SNID weakly prefers a Type Ib label over the Ic label; the best SNID matches are to the spectra of the Type Ib SNe 1995F (reclassified from Ic to Ib by Modjaz et al. 2014) and 1999ex (studied in detail by, e.g., Parrent et al. 2007). However, the He I λ6678 line in

SN 2002jz is so weak as to be nearly indiscernible (it is only detected as a notch out of an adjacent P-Cygni emission profile), and the He I λ7065 line is notably weaker than that of SN 1995F — see Figure 6.11. We give SN 2002jz equal weights in the Ib and Ic categories.

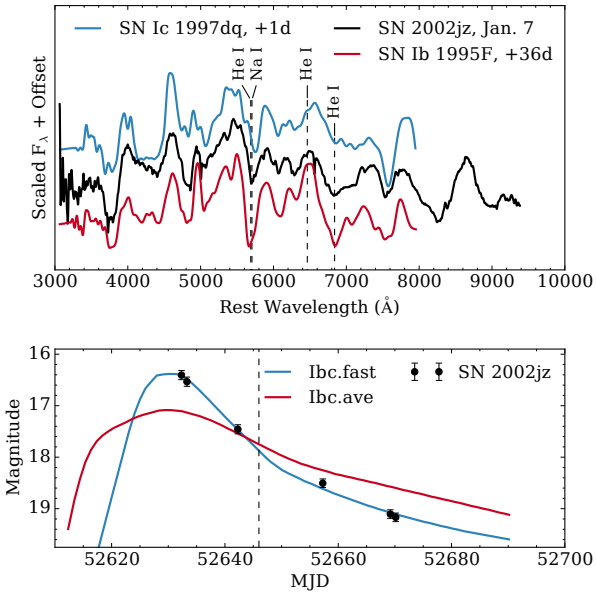

Figure 6.11: Top: spectrum of SN 2002jz from 2003-01-07 (corrected for a MW reddening of $E(B-V) = 0.4846$ mag) compared with that of SN Ic 1997dq and SN Ib 1995F (Matheson et al. 2001; Modjaz et al. 2014). Bottom: light curve of SN 2002jz compared to the stripped-envelope templates of L11, with the date of the spectrum shown with a vertical line.

SN 2003br (II $\rightarrow$ II/IIb)

SN 2003br was discovered in MCG-05-34-18 (Swift & Li 2003) and was classified as a Type II SN (Berlind et al. 2003). We present the classification spectrum of SN 2003br, but this alone is not enough to distinguish between a Type II or a Type IIb classification. The MW reddening toward the object is small ($E(B-V) = 0.0822$ mag), but the observed spectral energy distribution (SED) implies that there must be a moderate-to-large degree of host-galaxy reddening. Unfortunately, the spectrum has neither the signal nor the resolution to measure any possible narrow Na I D absorption features. Adopting a correction of $E(B-V) = 1.0$ mag appears to roughly correct the SED, and so we continue with that.

SNID indicates that the best match is with the Type IIb SN 2006T, but the Type IIP SN 1999em also shows a good match. The light curve is more similar to the Type IIL template, and so we prefer a Type II classification but cannot be sure. See Figure 6.12.

SN 2003id (Ic-pec)

SN 2003id was discovered in NGC 895 and classified as a SN Ibc-pec by Hamuy & Roth (2003), who identify several normal SN Ic lines as well as a strong blended feature around 5700 Å. Here we analyze spectra observed on Sep. 19 and Oct. 23, 2003 — see Figure 6.13. Our spectra confirm this to be an odd object with no good matches in the SNID template

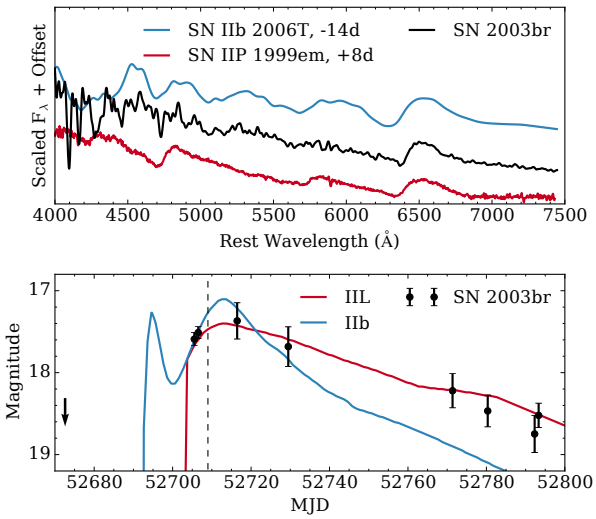

Figure 6.12: Top: spectrum of SN 2003br (corrected for $E(B-V) = 1.0$ mag and smoothed with a 40 Å Gaussian kernel), compared to that of the Type IIb SN 2006T (Modjaz et al. 2014) and the Type IIP SN 1999em (Leonard et al. 2002c) — both match well. Bottom: the light curve compared to the templates from L11, with the date of the spectrum marked.

set, though with many similarities to the peculiar SN Ib 2007uy (Roy et al. 2013; Modjaz et al. 2014).

The strong blended feature around 5700 Å persists and appears to grow stronger over time. We tentatively identify He I λ6678 at $v \approx 11,000\,\mathrm{km\,s^{-1}}$, which implies that the feature at 5700 Å may include some absorption from He I λ5876 in addition to Na I $\lambda\lambda$5890, 5896; perhaps this feature arises from multiple velocity components of these two ions. However, we find no clear sign of He I λ7065 absorption in either spectrum. (Note that these spectra have undergone a correction for telluric absorption and none of the features in them is telluric.)

We also identify a feature near 6140 Å that evolves from a strongly blended state into two clearly defined components, the redder of which is plausibly high-velocity Hα at $v \approx 17,500\,\mathrm{km\,s^{-1}}$, and we tentatively identify Hβ at $v \approx 17,500$–$18,500\,\mathrm{km\,s^{-1}}$ in the spectrum from Sep. 19. The bluer feature may be a second, even higher-velocity Hα line at $v \approx 23,500\,\mathrm{km\,s^{-1}}$; the bluemost edge of the Ca II IR triplet absorption implies similar velocities for the calcium in SN 2003id. Several authors have previously identified high-velocity Hα lines in SN Ib/c spectra (e.g., Branch et al. 2006; Elmhamdi et al. 2006; Parrent et al. 2007).

We compare the spectra of SN 2003id to the average spectra of Liu et al. (2016) in the middle panel of Figure 6.13. We estimate that the date of R-band maximum was 30 Sep. 2003, which means our two spectra were obtained at phases of -11 and $+22$ days; hence, we show the -10 d and $+20$ d average spectra. The peculiarity of SN 2003id is apparent here as well: our spectra deviate significantly from both SNe Ib and SNe Ic spectra at several wavelengths. As above, we find that the putative He I λ6678 line is SN Ib-like, while the lack of a He I λ7065 line is SN Ic-like, and the extreme widths of the Ca II and 5700 Å features are unlike both.

The light curves provide an additional wrinkle: SN 2003id distinctly shows a double-peaked evolution, with a rapid decline from the blue first peak followed by a rise to the second maximum a few days later. There is no evidence from the later spectrum that the second

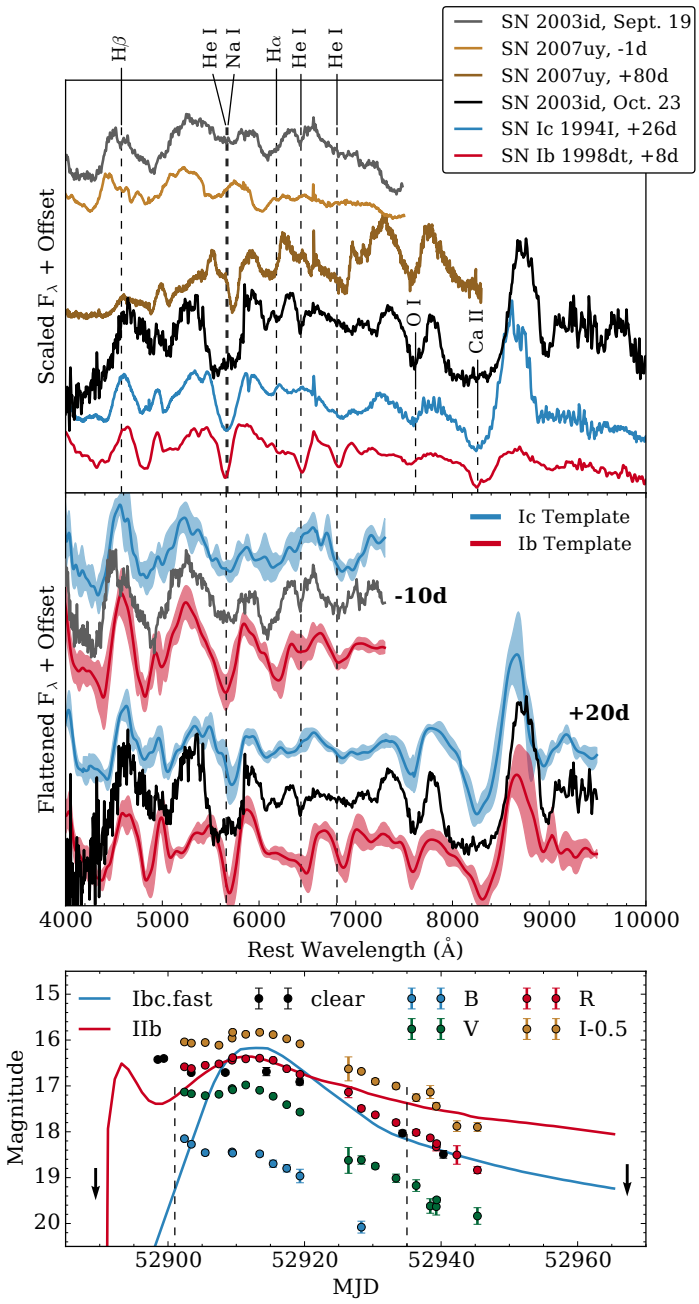

Figure 6.13: Top: spectra of SN 2003id smoothed with a 20 Å Gaussian kernel and compared to spectra of the peculiar Type Ib SN 2007uy (Modjaz et al. 2014), the normal Type Ic SN 1994I (Filippenko et al. 1995), and the normal Type Ib SN 1998dt (Matheson et al. 2001). Putative hydrogen and helium lines are marked at $v = 17,500\,\mathrm{km\,s^{-1}}$ and $11,000\,\mathrm{km\,s^{-1}}$, respectively. Middle: the continuum-normalized spectra of SN 2003id compared to the -10 d and $+20$ d average spectra of SNe Ib and SNe Ic from Liu et al. (2016), with the standard deviation shown as shaded regions and He I lines marked as above. Bottom: filtered light curves of SN 2003id, with phases of spectra marked by the dashed lines. Template SN IIb and "fast" SN Ib/c light curves from L11 are overplotted.

peak arises from interaction with dense circumstellar interaction (i.e., we find no narrow emission lines). Most SNe Ib and SNe Ic do not exhibit double-peaked light curves like those of SN 2003id, though similar behavior is often observed in SNe IIb. A very small number of double-peaked SNe Ib have been discovered (e.g., SNe 2005bf and 2008D; Tominaga et al. 2005; Folatelli et al. 2006; Modjaz et al. 2009), as has one double-peaked SN Ic (Taddia et al. 2016a). However, these events had early peaks which were notably less bright than their

main peaks, they exhibited a diversity of different peak absolute magnitudes, and none show the peculiar 5700 Å feature of SN 2003id.

Given the lack of He I λ7065 and the uncertain (and certainly peculiar) He I λ6678 Å and He I λ5876 Å lines, we classify SN 2003id as a peculiar and double-peaked SN Ic. We note that this object appears to be different from the other stripped-envelope SNe in this sample.

SN 2004bm (Ibc-pec/IIb → IIb/IIb-pec)

SN 2004bm was discovered in NGC 3437 (Armstrong et al. 2004) and originally classified as a SN Ic (though with some uncertainty; Foley et al. 2004a). L11 note that the light curve shows a dip. Though the data are sparse, the SN occurred near the core of its host galaxy, and this conclusion depends upon only one data point out of four total, our rereduction of the light curve also shows a dip indicated by the second detection — see Figure 6.14. Similar light-curve behavior has been observed in Type IIb SNe (e.g., L11; Arcavi et al. 2012), and L11 used the light curve to argue that SN 2004bm was a SN IIb.

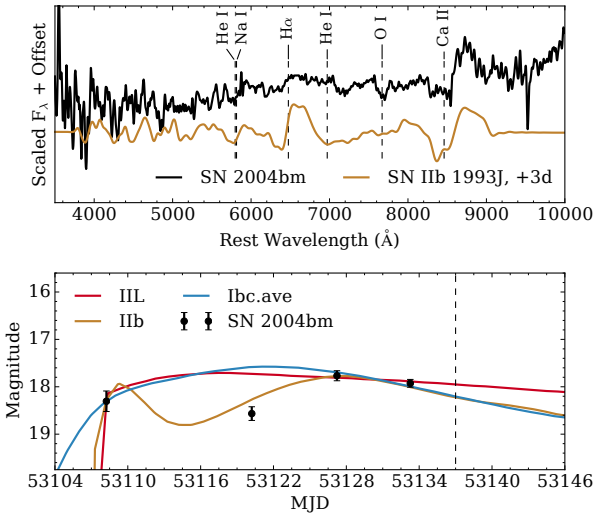

Figure 6.14: Top: spectrum of SN 2004bm smoothed with a Gaussian kernel 40 Å wide and compared to the near-maximum spectrum of the Type IIb SN 1993J (reddened by $E(B-V) = 0.4$ mag for comparison; Matheson et al. 2000b). Bottom: the light curve compared to the Type IIL, IIb, and average Ib/c template light curves from L11. A single data point indicates a light-curve dip and argues for a Type IIb classification. The date of the spectrum is marked by the vertical line.

The only spectrum we have of this SN is the one used for the original classification and it is of low quality — SNID does not provide a clear classification, but it does indicate that the best cross-correlations are with spectra of SNe IIb and IIP (though the phases are in disagreement). The spectrum of SN 2004bm does not correlate with spectra of Type Ic SNe well. Narrow Na I D absorption at the host-galaxy redshift is apparent but unresolved and very noisy, indicating moderate host-galaxy reddening atop the MW contribution of $E(B-V) = 0.0159$ mag. There are few spectral features in our spectrum, though we identify Ca II P-Cygni profiles, faint O I absorption, and a very shallow Hα P-Cygni line — see Figure 6.14.

Based on the above discussion, we prefer a classification of Type IIb for SN 2004bm, but the Hα line in the spectrum of SN 2004bm is much too weak for a normal Type IIb SN. We

also note that, if we discard the second photometric data point, the light curve of SN 2004bm is well-fit by normal Type II events or by stripped-envelope events.

SN 2004cc (Ic → Ib/Ic)

SN 2004cc was discovered in NGC 4568 (Monard & Li 2004). Matheson et al. (2004d) note the strong reddening toward SN2004cc and classify it as a Type I SN, though they prefer no subtype, while Foley et al. (2004b) present a SN Ic classification.

There is little MW reddening toward SN 2004cc ($E(B-V) = 0.0279$ mag), but the (unresolved) Na I D lines in our spectra indicate strong host-galaxy dust obscuration. The EW measured from these lines is well outside the relations of Poznanski et al. (2012), and so we only roughly estimate the total reddening, adopting $E(B-V) = 1.0$ mag for visual comparisons.

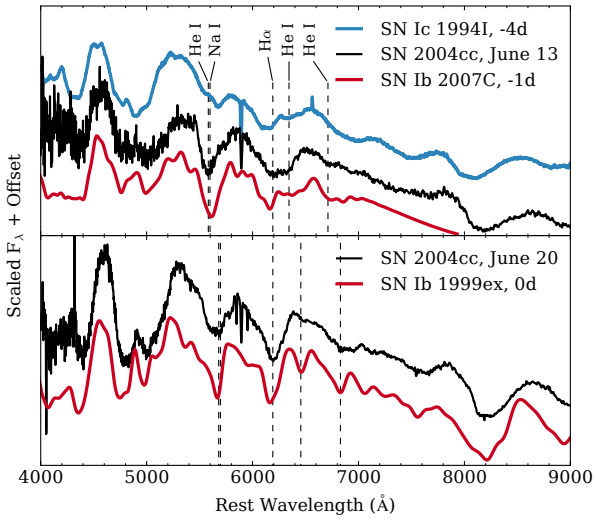

Figure 6.15: Top: spectrum of SN 2004cc observed on UT 2004-06-13 alongside premaximum spectra of SN Ic 1994I and SN Ib 2007C (Filippenko et al. 1995; Modjaz et al. 2014), and we mark He I lines at a velocity of 15,000 km s^{-1}. Bottom: spectrum of SN 2004cc observed on UT 2004-06-20 and a spectrum of the Type Ib SN 1999ex (Hamuy et al. 2002), with the helium line marked at 10,000 km s^{-1}, a deceleration consistent with the normal evolution of helium-line velocities in SNe Ib (Liu et al. 2016). Both spectra of SN 2004cc have been dereddened by $E(B-V) = 1.0$ mag.

SNID identifies reasonable correlations between the spectra of SN 2004cc and the spectra of both SNe Ib and SNe Ic, strongly disfavoring all other types and slightly preferring the Ib label over Ic. Unfortunately, we have only a single photometric detection of the SN, so there is little independent information about the phases of these spectra.

Figure 6.15 shows that the later spectrum of SN 2004cc matches that of SN Ib 1999ex quite well, while the earlier spectrum matches that of SN Ic 1994I. Weak Hα detections have been claimed for both of these events (Branch et al. 2006). Though hydrogen absorption may be present, we trust the SNID result (which prefers a Type Ib or Ic label, rather than a IIb), and we do not consider a Type IIb label for SN 2004cc — see the discussion in §6.3. Note also that, if the identification of the Hα line in Figure 6.15 is correct, it exhibits a much faster (and unchanging) Doppler velocity (∼17,000 km s^{-1}) than the He I lines (which are at ∼15,000 and ∼10,000 km s^{-1} on June 13 and June 20, respectively). This behavior is peculiar but not unique for this feature in stripped-envelope SNe (Liu et al. 2016).

The spectra of SN 2004cc present another puzzle. The early-time spectrum appears to show a strong He I λ6678 line (and a strong He I/Na I blend near 5500 Å), but very little He I λ7065 absorption. It is difficult to physically explain a strong He I λ6678 absorption line without a similarly strong λ7065 line; other ions may be contributing to this feature. Just one week later the He I λ6678 line has disappeared, though the width of the line near 5500 Å implies that He I λ5876 is still present. Given the above uncertainties and the weakness of the He I λ7065 line, we assign SN 2004cc the Ib/Ic label. Interestingly, Wellons et al. (2012) present a variable and long-lasting radio light curve, indicating the presence of a complex circumstellar medium near this object.

SN 2005H (II → II/IIb)

SN 2005H was discovered in NGC 838 (Graham et al. 2005) and classified as a Type II SN based upon a noisy spectrum (Pastorello et al. 2005a). Very few data exist on SN 2005H, and most of the spectra are entirely dominated by host-galaxy light. However, we were able to obtain the original classification spectrum (Harutyunyan et al. 2008) and we find clear detections of Hα absorption and P-Cygni profiles of Hβ and Na I on an otherwise smooth blue continuum; see Figure 6.16.

SNID shows this spectrum to be more similar to spectra of young SNe II than SNe IIb. We have very little information on the light-curve evolution of this object — the SN was discovered very near the bright ($R \approx 12 - 14$ mag) core of the host and our data are badly contaminated by galaxy light. Other than the discovery image we have no clear detections, only uninformative upper limits.

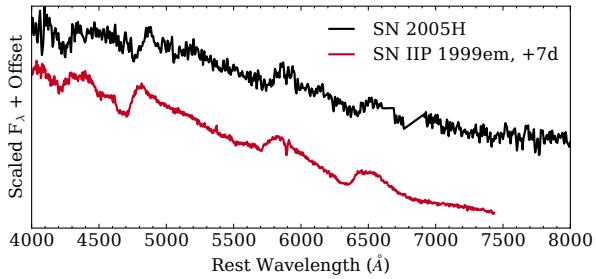

Figure 6.16: Spectrum of SN 2005H alongside a spectrum of the Type IIP SN 1999em (Leonard et al. 2002c).

SN 2005mg (II → II/IIb)

SN 2005mg was discovered in UGC 155 (Newton & Puckett 2005) and classified as a heavily reddened young Type II SN, with detections of Hα and Hβ in the noisy spectrum (Modjaz et al. 2005). We have a spectrum obtained one week later, but unfortunately we were unable to locate a digital copy of the spectrum cited above. We did, however, locate plots of both the classification spectrum and another one obtained the night prior, both in

image form.[14] Using an online tool,[15] we traced the spectra from these plots and consider the results in our analysis.

All three spectra exhibit extremely low S/N and SNID identifies no good matches. The KAIT light curve is similarly uninformative with only two detections and is consistent with template light curves of all types; see Figure 6.17. However, the spectra do appear to corroborate the Modjaz et al. (2005) classification of SN 2005mg as a Type II SN, with plausible detections of weak Hα and Hβ lines showing broad P-Cygni profiles. We therefore consider the original classification robust though we cannot determine whether SN 2005mg was a Type IIb or a normal Type II SN, and so we label it as II/IIb (unsure).

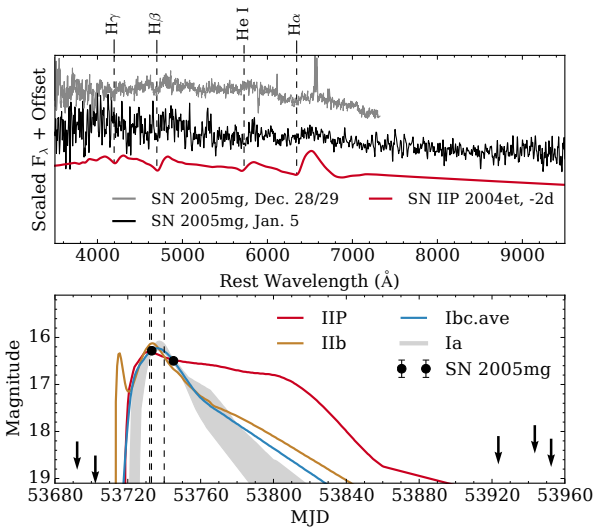

Figure 6.17: Top: spectra of SN 2005mg alongside a spectrum of the Type IIP SN 2004et (Sahu et al. 2006). In blue we show the co-addition of the traces obtained from plots of the two spectra from Dec. 2005, while in black we show the full spectrum from Jan. 2006. Bottom: the light curve compared to template light curves from L11, with the dates of spectra shown with dashed lines.

SN 2006eg (Ic → IIb/Ib/Ic/Ic-BL)

SN 2006eg was discovered in an anonymous galaxy (Madison & Li 2006) and classified as a SN Ib/c (Foley et al. 2006). SNID, GELATO, and Superfit identify no good matches, but the best cross-correlations are with spectra of SNe Ic-norm and SNe Ic-BL. The MW reddening toward SN 2006eg is small ($E(B-V) = 0.0933$ mag), and though the spectrum of SN 2006eg is noisy it does not appear that there could be more than a modest degree of host-galaxy reddening — we detect no narrow Na I D lines at the host galaxy's redshift. Our sparse and noisy light curve is most similar to that of a Type IIL SN, but it is also consistent with a stripped-envelope classification.

SN 2006eg had a peak measured magnitude of -14.86 ± 0.23 mag (unfiltered; L11), which makes the event an underluminous outlier from both the SN Ic-BL and normal SN Ib/Ic populations (L11, Drout et al. 2011). However, as Figure 6.18 shows, the true peak could

[14] https://www.cfa.harvard.edu/supernova/spectra/
[15] http://arohatgi.info/WebPlotDigitizer/app/

have occurred before discovery and the event may have been significantly more luminous at the true (unobserved) peak.

Our spectrum of SN 2006eg is not only noisy, it also exhibits a low contrast between the continuum and the SN features — this event occurred near the center of its spiral host galaxy, and it appears that our spectrum suffers from significant host-galaxy contamination (the strong, narrow absorption features are likely badly subtracted host-galaxy emission lines). It has been our experience that SNID sometimes mistakenly prefers a SN Ic-BL classification for low-contrast spectra, and so we are hesitant to assign much belief to that result.

The He I lines that mark the difference between SNe Ib and SNe Ic are, in general, time-dependent: they are most apparent soon after peak and generally fade completely away by $\sim$ 50–70 days (Modjaz et al. 2014; Liu et al. 2016). These types can be difficult to differentiate at these ages, and SNe Ic, Ib, and IIb all show strong features at the same wavelengths as those in SN 2006eg's spectrum. It is likely that our spectrum of SN 2006eg shows a nearly nebular SN IIb, Ib, or Ic "watered down" by host-galaxy contamination. If SN 2006eg was a mostly normal stripped-envelope SN discovered late, then its light curve was slowly declining, but it was not an extreme outlier from the diverse late-time decline rates observed for these SNe (e.g., Lyman et al. 2016).

Without better data, it is very difficult to firmly label SN 2006eg — our spectrum shows it was not a Type Ia or Type II SN, but it could have been a SN IIb, Ib, Ic, or Ic-BL.

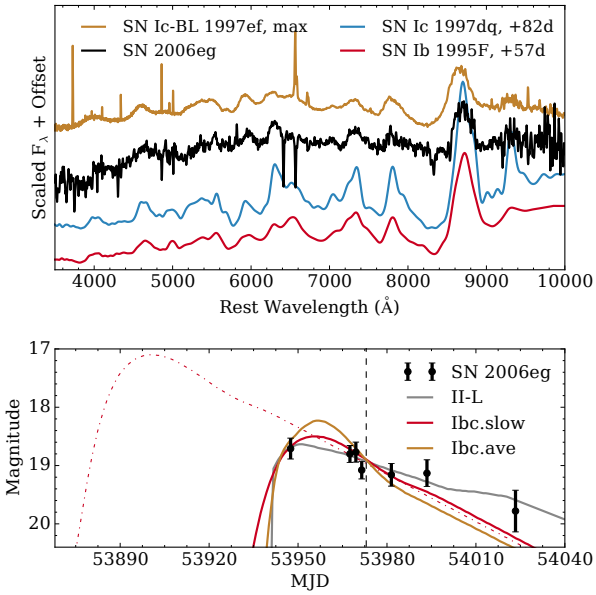

Figure 6.18: Top: spectrum of SN 2006eg (smoothed with a 20 Å Gaussian kernel) compared to that of the SN Ic-BL 1997ef, SN Ic 1997dq, and SN Ib 1995F (Matheson et al. 2001; Modjaz et al. 2014). Bottom: the light curve, with the date the spectrum was taken marked, alongside template light curves from L11. Our last prediscovery upper limit was 173 d before the first detection; though we show comparison light curves assuming the peak was observed, the true peak could have occurred months before discovery. The red dash-dot line shows the Ibc.slow template of L11 offset by 55 days, illustrating how the peak may have occurred prediscovery.

6.4.3 SNe Ia

We follow Silverman et al. (2012) when identifying the subtypes of SNe Ia, and in most cases simply duplicate the classifications from their Table 7. We propose some updated subtype classifications from L11, but no objects appear to be misclassified as SNe Ia, nor does it appear that any events labeled otherwise should be reclassified as SNe Ia.

We update the classifications of SNe 1999bh and 2002es, labeling them with the subtype "Ia-02es" as identified by Ganeshalingam et al. (2012). These events are subluminous and exhibit low expansion velocities, sharing properties with both the SN Ia-2002cx (i.e., SN Iax; Foley et al. 2013) and SN Ia-1991bg subtypes. Though L11 note that these two events may form their own subtype, they include them with the SNe Iax as the properties of the subtype were only partially understood at the time (subsequent work has furthered our understanding; e.g., Cao et al. 2015; White et al. 2015; Cao et al. 2016). Foley et al. (2013) show that SNe Iax display a wide range of peak luminosities, from the extremely subluminous SN 2008ha ($M_V \approx -14.2$ mag) up into the range of typical SNe Ia ($M_V \approx -18.5$ mag), and the rate calculations of L11 did not account for the low-luminosity members of this class and therefore underestimated the true rate of these events.

We also update several events previously labeled SNe Ia 1991T to the "SN Ia-1999aa" subtype (Garavini et al. 2004), a subclass that falls in between SNe Ia-norm and SNe Ia-1991T and another distinction intentionally not included in L11 (see Li et al. 2001). Three of these events (SNe 1998es, 1999aa, and 1999dq) were previously given a Ia-99aa label by Silverman et al. (2012). The spectral evolution of SN 1999ac was studied in detail by Garavini et al. (2005), who note that early-time spectra are similar to those of SN 1999aa with relatively weak silicon absorption, but SNID identifies both premaximum and postmaximum spectra as SN Ia-norm (Silverman et al. 2012, though Ia-99aa templates also provide reasonable fits) and subtle peculiarities exist throughout this object's evolution. Owing to this peculiarity, we give this event equal weights in the Ia-norm and Ia-99aa subclasses.

SN 2001V is grouped among the "shallow silicon" events by Branch et al. (2009), and the premaximum spectra of SN 2001V published by Blondin et al. (2012) are strongly classified as 99aa-like by SNID. The data on SN 2006cm are somewhat less conclusive and the early evolution is not well constrained. The spectra show strong Na I D absorption features from the host UGC 11723 and they are noticeably reddened by host-galaxy dust (Blondin et al. 2006; Sternberg et al. 2011). SNID prefers a SN Ia-normal classification for SN 2006cm (Silverman et al. 2012), but the spectra also exhibit good matches to those of Ia-99aa objects and the silicon absorption features are weaker than those in the SNID-preferred SN Ia-norm templates. We give SN 2006cm equal weights in the SN Ia-norm and SN Ia-99aa subclasses.

Finally, SN 2004bv is classified as a SN Ia-91T event by SNID, but unfortunately the only existing premaximum spectrum of this SN does not extend to sufficiently blue wavelengths to capture the Ca II H&K lines, which are the strongest indicator of a SN 1991T-like event at young epochs (Silverman et al. 2012, see their Fig. 5), and so this classification is somewhat suspect and this event may also have been SN 1999aa-like. These updates indicate that 91T/99aa-like events exhibit a continuum of spectroscopic properties, with normal SNe Ia

at one end and SN 1991T-like events at the other extreme; most "shallow silicon" events fall somewhere in between.

6.4.4 SNe Ic-BL

L11 grouped the broad-lined SNe Ic (SN Ic-BL, sometimes associated with gamma-ray bursts; e.g., Woosley & Bloom 2006) into the SN Ic-pec subclass, though they noted in the text that SN 2002ap is a member of that group (e.g., Mazzali et al. 2002). As discussed in §6.4.2, SNe 2002jj and 2006eg may plausibly also be of Type Ic-BL.

6.4.5 SN 1987A-like SNe

As discussed in §6.4.1, SN 2005io was very likely a SN 1987A-like event (for reviews of SN 1987A and related events, see, e.g., Arnett et al. 1989; McCray 1993). The LOSS volume-limited sample also includes the SN 1987A-like SNe 2000cb and 2005ci (Kleiser et al. 2011). All of these objects were grouped with the Type IIP SNe by L11.

6.4.6 Ca-Rich Transients

There are three examples of the recently identified class of "Ca-rich" SNe in our sample: SNe 2003H, 2003dr, and 2005E (e.g., Filippenko et al. 2003; Perets et al. 2010; Kasliwal et al. 2012; Foley 2015). All three were identified by Perets et al. (2010). Though discussed within the text as Ca-rich events, these three SNe were labeled SN Ibc-pec by L11 and were grouped with the other stripped-envelope SNe in their analysis.

Though the provenance of these events is not fully understood, it now seems likely that they do not arise from the core collapse of massive stars. Removing these three events from the sample of core-collapse SNe slightly reduces the ratio of stripped-envelope SNe relative to Type II SNe. Figure 6.19 shows spectra of all three Ca-rich SNe in the sample. We note that the photospheric spectra of these events are extremely similar to those of normal SNe Ib; it is their nebular spectra, their rapid evolution, and their low peak luminosities that primarily differentiate these events.

6.4.7 Type IIn SNe and SN Impostors

Type IIn SNe are hydrogen-rich SNe that exhibit narrow lines in their spectrum — indicative of dense circumstellar material surrounding the progenitor at the time of explosion (see, e.g., Filippenko 1989; Schlegel 1990; Chugai 1991; Smith 2014). There were seven Type IIn SNe in the sample identified by L11, but two of those (SNe 2002bu and 2006bv) were reclassified as SN impostors (luminous but nonterminal outbursts from massive stars) by Smith et al. (2011c). We group SNe 2002bu and 2006bv with the five other SN impostors from the original sample and do not include them when calculating the relative fractions of SNe.

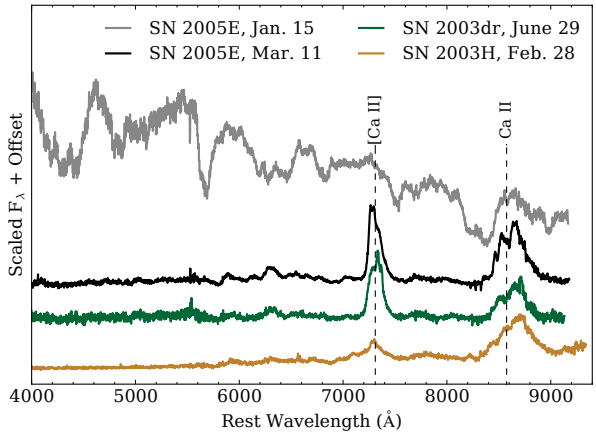

Figure 6.19: Spectra of the Ca-rich objects in our sample. For SN 2005E we present photospheric and nebular spectra; for the other objects we only have nebular spectra.

6.4.8 SNe That Lack Spectra

Every object in the L11 volume-limited sample was originally classified spectroscopically and announced through CBETs, but we have not been able to track down spectra for three events: see Table 6.2 and Figure 6.20. One of these (SN 2002ds) exhibits a light curve with a pronounced plateau, which corroborates the original CBET classification of a Type II SN. The light curve of SN 2003bw, however, does not rule out the possibility that this event was a low-hydrogen Type IIb SN (assuming that the hydrogen detection announced in the CBET is robust; Hamuy 2003b). For SN 2006bv we adopt the SN impostor reclassification of Smith et al. (2011c).

Table 6.2: SNe That Lack Spectra

Name	Previous (L11)	This Work	Ref.
SN 2002ds	IIP	II	1
SN 2003bw	IIP	II/IIb	2
SN 2006bv	IIn	*impostor*	3,4

References: [1] Li et al. (2002b); [2] Hamuy (2003b); [3] Sehgal et al. (2006); [4] Smith et al. (2011c)

6.5 Updated Fraction Calculations

Figure 6.21 and Table 6.3 summarize our updated fraction calculations. We follow L11 to estimate our uncertainties, running 10^6 Monte Carlo realizations of the sample assuming Poisson statistics and the control-time corrections from L11, Leaman et al. (2011), and Li et al. (2011a). (Note that the stated uncertainties are statistical only.) We do not recalculate the control times for each event after these updated classifications. Almost all of our updates

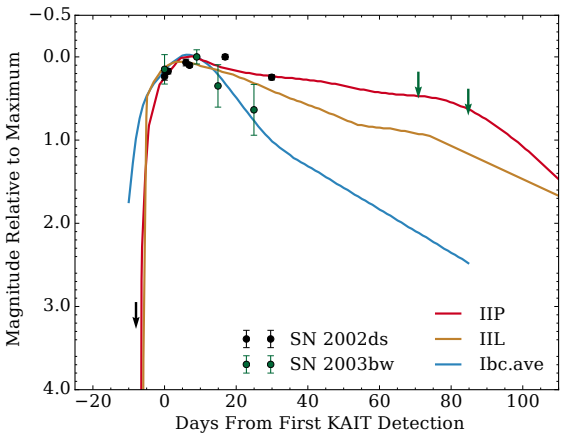

Figure 6.20: Unfiltered light curves for two SNe for which we have not been able to collect spectra, along with template light curves from L11 for comparison. Upper limits are shown with arrows. For SN 2002ds, the CBET classification of a Type II SN with a hydrogen-recombination plateau is robustly supported. The light curve of SN 2003bw appears to match the stripped-envelope template from L11 better than the Type II templates, but the data are noisy and are consistent with either classification. SN 2006bv (not shown) was likely a SN impostor; see Smith et al. (2011c).

are swaps between stripped-envelope subtypes which show very similar light curves, and so the control-time calculations should change very little. For events with more than one possible classification listed in Table 6.1 we assign a fractional weight to each given the relative frequencies of the subtypes among the well-classified events.

Many authors, based on both theory and observation, argue for trends in the relative SN rates as a function of metallicity (e.g., Modjaz et al. 2008b; Arcavi et al. 2010; Modjaz et al. 2011; Kelly & Kirshner 2012; Yoon 2015). Adopting the metallicity-luminosity relation of Garnett (2002) and noting that the galaxies hosting core-collapse SNe within the LOSS sample cover a range of luminosities of $M_K \approx -22$ to -25 mag, Smith et al. (2011b) estimate metal abundances of ~ 0.5–$2.0\,Z_\odot$ for these galaxies, and our results are therefore applicable to roughly that range. Graur et al. (2017a,b) use the LOSS sample and our updated classifications to examine correlations between SN rates and host galaxy properties in more detail, including the stellar masses, specific star-formation rates, and oxygen abundances (i.e., metallicities) of the host galaxies. Several authors have shown that local measures of host-galaxy metallicities are more informative than global ones (e.g., Modjaz et al. 2008b; Anderson et al. 2010; Modjaz et al. 2011; Anderson et al. 2016); a study of the explosion-site metallicities of the LOSS sample is a worthy endeavor we leave to future work.

As with L11, our calculations for several of the rarer subtypes suffer from the effects of small-number statistics, but Table 6.3 and Figure 6.21 indicate an important update: the percentage of SNe Ic is reduced while the percentage of SNe Ib is increased. Adopting our updated classifications, 83% of our Monte Carlo trials indicate that normal SNe Ib are more common than normal SNe Ic, while 99% of the trials using the L11 classifications indicate the opposite.

L11 and Smith et al. (2011b) found that SNe Ic are more than twice as common as SNe Ib (grouping the SNe Ic-BL with the SNe Ic, which only affects these rates by a small amount). L11 calculate a ratio of SNe Ic/SNe Ib $= 54.2 \pm 9.8\%/21.2^{+8.4}_{-7.7}\% = 2.6 \pm 1.1$, while

Table 6.3: Updated Relative SN Fractions in a Volume-Limited Survey

Type	Previous	This Work	Difference
	Core Collapse		
II	$68.9^{+6.0}_{-6.0}$	$69.6^{+6.7}_{-6.7}$	-
IIb+Ib+Ic	$31.1^{+4.6}_{-4.6}$	$30.4^{+5.0}_{-4.9}$	-
	Stripped Envelope		
IIb	$27.6^{+9.1}_{-9.1}$	$34.0^{+11.1}_{-11.1}$	+6.3
IIb-pec	-	$2.0^{+1.5}_{-2.0}$	-
Ib	$16.1^{+6.8}_{-6.6}$	$35.6^{+11.4}_{-11.4}$	+19.5
Ib-pec	-	-	-
Ibc-pec$^{\alpha}$	$12.4^{+5.9}_{-5.6}$	-	-
Ic	$41.1^{+11.5}_{-11.4}$	$21.5^{+8.6}_{-8.6}$	−19.6
Ic-pec	$2.8^{+2.6}_{-2.8}$	$3.2^{+3.1}_{-3.2}$	-
Ic-BL	-	$3.7^{+2.9}_{-3.7}$	-
	Hydrogen Rich		
II$^{\beta}$	$93.2^{+11.5}_{-11.3}$	$89.1^{+10.9}_{-10.9}$	-
II-87A	-	$4.2^{+2.4}_{-2.7}$	-
IIn	$6.8^{+3.0}_{-2.9}$	$6.7^{+3.0}_{-2.9}$	-

Relative fractions of core-collapse SNe in the LOSS volume-limited sample, within several different subsets, expressed in percentages. In the left column we present the fractions assuming the original classifications used by L11, in the center column we present our updated fractions, and in the right column we highlight the most notable updates.
$^{\alpha}$L11 included SNe Ic-BL and Ca-Rich transients with the Ibc-pec class. In our updated fractions we list the SNe Ic-BL seperately, and we do not group the Ca-Rich events with core-collapse SNe.
$^{\beta}$Including the II-L and II-P subclasses of L11.

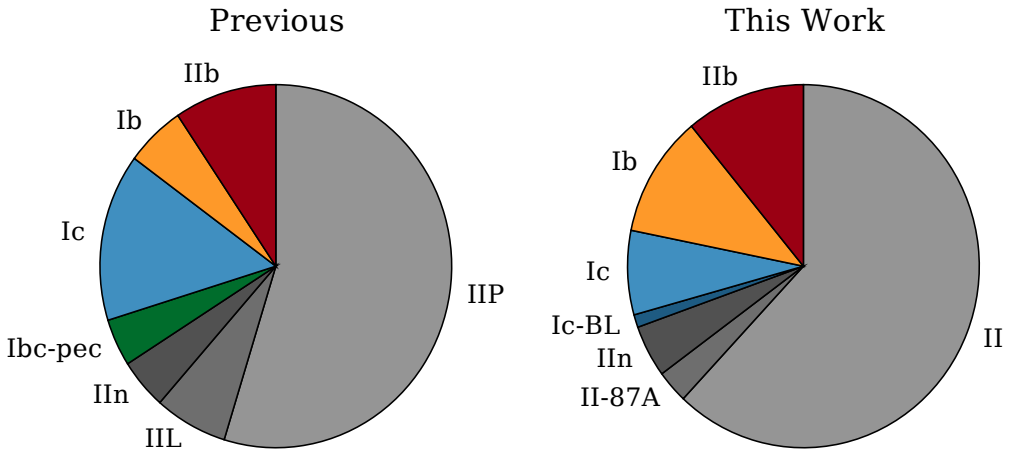

Figure 6.21: Relative fractions of core-collapse SN types within a volume-limited sample using the original classifications from L11 (left) compared to the updated classifications presented here (right). Subtypes are color-coded along with the other members of their major type, and the "peculiar" subtype labels are grouped with the appropriate "normal" events (except for the SN Ibc-pec group of L11, which included both SNe Ic-BL and Ca-Rich transients). All fractions are listed in Table 6.3 and any objects listed in Table 6.1 with more than one possible classification are given a fractional weight in each class, as described in §6.5.

Smith et al. (2011b, excluding SNe from highly inclined galaxies) calculated SNe Ic/Ib = $14.9^{+4.2}_{-3.8}\%/7.1^{+3.1}_{-2.6}\% = 2.1 \pm 1.1$ (in all cases the errors listed are statistical only, and were derived from Monte Carlo simulations similar to those described above).

We now calculate a ratio of normal SNe Ic to normal SNe Ib of 0.6 ± 0.3 and, if we include the SNe Ic-BL and other peculiar subtypes with the normal SNe Ib and Ic, we find a (SN Ic+Ic-BL+Ic-pec)/SN Ib ratio of 0.8 ± 0.4.

This update to the population fractions is driven by our reclassifications of seven stripped-envelope events. First, we relabeled four events from a Ic subtype to a Ib or IIb subtype (SNe 2001M, 2001ci, 2004C, and 2005lr). In each of these cases, the need for reclassification is easily understood: three of these events had spectra severely reddened by host-galaxy dust and were originally classified by eye without the aid of SNID, and one showed only weak He I lines in the spectrum (SN 2001M). Second, we created the SN Ib/Ic (unsure) category, which includes an additional two events that show weak He I lines with some uncertainty on their identification (SNe 2002jz and 2004cc) and one event with only sparse and noisy observations (SN 2006eg). If we assume that all of the SNe in the latter category deserve the Ic label, our Monte Carlo trials indicate that normal SNe Ib and SNe Ic (excluding peculiar subtypes) occur at similar rates: SNe Ic/Ib $= 0.9 \pm 0.5$. If we rather assume that they are

all SNe Ib, we get a ratio of normal SNe Ic/Ib $= 0.5 \pm 0.3$.

These results have implications for our understanding of the progenitors of stripped-envelope SNe, as we discuss below, and may affect other works that use the LOSS rates as input (e.g., Foley & Mandel 2013).

6.6 Progenitor Constraints on Stripped-Envelope SNe

Wolf-Rayet (WR) stars have long been discussed as Galactic analogues of SN Ib/c progenitors (e.g., Meynet & Maeder 2003; Crowther 2007), though many authors have argued that binary stars which undergo mass loss via Roche-lobe overflow before core collapse are likely the most common SN Ib/c progenitor (e.g., Podsiadlowski et al. 1992; Smartt 2009; Smith et al. 2011b; Eldridge et al. 2013). Regardless, stellar modeling efforts have found it difficult to match the SN Ic/Ib fractions presented by L11 and Smith et al. (2011b), which demand more SN Ic progenitors (stars that lose both their hydrogen envelope and a large fraction of their helium envelopes) than Ib progenitors (stars that lose just the hydrogen; e.g., Georgy et al. 2009; Yoon et al. 2010; Yoon 2015), though some success has been achieved by invoking rapid rotation of the progenitors (e.g., Cao et al. 2013; Groh et al. 2013c).

To address this putative issue, some authors have proposed that some amount of helium in SNe Ic may be "hidden" and remain neutral if the ^{56}Ni (which provides nonthermal excitations via radioactive decay) is insufficiently mixed with the helium-rich ejecta (e.g., Dessart et al. 2011, 2012). Comparisons to observation do not find evidence for large amounts of hidden helium in SNe Ic, however, and it is unclear from the models how much helium could truly be hidden in this way (e.g., Hachinger et al. 2012; Taddia et al. 2015; Liu et al. 2016). Our updated stripped-envelope fractions argue that this problem is less egregious than previously indicated.

Other discrepancies have arisen within the single WR-like progenitor scenario. The observed ejecta masses of normal SNe Ib/c ($M_{\rm ej} \approx 2.0$–$4\,{\rm M}_\odot$; Drout et al. 2011; Cano 2013; Lyman et al. 2016) are not in good agreement with the estimated masses of WR stars at the time of core collapse ($M \gtrsim 10\,{\rm M}_\odot$; Meynet & Maeder 2003; Yoon 2015), assuming that most SNe Ib/c produce neutron star remnants rather than black hole remnants. Note that SNe Ic-BL may have larger ejecta masses, and so this reasoning holds for normal SNe Ib/c only (Cano 2013). In addition, the rates of SNe Ib/c compared to those of Type II SNe are inconsistent with WR star progenitors (the incidence rate of WR stars is too low to explain the high fraction of SNe Ib/c; e.g., Smith et al. 2011b), and the search for SN Ib/c progenitors in pre-explosion images has, in several instances, ruled out normal WR stars (Eldridge et al. 2013, though see also Groh et al. 2013c).

The binary progenitor system scenario for normal SNe Ib/Ic does not suffer from the same problems. The modeled masses at the time of core collapse for post-mass-transfer binary members are generally in agreement with the observed SN Ib/c ejecta masses (Eldridge et al. 2013; Yoon 2015), constraints from SN Ib/c progenitor searches are largely compatible with binary progenitors (Eldridge et al. 2013), and the identified progenitors of some SNe IIb have

been shown to be the products of binary evolution (SNe 1993J and 2011dh; e.g., Maund et al. 2004, 2011; Van Dyk et al. 2011; Bersten et al. 2012).

Sana et al. (2012) show that more than 70% of O-type stars (zero-age main sequence $M \gtrsim 15\,M_\odot$) are formed in binary pairs that will undergo significant binary interaction (either mass gain or mass stripping) before core collapse, and so the population of core-collapse SN progenitors must necessarily be dominated by post-binary-interaction stars. We calculate a stripped-envelope fraction of $30 \pm 5\%$ amongst all core-collapse SNe, similar to fractions found by previous authors. As Smith et al. (2011b) note, this value is in remarkably good agreement with the $\sim$33% of O-type stars in our Galaxy found to experience envelope stripping via binary interaction before their deaths (Sana et al. 2012).

6.7 Conclusion

We have re-examined every SN classification within the LOSS volume-limited sample published by L11, have discussed the peculiar and rare events within the sample, and have found that several of the stripped-envelope SNe originally labeled as SNe Ic show clear signatures of helium and (in two cases) hydrogen. After relabeling these SNe as Type Ib or IIb appropriately, and discussing the intrinsically peculiar events and those for which we cannot assign a clear classification, we recalculate the implied fractions of these subtypes. We find that the relative fractions of Type Ia SNe, Type II SNe, and stripped-envelope SNe are unchanged, but the relative fractions between different stripped-envelope SN subtypes are.

Based on the prior spectral identifications, L11 and Smith et al. (2011b) found that SNe Ic are roughly twice as common as SNe Ib. We show that this measurement was hampered by the above misclassifications and, additionally, that the SN Ib/SN Ic ratio is strongly dependent on exactly where one draws the line between these subclasses. We find that SNe Ib are at least as common as SNe Ic in the local universe and in fact are likely to be more common. We present a best-estimate normal SN Ic/SN Ib ratio of 0.6 ± 0.3 — i.e., spectroscopically normal SNe Ib occur in the local universe 1.7 ± 0.9 times more often than do normal SNe Ic.

Other efforts (e.g., Smartt et al. 2009; Eldridge et al. 2013) found SN Ic/SN Ib ratios similar to those of L11, and we believe they may also have been plagued by systematically mislabeled stripped-envelope events. The updated stripped-envelope SN fractions published here should prove important for constraining the elusive progenitors of the various subtypes of stripped-envelope SNe, and we hope the public release of these data will be useful when exploring this valuable sample going forward.

6.8 Journal of Data Presented Here

Table 6.4 lists all light curves rereduced from images and published here, including data for 20 SNe. Table 6.5 lists every spectrum published here for the first time: a total of 151 spectra of 71 SNe. See §6.2 for a description of the observing and data-acquisition efforts. All data will be made public via the Berkeley SNDB (http://heracles.astro.berkeley.edu/sndb), WiseREP (http://wiserep.weizmann.ac.il), and the Open Supernova Catalog (https://sne.space/).

Table 6.4: Log of Light Curves Published Herein

SN Name	Telescope	Filters	N Detections	Date Range
SN 2000N	KAIT	clear	9	2000-03-04 – 2000-06-03
SN 2001J	KAIT	clear	2	2001-01-15 – 2001-01-16
SN 2001M	KAIT	clear	4	2001-01-21 – 2001-02-03
SN 2001ci	KAIT	clear	8	2001-04-25 – 2001-05-12
SN 2002ds	KAIT	clear	6	2002-06-25 – 2002-07-25
SN 2002jj	KAIT	clear	6	2002-10-24 – 2003-01-17
SN 2002jz	KAIT	clear	6	2002-12-24 – 2003-01-31
SN 2003bk	KAIT	clear	6	2003-02-28 – 2003-05-31
SN 2003br	KAIT	clear	8	2003-03-07 – 2003-06-03
SN 2003bw	KAIT	clear	4	2003-03-03 – 2003-03-28
SN 2003id	KAIT,Nickel	B,V,R,I,clear	8	2003-09-16 – 2003-10-28
SN 2004C	KAIT	clear	9	2004-01-21 – 2004-05-22
SN 2004al	KAIT	clear	5	2004-03-03 – 2004-04-22
SN 2004bm	KAIT	clear	4	2004-04-13 – 2004-05-08
SN 2004er	KAIT	clear	15	2004-09-25 – 2005-02-07
SN 2005ci	KAIT	clear	20	2005-06-10 – 2006-05-02
SN 2005io	KAIT	clear	13	2005-11-03 – 2006-02-24
SN 2005lr	KAIT	clear	5	2005-12-04 – 2006-01-06
SN 2005mg	KAIT	clear	2	2005-12-29 – 2006-01-10
SN 2006eg	KAIT	clear	7	2006-07-31 – 2006-10-15

Table 6.5: Log of Spectra Published Herein

SN Name	UT Date	Instrument[β]	WL Range (Å)	Resolution[γ] (Å)	Source[β]
SN 1999an	1999-03-10	OMR	3610–8580	10	NAOC
SN 1999br	1999-04-24.0	Kast	4300–7000	6/5	UCB
SN 1999bu	1999-04-18.21	FAST	3720–7540	7	CfA
SN 1999cd	1999-05-15.32	FAST	3720–7540	7	CfA
SN 1999cd	1999-05-16.27	FAST	3720–7540	7	CfA
SN 1999el	1999-11-05.0	Kast	3380–10,460	6/11	UCB
SN 1999gi	1999-12-10.0	Kast	3720–7540	6/5	UCB
SN 1999gi	1999-12-12.0	Kast	3720–7540	6/5	UCB
SN 1999gi	1999-12-13.0	Kast	3720–7540	6/5	UCB
SN 1999gi	2000-01-05.0	Kast	3720–7540	6/5	UCB
SN 1999gi	2000-01-10.0	Kast	3720–7540	6/5	UCB
SN 1999gi	2000-01-13.0	Kast	3720–7540	6/5	UCB
SN 1999gi	2000-03-04.0	Kast	3720–7540	6/5	UCB
SN 1999gi	2000-03-08.0	Kast	3720–7540	6/5	UCB
SN 1999gi	2000-03-15.0	Kast	3300–10,500	6/11	UCB
SN 1999gi	2000-03-25.0	LRIS	4380–6840	7	UCB
SN 1999gi	2000-03-29.0	Kast	3300–10,500	6/11	UCB
SN 1999gi	2000-04-25.0	Kast	3720–7540	6/5	UCB
SN 1999gi	2000-04-27.0	Kast	3300–10,350	6/11	UCB
SN 1999gi	2000-05-10.0	Kast	3720–7540	6/5	UCB
SN 1999gi	2000-05-26.0	Kast	3720–7540	6/5	UCB
SN 1999go	1999-12-28	DFOSC	3330–9040	14	Asiago
SN 1999go	1999-12-29	DFOSC	3330–9040	14	Asiago
SN 1999go	2000-01-02.23	FAST	3720–7540	7	CfA
SN 2000C	2000-01-25	B&C$_{1.2}$	4490–9090	22	Asiago
SN 2000C	2000-01-27	AFOSC	3520–7560	18	Asiago
SN 2000C	2000-01-28.14	FAST	3720–7540	7	CfA
SN 2000C	2000-01-29	AFOSC	3520–7490	18	Asiago
SN 2000C	2000-01-29.20	FAST	3720–7540	7	CfA
SN 2000C	2000-02-01	AFOSC	3550–7490	18	Asiago
SN 2000C	2000-02-05.25	FAST	3720–7540	7	CfA
SN 2000C	2000-02-11	AFOSC	3620–7590	18	Asiago
SN 2000L	2000-03-01.29	FAST	3720–7540	7	CfA

Table 6.5 (cont'd): Log of Spectra Published Herein

SN Name	UT Date	Instrument[β]	WL Range (Å)	Resolution[γ] (Å)	Source[β]
SN 2000L	2000-03-15.0	Kast	3300–10,500	6/11	UCB
SN 2000N	2000-03-08.43	FAST	3720–7540	7	CfA
SN 2000N	2000-03-09	DFOSC	3850–6840	6	Asiago
SN 2000N	2000-03-13	DFOSC	3550–9040	11	Asiago
SN 2000el	2000-11-29.0	Kast	3300–10,450	6/11	UCB
SN 2000eo	2000-12-21.0	Kast	3250–7810	6/5	UCB
SN 2000ex	2000-11-28.29	FAST	3760–7540	7	CfA
SN 2000ex	2000-11-29.0	Kast	3300–7800	6/5	UCB
SN 2001J	2001-01-19.45	FAST	3720–7540	7	CfA
SN 2001K	2001-03-30.0	Kast	3300–7800	6/5	UCB
SN 2001M	2001-02-01.0	Kast	3260–10,600	6/11	UCB
SN 2001Q	2001-02-01.0	Kast	3260–10,600	6/11	UCB
SN 2001ac	2001-03-14.45	FAST	3720–7540	7	CfA
SN 2001ac	2001-03-25.36	MMT-Blue	3250–8850	8	CfA
SN 2001ci	2001-05-30.285	ESI	3920–10,190	0.5	UCB
SN 2001fz	2001-11-19.50	FAST	3720–7540	7	CfA
SN 2001hf	2002-01-14.0	Kast	3260–7940	6/5	UCB
SN 2001is	2002-01-06.29	FAST	3720–7540	7	CfA
SN 2001is	2002-01-07.31	FAST	3720–7540	7	CfA
SN 2001is	2002-01-08	AFOSC	3360–7720	25	Asiago
SN 2001is	2002-01-09	AFOSC	3360–7720	25	Asiago
SN 2001is	2002-01-14.0	Kast	3260–10,570	6/11	UCB
SN 2002J	2002-02-11.0	Kast	3300–10,400	6/11	UCB
SN 2002J	2002-02-14.0	LRIS	3950–8830	7	UCB
SN 2002ce	2002-04-12.18	FAST	3720–7520	7	CfA
SN 2002ce	2002-05-07.0	Kast	3300–10,300	6/11	UCB
SN 2002dq	2002-08-09.0	Kast	3150–10,400	6/11	UCB
SN 2002gw	2002-10-29	LDSS-2	3600–9000	13.5	Asiago
SN 2002jj	2002-12-05.35	FAST	3720–7520	7	CfA
SN 2002jj	2002-12-12.0	Kast	3170–10,400	6/11	UCB
SN 2002jj	2003-01-28.0	Kast	3290–10,400	6/11	UCB
SN 2002jz	2003-01-07.0	LRIS	3080–9430	7	UCB
SN 2002jz	2003-01-28.0	Kast	3310–10,400	6/11	UCB

Table 6.5 (cont'd): Log of Spectra Published Herein

SN Name	UT Date	Instrument[β]	WL Range (Å)	Resolution[γ] (Å)	Source[β]
SN 2002jz	2003-02-28.0	LRIS	3120–9420	7	UCB
SN 2003E	2003-01-28.0	Kast	3270–10,400	6/11	UCB
SN 2003G	2003-01-28.0	Kast	3100–10,400	6/11	UCB
SN 2003G	2003-02-04.0	Kast	3100–10,400	6/11	UCB
SN 2003G	2003-02-28.0	LRIS	3040–9420	7	UCB
SN 2003H	2003-02-04.0	Kast	3210–10,400	6/11	UCB
SN 2003H	2003-02-28.0	LRIS	3170–9420	7	UCB
SN 2003aa	2003-02-04.0	Kast	3120–10,400	6/11	UCB
SN 2003aa	2003-02-28.0	LRIS	3050–9420	7	UCB
SN 2003aa	2003-04-08.0	Kast	3200–10,400	6/11	UCB
SN 2003aa	2003-05-25.0	LRIS	3220–9420	7	UCB
SN 2003ao	2003-02-22.31	FAST	3720–7540	7	CfA
SN 2003bk	2003-03-04	EFOSC	3380–10,030	14	Asiago
SN 2003br	2003-03-11.48	FAST	3720–7540	7	CfA
SN 2003dr	2003-06-29.0	LRIS	3250–9200	7	UCB
SN 2003dv	2003-07-06.366	Kast	3300–10,500	6/11	UCB
SN 2003ed	2003-05-25.0	LRIS	3220–9420	7	UCB
SN 2003ed	2003-05-30.0	Kast	3230–10,400	6/11	UCB
SN 2003ed	2003-06-07.378	Kast	3600–10,300	6/11	UCB
SN 2003ed	2003-07-06.329	Kast	3350–10,310	6/11	UCB
SN 2003ed	2003-09-03.0	Kast	3250–10,400	6/11	UCB
SN 2003ef	2003-05-21.19	FAST	3720–7540	7	CfA
SN 2003id	2003-09-19.41	FAST	3720–7540	7	CfA
SN 2003id	2003-10-23.432	Kast	3830–10,500	6/11	UCB
SN 2003ld	2004-01-13.16	FAST	3720–7540	7	CfA
SN 2004C	2004-01-15.50	FAST	3720–7540	7	CfA
SN 2004C	2004-01-17.0	Kast	3320–10,400	6/11	UCB
SN 2004C	2004-01-18.49	MMT-Blue	3270–8460	8	CfA
SN 2004C	2004-01-18.49	MMT-Blue	3720–7540	8	CfA
SN 2004C	2004-01-19.44	FAST	3720–7520	7	CfA
SN 2004C	2004-03-16.599	LRIS	3350–9230	7	UCB
SN 2004C	2004-03-17.40	FAST	3720–7540	7	CfA
SN 2004C	2004-04-26.336	LRIS	3150–9410	7	UCB

Table 6.5 (cont'd): Log of Spectra Published Herein

SN Name	UT Date	Instrument[β]	WL Range (Å)	Resolution[γ] (Å)	Source[β]
SN 2004C	2004-11-14.0	LRIS	3070–9400	7	UCB
SN 2004al	2004-03-13.26	FAST	3720–7540	7	CfA
SN 2004aq	2004-03-16.618	LRIS	3420–9230	7	UCB
SN 2004be	2004-04-13.22	FAST	3720–7540	7	CfA
SN 2004bm	2004-05-12.226	Kast	3390–10,580	6/11	UCB
SN 2004cc	2004-06-13.241	Kast	3320–10,400	6/11	UCB
SN 2004cc	2004-06-20.0	Kast	3300–10,400	6/11	UCB
SN 2004ci	2004-06-20.0	Kast	3300–10,400	6/11	UCB
SN 2004dd	2004-07-18.0	Kast	3300–10,400	6/11	UCB
SN 2004dk	2004-08-08.0	Kast	3310–10,400	6/11	UCB
SN 2004dk	2004-08-16.174	Kast	3320–10,400	6/11	UCB
SN 2004dk	2004-09-10.154	Kast	3310–10,500	6/11	UCB
SN 2004dk	2004-09-24.15	Kast	3320–10,500	6/11	UCB
SN 2004dk	2005-05-11.568	LRIS	3100–9350	7	UCB
SN 2004er	2004-10-24	LDSS-2	3600–8990	13.5	CSP
SN 2004fc	2004-12-17.168	Kast	3320–10,600	6/11	UCB
SN 2004fx	2004-11-14.0	LRIS	3080–9400	7	UCB
SN 2004fx	2004-12-17.342	Kast	3340–10,550	6/11	UCB
SN 2004gq	2004-12-12.482	LRIS	3200–9320	7	UCB
SN 2004gq	2004-12-13	WFCCD	3800–9230	6	CSP
SN 2004gq	2004-12-17.317	Kast	3370–10,300	6/11	UCB
SN 2004gq	2005-01-16.287	Kast	3300–10,500	6/11	UCB
SN 2004gq	2005-02-12.395	LRIS	3780–9250	7	UCB
SN 2004gq	2005-03-11.29	LRIS	3400–9260	7	UCB
SN 2005E	2005-01-15.353	LRIS	3380–9250	7	UCB
SN 2005E	2005-02-01.125	Kast	3310–10,500	6/11	UCB
SN 2005E	2005-03-11.257	LRIS	3400–9260	7	UCB
SN 2005H	2005-01-17.113	Kast	3300–10,500	6/11	UCB
SN 2005H	2005-03-11.238	LRIS	3390–9260	7	UCB
SN 2005J	2005-02-04	WFCCD	3800–9230	6	CSP
SN 2005ad	2005-03-11.222	LRIS	3400–9260	7	UCB
SN 2005an	2005-03-15	WFCCD	3800–9230	6	CSP
SN 2005aq	2005-03-11.284	LRIS	3400–9260	7	UCB

Table 6.5 (cont'd): Log of Spectra Published Herein

SN Name	UT Date	Instrument[β]	WL Range (Å)	Resolution[γ] (Å)	Source[β]
SN 2005bb	2005-04-07	WFCCD	3800–9230	6	CSP
SN 2005io	2005-11-05.636	LRIS	3200–9240	7	UCB
SN 2005lr	2005-12-18	EMMI	4000–10,200	9	CSP
SN 2005lr	2005-12-20	WFCCD	3800–9230	6	CSP
SN 2005mg	2005-12-28	FAST	3490–7400	7	CfA
SN 2005mg	2005-12-29.12	FAST	3490–7420	7	CfA
SN 2005mg	2006-01-05.145	Kast	3310–10,500	6/11	UCB
SN 2006F	2006-01-16	EMMI	4000–10,200	9	CSP
SN 2006T	2006-02-13	EMMI	4000–10,200	9	CSP
SN 2006T	2006-02-22.32	Kast	3320–10,300	6/11	UCB
SN 2006be	2006-03-30	WFCCD	3800–9230	6	CSP
SN 2006be	2006-05-05.419	Kast	3350–10,400	6/11	UCB
SN 2006bp	2006-04-28.26	Kast	3320–10,500	6/11	UCB
SN 2006ca	2006-05-05.399	Kast	3350–10,400	6/11	UCB
SN 2006ca	2006-06-20.367	Kast	3330–10,580	6/11	UCB
SN 2006ca	2006-07-04.363	Kast	3310–10,700	6/11	UCB
SN 2006eg	2006-08-24.399	Kast	3320–10,400	6/11	UCB
SN 2006qr	2006-12-01.49	Kast	3310–10,500	6/11	UCB
SN 2006qr	2006-12-13	B&C$_{2.5}$	3620–9820	8	CSP

Note. — [β]See §6.2 for a description of the instruments and observational efforts listed here.
[γ]Listed resolutions are estimates of the average resolution for the instrument (if two resolutions are given, they refer to the blue side and red side of the spectrograph separately).
[δ]Traced from image of plot; see §6.4.2.

Bibliography

Aazami, A. B., & Li, W. D. 2001, IAU Circ., 7568
Allington-Smith, J., Breare, M., Ellis, R., et al. 1994, PASP, 106, 983
Andersen, J., Andersen, M. I., Klougart, J., et al. 1995, The Messenger, 79, 12
Anderson, J. P., Covarrubias, R. A., James, P. A., Hamuy, M., & Habergham, S. M. 2010, MNRAS, 407, 2660
Anderson, J. P., González-Gaitán, S., Hamuy, M., et al. 2014, ApJ, 786, 67
Anderson, J. P., Gutiérrez, C. P., Dessart, L., et al. 2016, A&A, 589, A110
Anupama, G. C., Sivarani, T., & Pandey, G. 2001, A&A, 367, 506
Arcavi, I., Gal-Yam, A., Kasliwal, M. M., et al. 2010, ApJ, 721, 777
Arcavi, I., Gal-Yam, A., Yaron, O., et al. 2011, ApJ, 742, L18
Arcavi, I., Gal-Yam, A., Cenko, S. B., et al. 2012, ApJ, 756, L30
Arcavi, I., Wolf, W. M., Howell, D. A., et al. 2016, ApJ, 819, 35
Armstrong, M., Singer, D., Burket, J., & Li, W. 2004, IAU Circ., 8335, 1
Arnett, D. 1996, Supernovae and Nucleosynthesis (Princeton University Press)
Arnett, W. D. 1971, ApJ, 163, 11
—. 1982, ApJ, 253, 785
Arnett, W. D., Bahcall, J. N., Kirshner, R. P., & Woosley, S. E. 1989, ARA&A, 27, 629
Athem Alsabti, A. 2015, IAU General Assembly, 22, 2253696
Auer, L. H., & van Blerkom, D. 1972, ApJ, 178, 175
Axelrod, T. S. 1980, PhD thesis, Univ. California, Santa Cruz
Baek, M., & Li, W. 2005, IAU Circ., 8641
Barbon, R., Ciatti, F., & Rosino, L. 1979, A&A, 72, 287
Baron, D., Poznanski, D., Watson, D., Yao, Y., & Prochaska, J. X. 2015, MNRAS, 447, 545
Beckmann, S., & Li, W. D. 2001, IAU Circ., 7564, 2
Ben-Ami, S., Konidaris, N., Quimby, R., et al. 2012, in Proc. SPIE, Vol. 8446, Ground-based and Airborne Instrumentation for Astronomy IV, 844686
Benetti, S., Elias-Rosa, N., Blanc, G., et al. 2004, IAU Circ., 8312
Benetti, S., Cappellaro, E., Mazzali, P. A., et al. 2005, ApJ, 623, 1011
Benvenuto, O. G., Bersten, M. C., & Nomoto, K. 2013, ApJ, 762, 74
Berlind, P., Matheson, T., & Calkins, M. 2003, IAU Circ., 8091, 2
Bersten, M. C., Benvenuto, O. G., Nomoto, K., et al. 2012, ApJ, 757, 31
Bianco, F. B., Modjaz, M., Hicken, M., et al. 2014, ApJS, 213, 19

Bietenholz, M. F., Brunthaler, A., Soderberg, A. M., et al. 2012, ApJ, 751, 125
Bilinski, C., Smith, N., Li, W., et al. 2015, MNRAS, 450, 246
Bjorkman, J. E., & Cassinelli, J. P. 1993, ApJ, 409, 429
Blanco, V. M., Gregory, B., Hamuy, M., et al. 1987, ApJ, 320, 589
Blondin, S., Modjaz, M., Kirshner, R., Challis, P., & Calkins, M. 2006, CBETs, 526
Blondin, S., & Tonry, J. L. 2007, ApJ, 666, 1024
Blondin, S., Matheson, T., Kirshner, R. P., et al. 2012, AJ, 143, 126
Bowen, D. V., Roth, K. C., Meyer, D. M., & Blades, J. C. 2000, ApJ, 536, 225
Branch, D., Dang, L. C., & Baron, E. 2009, PASP, 121, 238
Branch, D., Jeffery, D. J., Blaylock, M., & Hatano, K. 2000, PASP, 112, 217
Branch, D., Jeffery, D. J., Young, T. R., & Baron, E. 2006, PASP, 118, 791
Breeveld, A. A., Landsman, W., Holland, S. T., et al. 2011, in AIP Conference Series, ed. J. E. McEnery, J. L. Racusin, & N. Gehrels, Vol. 1358, 373
Brocklehurst, M. 1971, MNRAS, 153, 471
Brown, P. J., Breeveld, A. A., Holland, S., Kuin, P., & Pritchard, T. 2014, Ap&SS, 354, 89
Buzzoni, B., Delabre, B., Dekker, H., et al. 1984, The Messenger, 38, 9
Byard, P. L., & O'Brien, T. P. 2000, in Proc. SPIE, Vol. 4008, Optical and IR Telescope Instrumentation and Detectors, ed. M. Iye & A. F. Moorwood, 934
Campana, S., & Immler, S. 2012, MNRAS, 427, L70
Cano, Z. 2013, MNRAS, 434, 1098
Cao, Y., Kulkarni, S. R., Gal-Yam, A., et al. 2016, ApJ, 832, 86
Cao, Y., Kasliwal, M. M., Arcavi, I., et al. 2013, ApJ, 775, L7
Cao, Y., Kulkarni, S. R., Howell, D. A., et al. 2015, Nature, 521, 328
Cardelli, J. A., Clayton, G. C., & Mathis, J. S. 1989, ApJ, 345, 245
Chandra, P., Chevalier, R. A., Chugai, N., et al. 2012, ApJ, 755, 110
Chandra, P., Chevalier, R. A., Chugai, N., Fransson, C., & Soderberg, A. M. 2015, ApJ, 810, 32
Chevalier, R. A. 1998, ApJ, 499, 810
Chevalier, R. A., & Fransson, C. 1994, ApJ, 420, 268
Chevalier, R. A., & Irwin, C. M. 2011, ApJ, 729, L6
Choi, J., Dotter, A., Conroy, C., et al. 2016, ApJ, 823, 102
Chornock, R., Filippenko, A. V., Branch, D., et al. 2006, PASP, 118, 722
Chornock, R., Filippenko, A. V., Li, W., et al. 2011, ApJ, 739, 41
Chugai, N. N. 1991, MNRAS, 250, 513
—. 1992, Soviet Astronomy Letters, 18, 239
—. 2001, MNRAS, 326, 1448
—. 2009, MNRAS, 400, 866
Chugai, N. N., Blinnikov, S. I., Fassia, A., et al. 2002, MNRAS, 330, 473
Chugai, N. N., & Danziger, I. J. 1994, MNRAS, 268, 173
Chugai, N. N., Blinnikov, S. I., Cumming, R. J., et al. 2004, MNRAS, 352, 1213
Clayton, G. C., & Mathis, J. S. 1988, ApJ, 327, 911
Clocchiatti, A., Wheeler, J. C., Brotherton, M. S., et al. 1996, ApJ, 462, 462

Colgate, S. A., & McKee, C. 1969, ApJ, 157, 623
Colgate, S. A., & White, R. H. 1966, ApJ, 143, 626
Contardo, G., Leibundgut, B., & Vacca, W. D. 2000, A&A, 359, 876
Corsi, A., Ofek, E. O., Gal-Yam, A., et al. 2014, ApJ, 782, 42
Couch, S. M., & O'Connor, E. P. 2014, ApJ, 785, 123
Couch, S. M., & Ott, C. D. 2014, in AAS Meeting Abstracts, Vol. 223, 216.05
Coyne, G. V., & Gehrels, T. 1966, AJ, 71, 355
Coyne, G. V., & McLean, I. S. 1982, in IAU Symposium, Vol. 98, Be Stars, ed. M. Jaschek & H.-G. Groth, 77
Crowther, P. A. 2007, ARA&A, 45, 177
Davidson, K., Dufour, R. J., Walborn, N. R., & Gull, T. R. 1986, ApJ, 305, 867
de Vaucouleurs, G., de Vaucouleurs, A., Corwin, Jr., H. G., et al. 1991, Third Reference Catalogue of Bright Galaxies (Springer)
Dekker, H., Delabre, B., & Dodorico, S. 1986, in Proc. SPIE, Vol. 627, Instrumentation in astronomy VI, ed. D. L. Crawford, 339
Dessart, L., Hillier, D. J., Gezari, S., Basa, S., & Matheson, T. 2009, MNRAS, 394, 21
Dessart, L., Hillier, D. J., Li, C., & Woosley, S. 2012, MNRAS, 424, 2139
Dessart, L., Hillier, D. J., Livne, E., et al. 2011, MNRAS, 414, 2985
Dessart, L., Hillier, D. J., Woosley, S., et al. 2015, MNRAS, 453, 2189
—. 2016, MNRAS, 458, 1618
Dolphin, A. E. 2000, PASP, 112, 1383
Drout, M. R., Soderberg, A. M., Gal-Yam, A., et al. 2011, ApJ, 741, 97
Drout, M. R., Soderberg, A. M., Mazzali, P. A., et al. 2013, ApJ, 774, 58
Drout, M. R., Chornock, R., Soderberg, A. M., et al. 2014, ApJ, 794, 23
Dudley, C. C., & Fischer, J. 2004, CBETs, 57, 1
Eastman, R. G., Schmidt, B. P., & Kirshner, R. 1996, ApJ, 466, 911
Eldridge, J. J., Fraser, M., Smartt, S. J., Maund, J. R., & Crockett, R. M. 2013, MNRAS, 436, 774
Elias-Rosa, N., Benetti, S., Cappellaro, E., et al. 2006, MNRAS, 369, 1880
Elmhamdi, A., Danziger, I. J., Branch, D., et al. 2006, A&A, 450, 305
Ergon, M., Sollerman, J., Fraser, M., et al. 2014, A&A, 562, A17
Faber, S. M., Phillips, A. C., Kibrick, R. I., et al. 2003, in Proc. SPIE, Vol. 4841, Instrument Design and Performance for Optical/Infrared Ground-based Telescopes, ed. M. Iye & A. F. M. Moorwood, 1657
Fabricant, D., Cheimets, P., Caldwell, N., & Geary, J. 1998, PASP, 110, 79
Falco, E. E., Kurtz, M. J., Geller, M. J., et al. 1999, PASP, 111, 438
Faran, T., Poznanski, D., Filippenko, A. V., et al. 2014a, MNRAS, 445, 554
—. 2014b, MNRAS, 442, 844
Fassia, A., Meikle, W. P. S., Vacca, W. D., et al. 2000, MNRAS, 318, 1093
Fassia, A., Meikle, W. P. S., Chugai, N., et al. 2001, MNRAS, 325, 907
Feldmeier, J. J., Ciardullo, R., & Jacoby, G. H. 1997, ApJ, 479, 231
Filippenko, A. V. 1982, PASP, 94, 715

—. 1988, AJ, 96, 1941
—. 1989, AJ, 97, 726
Filippenko, A. V. 1991, in ESO Conference and Workshop Proceedings, ed. I. J. Danziger & K. Kjaer, Vol. 37, 343
—. 1997, ARA&A, 35, 309
Filippenko, A. V. 2003, in From Twilight to Highlight: The Physics of Supernovae, ed. W. Hillebrandt & B. Leibundgut, 171
Filippenko, A. V. 2005, in Astronomical Society of the Pacific Conference Series, ed. R. Humphreys & K. Stanek, Vol. 332, 34
Filippenko, A. V., & Chornock, R. 2001, IAU Circ., 7638, 1
Filippenko, A. V., Chornock, R., & Modjaz, M. 2001a, IAU Circ., 7579, 2
Filippenko, A. V., Chornock, R., Swift, B., et al. 2003, IAU Circ., 8159
Filippenko, A. V., Desroches, L., Ganeshalingam, M., Chornock, R., & Serduke, F. J. D. 2004, IAU Circ., 8331
Filippenko, A. V., & Foley, R. J. 2005, CBETs, 274, 1
Filippenko, A. V., Li, W. D., Treffers, R. R., & Modjaz, M. 2001b, in Astronomical Society of the Pacific Conference Series, ed. B. Paczynski, W.-P. Chen, & C. Lemme, Vol. 246, 121
Filippenko, A. V., Matheson, T., & Barth, A. J. 1994, AJ, 108, 2220
Filippenko, A. V., Matheson, T., & Ho, L. C. 1993, ApJ, 415, L103
Filippenko, A. V., Porter, A. C., & Sargent, W. L. W. 1990a, AJ, 100, 1575
Filippenko, A. V., & Sargent, W. L. W. 1989, ApJL, 345, L43
Filippenko, A. V., & Shields, J. C. 1990, IAU Circ., 5111
Filippenko, A. V., Shields, J. C., & Richmond, M. W. 1990b, IAU Circ., 5069
Filippenko, A. V., Barth, A. J., Matheson, T., et al. 1995, ApJ, 450, L11
Fisher, A. K. 2000, PhD thesis, The University Of Oklahoma
Folatelli, G., Contreras, C., Phillips, M. M., et al. 2006, ApJ, 641, 1039
Folatelli, G., Morrell, N., Phillips, M. M., et al. 2013, ApJ, 773, 53
Foley, R. J. 2015, MNRAS, 452, 2463
Foley, R. J., & Filippenko, A. V. 2002, IAU Circ., 8031, 4
Foley, R. J., & Mandel, K. 2013, ApJ, 778, 167
Foley, R. J., Silverman, J. M., Moore, M., & Filippenko, A. V. 2006, CBETs, 604, 1
Foley, R. J., Smith, N., Ganeshalingam, M., et al. 2007, ApJ, 657, L105
Foley, R. J., Wong, D. S., Ganeshalingam, M., Filippenko, A. V., & Chornock, R. 2004a, IAU Circ., 8339, 2
Foley, R. J., Wong, D. S., Moore, M., & Filippenko, A. V. 2004b, IAU Circ., 8353, 3
Foley, R. J., Zheng, W., Filippenko, A. V., & Dyk, S. D. V. 2015, ATel, 7298
Foley, R. J., Papenkova, M. S., Swift, B. J., et al. 2003, PASP, 115, 1220
Foley, R. J., Chornock, R., Filippenko, A. V., et al. 2009, AJ, 138, 376
Foley, R. J., Challis, P. J., Chornock, R., et al. 2013, ApJ, 767, 57
Foley, R. J., Fox, O. D., McCully, C., et al. 2014, MNRAS, 443, 2887
Fox, O. D., Filippenko, A. V., Skrutskie, M. F., et al. 2013, AJ, 146, 2

Fox, O. D., Chevalier, R. A., Skrutskie, M. F., et al. 2011, ApJ, 741, 7
Fransson, C. 1984, A&A, 133, 264
Fransson, C., & Chevalier, R. A. 1989, ApJ, 343, 323
Fransson, C., Chevalier, R. A., Filippenko, A. V., et al. 2002, ApJ, 572, 350
Fransson, C., Challis, P. M., Chevalier, R. A., et al. 2005, ApJ, 622, 991
Fransson, C., Ergon, M., Challis, P. J., et al. 2014, ApJ, 797, 118
Friedman, S. D., York, D. G., McCall, B. J., et al. 2011, ApJ, 727, 33
Gal-Yam, A. 2012, Science, 337, 927
Gal-Yam, A., Arcavi, I., Ofek, E. O., et al. 2014, Nature, 509, 471
Ganeshalingam, M., Li, W., & Filippenko, A. V. 2013, MNRAS, 433, 2240
Ganeshalingam, M., Li, W., Filippenko, A. V., et al. 2010, ApJS, 190, 418
—. 2012, ApJ, 751, 142
Garavini, G., Folatelli, G., Goobar, A., et al. 2004, AJ, 128, 387
Garavini, G., Aldering, G., Amadon, A., et al. 2005, AJ, 130, 2278
Garnett, D. R. 2002, ApJ, 581, 1019
Gehrels, N., Chincarini, G., Giommi, P., et al. 2004, ApJ, 611, 1005
Gehrels, T., & Silvester, A. B. 1965, AJ, 70, 579
Georgy, C., Meynet, G., Walder, R., Folini, D., & Maeder, A. 2009, A&A, 502, 611
Gerardy, C. L., Fesen, R. A., Höflich, P., & Wheeler, J. C. 2000, AJ, 119, 2968
Gerardy, C. L., Fesen, R. A., Nomoto, K., et al. 2002, ApJ, 575, 1007
Glassgold, A. E., & Huggins, P. J. 1986, ApJ, 306, 605
Gorbikov, E., Gal-Yam, A., Ofek, E. O., et al. 2014, MNRAS, 443, 671
Graham, J., Li, W., Trondal, O., & Schwartz, M. 2005, IAU Circ., 8467, 1
Graham, M. L., Sand, D. J., Valenti, S., et al. 2014, ApJ, 787, 163
Graur, O., Bianco, F. B., Huang, S., et al. 2017a, ApJ, 837, 120
Graur, O., Bianco, F. B., & Modjaz, M. 2015, MNRAS, 450, 905
Graur, O., Bianco, F. B., Modjaz, M., et al. 2017b, ApJ, 837, 121
Graur, O., & Maoz, D. 2013, MNRAS, 430, 1746
Griga, T., Marulla, A., Grenier, A., et al. 2011, CBETs, 2736, 1
Groh, J. H. 2014, A&A, 572, L11
Groh, J. H., Georgy, C., & Ekström, S. 2013a, A&A, 558, L1
Groh, J. H., Meynet, G., & Ekström, S. 2013b, A&A, 550, L7
Groh, J. H., Meynet, G., Georgy, C., & Ekström, S. 2013c, A&A, 558, A131
Guillochon, J., Parrent, J., Kelley, L. Z., & Margutti, R. 2017, ApJ, 835, 64
Hachinger, S., Mazzali, P. A., Taubenberger, S., et al. 2012, MNRAS, 422, 70
Hammer, N. J., Janka, H.-T., & Müller, E. 2010, ApJ, 714, 1371
Hamuy, M. 2003a, ApJ, 582, 905
—. 2003b, IAU Circ., 8103, 2
Hamuy, M., Maza, J., & Morrell, N. 2005, CBETs, 321, 1
Hamuy, M., & Roth, M. 2003, IAU Circ., 8228, 2
Hamuy, M., & Suntzeff, N. B. 1990, AJ, 99, 1146
Hamuy, M., Maza, J., Pinto, P. A., et al. 2002, AJ, 124, 417

Hamuy, M., Folatelli, G., Morrell, N. I., et al. 2006, PASP, 118, 2
Hamuy, M., Deng, J., Mazzali, P. A., et al. 2009, ApJ, 703, 1612
Hanke, F., Marek, A., Müller, B., & Janka, H.-T. 2012, ApJ, 755, 138
Hanuschik, R. W., Thimm, G., & Dachs, J. 1988, MNRAS, 234, 41P
Harper, G. M., Brown, A., & Lim, J. 2001, ApJ, 551, 1073
Harutyunyan, A. H., Pfahler, P., Pastorello, A., et al. 2008, A&A, 488, 383
Haynes, M. P., van Zee, L., Hogg, D. E., Roberts, M. S., & Maddalena, R. J. 1998, AJ, 115, 62
Heiles, C. 2000, AJ, 119, 923
Herbig, G. H. 1995, ARA&A, 33, 19
Hershkowitz, S., Linder, E., & Wagoner, R. V. 1986, ApJ, 301, 220
Hillier, D. J. 1991, A&A, 247, 455
Hillier, D. J., & Miller, D. L. 1998, ApJ, 496, 407
Horesh, A., Stockdale, C., Fox, D. B., et al. 2013, MNRAS, 436, 1258
Hosseinzadeh, G., Arcavi, I., Valenti, S., et al. 2017, ApJ, 836, 158
Houck, J. C., & Fransson, C. 1996, ApJ, 456, 811
Howell, D. A., Sullivan, M., Perrett, K., et al. 2005, ApJ, 634, 1190
Humphreys, R. M., & Davidson, K. 1994, PASP, 106, 1025
Humphreys, R. M., Weis, K., Davidson, K., & Gordon, M. S. 2016, ApJ, 825, 64
Hutchings, D., & Li, W. 2002, IAU Circ., 8026, 1
Ignace, R., Cassinelli, J. P., & Bjorkman, J. E. 1996, ApJ, 459, 671
Jeffery, D. J., & Branch, D. 1990, in Jerusalem Winter School for Theoretical Physics, ed. J. C. Wheeler, T. Piran, & S. Weinberg, 149
Jerkstrand, A., Fransson, C., Maguire, K., et al. 2012, A&A, 546, A28
Jha, S., Matheson, T., Challis, P., Kirshner, R., & Calkins, M. 2001, IAU Circ., 7566, 2
Jha, S., Challis, P., Kirshner, R., et al. 2000, IAU Circ., 7377, 2
Kamble, A., Soderberg, A. M., Chomiuk, L., et al. 2014, ApJ, 797, 2
Kamble, A., Margutti, R., Soderberg, A. M., et al. 2016, ApJ, 818, 111
Kankare, E., Ergon, M., Bufano, F., et al. 2012, MNRAS, 424, 855
Kasen, D., & Woosley, S. E. 2009, ApJ, 703, 2205
Kasliwal, M. M., Kulkarni, S. R., Gal-Yam, A., et al. 2010, ApJ, 723, L98
—. 2012, ApJ, 755, 161
Kelly, P. L., & Kirshner, R. P. 2012, ApJ, 759, 107
Khazov, D., Yaron, O., Gal-Yam, A., et al. 2016, ApJ, 818, 3
Kiewe, M., Gal-Yam, A., Arcavi, I., et al. 2012, ApJ, 744, 10
Kim, H.-J., Yoon, S.-C., & Koo, B.-C. 2015, ApJ, 809, 131
Kleiser, I. K. W., & Kasen, D. 2014, MNRAS, 438, 318
Kleiser, I. K. W., Poznanski, D., Kasen, D., et al. 2011, MNRAS, 415, 372
Krauss, M. I., Soderberg, A. M., Chomiuk, L., et al. 2012, ApJl, 750, L40
Krist, J. E., Hook, R. N., & Stoehr, F. 2011, in Proc. SPIE, Vol. 8127, Optical Modeling and Performance Predictions V, 81270J
Kumar, S., Yuk, H., Zheng, W., & Filippenko, A. V. 2015, CBETs, 4164, 1

Laidler, V. G., Greenfield, P., & Busko, I. andJedrzejewski, R. 2008, in SciPy Proceedings, ed. G. Varoquaux, T. Vaught, & J. Millman, Vol. 7, Pasadena, CA USA, 36
Lan, T.-W., Ménard, B., & Zhu, G. 2015, MNRAS, 452, 3629
Law, N. M., Kulkarni, S. R., Dekany, R. G., et al. 2009, PASP, 121, 1395
Leaman, J., Li, W., Chornock, R., & Filippenko, A. V. 2011, MNRAS, 412, 1419
Lee, E., Li, W., Boles, T., et al. 2005, IAU Circ., 8628, 1
Lentz, E. J., Baron, E., Lundqvist, P., et al. 2001, ApJ, 547, 406
Leonard, D. C., Filippenko, A. V., Barth, A. J., & Matheson, T. 2000, ApJ, 536, 239
Leonard, D. C., Filippenko, A. V., Chornock, R., & Foley, R. J. 2002a, PASP, 114, 1333
Leonard, D. C., Li, W., Filippenko, A. V., Foley, R. J., & Chornock, R. 2005, ApJ, 632, 450
Leonard, D. C., Filippenko, A. V., Li, W., et al. 2002b, AJ, 124, 2490
Leonard, D. C., Filippenko, A. V., Gates, E. L., et al. 2002c, PASP, 114, 35
Li, H., & McCray, R. 1992, ApJ, 387, 309
Li, W., Chornock, R., Leaman, J., et al. 2011a, MNRAS, 412, 1473
Li, W., & Filippenko, A. V. 2011, ATel, 3399, 1
Li, W., Filippenko, A. V., Chornock, R., & Jha, S. 2003, PASP, 115, 844
Li, W., Filippenko, A. V., Treffers, R. R., et al. 2001, ApJ, 546, 734
Li, W., Filippenko, A. V., Van Dyk, S. D., et al. 2002a, PASP, 114, 403
Li, W., Qui, Y., Qiao, Q., Hu, J., & Li, Q. 1999, Science in China A: Mathematics, 42, 1075
Li, W., Leaman, J., Chornock, R., et al. 2011b, MNRAS, 412, 1441
Li, W. D., Chornock, R., Filippenko, A. V., & Phillips, M. M. 2002b, IAU Circ., 7929, 3
Li, W.-D., Li, C., Filippenko, A. V., & Moran, E. C. 1998, IAU Circ., 6829, 1
Li, W. D., Filippenko, A. V., Treffers, R. R., et al. 2000, in AIP Conference Series, ed. S. S. Holt & W. W. Zhang, Vol. 522, 103
Liu, Y., & Modjaz, M. 2014, ArXiv e-prints, arXiv:1405.1437
Liu, Y.-Q., Modjaz, M., Bianco, F. B., & Graur, O. 2016, ApJ, 827, 90
Lobel, A., Dupree, A. K., Stefanik, R. P., et al. 2003, ApJ, 583, 923
Lucy, L. B. 1991, ApJ, 383, 308
Lunnan, R., Kasliwal, M. M., Cao, Y., et al. 2017, ApJ, 836, 60
Lyman, J. D., Bersier, D., James, P. A., et al. 2016, MNRAS, 457, 328
Madison, D. R., & Li, W. 2006, CBETs, 600, 1
Maeda, K., Kawabata, K., Mazzali, P. A., et al. 2008, Science, 319, 1220
Maoz, D., Mannucci, F., Li, W., et al. 2011, MNRAS, 412, 1508
Maoz, D., & Poznanski, D. 2015, ATel, 7563
Margutti, R., Milisavljevic, D., Soderberg, A. M., et al. 2014, ApJ, 780, 21
Margutti, R., Kamble, A., Milisavljevic, D., et al. 2017, ApJ, 835, 140
Marion, G. H., Vinko, J., Kirshner, R. P., et al. 2014, ApJ, 781, 69
Martins, F., & Hillier, D. J. 2012, A&A, 545, A95
Matheson, T. 2001, PASP, 113, 1155
Matheson, T., Challis, P., Kirshner, R., & Berlind, P. 2004a, IAU Circ., 8311
—. 2004b, CBETs, 57, 2
—. 2004c, IAU Circ., 8303, 1

Matheson, T., Challis, P., Kirshner, R., & Penev, K. 2004d, IAU Circ., 8353, 2
Matheson, T., Filippenko, A. V., Chornock, R., Leonard, D. C., & Li, W. 2000a, AJ, 119, 2303
Matheson, T., Filippenko, A. V., Li, W., Leonard, D. C., & Shields, J. C. 2001, AJ, 121, 1648
Matheson, T., Filippenko, A. V., Barth, A. J., et al. 2000b, AJ, 120, 1487
Matheson, T., Kirshner, R. P., Challis, P., et al. 2008, AJ, 135, 1598
Mattila, S., Meikle, W. P. S., Lundqvist, P., et al. 2008, MNRAS, 389, 141
Mauerhan, J., & Smith, N. 2012, MNRAS, 424, 2659
Mauerhan, J. C., Smith, N., Silverman, J. M., et al. 2013a, MNRAS, 431, 2599
Mauerhan, J. C., Smith, N., Filippenko, A. V., et al. 2013b, MNRAS, 430, 1801
Mauerhan, J. C., Williams, G. G., Leonard, D. C., et al. 2015, MNRAS, 453, 4467
Maund, J. R., Pastorello, A., Mattila, S., Itagaki, K., & Boles, T. 2016, ApJ, 833, 128
Maund, J. R., Smartt, S. J., Kudritzki, R. P., Podsiadlowski, P., & Gilmore, G. F. 2004, Nature, 427, 129
Maund, J. R., Smartt, S. J., Kudritzki, R.-P., et al. 2006, MNRAS, 369, 390
Maund, J. R., Fraser, M., Ergon, M., et al. 2011, ApJ, 739, L37
Maurer, I., Mazzali, P. A., Taubenberger, S., & Hachinger, S. 2010, MNRAS, 409, 1441
Mazzali, P. A., Deng, J., Hamuy, M., & Nomoto, K. 2009, ApJ, 703, 1624
Mazzali, P. A., & Hachinger, S. 2012, MNRAS, 424, 2926
Mazzali, P. A., Maurer, I., Valenti, S., Kotak, R., & Hunter, D. 2010, MNRAS, 408, 87
Mazzali, P. A., Nomoto, K., Patat, F., & Maeda, K. 2001, ApJ, 559, 1047
Mazzali, P. A., Deng, J., Maeda, K., et al. 2002, ApJ, 572, L61
Mazzali, P. A., Kawabata, K. S., Maeda, K., et al. 2005, Science, 308, 1284
—. 2007, ApJ, 670, 592
McCray, R. 1993, ARA&A, 31, 175
Meixner, M., Smee, S., Doering, R. L., et al. 2008, in Proc. SPIE, Vol. 7014, Ground-based and Airborne Instrumentation for Astronomy II, 70142W
Meynet, G., & Maeder, A. 2003, A&A, 404, 975
Milisavljevic, D., Fesen, R. A., Gerardy, C. L., Kirshner, R. P., & Challis, P. 2010, ApJ, 709, 1343
Milisavljevic, D., Margutti, R., Soderberg, A. M., et al. 2013, ApJ, 767, 71
Milisavljevic, D., Margutti, R., Kamble, A., et al. 2015, ApJ, 815, 120
Miller, J., & Stone, R. 1993, Lick Observatory Techical Reports, 66
Modjaz, M., Kewley, L., Bloom, J. S., et al. 2011, ApJ, 731, L4
Modjaz, M., Kirshner, R., Challis, P., Blondin, S., & Berlind, P. 2005, CBETs, 342, 1
Modjaz, M., Kirshner, R. P., Blondin, S., Challis, P., & Matheson, T. 2008a, ApJ, 687, L9
Modjaz, M., Li, W., Filippenko, A. V., et al. 2001, PASP, 113, 308
Modjaz, M., Liu, Y. Q., Bianco, F. B., & Graur, O. 2016, ApJ, 832, 108
Modjaz, M., Kewley, L., Kirshner, R. P., et al. 2008b, AJ, 135, 1136
Modjaz, M., Li, W., Butler, N., et al. 2009, ApJ, 702, 226
Modjaz, M., Blondin, S., Kirshner, R. P., et al. 2014, AJ, 147, 99

Monard, L. A. G., & Li, W. 2004, IAU Circ., 8350, 2
Moriya, T., Tominaga, N., Blinnikov, S. I., Baklanov, P. V., & Sorokina, E. I. 2011, MNRAS, 415, 199
Moriya, T. J., Maeda, K., Taddia, F., et al. 2014, MNRAS, 439, 2917
Murphy, J. W., Jennings, Z. G., Williams, B., Dalcanton, J. J., & Dolphin, A. E. 2011, ApJ, 742, L4
Nachman, P., & Hobbs, L. M. 1973, ApJ, 182, 481
Nakano, S., Itagaki, K., Puckett, T., & Gorelli, R. 2006, CBETs, 666, 1
Newton, J., & Puckett, T. 2005, CBETs, 336
Nomoto, K., Tominaga, N., Umeda, H., Kobayashi, C., & Maeda, K. 2006, Nuclear Physics A, 777, 424
Ochner, P., Benetti, S., Pastorello, A., et al. 2015, ATel, 7105, 1
Ofek, E. O., Cameron, P. B., Kasliwal, M. M., et al. 2007, ApJ, 659, L13
Ofek, E. O., Rabinak, I., Neill, J. D., et al. 2010, ApJ, 724, 1396
Ofek, E. O., Sullivan, M., Shaviv, N. J., et al. 2014, ApJ, 789, 104
Oke, J. B., Cohen, J. G., Carr, M., et al. 1995, PASP, 107, 375
Osterbrock, D. E., & Ferland, G. J. 2006, Astrophysics of gaseous nebulae and active galactic nuclei (University Science Books)
Parrent, J., Branch, D., Troxel, M. A., et al. 2007, PASP, 119, 135
Parrent, J. T., Milisavljevic, D., Soderberg, A. M., & Parthasarathy, M. 2016, ApJ, 820, 75
Pastorello, A., Taubenberger, S., Patat, F., et al. 2005a, IAU Circ., 8467, 2
Pastorello, A., Zampieri, L., Turatto, M., et al. 2004, MNRAS, 347, 74
Pastorello, A., Baron, E., Branch, D., et al. 2005b, MNRAS, 360, 950
Pastorello, A., Smartt, S. J., Mattila, S., et al. 2007, Nature, 447, 829
Pastorello, A., Mattila, S., Zampieri, L., et al. 2008a, MNRAS, 389, 113
Pastorello, A., Quimby, R. M., Smartt, S. J., et al. 2008b, MNRAS, 389, 131
Pastorello, A., Kasliwal, M. M., Crockett, R. M., et al. 2008c, MNRAS, 389, 955
Pastorello, A., Pumo, M. L., Navasardyan, H., et al. 2012, A&A, 537, A141
Pastorello, A., Benetti, S., Brown, P. J., et al. 2015a, MNRAS, 449, 1921
Pastorello, A., Hadjiyska, E., Rabinowitz, D., et al. 2015b, MNRAS, 449, 1954
Pastorello, A., Tartaglia, L., Elias-Rosa, N., et al. 2015c, MNRAS, 454, 4293
Pastorello, A., Wang, X.-F., Ciabattari, F., et al. 2016, MNRAS, 456, 853
Patat, F., Chugai, N., & Mazzali, P. A. 1995, A&A, 299, 715
Patat, F., Chandra, P., Chevalier, R., et al. 2007, Science, 317, 924
Patat, F., Taubenberger, S., Cox, N. L. J., et al. 2015, A&A, 577, A53
Paxton, B., Bildsten, L., Dotter, A., et al. 2011, ApJS, 192, 3
Paxton, B., Cantiello, M., Arras, P., et al. 2013, ApJS, 208, 4
Paxton, B., Marchant, P., Schwab, J., et al. 2015, ApJS, 220, 15
Pereira-Santaella, M., Alonso-Herrero, A., Colina, L., et al. 2015, A&A, 577, A78
Perets, H. B., Gal-Yam, A., Mazzali, P. A., et al. 2010, Nature, 465, 322
Pérez, F., & Granger, B. E. 2007, Computing in Science and Engineering, 9, 21
Peri, C. S., Benaglia, P., & Isequilla, N. L. 2015, A&A, 578, A45

Petre, R., Becker, C. M., & Winkler, P. F. 1996, ApJ, 465, L43
Phillips, M. M., & Heathcote, S. R. 1989, PASP, 101, 137
Phillips, M. M., Li, W., Frieman, J. A., et al. 2007, PASP, 119, 360
Phillips, M. M., Simon, J. D., Morrell, N., et al. 2013, ApJ, 779, 38
Piascik, A. S., Steele, I. A., Bates, S. D., et al. 2014, in Proc. SPIE, Vol. 9147, Ground-based and Airborne Instrumentation for Astronomy V, 91478H
Podsiadlowski, P., Joss, P. C., & Hsu, J. J. L. 1992, ApJ, 391, 246
Poole, T. S., Breeveld, A. A., Page, M. J., et al. 2008, MNRAS, 383, 627
Pooley, D., Lewin, W. H. G., Fox, D. W., et al. 2002, ApJ, 572, 932
Popov, D. V. 1993, ApJ, 414, 712
Poznanski, D., Prochaska, J. X., & Bloom, J. S. 2012, MNRAS, 426, 1465
Poznanski, D., Butler, N., Filippenko, A. V., et al. 2009, ApJ, 694, 1067
Poznanski, D., Chornock, R., Nugent, P. E., et al. 2010, Science, 327, 58
Prentice, S. J., Mazzali, P. A., Pian, E., et al. 2016, MNRAS, 458, 2973
Puckett, T., Tigner, D., & Sehgal, A. 2002, IAU Circ., 8037, 1
Qiu, Y. L., Yoshida, S., Merlin, J. C., & Schmeer, P. 1998, IAU Circ., 6835, 1
Quataert, E., & Shiode, J. 2012, MNRAS, 423, L92
Qui, Y., Li, W., Zhao, Z., et al. 1999, Science in China A: Mathematics, 42, 220
Rabinak, I., & Waxman, E. 2011, ApJ, 728, 63
Rau, A., Kulkarni, S. R., Law, N. M., et al. 2009, PASP, 121, 1334
Riess, A. G., Filippenko, A. V., Li, W., et al. 1999, AJ, 118, 2675
Rockosi, C., Stover, R., Kibrick, R., et al. 2010, in Proc. SPIE, Vol. 7735, Ground-based and Airborne Instrumentation for Astronomy III, 77350R
Roming, P. W. A., Kennedy, T. E., Mason, K. O., et al. 2005, Space Sci. Rev., 120, 95
Roy, R., Kumar, B., Maund, J. R., et al. 2013, MNRAS, 434, 2032
Rubin, A., & Gal-Yam, A. 2016, ApJ, 828, 111
Rubin, A., Gal-Yam, A., De Cia, A., et al. 2016, ApJ, 820, 33
Ruiz-Lapuente, P., & Lucy, L. B. 1992, ApJ, 400, 127
Rush, B., Malkan, M. A., & Edelson, R. A. 1996, ApJ, 473, 130
Sahu, D. K., Anupama, G. C., & Chakradhari, N. K. 2013, MNRAS, 433, 2
Sahu, D. K., Anupama, G. C., Srividya, S., & Muneer, S. 2006, MNRAS, 372, 1315
Sakon, I., Onaka, T., Wada, T., et al. 2009, ApJ, 692, 546
Sana, H., de Mink, S. E., de Koter, A., et al. 2012, Science, 337, 444
Sanders, N. E., Soderberg, A. M., Foley, R. J., et al. 2013, ApJ, 769, 39
Sanders, N. E., Soderberg, A. M., Gezari, S., et al. 2015, ApJ, 799, 208
Sasaki, M., & Ducci, L. 2012, A&A, 546, A80
Sato, Y., Li, W. D., & Puckett, T. 2000, IAU Circ., 7374, 1
Sauer, D. N., Mazzali, P. A., Blondin, S., et al. 2008, MNRAS, 391, 1605
Schlafly, E. F., & Finkbeiner, D. P. 2011, ApJ, 737, 103
Schlegel, D. J., Finkbeiner, D. P., & Davis, M. 1998, ApJ, 500, 525
Schlegel, E. M. 1990, MNRAS, 244, 269
Schmidt, G. D., Weymann, R. J., & Foltz, C. B. 1989, PASP, 101, 713

Schulte-Ladbeck, R. F., Nordsieck, K. H., Taylor, M., et al. 1992, ApJ, 387, 347
Sehgal, A., Gagliano, R., & Puckett, T. 2006, CBETs, 493, 1
Serkowski, K., Mathewson, D. S., & Ford, V. L. 1975, ApJ, 196, 261
Sheinis, A. I., Bolte, M., Epps, H. W., et al. 2002, PASP, 114, 851
Shivvers, I., Groh, J. H., Mauerhan, J. C., et al. 2015, ApJ, 806, 213
Shivvers, I., Mazzali, P., Silverman, J. M., et al. 2013, MNRAS, 436, 3614
Shivvers, I., Zheng, W. K., Mauerhan, J., et al. 2016, MNRAS, 461, 3057
Shivvers, I., Modjaz, M., Zheng, W., et al. 2017a, PASP, 129, 054201
Shivvers, I., Zheng, W., Van Dyk, S. D., et al. 2017b, ArXiv e-prints, arXiv:1704.04316
Silverman, J. M., Filippenko, A. V., & Cenko, S. B. 2011, ATel, 3398, 1
Silverman, J. M., Kleiser, I. K. W., Morton, A. J. L., & Filippenko, A. V. 2010, CBETs, 2223
Silverman, J. M., Mazzali, P., Chornock, R., et al. 2009, PASP, 121, 689
Silverman, J. M., Foley, R. J., Filippenko, A. V., et al. 2012, MNRAS, 425, 1789
Silverman, J. M., Nugent, P. E., Gal-Yam, A., et al. 2013a, ApJ, 772, 125
—. 2013b, ApJS, 207, 3
Singer, D., Pugh, H., & Li, W. 2004, IAU Circ., 8297, 2
Skrutskie, M. F., Cutri, R. M., Stiening, R., et al. 2006, AJ, 131, 1163
Smartt, S. J. 2009, ARA&A, 47, 63
Smartt, S. J., Eldridge, J. J., Crockett, R. M., & Maund, J. R. 2009, MNRAS, 395, 1409
Smith, L. F. 1968, MNRAS, 138, 109
Smith, L. F., Shara, M. M., & Moffat, A. F. J. 1996, MNRAS, 281, 163
Smith, N. 2010, MNRAS, 402, 145
—. 2014, ARA&A, 52, 487
Smith, N., Andrews, J. E., & Mauerhan, J. C. 2016, MNRAS, 463, 2904
Smith, N., & Arnett, W. D. 2014, ApJ, 785, 82
Smith, N., Chornock, R., Silverman, J. M., Filippenko, A. V., & Foley, R. J. 2010, ApJ, 709, 856
Smith, N., Foley, R. J., & Filippenko, A. V. 2008, ApJ, 680, 568
Smith, N., Gehrz, R. D., Campbell, R., et al. 2011a, MNRAS, 418, 1959
Smith, N., Hinkle, K. H., & Ryde, N. 2009, AJ, 137, 3558
Smith, N., Li, W., Filippenko, A. V., & Chornock, R. 2011b, MNRAS, 412, 1522
Smith, N., Li, W., Silverman, J. M., Ganeshalingam, M., & Filippenko, A. V. 2011c, MNRAS, 415, 773
Smith, N., Mauerhan, J. C., Silverman, J. M., et al. 2012, MNRAS, 426, 1905
Smith, N., & Tombleson, R. 2015, MNRAS, 447, 598
Smith, N., Mauerhan, J. C., Cenko, S. B., et al. 2015, MNRAS, 449, 1876
Soderberg, A. M. 2007, in AIP Conference Series, ed. S. Immler, K. Weiler, & R. McCray, Vol. 937, 492
Soderberg, A. M., Margutti, R., Zauderer, B. A., et al. 2012, ApJ, 752, 78
Somerville, W. B. 1988, The Observatory, 108, 44
Sternberg, A., Gal-Yam, A., Simon, J. D., et al. 2011, Science, 333, 856

Stetson, P. B. 1987, PASP, 99, 191
Stritzinger, M., Mazzali, P., Phillips, M. M., et al. 2009, ApJ, 696, 713
Strömgren, B. 1948, ApJ, 108, 242
Suntzeff, N., Colianni, J., Gokas, T., et al. 2001, IAU Circ., 7576, 5
Suntzeff, N. B., Phillips, M. M., Elias, J. H., Walker, A. R., & Depoy, D. L. 1992, ApJ, 384, L33
Suwa, Y., Kotake, K., Takiwaki, T., et al. 2010, PASJ, 62, L49
Swift, B., & Li, W. 2003, IAU Circ., 8090, 1
Swift, B., Li, W. D., & Filippenko, A. V. 2001, IAU Circ., 7618, 1
Taddia, F., Stritzinger, M. D., Sollerman, J., et al. 2012, A&A, 537, A140
Taddia, F., Sollerman, J., Leloudas, G., et al. 2015, A&A, 574, A60
Taddia, F., Fremling, C., Sollerman, J., et al. 2016a, A&A, 592, A89
Taddia, F., Sollerman, J., Fremling, C., et al. 2016b, A&A, 588, A5
Taubenberger, S., Valenti, S., Benetti, S., et al. 2009, MNRAS, 397, 677
Taubenberger, S., Navasardyan, H., Maurer, J. I., et al. 2011, MNRAS, 413, 2140
Thielemann, F.-K., Nomoto, K., & Hashimoto, M.-A. 1996, ApJ, 460, 408
Thomas, R. C., Nugent, P. E., & Meza, J. C. 2011, PASP, 123, 237
Tomasella , L., Benetti, S., Cappellaro, E., et al. 2014, Astronomische Nachrichten, 335, 841
Tominaga, N., Tanaka, M., Nomoto, K., et al. 2005, ApJ, 633, L97
Tonry, J., & Davis, M. 1979, AJ, 84, 1511
Tonry, J. L., Dressler, A., Blakeslee, J. P., et al. 2001, ApJ, 546, 681
Tsvetkov, D. Y., Volkov, I. M., & Pavlyuk, N. N. 2015, Information Bulletin on Variable Stars, 6140, 1
Tsvetkov, D. Y., Volkov, I. M., Sorokina, E., et al. 2012, Peremennye Zvezdy, 32
Tully, R. B. 1974, ApJS, 27, 437
—. 1994, VizieR Online Data Catalog, 7145, 0
Tully, R. B., & Fisher, J. R. 1988, Catalog of Nearby Galaxies (Cambridge University Press)
Utrobin, V. P., Chugai, N. N., & Andronova, A. A. 1995, A&A, 295, 129
Valenti, S., Fraser, M., Benetti, S., et al. 2011, MNRAS, 416, 3138
Valenti, S., Howell, D. A., Stritzinger, M. D., et al. 2016, MNRAS, 459, 3939
Van Dyk, S. D., Li, W., Filippenko, A. V., et al. 2006, ArXiv e-prints, astro-ph/0603025
Van Dyk, S. D., Peng, C. Y., King, J. Y., et al. 2000, PASP, 112, 1532
Van Dyk, S. D., Li, W., Cenko, S. B., et al. 2011, ApJ, 741, L28
Van Dyk, S. D., Zheng, W., Clubb, K. I., et al. 2013, ApJ, 772, L32
Verheijen, M. A. W., & Sancisi, R. 2001, A&A, 370, 765
Vinkó, J., Takáts, K., Szalai, T., et al. 2012, A&A, 540, A93
Vogt, S. S., Allen, S. L., Bigelow, B. C., et al. 1994, in Proc. SPIE, Vol. 2198, Instrumentation in Astronomy VIII, ed. D. L. Crawford & E. R. Craine, 362
Wagner, R. M., Vrba, F. J., Henden, A. A., et al. 2004, PASP, 116, 326
Wang, L., Howell, D. A., Höflich, P., & Wheeler, J. C. 2001, ApJ, 550, 1030
Wang, X., Filippenko, A. V., Ganeshalingam, M., et al. 2009a, ApJ, 699, L139
Wang, X., Li, W., Filippenko, A. V., et al. 2009b, ApJ, 697, 380

Wellons, S., Soderberg, A. M., & Chevalier, R. A. 2012, ApJ, 752, 17
Weyant, A., Wood-Vasey, W. M., Allen, L., et al. 2014, ApJ, 784, 105
Wheeler, J. C., & Harkness, R. P. 1990, Reports on Progress in Physics, 53, 1467
Wheeler, J. C., Harkness, R. P., Clocchiatti, A., et al. 1994, ApJ, 436, L.135
Wheeler, J. C., Johnson, V., & Clocchiatti, A. 2015, MNRAS, 450, 1295
White, C. J., Kasliwal, M. M., Nugent, P. E., et al. 2015, ApJ, 799, 52
Whittet, D. C. B., Martin, P. G., Hough, J. H., et al. 1992, ApJ, 386, 562
Woosley, S. E., & Bloom, J. S. 2006, ARA&A, 44, 507
Woosley, S. E., Heger, A., & Weaver, T. A. 2002, Reviews of Modern Physics, 74, 1015
Woosley, S. E., Langer, N., & Weaver, T. A. 1995, ApJ, 448, 315
Woosley, S. E., Pinto, P. A., Martin, P. G., & Weaver, T. A. 1987, ApJ, 318, 664
Wright, E. L. 2006, PASP, 118, 1711
Yaron, O., & Gal-Yam, A. 2012, PASP, 124, 668
Yoon, S.-C. 2015, PASA, 32, e015
Yoon, S.-C., Woosley, S. E., & Langer, N. 2010, ApJ, 725, 940
Yusa, T., Buczynski, D., Noguchi, T., et al. 2015, CBETs, 4087
Zickgraf, F.-J., Wolf, B., Stahl, O., Leitherer, C., & Klare, G. 1985, A&A, 143, 421